Improved Equipment and Techniques for Dynamic Shimming in High Field MRI

by

Michael Poole, MSci.

Thesis submitted to
The University of Nottingham
for the degree of
Doctor of Philosophy

August 2007

Contents

Abstract

The work in this thesis is primarily concerned with overcoming technical challenges involved in implementing dynamic shimming for high field ($\geq$ 3 T) magnetic resonance imaging (MRI). The methods developed here to improve the equipment and techniques for dynamic shimming have additionally lead to advanced gradient and shim coil design, as well as opening up new avenues of research related to the development of novel hardware and techniques for MRI.

One obstacle to the advancement of high field MRI is the problem of susceptibility-induced magnetic field inhomogeneities, which cause image distortion and signal losses which become increasingly severe at high static field strengths. Dynamic shimming is one promising technique for ameliorating these effects. However, most MR scanners would require additional hardware in order to implement dynamic shimming.

Here, a set of insertable head gradient and shim coils with low inductance as required for dynamic shimming has been designed. Limits on the radii of the coil set meant that the shoulders of subjects be accommodated by the geometry. These gradient and shim coils were designed, using an inverse boundary element method (IBEM), with slots removed from the otherwise cylindrical surface geometry. This coil set was built with collaboration from Magnex Scientific Ltd. (now Varian Inc., Yarnton, Oxon, UK.) and tested at 3T. The IBEM was found to be an extremely powerful method by which many more gradient, shim and other coils with asymmetric geometries have been designed.

A generalised version of dynamic shimming has been developed that is shown by simulation to reduce magnetic field inhomogeneity to a greater extent than conventional dynamic shimming. Parcellated dynamic shimming involves shimming cuboidal sub-volumes of the whole volume and achieves a similar homogeneity with linear shims as conventional dynamic shimming with up to 3^{rd} order shims, potentially reducing the need for extra hardware.

Another novel shimming technique is developed here using prinipal component analysis to design a set of shim coils that generate the common shape of magnetic fields inside the head.

Acknowledgements

I would like to take this opportunity to express my gratitude to all those that have helped me during my PhD study.

First and foremost I would like thank my supervisor, **Professor Richard Bowtell**, for giving me the opportunity to work with him on this project and for then deftly guiding me through it. His inspired ideas have made this project what it is.

This project was jointly funded by the EPSRC, and by Magnex Scientific Ltd., now part of Varian Inc., Yarnton, Oxon., UK. Dan Green, Simon Pittard and Steve Harrison at Magnex have been a great help in making this project happen.

I would like to thank the following people from the Sir Peter Mansfield Magnetic Resonance Centre at the University of Nottingham; James Leggett and Jose Marques for helping me to get started and Clemente Cobos Sanchez for helping me to get finished, Arthur Magill and Andrew Peters for their much needed technical computing support, Olivier Mougin and Christopher Short for their phase unwrapping skills and all the rest of my colleagues that I have been fortunate enough to share a building with.

I also appreciate the engineering expertise that no academic could have afforded me, particularly Malcolm at Magnex, Ian Thexton and Jeff Smith at the SPMMRC and Simon Harrison and Andrew Stone at the School of Mechanical, Materials & Manufacturing Engineering at the University of Nottingham.

I would have been driven to despair long ago if it were not for the welcome distractions of my good friends Ben, Dan, Chris and Clemente. A special thank you goes to Fran, who has been my inspiration at all times.

I would finally like to thank my parents for supporting me throughout my education and my Grandpa for enthusing me to watch the Christmas lectures.

Chapter 1

Introduction

Since Mansfield and Maudsley's first *in vivo* cross-sectional nuclear magnetic resonance (NMR) images of a finger in 1977 [1], magnetic resonance imaging (MRI) has developed rapidly into the routine diagnostic imaging modality it is today. This technological development has been motivated by its many uses in clinical diagnostics, and accelerated by the innovations of the basic scientists and engineers. MRI has played its part in early diagnosis of many diseases, particularly cancer, and has saved many lives.

The principal component of the MRI scanner is the large electromagnet that generates an intense magnetic field. There is an increase in the signal-to-noise ratio (SNR) in MRI with increasing magnetic field strength. Since nuclear magnetic resonance (NMR) signals, the basis of MRI, are inherently weak, the striving for high SNR is fuelling the desire for ever more powerful superconducting magnets to generate stronger magnetic fields. This increase in field strength is accompanied by many technical challenges arising from the physical interaction between the MRI scanner and the object being scanned.

One such challenge is the requirement in MRI for the static magnetic field to be highly homogeneous. For empty scanners, this is an engineering challenge that can be met by fine adjustments in the design of the MRI scanners. However, when an object is placed in the scanner, differences in magnetic susceptibility within it cause object-specific magnetic field inhomogeneities to be generated. More specifically, living organisms are composed of different tissues possessing different magnetic susceptibilities with complex morphology. Magnetic fields are generated at the interface between tissues of different magnetic susceptibility, proportional to the strength of the static magnetic field.

Inhomogeneities in the static magnetic field can cause geometric distortion of images, loss of signal, reduction of sensitivity to the blood oxygenation level dependent (BOLD) contrast, the signal behind functional MRI (fMRI), and many more problems besides. Reduction of

the susceptibility-induced magnetic field inhomogeneities is essential to allow new methods to be developed for high field MRI, and to open up previously inaccessible avenues of research.

There are many ways to perform shimming, the method by which the magnetic field is made more homogeneous. Commonly, a set of current carrying coils of wire that each generate a different spherical harmonic shaped magnetic field are provided for shimming on a subject-specific basis. The currents in these shim coils are set to cancel maximally the susceptibility-induced magnetic field inhomogeneities. Because the inhomogeneities are generated locally and the magnetic fields of the shim coils are generated externally, shimming cannot be perfect since static magnetic fields are not focusable. The shimming performance has previously been shown to be increased by dynamic shimming, a method whereby shimming of each slice individually is performed for a multi-slice data acquisition. Because the extent of the shimming region is reduced, the efficacy of dynamic shimming is increased over that of conventional global shimming given the same number of shim coils.

There are however, some technical challenges that need to be overcome in order to implement dynamic shimming since the hardware supplied with most MRI scanners is not compatible with dynamic shimming. In this work we aim to overcome some of these hardware challenges, and propose a novel, more effective solution to the shimming problem.

1.1 Scope of this Thesis

The first chapter of this thesis describes the basic physical principles required to understand the content of the rest of the thesis. It is assumed that the reader has university-level physics knowledge, or at least an enthusiastic attitude to learning the physical principles herein. It begins, somewhat abruptly, with Maxwell's equations, which were a landmark achievement in physics which, at the end of the 19^{th} century, prompted some to consider that "the only occupation which will be left to men of science will be to carry these measurements to another place of decimals"[1], shortly before the advent of quantum theory and the theory of special relativity.

Maxwell's equations provide a general description of electromagnetism. In the subsequent sections a number of assumptions about the length and time scales to be considered are used to simplify the form of Maxwell's equations employed in later work. Magnetic susceptibility is also described with relevance to this work.

Two mathematical sections are provided for the reader on the subjects of spherical harmonics, and Fourier transforms, key concepts for this thesis and for MRI in general.

[1] James Clerk Maxwell *Scientific Papers* **2**, 244, October 1871. In vehement opposition to this view.

The next section goes on to describe the nuclear magnetic resonance (NMR) phenomenon, and its application in magnetic resonance imaging (MRI) briefly. The key concepts and common methods in MRI are described at a level of detail that befits this thesis, and references to further detailed discussions on these topics are given in the text. Lastly a diagram showing the principal hardware components of a typical MRI scanner is shown.

The third and fourth chapters form literature reviews of the subjects of shimming and coil design. These give a detailed, though not exhaustive, perspective on the subjects so as to set in place the context within which this work may be placed.

Chapter 5 details inverse boundary element method (IBEM) coil design in mathematical, and practical terms. It is hoped that this chapter gives the reader a self-contained recipe for implementing the IBEM for coil design.

Examples of how this IBEM can be used to design a wide variety of coils are given in Chapter 6 to demonstrate the power and versatility of our implementation of this method. Thirteen examples of coil design problems that have been solved or improved with this method are presented here, including gradient coils, shim coils and coils that generate asymmetric magnetic fields.

Chapter 7 presents work on parcellated dynamic shimming. This method is an extension of the shimming technique used to homogenise the magnetic field during an MRI scan. It is shown by simulation that this method has the potential to out-perform the shimming capabilities of conventional dynamic shimming and may also reduce the requirement for extra hardware at the expense of increased complexity of data acquisition.

The final chapter in the main body of this thesis is a discussion of the research presented here. Brief details of where the work of this thesis might lead and future projects that would naturally follow from this work are also detailed.

The end matter of this thesis is composed of a Bibliography and an Appendix. The latter details the properties of all the coils described in this thesis. It is intended to serve as a way of comparing the performance of these coils with each other and with coils presented by other authors.

Chapter 2

Basic Principles

In this chapter, the physical principles pertinent to the work in this thesis are outlined. Firstly, in § 2.1, the essential electromagnetic theory and in particular, electrostatics is explained briefly, primarily adapted from Jackson [2]. This is followed, in § 2.2 and § 2.3, by the mathematics of spherical harmonics and Fourier transforms. In § 2.4, a description of the nuclear magnetic resonance (NMR) phenomenon is given, followed by, in § 2.5, a discussion of how NMR can be exploited to gather information about the internal properties of objects with magnetic resonance imaging (MRI). The basic theories on which MRI is founded have already been explained in detail in a number of authoritative texts [3, 4].

2.1 Electromagnetism

Maxwell's equations form the starting point for all electromagnetic analysis. Equations (2.1) to (2.4) are the differential forms of Gauss's Law, Ampere's law, Faraday's law, and Gauss's law (magnetic) respectively,

$$\nabla \cdot \mathbf{D} = \rho \tag{2.1}$$

$$\nabla \times \mathbf{H} - \frac{\partial \mathbf{D}}{\partial t} = \mathbf{J} \tag{2.2}$$

$$\nabla \times \mathbf{E} - \frac{\partial \mathbf{B}}{\partial t} = 0 \tag{2.3}$$

$$\nabla \cdot \mathbf{B} = 0. \tag{2.4}$$

Here $\mathbf{D}$ is the displacement and $\mathbf{E}$ is the electric field, related to each other by $\mathbf{D} = \epsilon\mathbf{E}$ where ϵ is the dielectric constant of the media; ρ is the charge density; $\mathbf{H}$ is the magnetic field and $\mathbf{B}$ is the magnetic induction, related to each other by $\mathbf{B} = \mu\mathbf{H}$ where μ is the

magnetic permeability of the media; $\mathbf{J}$ is the current density related to $\mathbf{E}$ by $\mathbf{J} = \sigma\mathbf{E}$, where σ is the conductivity of the material.

The continuity equation (2.5) is also employed in electromagnetic studies, and can be derived from Eqs. (2.1) and (2.2).

$$\frac{\partial \rho}{\partial t} + \nabla \cdot \mathbf{J} = 0 \tag{2.5}$$

2.1.1 Magnetostatics

The current work primarily involves magnetostatics, the study of time-invariant magnetic fields. Hence, in the absence of magnetic materials, Ampere's law (2.2) reduces to

$$\nabla \times \mathbf{B} = \mu_0 \mathbf{J} \tag{2.6}$$

where μ_0 is the permeability of free space and is equal to $4\pi \times 10^{-7}$ $\mathrm{WbA^{-1}m^{-1}}$. Furthermore, the continuity equation (2.5) reduces to

$$\nabla \cdot \mathbf{J} = 0. \tag{2.7}$$

2.1.2 Source-Free Magnetostatics

In regions of space containing no charge density, ρ, the equations that govern the magnetic fields reduce even further,

$$\nabla \cdot \mathbf{B} = 0 \tag{2.8}$$

$$\nabla \times \mathbf{B} = 0. \tag{2.9}$$

Then, using the vector identity $\nabla \times \nabla \times \mathbf{B} = \nabla(\nabla \cdot \mathbf{B}) - \nabla^2 \mathbf{B}$ (2.8) and (2.9) yield Laplace's equation

$$\nabla^2 \mathbf{B} = 0 \tag{2.10}$$

The Laplace operator, ∇^2, applied to each component of the magnetic flux density must therefore be equal to zero. If only the z-component of the magnetic flux density is considered this gives

$$\nabla^2 B_z = 0 \tag{2.11}$$

2.1.3 Magnetic Vector Potential and the Biot-Savart Law

The magnetic vector potential, $\mathbf{A}$, is defined by

$$\mathbf{B} = \nabla \times \mathbf{A} \tag{2.12}$$

Combining this with Eq. (2.6) gives

$$\nabla \times \nabla \times \mathbf{A} = \mu_0 \mathbf{J} \tag{2.13}$$

Using the identity, $\nabla \times \nabla \times \mathbf{A} = \nabla^2 \mathbf{A} - \nabla(\nabla \cdot \mathbf{A})$, and Coulomb's gauge, $\nabla \cdot \mathbf{A} = 0$, yields

$$\nabla^2 \mathbf{A} = \mu_0 \mathbf{J} \tag{2.14}$$

which has the solution

$$\mathbf{A}(\mathbf{r}) = \frac{\mu_0}{4\pi} \iiint \frac{\mathbf{J}(\mathbf{r}')}{|\mathbf{r} - \mathbf{r}'|} dV' \tag{2.15}$$

Using $\nabla \times (u\mathbf{J}) = u\nabla \times \mathbf{J} - \mathbf{J} \times \nabla u$, and $\nabla \frac{1}{||\mathbf{r}-\mathbf{r}'||} = -\frac{\mathbf{r}-\mathbf{r}'}{||\mathbf{r}-\mathbf{r}'||^3}$ results in the integral form of Biot-Savart law

$$\mathbf{B}(\mathbf{r}) = \frac{\mu_0}{4\pi} \iiint \frac{(\mathbf{r} - \mathbf{r}') \times \mathbf{J}(\mathbf{r}')}{|\mathbf{r} - \mathbf{r}'|^3} dV' \tag{2.16}$$

2.1.4 Magnetic Susceptibility

When an object experiences a magnetic field it will tend to generate its own magnetic field in response. The resulting magnetisation, $\mathbf{M}$, is related to the applied magnetic field, $\mathbf{H}$, by $\mathbf{M} = \chi \mathbf{H}$ where the dimensionless constant of proportionality, χ, is the magnetic susceptibility of the material. The susceptibility is related to the permeability via the relation $\mu = \mu_0(1 + \chi)$. Diamagnetic materials, such as water, possess a negative χ, such that the magnetisation induced in them opposes the applied magnetic field. Paramagnetic materials have positive χ values and thus generate a magnetisation that reinforces the magnetic field experienced by the object. Table 2.1 shows some values of magnetic susceptibility of different tissues found in the body after Collins *et al.* [5].

Ferromagnetic materials, such as iron, exhibit a stronger magnetisation in the presence of an applied magnetic field with a characteristic magnetic susceptibility which is a function of field strength and maybe of the order of $\chi = 200$.

Material	$\chi \quad (\times 10^{-6})$
Air	0.4
Water	-9.0
Fat	-7.8
Bone	-8.4
Blood	-8.5
Grey matter	-9.0
White matter	-8.8

Table 2.1: Magnetic susceptibilities, χ, of common tissues of the human body.

2.2 Spherical Harmonics

The general solution to the Laplace equation (2.11) in spherical polar coordinates (r, θ, ϕ) is any linear combination of regular spherical harmonic (also known as solid harmonic) functions of the form

$$R_n^m(r, \theta, \phi) = r^n P_n^m(\cos\theta) e^{im\phi} \tag{2.17}$$

where P_n^m are associated Legendre polynomials with positive integer order n and positive integer degree $m \leq n$. Equation (2.17) can be rewritten in Cartesian coordinates [6]

$$R_n^m(x, y, z) = (n+m)! \sum_k \frac{(-1)^k (x+iy)^{(k+m)} (x-iy)^k z^{(n-m-2k)}}{2^{(2k+m)} (k+m)! (n-m-2k)!} \tag{2.18}$$

where k is each positive integer for which $k \leq \frac{1}{2}(n-m)$.

Therefore the z-component of the magnetic induction, $B_z(\mathbf{r})$, can be expanded in terms of a weighted sum of orthogonal spherical harmonic basis functions.

$$B_z(\mathbf{r}) = \sum_{n=0}^{\infty} \sum_{m=-n}^{n} C_n^m R_n^m(\mathbf{r}) \tag{2.19}$$

where C_n^m is the amount of the n^{th} order, m^{th} degree spherical harmonic present in $B_z(\mathbf{r})$. Figure 2.1 shows all the 0^{th}, 1^{st}, 2^{nd} and 3^{rd} order spherical harmonic functions plotted on the surface of a sphere. The order, degree, name, and the equations in spherical polar and Cartesian coordinates of each harmonic are given next to the plots. In this thesis we adopt the convention that the imaginary part, $\Im$, of tesseral ($m \neq 0$) harmonics is written with negative degree, *i.e.* $\Re(R_n^m)$ is simply written as R_n^m and $\Im(R_n^m)$ is written as R_n^{-m}.

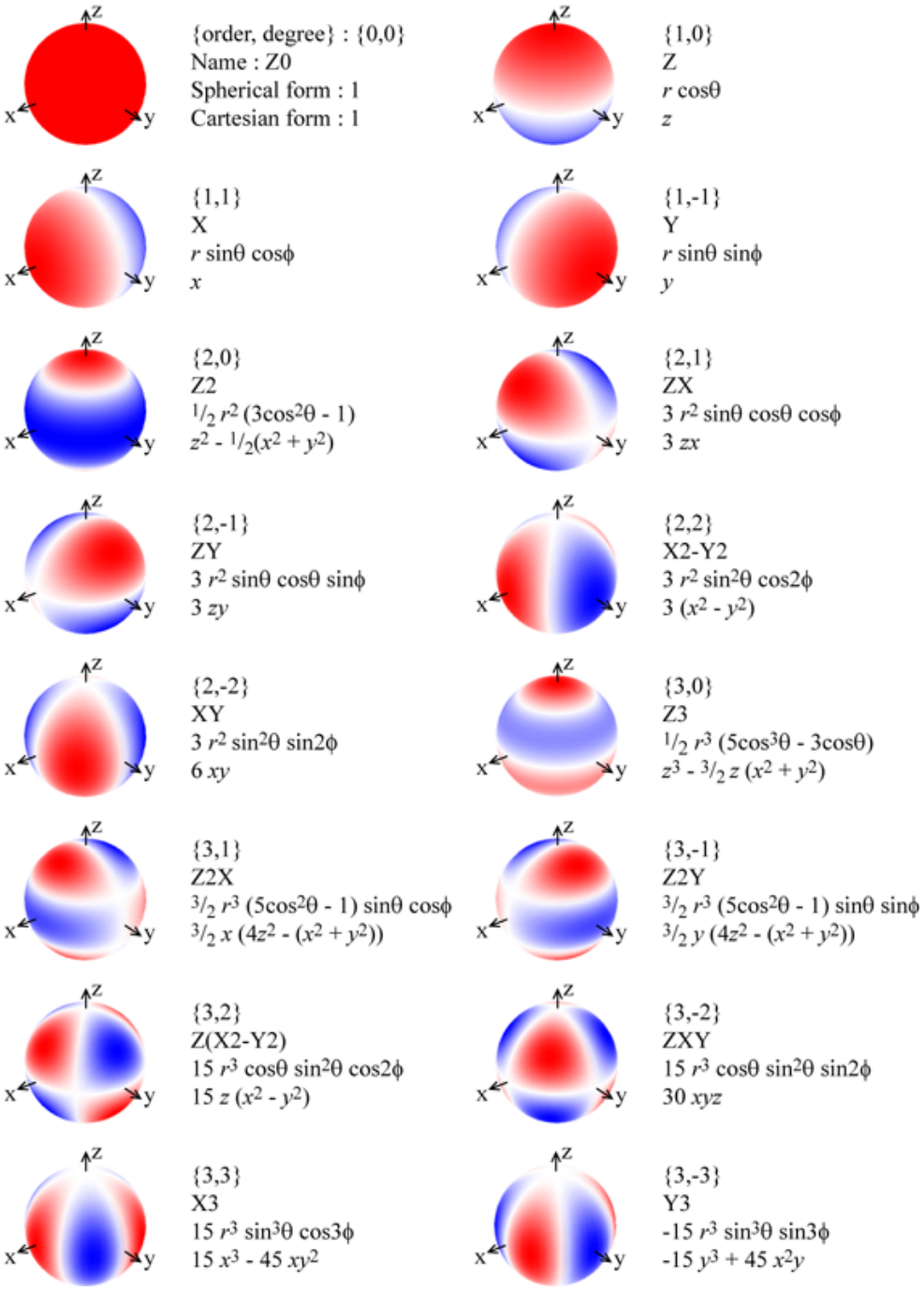

Figure 2.1: Plots of the spherical harmonics up to 3^{rd} order on the surface of a sphere shown in red (positive) and blue (negative). The equations for the spherical harmonics are given in spherical polar (r, θ, ϕ) and Cartesian (x, y, z) coordinates.

2.3 Fourier Transforms

The Fourier transform, $\mathcal{F}$, is a mathematical operator regularly used in NMR. It allows a function, $f(x)$, to be decomposed into a function, $F(k)$, of its frequency components, k. The spatial frequencies from a 1D function in x are obtained via

$$F(k) = \mathcal{F}\{f(x)\} = \int_{-\infty}^{\infty} f(x)e^{-ikx}dx. \tag{2.20}$$

It follows then that the inverse Fourier transform operation, $\mathcal{F}^{-1}$, is

$$f(x) = \mathcal{F}^{-1}\{F(k)\} = \frac{1}{2\pi}\int_{-\infty}^{\infty} F(k)e^{ikx}dk. \tag{2.21}$$

The Fourier transform can be applied to time-varying functions (Fig. 2.2 **a)**), as well as spatially-varying functions (Fig. 2.2 **b)**) and can be extended to 2-dimensions (Fig. 2.2 **c)**) or more.

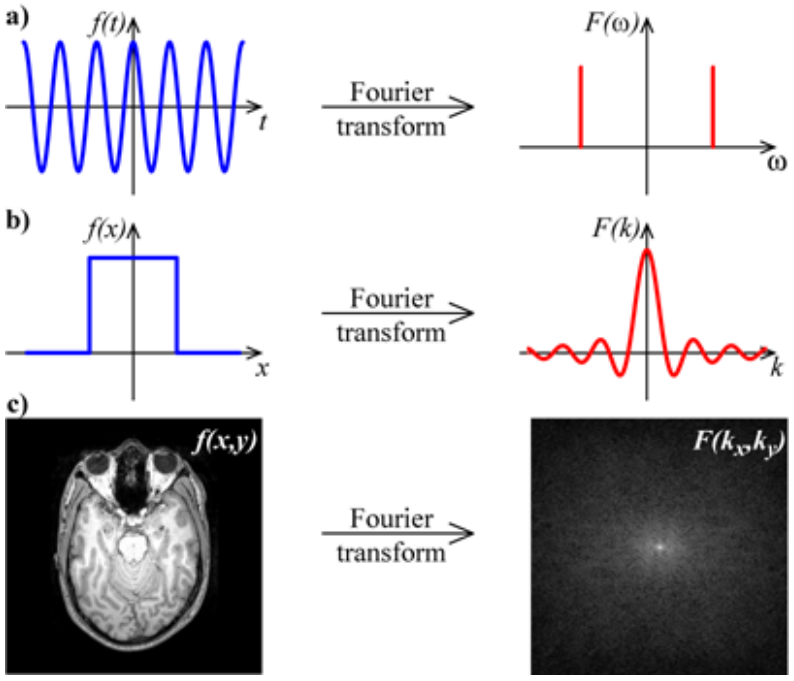

Figure 2.2: Examples of the Fourier transform; **a)** a single cosine wave transforms to a pair of Dirac delta functions at the frequency of the signal, **b)** a 'top-hat' spatial function transforms to a sinc function of spatial frequency and, **c)** a 2D axial, grey-scale image transforms to its 2D Fourier transform (shown here with the modulus scaled logarithmically to show detail, and the centre of which corresponds to $k_x = k_y = 0$).

2.4 Nuclear Magnetic Resonance

Nuclear magnetic resonance (NMR) is the study of the resonant behavior of nuclei under the influence of magnetic fields. This section outlines basic NMR theory.

2.4.1 Nuclei, Spin and Energy Levels

Hydrogen atoms, ^{1}H, consist of an electron orbiting a nucleus of a single proton. Since the proton has a spin quantum number $m_s = \frac{1}{2}$, the hydrogen nucleus may exist in two spin states, either the 'up' state, $|\alpha\rangle$, or the 'down' state $|\beta\rangle$. These states correspond to the two possible quantised angular momentum values, $\mathbf{I}$, it can have; The z-component of the nuclear angular momentum may take the values $I_z = -\frac{1}{2}\hbar$ or $I_z = +\frac{1}{2}\hbar$ for the down and up states respectively, where $\hbar = 1.054 \times 10^{-34}$ Js is the reduced Planck's constant. In fact, all nuclei with unpaired nucleons (proton or neutrons) have a net nuclear angular momentum; carbon-13, ^{13}C has one unpaired neutron and therefore also has a spin of $\frac{1}{2}$.

Nuclei also possess a positive charge and rotating charges generate magnetic dipole moments, $\mu = \gamma\mathbf{I}$, where γ is the gyromagnetic ratio ($\gamma = 2.675 \times 10^8$ s^{-1}T^{-1} for ^{1}H). When a dipole is subjected to a magnetic field, $\mathbf{B}_0$, it will tend to align 'parallel' or 'antiparallel' with the direction of $\mathbf{B}_0$ depending on whether its spin state is up or down. These parallel and anti-parallel states have a difference in energy, E, proportional to the strength of the magnetic field that the nuclei experience, $E = \pm\frac{1}{2}\gamma\hbar B_0$, (Fig. 2.3). This was experimentally verified by Rabi in 1938 [7].

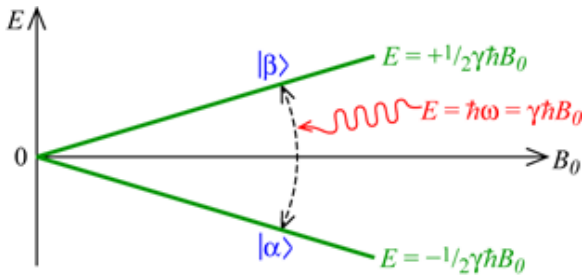

Figure 2.3: Energy level diagram of a spin $\frac{1}{2}$ nucleus in a magnetic field, B_0. Transitions can be induced between states by irradiating with energy, E, equal to the energy level splitting, ΔE.

Quantisation of the nuclear angular momentum, $\mathbf{I}$, dictates that the magnetic moment vector, μ, cannot align exactly parallel to $\mathbf{B}_0$, rather it precesses about $\mathbf{B}_0$ at a specific frequency, called the Larmor frequency, $\omega_0 = \gamma B_0$. Applying energy at this frequency

induces transitions between the up and down spin states, as it is equal to the energy level splitting, ΔE, of the two states. For ^{1}H nuclei in a 1 Tesla (T) magnetic field $\frac{\nu_0}{2\pi} = 42.58$ MHz, which is in the radio-frequency (RF) range of the electromagnetic spectrum. Only RF of the correct frequency will drive transitions between the spin states, hence the use of the term 'resonance' in nuclear magnetic resonance (NMR). Bloch and Purcell observed the NMR effect in water [8] and paraffin [9] in separate experiments, for which they were awarded the Nobel Prize for Physics in 1952.

2.4.2 Boltzmann Statistics

In a system where there are states with separate energy levels, the numbers of nuclei in each state are described by Boltzmann statistics. Boltzmann statistics give the ratio of the number of nuclei in the high, N^-, and low, N^+, energy states as a function of the energy level difference, ΔE, and the temperature, T, of the system,

$$\frac{N^-}{N^+} = e^{-\Delta E/kT} \tag{2.22}$$

where $k = 1.38 \times 10^{-23}$ JK^{-1} is Boltzmann's constant. For Hydrogen nuclei at 300K this ratio is very close to 1, in fact in a 1 T magnetic field there will be approximately 1,000,006 nuclei in the low energy level for every 1,000,000 in the high energy level state.

2.4.3 Bulk Magnetisation

In NMR, the myriad spins in a material cannot be treated individually, and so we consider the combined effect of the excess up spins in an ensemble (Fig. 2.4). These spins precess about the direction of the magnetic field, conventionally the z-direction. With only a static magnetic field applied, the phase of the precession is entirely random, so when they are considered *en masse* the overall magnetisation appears to be static in the z-direction (Fig. 2.4 **c)**). This induced magnetisation due to the static magnetic field is the equilibrium magnetisation, M_0, and is proportional to the difference in the numbers of nuclei in high- and low-energy states.

2.4.4 Radio-Frequency Pulses

As stated in § 2.4.1, applying radio-frequency (RF) energy at the Larmor frequency, ω_0, will induce transitions between spin states. This oscillating electromagnetic field, B_1, causes the phases of the precessing spins to align. When the spins are considered together, the bulk magnetisation vector, $\mathbf{M}$, no longer points along the z-direction but circulates around it

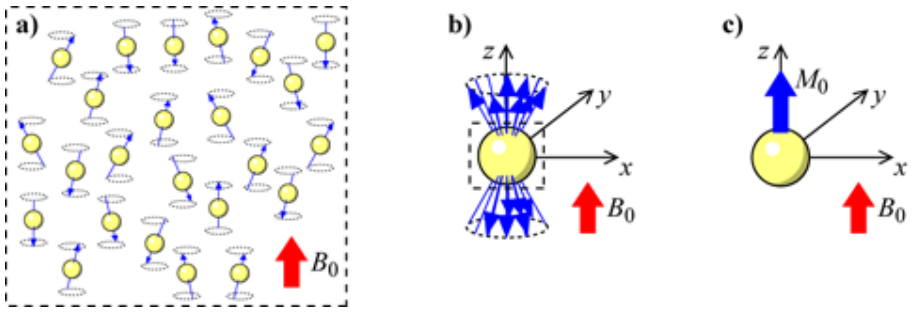

Figure 2.4: The nuclei in a sample may be treated *en masse*. **a)** An ensemble of magnetic moments precessing in an applied magnetic field, B_0, **b)** can be treated as spatially indistinct. The phases are random and there are more spins in the low energy state, $|\alpha\rangle$, than the high energy state, $|\beta\rangle$ resulting in **c)** the bulk magnetisation, M_0, aligned with B_0.

with increasing angle to $\mathbf{B}_0$, shown in Fig. 2.5 **a)**, in a process called nutation. Since the B_1 field, and $\mathbf{M}$ are rotating about the z-direction at ω_0, a rotating frame of reference is introduced. This can be compared to a merry-go-round. Watching from outside, the horses appear to be going up and down and circulating around. If one gets onto the fairground ride, the horses simply appear to be moving up and down. This is done mathematically with a change of coordinates from the usual Cartesian (x, y, z) frame to a frame of reference rotating at the Larmor frequency, denoted (x', y', z) (operating a fairground ride at the Larmor frequency is not recommended).

In the rotating frame (Fig. 2.5 **b)**) the magnetisation vector, $\mathbf{M}$ appears to tip from its equilibrium position, aligned with the z-axis, down towards the y' axis. In fact, the greater the length of time that the RF pulse is applied for, the greater the angle through which the magnetisation is tipped. A 90° pulse is an RF pulse that is applied such that $\mathbf{M}$ is tipped entirely into the xy plane. An inversion pulse is one that rotates the magnetisation though 180°.

2.4.5 Relaxation

The system at equilibrium has a random phase and a spin population conforming to Boltzmann's statistics. After the application of an RF pulse there may be a non-equilibrium number of parallel and anti-parallel spins and the phases of their precession will be similar. The spin population will tend back to equilibrium by spin-lattice relaxation processes and the phase will randomise by spin-spin relaxation processes.

Spin-lattice relaxation processes equilibrate the spin population and thereby return the longitudinal magnetisation, M_z, to its equilibrium value, M_0, exponentially. After an RF

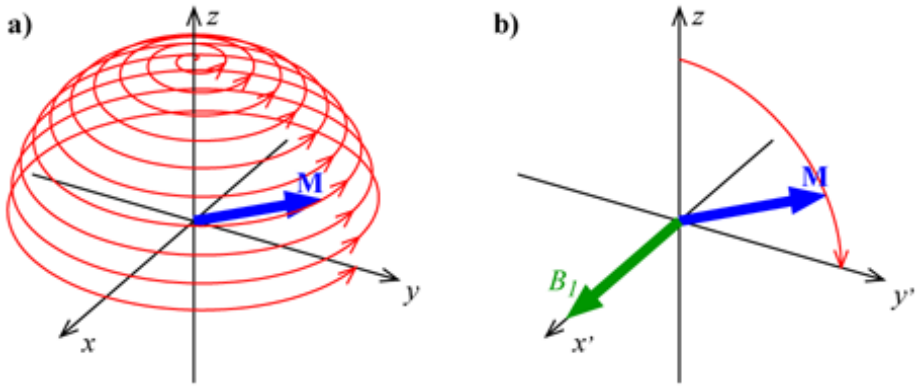

Figure 2.5: The evolution of the bulk magnetisation vector **M** under the application of an RF pulse at the resonance frequency in **a)** the laboratory frame and, **b)** the rotating frame.

pulse, the magnetisation is disturbed to $M_z(0)$, but will return to equilibrium in a manner described by

$$M_z(t) = M_0 \left[1 - \left(1 - \frac{M_z(0)}{M_0}\right) e^{-t/T_1}\right] \tag{2.23}$$

where T_1 is the spin-lattice relaxation time constant that governs the decay of $M_z(t)$ from $M_z(0)$ to M_0. Figure 2.6 **a)** shows examples of this decay.

Spin-spin relaxation processes equilibrate the transverse magnetisation, M_{xy}, from the non-equilibrium value, $M_{xy}(0)$, after an RF pulse, so that

$$M_{xy}(t) = M_{xy}(0)e^{-t/T_2^*} \tag{2.24}$$

where T_2^* is the spin-spin relaxation time constant that governs the decay of $M_{xy}(t)$ from $M_{xy}(0)$ to 0. The decay of M_{xy} is a combination of 'true' T_2 processes that are stochastic and therefore irreversible, and T_2' processes arising from inhomogeneities in B_0 (chapter 3) that are reversible,

$$\frac{1}{T_2^*} = \frac{1}{T_2} + \frac{1}{T_2'} \tag{2.25}$$

2.4.6 Free-Induction Decay: The NMR Signal

The transverse magnetisation of the precessing spins in the sample is detected externally, often with the same coil that generates the RF radiation. After an RF pulse, the detected

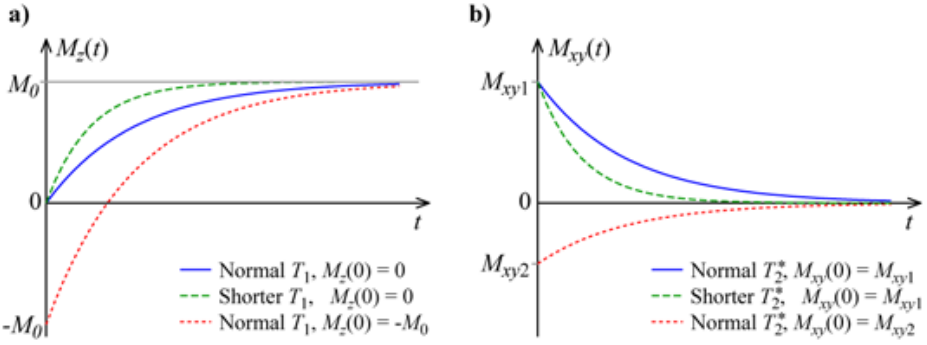

Figure 2.6: Relaxation of **a)** the longitudinal magnetisation, $M_z(t)$, and **b)** the transverse magnetisation, $M_{xy}(t)$. Example decay curves are plotted for lower decay constants (green dashed lines) and different initial magnetisation (red dotted lines) in comparison to a standard decay (blue solid lines).

signal decays in amplitude due to the relaxation processes described above. This signal, the free-induction decay (FID), carries the NMR information. From a single FID, information can be inferred about the chemical environment of the nuclei in the sample. The Larmor frequency oscillations are filtered from the FID (conceptually equivalent to observing the signal in the rotating frame), which is then Fourier transformed to analyse the frequency spectrum. In order to distinguish peaks in the spectrum that are close, the width of the peaks, known as the linewidth, must be as small as possible. This means the FID must decay as slowly as possible. This is achieved by making the magnetic field as homogeneous as possible (Chapter 3).

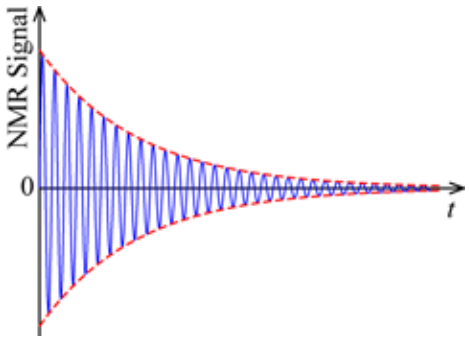

Figure 2.7: An idealised free-induction decay (FID) NMR signal (solid blue line) with its T_2^* decay envelope (dashed red line).

2.4.7 Echoes

At the start of the FID the phases of the excited spins are coherent; this coherence is lost due to systematic T_2' processes that can be recovered, and stochastic, true T_2 processes that cannot. Partial recovery of phase coherence, and therefore signal intensity, may be achieved by applying a 180° RF pulse at time, $t = T_E/2$, as illustrated in Fig. 2.8. A spin may accrue a phase, ϕ, during the time $T_E/2$, but immediately after the application of an 180° pulse, its phase will be $-\phi$. Between the times $T_E/2$ and T_E the spin will gain another ϕ radians of phase which makes its total phase at $t = T_E$ from T_2' processes equal to zero. The resulting increase in signal, an 'echo', was first studied by Hahn in [10], and the time at which echoes occur, T_E, is the echo-time. Echoes are fundamental to magnetic resonance imaging (MRI) and two ways by which echoes can be generated are described in § 2.5.7 and § 2.5.8.

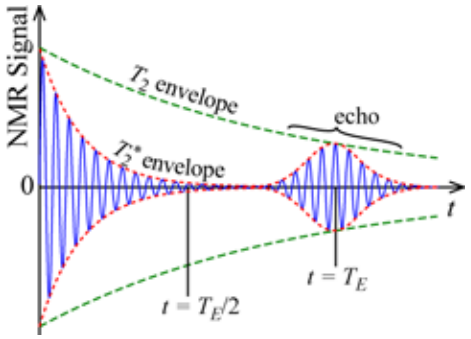

Figure 2.8: An echo is formed in the NMR signal (solid blue line) at $t = T_E$, with a magnitude dependant on the T_2 decay (green dashed line), due to the refocussing of the systematic decay processes within the T_2^* decay (red dotted line) by a 180° RF pulse at $t = T_E/2$.

2.5 Magnetic Resonance Imaging

Until 1973, NMR was primarily used for spectroscopy to study the chemical environment of magnetic resonant species, such as ^{1}H and ^{13}C. Although others had applied magnetic field gradients to samples before, in 1973 Lauterbur applied a linear gradient at different angles to a sample and, together with a back-projection technique, obtained 2D images of two tubes of water [11]. Two years later, Kumar *et al.* [12] used switched orthogonal linear gradients to generate 2D Fourier encoded images, which led to the first *in vivo* cross-section image of a human finger, which was produced in 1977 by Mansfield [1]. From this gradient

encoding technique a multitude of imaging methods have been conceived such as fast, low-angle shot (FLASH) imaging [13, 14], and echo-planar imaging (EPI) [15] which later led to functional MRI (fMRI) [16].

2.5.1 Gradients

Three orthogonal linear field gradients are used in MRI. These are usually oriented in the x-, y-, and z-directions in conventional MRI coordinates (see centre of Fig. 2.17) and are generated by passing current through specially arranged coils of wire. The magnetic fields produced when a current is passed through these coils have magnitudes that are proportional to the position from the centre of the magnet system as shown in Fig. 2.9. Applying these gradients slightly modifies the main, uniform magnetic field, B_0, and therefore introduces a spatial dependance to the Larmor frequency of the precessing spins in the sample.

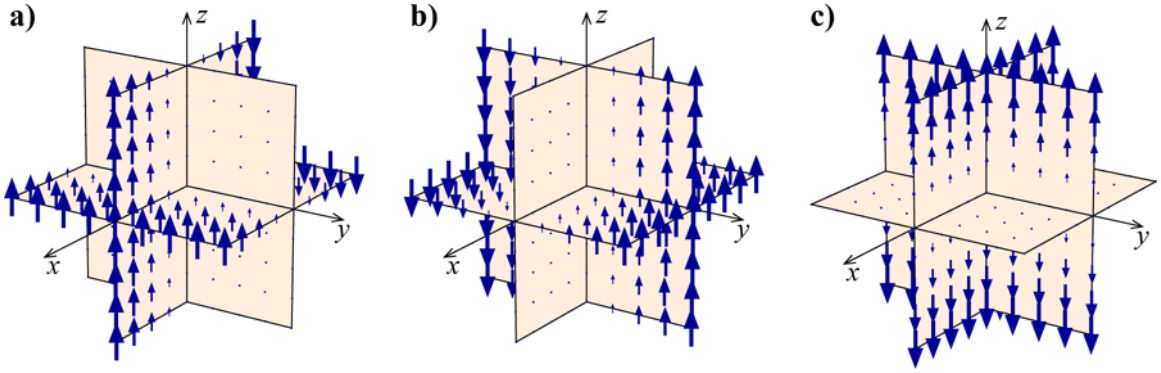

Figure 2.9: Diagrams of the B_z component of the 3D magnetic field variation of **a)** x-, **b)** y-, and **c)** z-gradients. The field is aligned with the direction of the arrows. The scale of the arrows indicates the magnitude of the magnetic field strength at that point.

2.5.2 Slice Selecting

The RF pulses described in § 2.4.4 excite the whole sample. In MRI it is common to excite just a thin slab of spins known as a 'slice', an approach which was first proposed in 1974 by Garroway *et al.* [17]. A slice is selected by irradiating the sample with an RF pulse containing a limited a range of frequencies in the presence of a linear gradient. The gradient field, G_z (where $B_z = G_z z$), causes a linear variation in the Larmor frequency in the z-direction across the sample; $\omega_L(z) = -\gamma(B_0 + G_z z)$. Therefore, an RF pulse containing frequencies in the range $(\omega_0 - \frac{1}{2}\Delta\omega) > \omega > (\omega_0 + \frac{1}{2}\Delta\omega)$ will excite only those spins in

the slice $(z_0 - \frac{1}{2}\Delta z) > z > (z_0 + \frac{1}{2}\Delta z)$ (see Fig. 2.10). The longitudinal magnetisation in this slice is tipped into transverse magnetisation while the magnetisation of the rest of the object remains relatively undisturbed. Using the small-tip-angle approximation [18] the time evolution of an RF pulse made up of equal contributions from a finte range of frequencies is a sinc-shaped pulse (Fig. 2.2 **e)**) modulating a sine wave (Fig. 2.2 **a)**) at the centre frequency, ω_0. Generation of an exactly rectangular slice profile is not possible due to time constraints on the pulse length. RF pulses may be tailored to give a good slice profile with finite duration RF pulses.

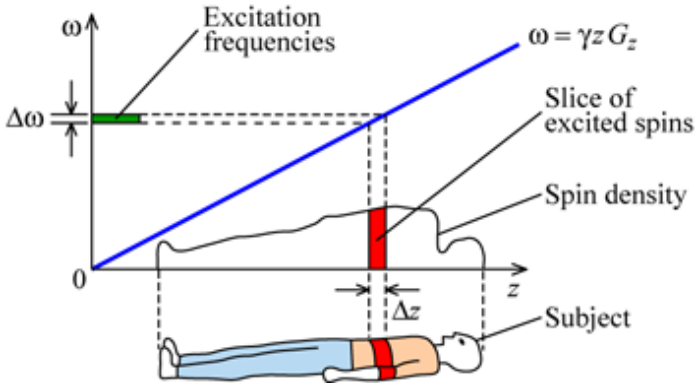

Figure 2.10: Illustration of selectively exciting spins in a slice, of thickness Δz, with a range of frequencies $d\omega$ and the slice select gradient G_z.

2.5.3 Fourier Imaging with Field Gradients

In the absence of relaxation (§ 2.4.5), the signal emanating from a point $\mathbf{r}$ at a time t is proportional to the spin density, $\rho(\mathbf{r})$, and dependant on the evolution of the local Larmor frequency, $\omega_L(\mathbf{r}, t')$ from time $t' = 0$ to $t' = t$.

$$S(\mathbf{r}, t) \propto \rho(\mathbf{r}) e^{i \int_0^t \omega_L(\mathbf{r}, t') dt'}. \tag{2.26}$$

Signals are generally received from an extended region of the sample and therefore

$$S(t) \propto \iiint \rho(\mathbf{r}) e^{i \int_0^t \omega_L(\mathbf{r}, t') dt'} dx dy dz. \tag{2.27}$$

Since the Larmor frequency is determined by the magnetic field experienced by spins, that is related to the static field, B_0, and the three orthogonal gradient fields, G_x, G_y, and G_z, the signal can be written in terms of the evolution of the gradients over time. Equation

(2.28) shows this signal after demodulation of the central Larmor frequency, ω_0, due to B_0.

$$S'(t) \propto \iiint \rho(\mathbf{r}) e^{-i\gamma \int_0^t \mathbf{r}\cdot\mathbf{G}(t')dt'} dxdydz \tag{2.28}$$

where $\mathbf{G}(t') = G_x(t')\mathbf{i} + G_y(t')\mathbf{j} + G_z(t')\mathbf{k}$. Eq. (2.28) shows that the received signal is related to the evolution of the gradients. Now let

$$\mathbf{k}(t) = -\gamma \int_0^t \mathbf{G}(t')dt' \tag{2.29}$$

and Eq. (2.28) reduces to

$$S'(t) \propto \iiint \rho(\mathbf{r}) e^{i(\mathbf{r}\cdot\mathbf{k}(t))} dxdydz \tag{2.30}$$

This is now in the form of a 3D Fourier transform (3DFT), meaning that by appropriate signal acquisition and gradient adjustment, information can be obtained about the spin density of objects from an inverse Fourier transform (IFT) of the received signal. This concept forms the basis of modern imaging techniques in MRI.

2.5.4 Frequency Encoding

Spatial localisation of the NMR signal in one-dimension is achieved by applying a constant linear gradient in one direction while the signal is measured, e.g. $\mathbf{G}(t') = G_x\mathbf{i}$ from $t' = 0$ to $t' = t$.

$$S'(t) \propto \iiint \rho(\mathbf{r}) e^{-i\gamma x G_x t} dxdydz \tag{2.31}$$

Again, using Eq. (2.29) gives

$$S'(t) \propto \iiint \rho(\mathbf{r}) e^{ixk_x} dxdydz = \iint FT_x[\rho(\mathbf{r})]dydz \tag{2.32}$$

If a thin slice is selected (§ 2.5.2) the integral over z is an integral from $(z_0 - \frac{1}{2}\Delta z)$ to $(z_0 + \frac{1}{2}\Delta z)$, which, in the limit of small Δz, reduces the system to just two-dimensions, and therefore

$$S'(t) \propto \int FT_x[\rho(\mathbf{r})]dy \tag{2.33}$$

This is how the x-position is encoded: the Larmor frequency varies across the sample in a linear way, so that inverse Fourier transformation of the received, demodulated signal

gives a breakdown of the frequencies and therefore information about the distribution of spin density in the x-direction.

2.5.5 Phase Encoding

Phase encoding localises the NMR signal in a second direction. It similarly employs a short-lived pulse of field gradient, in this case, the y-gradient, G_y. The y-gradient is pulsed on before signal acquisition in the presence of G_x as described in § 2.5.4. This modifies the phase before signal acquisition and this process is repeated for a range of gradient pulse duration so as to encode the y-dimension via the phases of the signals. Considering the signal from spins experiencing a gradient $\mathbf{G}(t') = G_y\mathbf{j}$ applied from $t' = 0$ to $t' = t_1$. and another gradient $\mathbf{G}(t') = G_x\mathbf{i}$ applied from $t' = t_1$ to $t' = t_2$, the signal acquired in the time interval $t' = t_1$ to $t' = t_2$, where $t = t' - t_1$ is

$$S'(t) \propto \iiint \rho(\mathbf{r}) e^{-i\phi_y - i\gamma x G_x t} dxdydz \tag{2.34}$$

where $\phi_y = \gamma y G_y t_1$ is the amount of phase introduced to the signal due to G_y (c.f. Eq. (2.31)) before acquisition. This means that Eq. (2.35) can be obtained using the same analogies as Eqs. (2.30), (2.32), (2.33), for a thin slab of excited spins

$$S'(t) \propto 2DFT_{xy}[\rho(\mathbf{r})] \tag{2.35}$$

2.5.6 k-Space

As we have seen in § 2.5.4 and 2.5.5 the Fourier transform is a central concept in spatially encoded MRI. It is therefore convenient to analyse different imaging methods in terms of spatial frequencies [19, 20]. k-space is the name given to the (k_x, k_y, k_z) space whose co-ordinates form the Fourier pairs of the Cartesian coordinates (x, y, z). The centre of k-space corresponds to low spatial frequencies, and the edges are where the high spatial frequencies reside (see Fig. 2.2 **c)**). It has been shown previously (§ 2.5.3 to 2.5.5) that applying field gradients in the correct manner in the imaging plane encodes the spatial position of signals as frequencies and phases. Immediately after excitation, the sampling position is at the centre of k-space and the position in k-space at a time t after excitation is proportional to the integrated gradient at that time. So, signal acquired in the presence of a constant x-gradient samples k-space along a line in the k_x-direction. To reconstruct a 2D image one must have information about a central 2D region of k-space so data are acquired in a way to fully sample this k-space region. A full k_x line is measured from $-k_{x,max}$ to $k_{x,max}$.

Moving to $-k_{x,max}$ from $k_x = 0$ after excitation can be achieved by application of a negative x-gradient of the correct amplitude and duration. The spacing of the measurements made in k-space determines the field-of-view (FOV) of the resulting image and the further from the centre of k-space one measures, the greater the resolution of the reconstructed image.

2.5.7 Gradient Echo Imaging

Spin-warp imaging, now often referred to as Fourier imaging, was proposed by Edelstein *et al.* in 1980 [21] and was one of the first 2D slice selective imaging sequences. Figure 2.11 **a)** shows the timing diagram of the RF and gradient channels and the received signal for the gradient echo imaging version of this sequence and **b)** shows its corresponding k-space trajectory.

A slice-selective RF pulse that rotates the magnetisation by α° into the transverse plane using a simultaneously applied z-gradient (an α° pulse) excites the spins in an xy slice during the time interval 1 in Fig. 2.11. In interval 2, a negative x-gradient is applied with a variable phase encoding gradient in the y-direction to move the sampling position to $(-k_{x,max}, k_{yn})$. Also in interval 2 a negative G_z pulse ensures that the phase of the spins is uniform across the slice. The signal is then acquired in the presence of an x-gradient during interval 3 when an echo is formed and data are acquired at points along a k-space line. Immediately after the RF pulse the excited spins have the same phase. The spins become dephased during period 2 due to T_2^* processes (§ 2.4.5) including the effect of the x- and y-gradients. The frequency encoding gradient causes the spins to rephase partially and allows the detection of an echo. The system is then allowed to relax to equilibrium before the sequence is repeated with a different strength of phase encoding gradient so as to sample 2D k-space fully and obtain data like Fig. 2.2 **f)**, which is simply inverse Fourier transformed in 2-dimensions to obtain an image of the form shown in Fig. 2.2 **c)**.

2.5.8 Spin Echo Imaging

Spin echo imaging [10] is similar to gradient echo imaging (§ 2.5.7), but differs in the mechanism by which the echo is created. Fig. 2.12 shows the timing diagram and k-space trajectory of a typical spin echo sequence. In spin echo imaging, echoes are formed via a second RF pulse applied at $t = T_E/2$ that rotates the magnetisation through 180° in the $x'z$ plane (see Fig. 2.5).

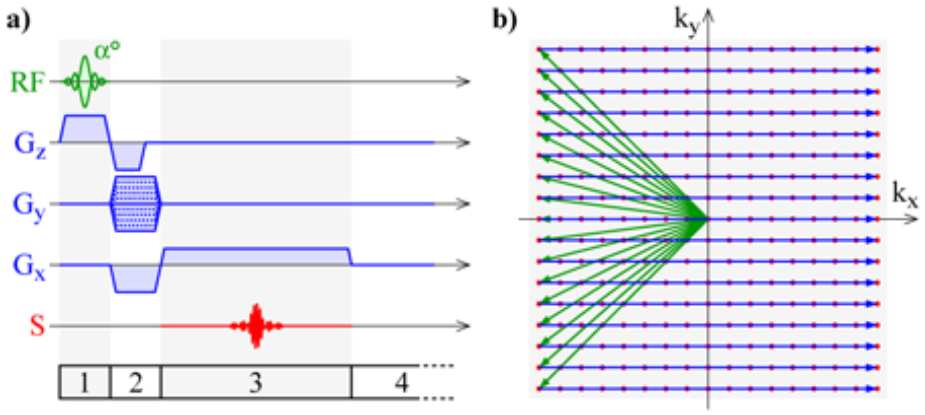

Figure 2.11: **a)** Timing diagram for one phase encoding step of a gradient echo sequence. The slice is excited during period 1, and the gradients in periods 2 and 3 cause an echo to be formed in period 3. The 5 channels shown are the transmitted radio-frequency (RF), the x-, y- and z-gradients (G_x, G_y, G_z), and the received signal (S) channels. **b)** The k-space trajectory of the sequence. The signal is acquired along the blue lines at the positions indicated by red dots. The k-space shift due to the gradients in period 2 is shown in green.

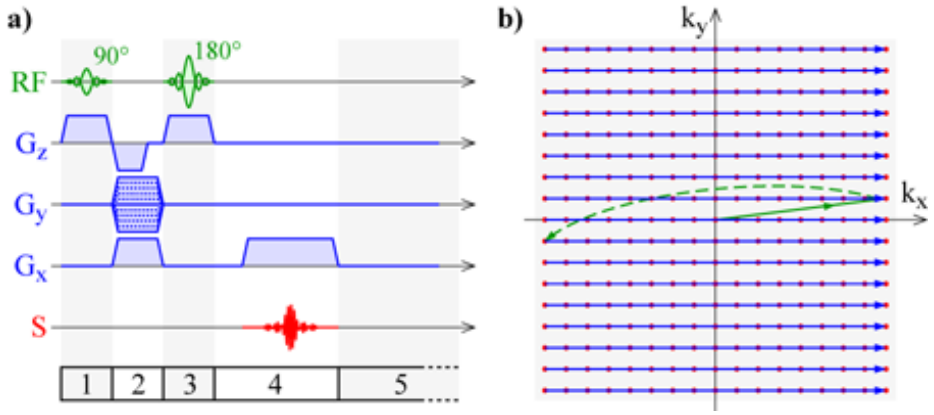

Figure 2.12: **a)** Timing diagram for one phase encoding step of a spin echo sequence. The slice is excited during period 1, and the RF pulse in period 3 combined with the gradients in periods 2 and 4 cause and echo to be formed in period 4. The 5 channels shown are the transmitted radio-frequency (RF), the x-, $y-$ and z-gradients (G_x, G_y, G_z), and the received signal (S) channels. **b)** shows the k-space trajectory of the sequence. The signal is acquired along the blue lines at the positions indicated by red dots. The solid green line represents the k-space shift that occurs during period 2 and the dashed line shows the effect of the 180° pulse in period 3.

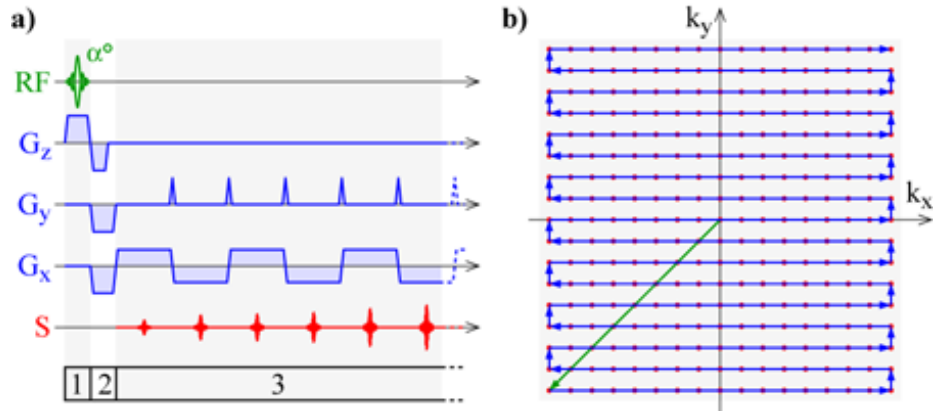

Figure 2.13: **a)** Timing diagram for an echo planar imaging sequence, and **b)** k-space trajectory. The spins are excited in period 1 and the repeatedly reversed readout gradient and blipped phase encoding gradient forms a series of echoes from a single RF pulse.

2.5.9 Fast Imaging Methods

The k-space [19, 20] concept provides us with a useful tool to design fast imaging sequences. In 1977, Mansfield [15] proposed echo-planar imaging (EPI), a fast imaging modality that traverses k-space after application of a single RF pulse (a single "shot") rather than using the many RF pulses and relaxation periods of gradient echo imaging. EPI samples k-space in a raster fashion by repeatedly reversing the readout gradient, G_x, to move back and forth across k_x. Small blips in the phase encoding gradient, G_y, increments the k_y position in k-space. The timing and k-space diagrams for the EPI sequence and are shown in Fig 2.13. Spiral imaging [22] is another single-shot imaging sequence that samples 2D k-space quickly in a manner shown in Fig 2.14.

2.5.10 Field Mapping Sequences

It is possible to measure the magnetic field inside objects with the 2-echo, gradient echo sequence, shown in Figure 2.15. Local magnetic field distortions, ΔB_z, will modify the phases of the spins in that area. The phase difference, $\Delta\phi$, induced in the time ΔT_E between the first and second echo is due to these local fields, and is related by

$$\Delta\phi(\mathbf{r}) = -\gamma \Delta B_z(\mathbf{r}) \Delta T_E \tag{2.36}$$

If it is possible to switch the magnetic field that is to be measured, such as that generated by a coil of wire, then the modified EPI sequence with an added pulse of magnetic field,

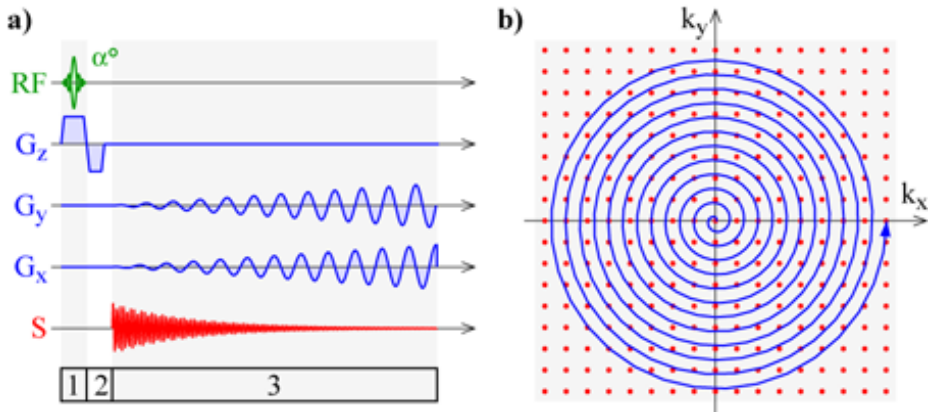

Figure 2.14: **a)** Timing diagram for a spiral imaging sequence, and **b)** k-space trajectory. The signal is received in the presence of oscillatory x and y gradients such that k-space is traversed in a spiral fashion. Data acquired on the spiral must be interpolated onto a regular grid of points (red dots).

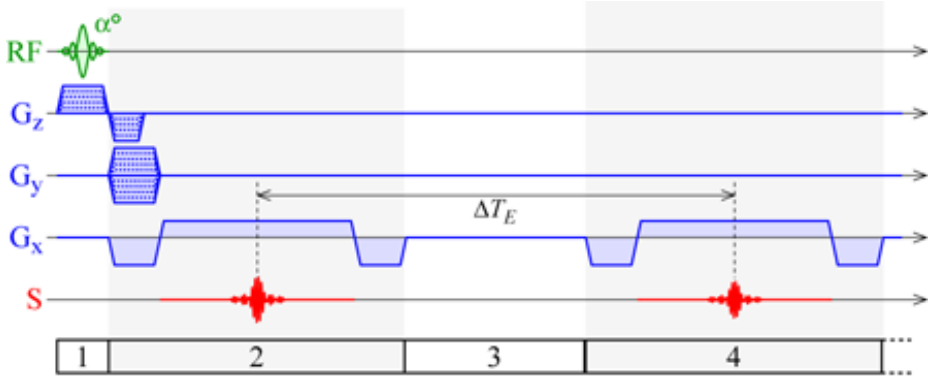

Figure 2.15: Timing diagram for a two-echo, gradient echo field mapping sequence. The slice is excited during period 1, and the gradients in period 2 cause an echo to be formed. No gradients are applied during period 3, and the gradient applied in period 4 cause another echo to form along the same k-space line.

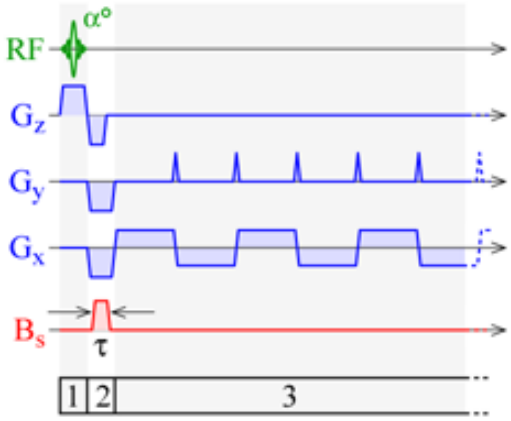

Figure 2.16: Timing diagram for the EPI field mapping sequence. The spins are excited during period 1, and an additional pulse of magnetic field, B_s, is generated during period 2 that modifies the phase, which is acquired with the EPI readout train in period 3.

$B_s(\mathbf{r})$, shown in Fig. 2.16 can be used. The change in phase effected over the duration, τ, of this pulsed magnetic field is

$$\Delta\phi(\mathbf{r}) = -\gamma B_s(\mathbf{r})\tau. \tag{2.37}$$

A field map can be obtained by subtracting the phase of an image acquired with the B_s on from the phase of an image no B_s applied.

2.5.11 A Schematic MRI System

MRI scanners are composed of a number of current-carrying coils, as shown in the schematic diagram in Fig. 2.17. The principal component of an MRI scanner is the main electromagnet. This is usually comprised of a coil of super-conducting material such as Niobium-Titanium (Nb_3Ti), and is used to generate an intense, uniform magnetic field with negligible resistance. Nb_3Ti has a critical superconducting temperature of 10 K. The wire is therefore kept immersed in liquid helium (with a boiling point of 4.2K) to maintain a temperature below the critical temperature. Shim coils are placed within the bore of the magnet to ensure the magnetic field generated by the main electromagnet is as homogeneous as possible (this process is further explained in Chapter 3). Shim coils may be super-conducting and/or room-temperature resistive coils of wire. Gradient coils are usually positioned inside the shim coils; when energised, magnetic fields in the z-direction that are proportional to the x-, y-, and z-coordinates are generated. These fields are used for spatially encoding the NMR

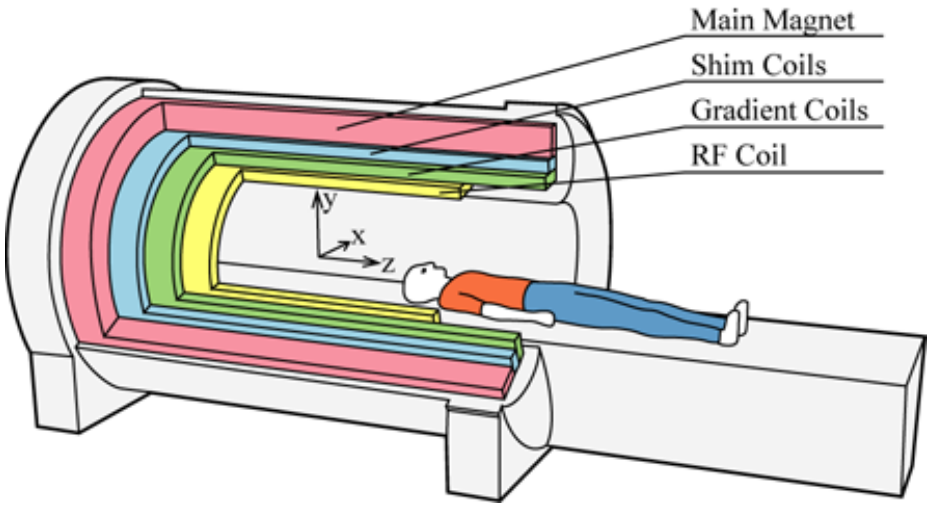

Figure 2.17: Schematic of a whole-body MRI scanner with cut-away section to show the principal components.

signal for MRI as described in § 2.5.3 to § 2.5.5. The RF coil is located within the gradient coils closest to the object that is to be scanned. It excites the protons at their resonant frequency, and also detects the signal generated by the precessing spins after excitation. A single RF coil may both transmit and receive the RF signals or two coils may be used to transmit and receive separately. The subject is slid into the scanner on a bed so that the region of the body to be scanned is in the centre of the magnet.

Most of the electronic apparatus is located outside the main magnet usually in a separate room, since the components may be sensitive to the stray magnetic fields from the scanner. The principal component is the computer system that controls the scanner, but there are also other items of electronic equipment, such as amplifiers, pre-amplifiers, frequency synthesizers, and duplexers that drive the scanner hardware.

Chapter 3

Shimming

In the early days of experiments with strong magnets, magnetic fields were generated by permanent bipolar magnets with a small gap between them, much like the familiar horseshoe magnets. On the pole faces, flat plates of metal could be used to control the shape of the magnetic field. For NMR, the field should be highly homogeneous across the experimental region. This was controlled by adding small slivers of material behind the pole pieces to adjust their angle and so correct the magnetic field. Such slivers of material are called shims in engineering, and the process of homogenising the magnetic field thus became known as shimming.

The majority of magnets for modern magnetic resonance imaging (MRI) systems are cylindrical electromagnets, although some 'open' scanners employ permanent magnetic material (*e.g.* $Nd_2Fe_{14}B$) to provide the magnetic field. The magnetic fields of such systems are homogenised principally by two methods: use of ferroshims (§ 3.2.7) and shim coils (§ 3.2.3 to 3.2.6). Ferroshims are pieces of ferromagnetic material placed in the bore of the magnet so as to correct gross inhomogeneities. Shim coils are resistive coils of wire carrying currents which the user controls to further homogenise the magnetic field. In this chapter, the sources of magnetic field inhomogeneity, ΔB_0, and the effect of inhomogeneity on MRI and several methods of reducing these effects are discussed. Chapter 7 details the improvements in shimming in the context of the current work. A description of the effects of ΔB_0 in magnetic resonance spectroscopy (MRS) is given in Chapter 9.3 of de Graaf [23].

The ideal situation for MRI is availability of an intense magnetic field that has the same magnitude and orientation over the whole region of interest (ROI). It is not possible to have a perfect magnetic field; there will always be some ΔB_0. ΔB_0 originates from a variety of sources that have a variety of magnitudes. Any physically realisable magnetic field can be represented as an infinite series of basis functions such as spherical harmonics [24] (§ 2.2).

The magnitude of the spherical harmonics present tends to zero with increasing order, n [25]. Therefore, ΔB_0 can be reduced to reasonable levels for MRI by compensating for a few low orders of spherical harmonics in a systematic way since, over a spherical ROI centered at the origin at least, spherical harmonics are orthogonal.

3.1 Build Tolerances and the Magnetic Environment

The main, often superconducting, electromagnet is built to certain engineering tolerances and is subject to small, but inevitable, fabrication errors. In addition, upon siting the magnet, and energising it, the physical structure of the magnet coils may be distorted due to gravitational forces and self generating magnetic forces [26]. Also, material in the local environment of the magnet such as iron impurities in the gradient assembly and cryostat or iron-containing objects close to the scanner or magnetic shielding around the scanner room contribute to small changes in the magnetic field in the ROI. The ΔB_0 caused by build tolerances and the local environment are of the order of 100 parts-per-million (ppm) over the ROI, which is intolerable for MRI. This gross ΔB_0 is usually corrected for upon siting the magnet with ferroshims (§ 3.2.7).

3.2 Susceptibility-Induced Magnetic Field Inhomogeneities

A well-installed MRI magnet may generate a highly homogeneous magnetic field ($\sim$0.5 ppm), but once an object is introduced, the field once again becomes inhomogeneous. This ΔB_0 originates at boundaries between materials of different magnetic susceptibility (§ 2.1.4) and has an intensity of a few ppm. Several authors have simulated susceptibility-induced ΔB_0 [27–29] producing results which compare well with *in vivo* MRI field-map data [5, 30–33]. Head phantoms with realistic magnetic susceptibility distributions have been constructed, *e.g.* [34], that generate a ΔB_0 that also compares well with *in vivo* data.

The simplest method by which to reduce the effects of ΔB_0 is to reduce the echo-time (§ 2.4.7), T_E, of the scan; less phase-dispersion, $\Delta\phi$, will result from a shorter T_E in the presence of ΔB_0. Another way to reduce the effects of ΔB_0 is to image at higher resolution [35] and with thinner slices [36]. The phase-dispersion within a smaller voxel is less; however, the signal-to-noise ratio (SNR) is also reduced to the detriment of quality of the image. It has also been demonstrated that the susceptibility-induced ΔB_0 in the frontal lobe due to the sphenoid sinus can be reduced by tilting the head of the subject with respect to the main magnetic field [33, 37].

Other methods of reducing the effects of susceptibility induced field distortions and signal losses are described in sections (§ 3.2.3 to § 3.2.9).

3.2.1 Through-Slice Gradients and Signal Loss

Signal is lost due to ΔB_0 by two principal mechanisms. The first involves magnetic field gradients in the slice-direction. Figure 3.1 **a)** shows a slice-select gradient, G_z, pulse and the resultant evolution of the phase, $\Delta\phi$, of the spins in the slice. **b)** shows the effect of an additional, susceptibility-induced gradient, ΔG_z, on the gradient pulse and the phase dispersion; the G_z pulse no longer ensures the phases of the spins are the same. Signal from pairs of spins with opposite phase cancel, leading to signal loss in areas with large ΔG_z. The amount of signal loss is dependant upon G_z, ΔG_z, T_E, and the slice thickness [35]. Therefore single shot sequences (§ 2.5.9) are often significantly affected [38], since they often have a long minimum echo time (§ 2.5.9). Effects are particularly large at high static field strengths [39], where ΔG_z is large. § 3.2.5, § 3.2.6 and § 3.2.8 describe methods employed to ameliorate susceptibility-induced signal losses.

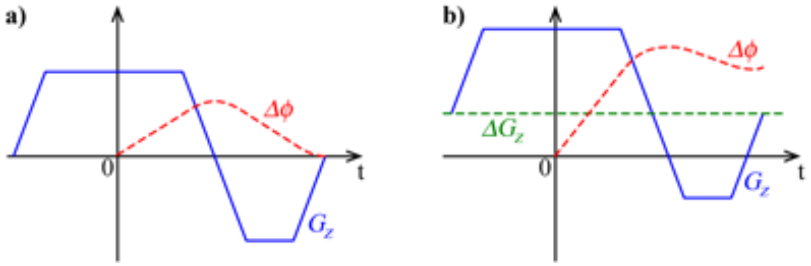

Figure 3.1: Evolution of the phase-dispersion, $\Delta\phi$, across a slice (red dashed line) under the influence of **a)** a refocussed slice-select gradient pulse, G_z, (solid blue line), and **b)** G_z with an additional susceptibility-induced gradient in the slice-select direction, ΔG_z, (dotted green line).

3.2.2 In-Slice Gradients, Signal Loss and Image Distortion

MRI uses magnetic field gradients, G_x and G_y, to localise the MR signals spatially. In-slice gradients in ΔB_0 , ΔG_x and ΔG_y, modify G_x and G_y causing a positional misregistration of the signals. Lüdeke *et al.* [40] provided a mathematical description of the geometric distortion artefacts that occur in Fourier encoded imaging. Other treatments, specifically for gradient echo [41–44], spin echo [40, 41, 43, 44], and echo-planar [38, 45] imaging, have also been described. The extent to which the image is affected can be inferred from the

pixel bandwidth. The pixel bandwidth is the inverse of the time needed to acquire a full line of k-space data in a particular direction [46]. For example, a typical EPI sequence (Fig. 2.13) might have a pixel bandwidth of 2000 Hz in the frequency-encoding direction, but just 31 Hz in the phase-encoding direction [25]. An image becomes significantly distorted when ΔB_0 is of similar magnitude to the pixel bandwidth. Therefore, EPI exhibits significant geometric distortion in the phase-encoding direction, but not in the frequency-encoding direction; 31 Hz corresponds to 0.1 ppm at 7 T.

3.2.3 FID Shimming

Fig. 3.2 shows two examples of free-induction decay (FID) signals received from an excited volume. ΔB_0 causes a decrease in T_2^* and the FID decays more rapidly. With expert knowledge of how each of the spherical harmonic components contributing to ΔB_0 manifests itself in the FID, currents in the shim coils (§ 4.3.2) can be manually adjusted to minimise the rate of signal decay [47, 48] to obtain an FID more like Fig. 3.2 **b)**.

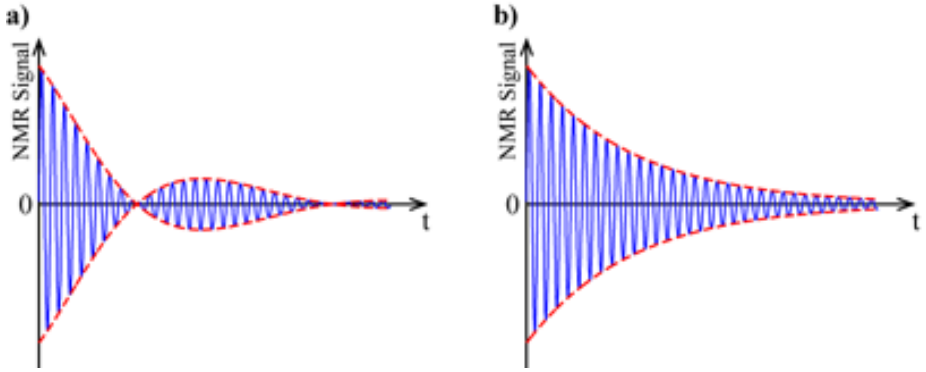

Figure 3.2: FID signals received from **a)** a poorly-shimmed sample and **b)** a well-shimmed sample.

Automatic FID shimming was first proposed by Ernst [49], and successfully implemented by Tochtrop [50] and Holz [51]. The sample may be shimmed by finding the shim currents that maximise the time integral of the magnitude of the complex FID signal with a search algorithm such as the simplex algorithm (*e.g.* § 10.4 in [52]). This is a 'blind' shimming method in that ΔB_0 is not measured directly, but the effects on the FID are observed and minimised.

3.2.4 Field-Map-Based Shimming

Prammer *et al.* [53] introduced the concept of measuring ΔB_0, analysing its spherical harmonic content and setting currents in the shim coils accordingly. In this approach, the 3D magnetic field generated by each shim coil, the shim field, is measured for a spherical phantom centered at the isocentre of the coil set. The shim currents, I^{shim}, can be obtained by pseudinversion, †, of a matrix describing the shim fields, $\mathbf{B}_0^{\text{shim}}$, multiplied by the field required to maximally null ΔB_0 for each new object scanned

$$I^{\text{shim}} = -\Delta B_0 \left(\mathbf{B}_0^{\text{shim}}\right)^{\dagger} \tag{3.1}$$

where $I^{\text{shim}} = \left[I^{\{0,0\}}, I^{\{1,0\}}, I^{\{1,1\}}, \ldots, I^{\{n,m\}}\right]$, $I^{\{n,m\}}$ is the current needed for the n^{th} order, m^{th} degree shim coil, $\mathbf{B}_0^{\text{shim}} = \left[\mathbf{B}_0^{\{0,0\}}, \mathbf{B}_0^{\{1,0\}}, \mathbf{B}_0^{\{1,1\}}, \ldots, \mathbf{B}_0^{\{n,m\}}\right]$ and $\mathbf{B}_0^{\{n,m\}}$ is the shim field per unit current for the n^{th} order, m^{th} degree shim coil, *e.g.* $I^{\{1,1\}}$ is the amount of current needed in the X-gradient coil. Figure 3.3 shows the residual field, ΔB_0^{res}, in a head **a)** before and after simulated field-map-based shimming with **b)** up to 1^{st}, **c)** up to 2^{nd} **d)** up to 3^{rd} order shim coils. σ_0^{res}, The root-mean-squared (RMS) of ΔB_0^{res}, maximum and minimum magnetic field values are shown in ppm.

Gruetter [54, 55] developed a more time-efficient field mapping approach , called '**f**ast, **a**utomatic **s**himming **t**echnique by **m**apping **a**long **p**rojections' (FASTMAP), involving measurement of ΔB_0 along 6 'pencil-beam' lines to give enough information to determine the optimal settings for all 1^{st} and 2^{nd} order shim currents unequivocally. This was improved upon by the tenuously acronymed '**f**ast, **a**utomatic **s**himming **t**echnique with improved **e**fficiency and **r**eliabilty for **m**apping **a**long **p**rojections' (FASTERMAP) [56], and '**r**obust **a**utomated **s**himming **t**echnique using **a**rbitrary **m**apping **a**cquisition **p**arameters' (RASTAMAP) [57] techniques. FASTMAP and its derivatives assume the shim coils generate exact spherical harmonics, which can introduce errors. Many clinical MRI scanners now perform automatic shimming in this way.

There is a limit to the magnitude of the spherical harmonic that a shim coil can generate resulting from the limit on the amount of current that can be passed through the coil. Rather than arbitrarily truncating the shim currents, taking the limits into consideration when solving Eq. (3.1) results in a better shim [58].

3.2.5 z-Shimming

In multi-slice imaging, the effects of ΔB_0 can be separated into those that vary within the slice § 3.2.2, ΔG_{xy}, and those that vary through the slice § 3.2.1, ΔG_z. ΔG_z effects are

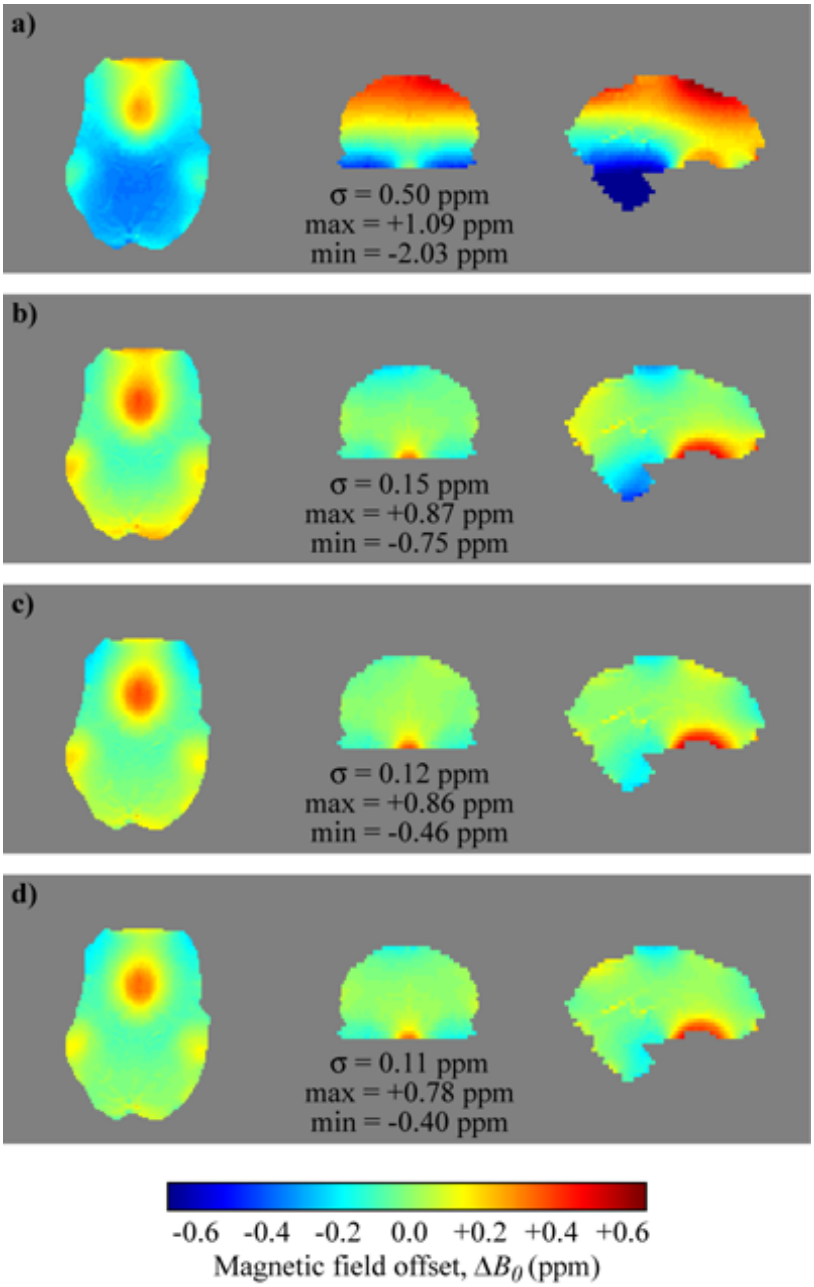

Figure 3.3: Axial, coronal and sagittal slice images of the residual magnetic field inhomogeneity, ΔB_0^{res}, in a head **a)** before and after simulated field-map-based shimming with **b)** up to 1$^{\text{st}}$, **c)** up to 2$^{\text{nd}}$ and **d)** up to 3$^{\text{rd}}$ order shim coils.

compensated for by the z-shimming technique [59, 60]. After acquiring a normal image of the slice (Fig. 3.4 **a)**), additional images are acquired (Fig. 3.4 **b)** and **c)**) with additional positive and negative z-gradients applied, which increases the scan time. This results in a set of images with different compensation for the susceptibility induced through-slice gradients. These images can be recombined by various methods [60–63] to give an image with good signal over the whole slice (Fig. 3.4 **d)**).

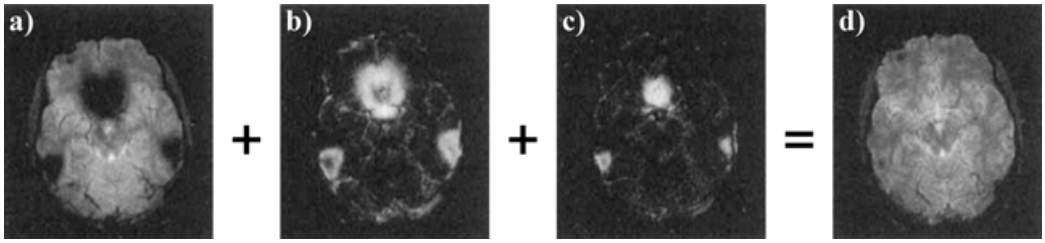

Figure 3.4: An example of z-shimming by Yang *et al.* [60] showing gradient-echo brain images with the time integral of the refocussing lobe of the slice-select gradient pulse increased by **a)** 0%, **b)** 20%, and **c)** 40%. This data is combined to give **d)** a single image of more uniform intensity.

A '3D' approach to z-shimming [64] acquires a full 3D data set with extended acquisitions in the k_z direction. This extra information may be reduced using methods similar to those used in reconstructing 2D z-shim data and the signal lost from affected areas may be recovered.

Functional MRI (fMRI) [16] is generally based on the use of EPI (§ 2.5.9) with echo times matched to the grey matter T_2^* and therefore exhibits significant loss of sensitivity due to ΔG_y as well as ΔG_z. Artefacts are more intense in the phase encoding direction in EPI because the time between successive k_y measurements is much greater than k_x. In-plane susceptibility gradients in the phase encoding direction shift the echo time and can cause BOLD sensitivity losses. Deichmann *et al.* [65] applied preparation phase encoding pulses in combination with z-shimming to restore these shifted echoes and thereby mitigate the loss of BOLD sensitivity. This technique also requires additional data acquisition with different preparation pulse strengths which reduces the time resolution of the fMRI study.

3.2.6 Dynamic Shimming

Dynamic shimming [66–68], also known as dynamic shim updating (DSU), is similar to the field-map-based shimming of Prammer *et al.* [53] in that it involves calculation of the shim currents by fitting the shim fields to $-\Delta B_0$. In dynamic shimming, however, this fitting is

separately performed for each slice of a multi-slice data acquisition [66]. Reducing the size of the shimming region in one dimension to a single slice reduces the extent over which the field can vary and therefore the number of spherical harmonics needed to characterise the field variation. Figure 3.5 **a)** shows field maps of a brain obtained using the sequence described in § 2.5.10. Furthermore, it shows ΔB_0^{res} after simulated **b)** global and **c)** dynamic shimming using shim coils up to and including all 2^{nd} order coil terms. Figure 3.6 shows the root-mean-squared residual magnetic field variation, σ_0^{res} after global and dynamic shimming with different numbers of shim coils and different slice-select directions.

A more homogeneous magnetic field results from dynamic shimming, but larger shim currents may be required and, in addition, the current in the shim coils needs to be switched rapidly. Dynamic shimming may therefore require supplementary hardware to that which is available in most clinical scanners. For instance, the shim coils must have low inductances to reduce their rise time to $\lesssim 10$ ms rather than $\lesssim 1$ s. Shim coils may also need to be actively shielded (§ 4.5) or driven with pre-emphasised currents (§ 3.3.1) to limit the effects of eddy currents when the shim currents are altered.

3.2.7 Local Shimming

Adding paramagnetic material close to the area that experiences large susceptibility induced field gradients allows the field to be locally shimmed in a specific area. It has been demonstrated that ferromagnetic Nickel [69, 70] or photocopier toner [71] placed around the head can be used to disrupt the magnetic field in a predictable way so as to ameliorate ΔB_0. Alternatively, use of mouth (or ear) inserts (Fig. 3.7 **a)** made of a strongly diamagnetic material [72] can cause localised correction of the large field offsets in the frontal cortex. A mouth shim based on current carrying wires has also been demonstrated [73].

3.2.8 Shimming Via Selective Excitation

Susceptibility-induced ΔB_0 imaging artefacts can also be reduced by modifying the RF excitation pulse. Cho and Ro [74] showed that by using an RF pulse with a quadratic through-slice phase profile, $\Delta\phi_z$, the effects of ΔG_z can be reduced, at the expense of a reduction in the signal-to-noise ratio (SNR) of the received NMR signal. In the method of Chen and Wyrwicz [75] the shape of ΔG_z across the slice is measured and an RF excitation pulse whose phase response cancels the effect of ΔG_z over the slice then used in signal excitation. Images obtained for different through-slice phase profiles are similar to those obtained with z-shimming and can be recombined in similar ways.

Stenger *et al.* [76] used 3D tailored RF excitation pulses [77] simultaneously to excite

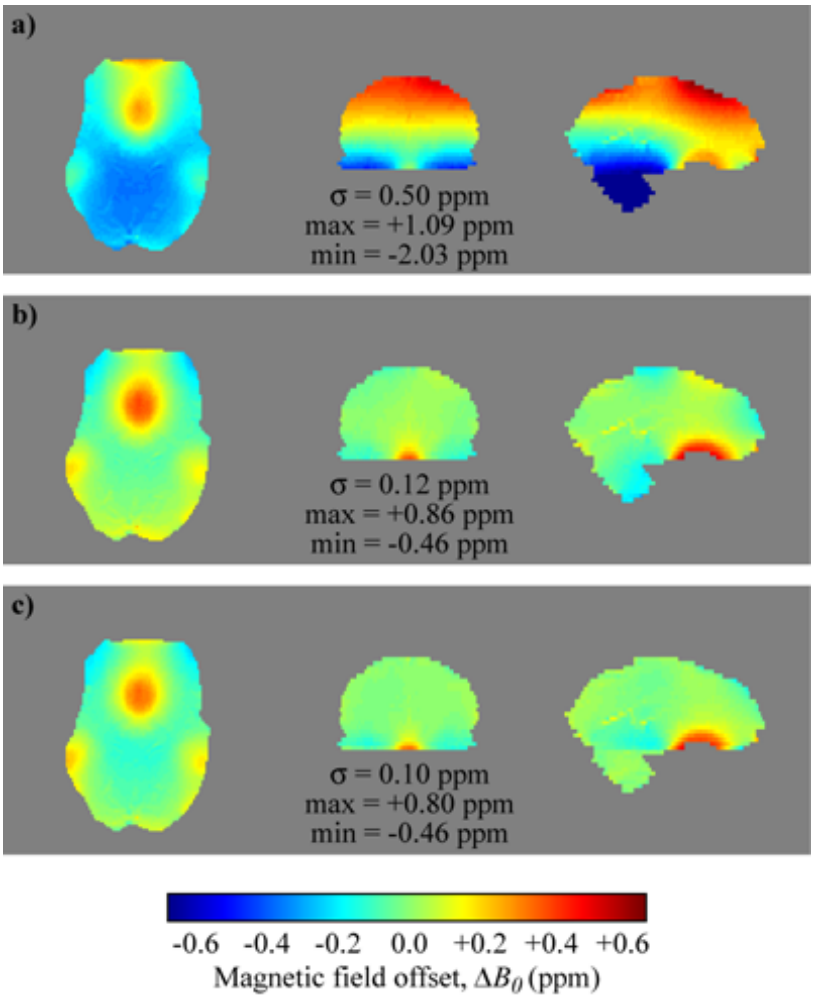

Figure 3.5: Susceptibility-induced residual field, ΔB_0^{res}, maps **a)** before and after simulated **b)** 2^{nd} order global and **c)** dynamic shimming of axial slices. The RMS, maximum and minimum values of ΔB_0^{res} are also given.

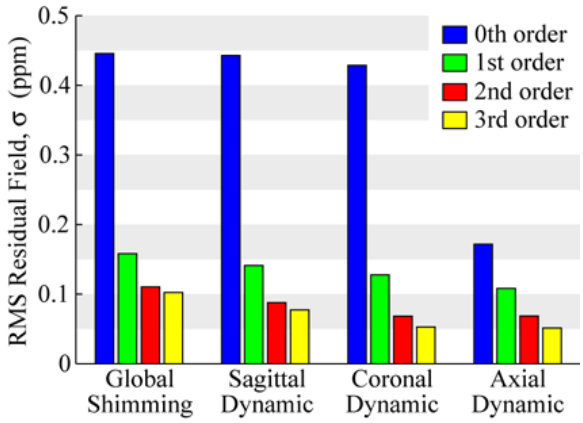

Figure 3.6: Graph showing RMS deviation of the field values in the head after global shimming, and dynamic shimming of sagittally, coronally, and axially orientated slices are simulated with 0^{th}, 1^{st}, 2^{nd} and 3^{rd} order shim fields.

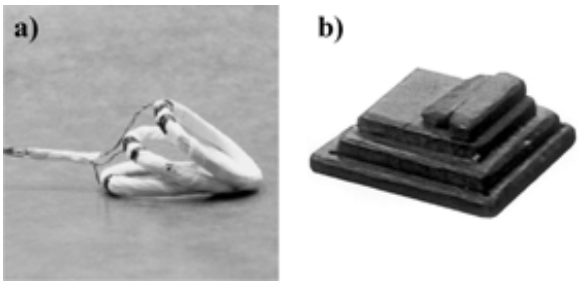

Figure 3.7: **a)** Coils of current carrying wire [73] or **b)** highly diamagnetic material [72] can be placed in the mouth for localised shimming of the frontal cortex.

a small area with a different phase profile and the rest of the slice with a normal phase profile. At the echo-time, T_E, the phases of spins across the slice become the same, and the signal is recovered. In theory, it is possible to measure $\Delta\phi_z$ over the whole slice and use its inverse as the phase profile of a two-dimensional RF excitation pulse to completely recover the signal at T_E. In practice, however, such RF pulses are too long for fMRI ($\gtrsim 60$ ms). Using multi-shot pulses shortens the RF excitation pulse, but reduces the temporal resolution of fMRI [78, 79].

3.2.9 Other Shimming Techniques

In addition to the methods described in this section so far, there are many other ways to decrease the effects of susceptibility-induced ΔB_0. Combinations, optimisations and

variations of the previously described methods are all possible.

Receiving the signal with multiple coil arrays [80] and parallel acquisition schemes [81, 82] allows k-space to be traversed more quickly, reducing the length of the echo-train in single-shot imaging, which inherently causes a reduction in the $\Delta\phi$ with a corresponding reduction in the artefacts [83–85].

Glover and Law [86] used a spiral imaging method (see Fig. 2.14) for fMRI with reduced susceptibility artefacts by acquiring a spiral-out and a spiral-in k-space trajectory.

In a variant of automatic shimming procedures, § 3.2.4, the brain can be segmented into regions where ΔB_0 is approximately the same, and then locally shimmed [87]. This works on a similar premise to dynamic shimming; if the shim region is smaller it is possible to approximate the field in that region with fewer spherical harmonics. This is also the principle behind some of the current work (Chapter 7).

3.2.10 Post-Processing Inhomogeneity Artefacts

If the image is distorted after acquisition, with knowledge of ΔB_0 the distortion can be modelled and unwarped [45, 88, 89]. This is a particularly useful approach in EPI (§ 2.5.9), but it cannot recover signal lost due to through-slice dephasing. A generalised method for using field maps to reverse the effects of ΔB_0 on images obtained from more complicated sequences was presented by Kadah and Hu [90], and is called '**s**imulated **ph**ase **e**volution **re**winding (SPHERE).

3.3 Eddy-Currents and Gradient Error

Transient magnetic field inhomogeneity, $\Delta B_0(t)$, may be introduced by the imaging gradient coils themselves. Gradients coils are designed (Chapter 4) with tolerated ΔB_0 to facilitate minimisation of the inductance and/or resistance of the coil. Any such ΔB_0 will be small at the centre of the region of uniformity (ROU), which is the region over which the gradient coils are designed to be generate linear magnetic field gradients, but at the edge or outside of the ROU, the magnetic field can have a nonlinear form (see Fig. 3.8 after Alsop and Connick [91]). Severe distortions therefore occur outside of the ROU where the gradient coils erroneously encode the position of the magnetic resonance signals.

Another significant contribution to $\Delta B_0(t)$ may come from eddy-currents. Switching current in the gradient coils generates an electric field at any close conducting surface (*e.g.* the metallic shell of the cryostat). It can be seen from Faraday's Law, Eq. (2.3), that a time-varying magnetic field, $\mathbf{B}$ must be accompanied by an electric field, $\mathbf{E}$. Also, from

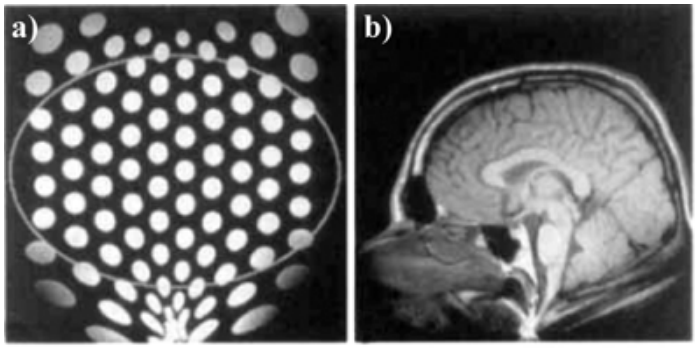

Figure 3.8: Imaging outside the linear region of the gradients (oval) for **a)** a phantom and **b)** a head.

Ampere's Law (Eq (2.2)) it can be seen that such electric fields will induce current flow, **J** in conducting media. These are eddy-currents. Eddy-currents in the bore of the scanner will, in turn, generate $\Delta B_0(t)$ within the ROU. Eddy-current induce magnetic fields that decay multi-exponentially. The cumulative magnetic field gradient that the spins in the sample experience will be different to what would be expected. Eddy-currents are mitigated by use of shielded gradient coils (§ 4.5) and/or gradient pre-emphasis (§ 3.3.1).

3.3.1 Gradient Pre-Emphasis

Gradient pre-emphasis [92] can be employed to mitigate $\Delta B_0(t)$ generated from eddy-currents (§ 3.3). The magnetic field gradient experienced by the sample from a step function current in the gradient coil is modified by a multi-exponential decay as shown in Fig. 3.9 **a)**. This can be modelled in terms of current flow in inductively coupled electrical circuits [93]. The multi-exponential decay is analysed and the current pulse that drives the gradient coils is modified by the inverse of the decay transfer function, to ensure the sample experiences the desired step-function magnetic field gradient (see Fig. 3.9 **b)**).

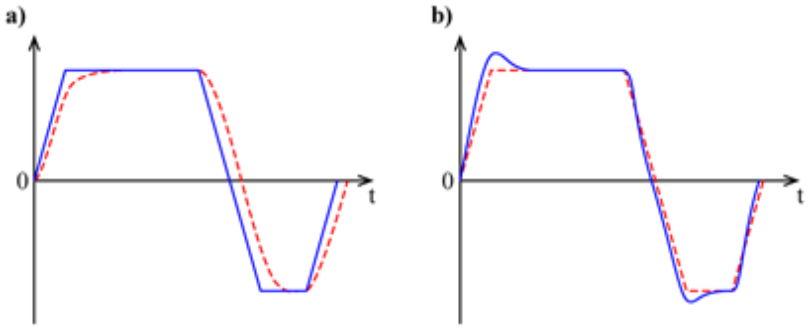

Figure 3.9: The gradient drive current (solid blue lines) and the magnetic field gradient that the sample experiences (dashed red lines) for **a)** an uncompensated pulse with eddy-current effects, and **b)** a pre-emphasised pulse that give the desired magnetic field gradient response.

Chapter 4

Coil Design

The various methods of designing current-carrying coils of wire that, when energised, generate a magnetic field whose axial component conforms to the shape of a spherical harmonic (§ 2.2) are described in this chapter. In addition, two reviews of gradient and shim coil design [94, 95] are recommended to the reader.

4.1 Biot-Savart Law

The Biot-Savart Law (Eq. (2.16)) is the principal equation used in coil design. It can be expressed in a differential form to calculate the contribution to the magnetic field, $d\mathbf{B}(\mathbf{r})$, at a point $\mathbf{r}$ generated by passing a current, I, through a thin wire element, of length $d\mathbf{l}$, at a position $\mathbf{r}'$,

$$d\mathbf{B}(\mathbf{r}) = \frac{\mu_0 I d\mathbf{l} \times (\mathbf{r}' - \mathbf{r})}{4\pi r^3} \tag{4.1}$$

where $r = |\mathbf{r}' - \mathbf{r}|$. Integration of Eq. (4.1) over the whole circuit reveals the magnetic field, $\mathbf{B}(\mathbf{r})$, due to the energised coil. Commonly we only consider the axial component of $\mathbf{B}$ since the presence of the very large static magnetic field in z, $B_0\hat{\mathbf{z}}$, means that the other components are insignificant when evaluating the local Larmor frquency

$$||B_0\hat{\mathbf{z}} + \mathbf{B}(\mathbf{r})|| \approx (B_0\hat{\mathbf{z}} + B_z(\mathbf{r}))\hat{\mathbf{z}} \tag{4.2}$$

4.2 Coil Performance

The amount of spherical harmonic magnetic field that the coil generates when carrying a 1 Amp current is known as the efficiency, η, of the coil and has units of $\mathrm{Tm}^{-n}\mathrm{A}^{-1}$, where n is

the order of the spherical harmonic the coil is designed to generate (*e.g.* $n = 1$ for gradient coils). η varies as $a^{-(n+1)}$, where a is the radius or characteristic length scale of the coil.

It is also necessary to assess the accuracy with which the coil generates the desired magnetic field variation. Here we measure the field error, $\Delta B_z(\mathbf{r})$, at any point $\mathbf{r}$ using

$$\Delta B_z(\mathbf{r}) = \frac{|B_z(\mathbf{r}) - B_z^t(\mathbf{r})|}{\max(|B_z^t(\mathbf{r}_k)|)} \times 100 \tag{4.3}$$

where $B_z(\mathbf{r})$ is the z-component of the magnetic field at $\mathbf{r}$ that the coil generates when 1 Amp is passed through it, $B_z^t(\mathbf{r})$ is the ideal field (*e.g.* for a Z gradient $B_z^t(\mathbf{r}) = \eta z$), and $\max(B_z^t(\mathbf{r}_k))$ is the maximum value of $B_z^t(\mathbf{r})$ inside the region of uniformity (ROU). This measure is used because it works well for all types of gradient as well as shim coils.

Other important properties of a coil are its inductance, L (H), and resistance, R (Ω), which dictate the speed at which current can be put into the coil and the amount of heating that occurs, respectively. Unless otherwise stated, in this work, L and R are calculated by multipole expansion impedance extraction using a program called FastHenry© [96] and it is assumed that 3 mm diameter, circular cross-section wire is used. Under these circumstances, L and R are both proportional to a.

The component of the torque vector, $d\mathbf{M}$ produced by an element of the coil, Idl, when energised in the presence of a uniform, external magnetic field, $\mathbf{B}_0$, can be calculated using

$$d\mathbf{M} = I\mathbf{r} \times (d\mathbf{l} \times \mathbf{B}_0) \tag{4.4}$$

where $\mathbf{r}$ is a vector linking the current element to the point about which the torque is evaluated.

A figure-of-merit (FOM) is useful for comparing the performance of gradient and shim coils that is independent of the number of turns of wire used in the coil [97], and proportional to $a^{-(2n+3)}$

$$\text{FOM} = \frac{\eta^2}{L}. \tag{4.5}$$

This FOM is useful because the power of the amplifier, P_a, needed to generate a field gradient, G, with a rise-time, τ, is

$$P_a = I_a V_a = \frac{G^2 L}{\eta^2 \tau} \propto \frac{1}{\text{FOM}} \tag{4.6}$$

where I_a and V_a represent the amplifier current and voltage. Other FOMs are often quoted, such as those that include a (*e.g.* [98]), the integral of $\Delta B_z(\mathbf{r})$ over a volume (*e.g.*

[99]), R (*e.g.* [100]), or **M**, (*e.g.* [101]). Due to the asymmetric geometry of some of the coils in this work, we simply use the FOM in Eq. (4.5) and quote the other properties of the coil as appropriate. Appendix A lists the properties of all the coils described in this thesis for comparison.

It is also useful to know some electric properties such as the slew rate ($SR = \frac{V_a \eta}{L}$), peak gradient amplitude ($G_{\max} = \eta I_a$), rise time ($\tau = \frac{L I_a}{V_a}$), maximum allowed duty cycle and acoustic noise levels. These are all dependent on the coil properties mentioned above and the operating voltage and current of the gradient power supply, as well as the cooling and static magnetic field present.

4.3 Discrete, Analytic Coil Design

The first coils that were used to generate a prescribed magnetic field in MRI applications were designed analytically. This was made possible by the well-known forms of the magnetic field generated by passing a current through straight wires, circular loops, and arcs of wire.

4.3.1 Helmholtz and Maxwell Coils

A Helmholtz coil generates a uniform magnetic field at its centre, and comprises two loops of wire arranged on an axis perpendicular to the plane of the loops, separated by a distance, a, equal to the loop radius. Figure 4.1 **a)** shows the Helmholtz coil arrangement and **b)** is a contour plot of the magnetic field it produces. The contour where the magnetic field deviates by 5%, as defined by Eq. (4.3), is also shown in **b)**.

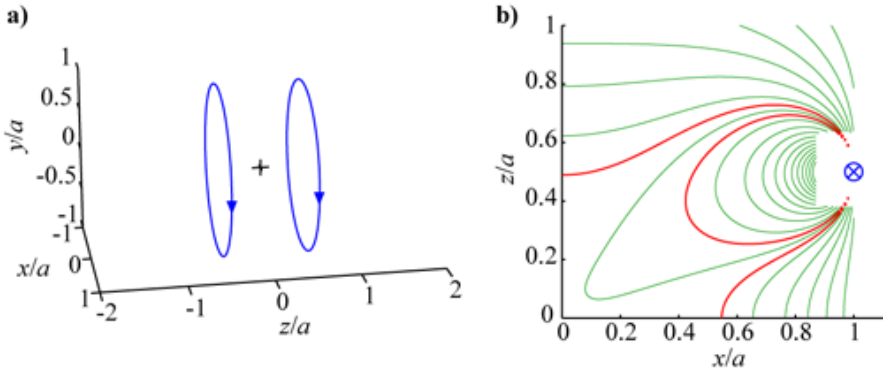

Figure 4.1: **a)** Wires of a Helmholtz coil and **b)** contours of the magnetic field generated by the coil, with 0.1 $a^{-1}\mu\mathrm{TA}^{-1}$ contour spacing (thin green), overlaid with the $\Delta B_z(\mathbf{r}) = 5\%$ contour (thick red). The wire that crosses into the contour plane is also shown as $\otimes$.

A Maxwell coil is similar to the Helmholtz coil, but with a loop separation of $\sqrt{3}a$, and the current flow in the loop located at $z = -\frac{\sqrt{3}}{2}a$ is reversed, such that a magnetic field that varies linearly with z is produced. Figure 4.2 shows the Maxwell coil and the magnetic field it generates.

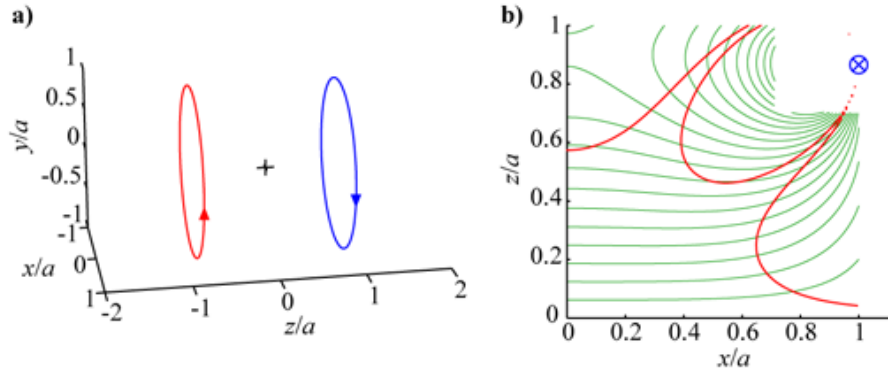

Figure 4.2: **a)** Wires of a Maxwell coil (red wires indicate reversed current flow with respect to blue) and **b)** contours of the magnetic field generated by the coil, with 0.05 $a^{-1}\mu\mathrm{TA}^{-1}$ contour spacing (thin green), overlaid with the $\Delta B_z(\mathbf{r}) = 5\%$ contour (thick red). The wire that crosses into the contour plane is also shown as $\otimes$.

4.3.2 Spherical Harmonic Generating Coils

Helmholtz and Maxwell coils provide the starting point for designing coils that generate zonal (those with no ϕ dependence, $m = 0$) spherical harmonics (§ 2.2) [24, 102]. The process of designing a discrete wire coils generally involves the annulment of the unwanted harmonics so as to leave the desired harmonics as the dominant form of field variation. Loops of wire placed symmetrically (or anti-symmetrically) about $z = 0$ generate only even (or odd) zonal harmonics. Then, by careful placement of the loops, harmonics whose order is lower than that of the desired harmonic can be annulled. In addition, some higher order harmonics may also be eliminated. Figure 4.3 **a)** shows a Z2 shim coil designed by positioning the loops so as to annul the 0^{th} and 4^{th} order zonal harmonics. Its magnetic field contour plot is shown in Fig. 4.3 **b)** which illustrates that cancelling the 4^{th} order zonal harmonic results in low ΔB_z at relatively large z extent. Higher orders are neglected as they are much weaker than the lower orders over the same volume.

Using arcs of wire on a cylindrical surface as building blocks enables the design of tesseral ($m \neq 0$) and sectoral ($m = n$) spherical harmonic shaped magnetic fields [24, 103]. A similar design process is applied for tesseral and sectoral harmonic coils: symmetry or

antisymmetry about the origin removes unwanted odd or even order harmonics that are generated, the angular length of the arcs and their placement dictate the degree, m, of the harmonics, and appropriate z placement annuls lower and some higher remaining unwanted harmonics. Figure 4.4 **a)** shows an X gradient coil designed by placing 120° arcs of current with opposite sense at appropriate z positions so as to null the $\{n, m\} = \{3, 1\}$ spherical harmonic leaving the $\{1, 1\}$ harmonic as dominant. Axial return paths linking the arcs produce no B_z, since $B_z \perp d\mathbf{l}$.

Coils comprised of different building blocks such as straight wires are also possible [24, 104–108].

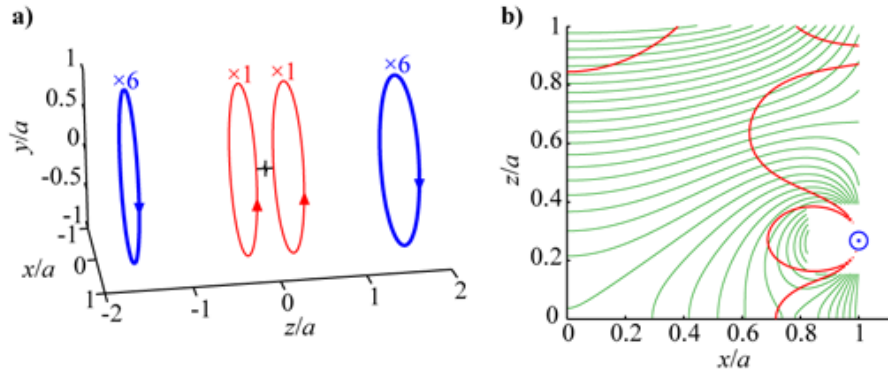

Figure 4.3: **a)** Wires of a discrete Z2 shim coil (red wires indicate reversed current flow with respect to blue) and **b)** contours of the magnetic field generated by the coil, with 0.1 $a^{-1}\mu\text{TA}^{-1}$ contour spacing (thin green), overlaid with the $\Delta B_z(\mathbf{r}) = 5\%$ contour (thick red). The wire that crosses out of the contour plane is also shown as $\odot$.

Many turns of wire are used with these discrete designs to achieve high magnetic field intensities, as demanded in MRI. There is a limit however, to the number of turns that can be added because the new turns have to be positioned further and further from the analytically correct location and therefore introduce field errors. Also, these designs have intrinsically high inductance, since the wires are close together and therefore inhabit a region of very high magnetic field intensity.

4.4 Distributed Windings

It is possible to increase the efficiency and lower the inductance of a coil by allowing the positions of the extra turns to spread out away from the positions of the first wires. These distributed windings must be so positioned to keep or even increase the extent of the region

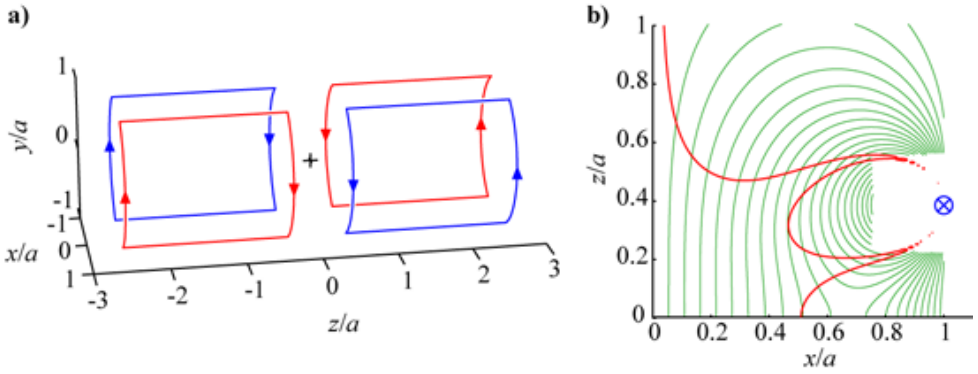

Figure 4.4: **a)** Wires of a discrete X gradient coil (red wires indicate reversed current flow with respect to blue) and **b)** contours of the magnetic field generated by the coil, with 0.05 $a^{-1}\mu\text{TA}^{-1}$ contour spacing (thin green), overlaid with the $\Delta B_z(\mathbf{r}) = 5\%$ contour (thick red). The wire that crosses into the contour plane is also shown as $\otimes$.

over which the magnetic field is uniform. Several methods for designing gradient coils (also applicable to shim coils) with distributed windings are described in the following sections.

At this point, it is convenient to describe the common geometry of the system. Figure 4.5 shows the cylindrical coil system where the cylindrical coordinates, (ρ, ϕ, z), Cartesian coordinates, (x, y, z), and the components of the current density that flow in the surface, J_ϕ and J_z are all indicated. There is no J_ρ component of $\mathbf{J}(\rho, \phi, z)$ since the current must flow on the surface

$$\mathbf{J}(\rho, \phi, z) = \mathbf{J}(\phi, z)\delta(\rho - a) \tag{4.7}$$

where a is the radius of the cylindrical conducting surface.

In the static case, $\nabla \cdot \mathbf{J} = 0$ so the components of current density flowing on the surface of a cylinder are related by

$$\frac{1}{a}\frac{\partial}{\partial \phi}J_\phi = -\frac{\partial}{\partial z}J_z \tag{4.8}$$

The wire pattern that approximates $\mathbf{J}(\phi, z)$ is found from N_c equally-spaced contours of the integrated current density. More generally, the wires follow equally-spaced contours of the stream function, $\psi(\mathbf{r})$, of the current density, $\mathbf{J}(\mathbf{r})$, flowing in any surface, S, defined by $\hat{\mathbf{n}}(\mathbf{r})$, the unit vector normal to the surface, such that

$$\mathbf{J}(\mathbf{r}) = \nabla \times [\psi(\mathbf{r})\hat{\mathbf{n}}(\mathbf{r})] \tag{4.9}$$

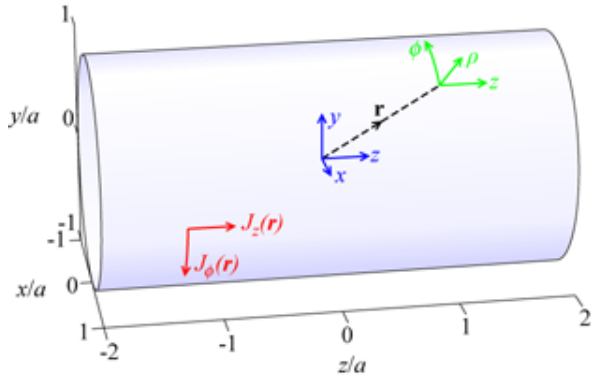

Figure 4.5: The cylindrical coordinate system showing the radial, ρ, azimuthal, ϕ, and axial, z coordinates with the azimuthal and axial components of the current density, $J_\phi(\mathbf{r})$ and $J_z(\mathbf{r})$ respectively, on the cylindrical conducting surface.

In the cylindrical case, this becomes

$$J_\phi = \frac{\partial \psi}{\partial z} \qquad \text{and} \qquad J_z = \frac{-1}{a}\frac{\partial \psi}{\partial \phi} \tag{4.10}$$

so, integrating $J_\phi(z)$ with respect to z generates ψ. The property that equally spaced contours of ψ give an approximation to $\mathbf{J}$ was proven by e.g. Brideson *et al.* [109]. It has also been demonstrated that continuous current densities can be approximated by multiple layers to increase the efficiency of the coil [100].

4.4.1 Distributed Discrete Coils

A method of spreading discrete loops of wire along a cylindrical surface to achieve more efficient coils with lower resistance is given in the first part of ref. [110]. This paper shows a way of using an array of co-axial circular coils and the well-known magnetic field that each coil generates on-axis, to generate a prescribed magnetic field at a series of points. Other distributed design methods that use discrete wires rather than a stream-function approach and are iterative, and are discussed in § 4.4.7.

4.4.2 Target Field

Turner [111–113] developed a method, using a Green's function expansion of $\frac{1}{|\mathbf{r}-\mathbf{r}'|}$ [2], in which the current density on a cylindrical surface, $\mathbf{J}(\phi, z)$, can be related to the axial magnetic field at any point in the region where $\rho < a$, $B_z(\rho, \phi, z)$ by

$$B_z(\rho,\phi,z) = -\frac{\mu_0 a}{2\pi}\sum_{m=-\infty}^{\infty}\int_{-\infty}^{\infty}|k|e^{im\phi}e^{ikz}j_\phi^m(k)K'_m(|k|a)I_m(|k|\rho)dk \tag{4.11}$$

where $j_\phi^m(k)$ is the Fourier transform (§ 2.3) of the ϕ component of $\mathbf{J}(\phi,z)$ and $K_m(x)$ and $I_m(x)$ are Modified Bessel functions ($K'_m(x)$ is the derivative of $K_m(x)$ and here, m is the order of the Bessel function).

Equation (4.11) can be used to allow the calculation of $\mathbf{J}(\phi,z)$ from a prescribed "target" magnetic field function, $B_z^t(\rho,\phi,z)$. The target field function must be chosen to satisfy Laplace's equation, and its Fourier transform must tend to zero faster than $e^{-k(a-c)}$ (where c is the radius of the cylinder on which the target field is prescribed) to allow only low spatial frequencies to contribute to $\mathbf{J}(\phi,z)$. In Turner's work [111] the function

$$B_z^t(\rho_c,0,z) = \frac{G_x}{d_2-d_1}\left[\frac{d_2}{1+(z/d_1)^n} - \frac{d_1}{1+(z/d_2)^n}\right] \tag{4.12}$$

was used as the analytic target field function to design an X-gradient coil. Figure 4.6 shows an X-gradient coil designed with the target field method, with the associated magnetic field plot.

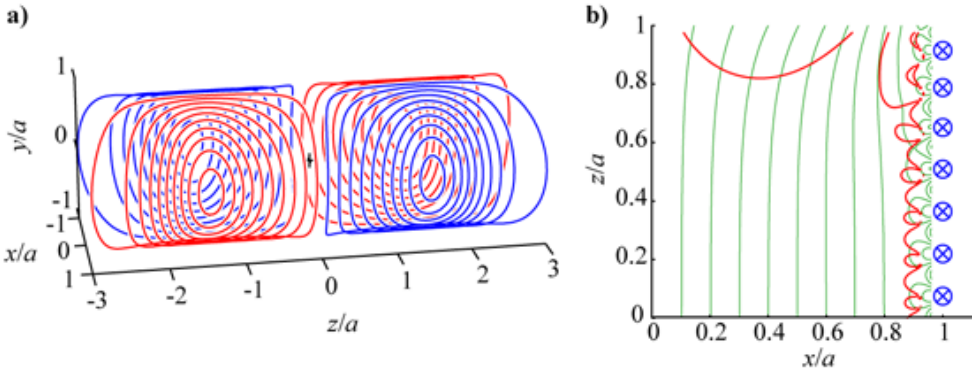

Figure 4.6: **a)** Wires of an X-gradient coil designed using the target field method (red wires indicate reversed current flow with respect to blue) and **b)** contours of the magnetic field generated by the coil, with 0.5 $a^{-1}\mu$TA^{-1} contour spacing (thin green), overlaid with the $\Delta B_z(\mathbf{r}) = 5\%$ contour (thick red) (the coil was designed using Eq. (4.12) with $\frac{d_1}{a} = 1.5$, $\frac{d_2}{a} = 2.5$, $n = 10$ and $\frac{c}{a} = 0.5$). The wires that cross into the contour plane is also shown as $\otimes$.

4.4.3 Minimum Inductance

In addition to the target field method (§ 4.4.2), Turner developed a way to design gradient and shim coils with minimum inductance [99], L, based on

$$L = -\frac{\mu_0 a^2}{I^2} \sum_{m=-\infty}^{\infty} \int_{-\infty}^{\infty} |j_\phi^m(k)| I'_m(|k|a) K'_m(|k|a) dk \tag{4.13}$$

where I is the current in the coil. Rather than using an analytic function for the form of the target magnetic field on the surface of a cylinder, the target field is prescribed at a series of N target points, $B_z^t(\mathbf{r}_n)$, at positions $\mathbf{r}_n$, where $n = 1, \ldots, N$. The difference between the actual field, $B_z(\rho_n, \phi_n, z_n)$, as calculated by Eq. (4.11), and the target field is minimised using Lagrange multipliers, λ_n, via the functional, U,

$$U = L + \frac{1}{I} \sum_{n=1}^{N} \lambda_n \left[B_z^t(\mathbf{r}_n) - B_z(\rho_n, \phi_n, z_n) \right] \tag{4.14}$$

Differentiation of U with respect to λ_n, leads to a system of N simultaneous equations which can be solved to yield the optimal current distribution.

The minimum inductance approach is made possible by defining the field as a finite set of target points. There are thereby an infinite number of solutions that $\mathbf{J}$ can take, and Eq. (4.14) finds the solution with the lowest inductance. Figure 4.7 shows an X-gradient coil designed with the minimum inductance method.

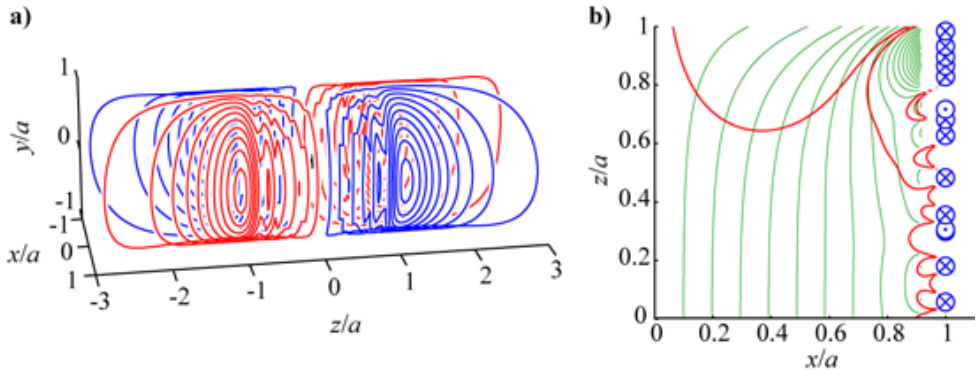

Figure 4.7: **a)** Wires of an X-gradient coil designed using the minimum inductance method (red wires indicate reversed current flow with respect to blue) and **b)** contours of the magnetic field generated by the coil, with 0.5 $a^{-1}\mu\mathrm{TA}^{-1}$ contour spacing (thin green), overlaid with the $\Delta B_z(\mathbf{r}) = 5\%$ contour (thick red). The wires are also shown that cross into, $\otimes$, and out of, $\odot$, the contour plane.

4.4.4 Apodisation

The coils designed with the minimum inductance method can exhibit high spatial frequency oscillations in J_z (as shown in Fig. 4.7 **a** in the region where $-a < z < a$). These increase the inductance and resistance, as well as reducing the efficiency of the coil. This occurs because this approach attempts to exactly match the actual field to the target field. It is therefore beneficial to slacken this constraint slightly so as to lower the inductance of the coil appreciably. This may be simply done by smoothing, or apodisation (latin for "removing the foot") of J_z. To achieve this apodisation the Fourier transform of J_z can be multiplied by a gaussian function to reduce its higher frequency components

$$j_\phi^A(k) = j_\phi(k)e^{-2h^2k^2} \tag{4.15}$$

where h is known as the apodisation length. The result of this apodisation is illustrated in Fig. 4.8.

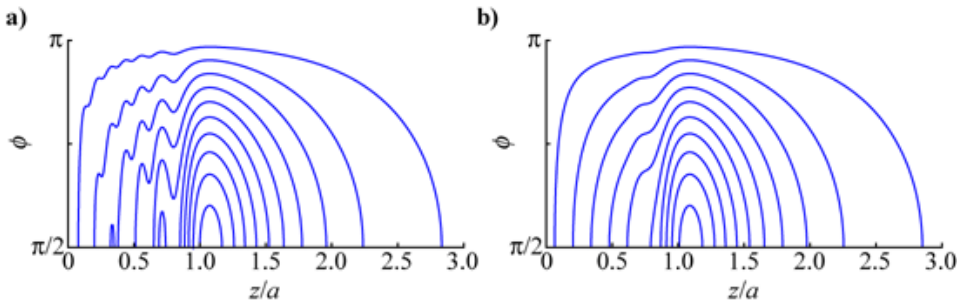

Figure 4.8: One octant of the wire paths for the **a)** unapodised minimum inductance X-gradient coil from Fig. 4.7 and the **b)** apodised version using $h = 0.03a$.

4.4.5 Functional Minimisation by Matrix Inversion

The minimum inductance coil design method produces a set of equations which are solved numerically using a matrix, $\mathbb{A}$, of coefficients A_{pn} that relate the field at P target field points, $B_z^t(\mathbf{r}_p)$, and the N Lagrange multipliers, λ_n, that are used to generate $\mathbf{J}$,

$$\mathbf{B} = \mathbb{A}\boldsymbol{\lambda}. \tag{4.16}$$

$\mathbb{A}$ is square for coils designed using Turner's minimum inductance method, since $P = N$, and can be inverted by using Gaussian elimination to obtain $\boldsymbol{\lambda}$.

$$\boldsymbol{\lambda} = \mathbb{A}^{-1}\mathbf{B} \tag{4.17}$$

Hoult and Deslauriers formulated a similar matrix-based coil design method with fewer parameters describing the target field than the current density [110]. This overdetermined system results in a rectangular $\mathbb{A}$ matrix of size $N \times P$ where $P < N$. A Moore-Penrose pseudoinversion of the matrix, $\mathbb{A}^{\dagger} = (\mathbb{A}^T\mathbb{A}^{-1})\mathbb{A}^T$ can be performed which provides the least-squares solution, which is usefully the coil with the minimum power dissipation and hence resistance. In this scheme, the target field, B_z^t may be parameterised in terms of spherical harmonic (§ 2.2) basis functions, and/or the current density may be expressed as a linear combination of some basis set (e.g. a Fourier series).

4.4.6 Finite-Length Coil Design

Carlson *et al.* expressed the current density as a weighted, finite, set of truncated sinusoidal basis functions spanning a length, l [97]. For zonal coils antisymmetric in z

$$\begin{aligned} J_\phi(z) &= \sum_{n=1}^{N} \lambda_n \sin\left(\frac{2\pi n z}{l}\right) && |z| < \tfrac{l}{2} \\ &= 0 && |z| > \tfrac{l}{2} \end{aligned} \tag{4.18}$$

and for symmetric coils, cosine rather than sine functions are used. The inductance, L, and the magnetic field at a series of points can be expressed in terms of these basis functions since their Fourier transform is well known. The field error (the difference between the target field and the actual field) and the inductance is once again combined into a functional, U,

$$U = \sum_{p=1}^{P} w_p \left[B_z^t(\mathbf{r}_p) - B_z(\rho_p, \phi_p, z_p)\right]^2 + \alpha L \tag{4.19}$$

where w_p is a weighting factor allowing control over the relative accuracy of the p^{th} target point, and α is a trade-off parameter for the extent by which the inductance is minimised. An additional term for the resistance of the coil, βR, may be added so that there are two user definable trade-off parameters. Increasing the value of these parameters has the effect of making the field conform less well to the target field, while reducing the inductance and/or resistance of the coil.

Equation (4.19) is again differentiated to obtain a set of simultaneous equations, representable in matrix form. Since the field error is squared, a square matrix results, of the same size as the matrix that controls the inductance ($N \times N$). Therefore matrix inversion

via Gaussian elimination as for Eq. (4.17) yields the weightings, λ_n, that can be used to reconstruct **J**. Figure 4.9 shows an X-gradient coil produced using this finite-length coil design method. The length of the coil is restricted to $l = 3.2a$ m in this example.

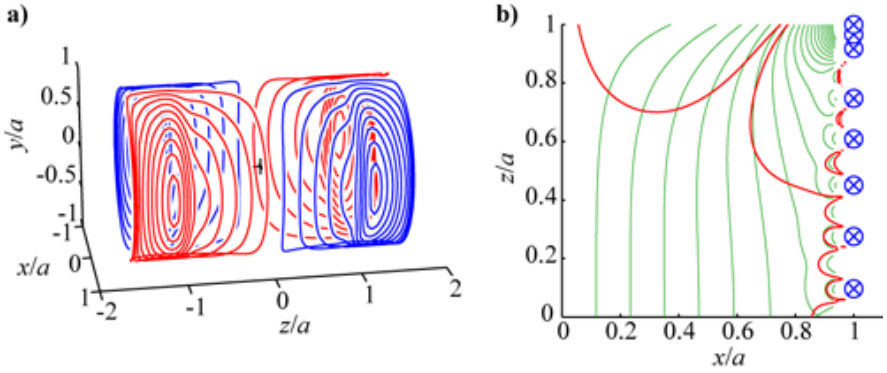

Figure 4.9: **a)** Wires of a finite-length X gradient coil (red wires indicate reversed current flow with respect to blue) and **b)** contours of the magnetic field generated by the coil, with 0.5 $a^{-1}\mu\mathrm{TA}^{-1}$ contour spacing (thin green), overlaid with the $\Delta B_z(\mathbf{r}) = 5\%$ contour (thick red). The wires that cross into the contour plane is also shown as $\otimes$.

4.4.7 Iterative Methods

Optimisation of the homogeneity, efficiency, inductance etc. may also be achieved by iterative techniques. Most optimisation methods work by allowing the positions of discrete wires as free parameters in the optimisation routine. Wong *et al.* [114] used an iterative technique to design a Z-gradient coil by allowing the positions of the loops of wires to be iteratively adjusted so as to minimise an error function characterising the field error and/or the coil inductance. The gradient of the error function with respect to the free parameters is also calculated for each iteration and the parameter space is searched by conjugate gradient descent (CGD), a first-order optimisation algorithm. There are several other examples of the use of CGD in gradient coil design [115–118].

The most commonly used iterative optimisation algorithm in gradient coil design has been simulated annealing (SA). This is because it is excellent at avoiding local minima in the error function when finding the global minimum. It was first used to adjust the positions of circular loops of wire so as to generate a coil producing a highly uniform Z-gradient [119]. SA was later used to design X-gradient coils by parameterising the positions of the wire elements [120]. Crozier *et al.* described one quadrant of the X-gradient coil as a series of concentric circles deformed by transformation mapping with much fewer free parameters

[121]. The SA algorithm has been used extensively to optimise parameters in the design of various gradient and shim coil [98, 122–138].

Another common stochastic optimisation technique is to mimic Mendelian evolution, and allow better solutions to the problem to "survive", "mutate" and "breed" to form the solutions to the next iteration. This genetic algorithm (GA) has been applied to the design of gradient coils in a similar way to CGD and SA so as to produce more linear and compact cylindrical Z-gradient coils [139], X-gradient coils [140, 141], and bi-planar coils [142, 143].

Adamiak *et al.* [144] used a zeroth-order Powell optimisation (one that only uses the result of the Biot-Savart calculation, and not its derivative) to adjust the positions of wire segments iteratively so as to generate a four-turn X-gradient coil. The Monte Carlo (MC) method has also been applied to gradient and shim coil design [145, 146]. Linear [147] and quadratic [148] programming are other options for optimising gradient coil design.

Iterative coil design techniques often have the advantage that they work directly with the wires of the coil design. The magnetic field, and therefore the error function to optimise, is calculated by direct integration of the Biot-Savart Law (Eq. (4.1)) over the wires. When approximating the continuous current density (§ 4.4.2 to § 4.4.6) in terms of a small number of turns of wire, the approximation becomes less valid. Hence, iterative methods, using discrete wires work better for few wires than continuous current density methods. However, iterative methods are considerably more computationally intensive, and tend to produce wire patterns with abrupt changes in directions. These changes can introduce high order spherical harmonics in the magnetic field. These methods also do not need there to be more free coil design coil parameters than field parameters.

4.4.8 Slack, Finite-Length Coil Design

A modification to the finite-length coil design method described in the previous section was developed during the course of the work described in this thesis [149]. Equations (4.11) and (4.13) are again used for the parameterisation of the magnetic field and inductance of the coil respectively. Unlike the method described in § 4.4.6, a functional is not differentiated to obtain the parameters that define the current density. Rather, an inequality relationship is constructed that describes the error in the magnetic field E_p at each of the P target points

$$E_p = \left| \frac{B_z^t(\mathbf{r}_p) - B_z(\rho_p, \phi_p, z_p)}{\max(B_z^t(\mathbf{r}_p))} \right| \leq \delta_p \tag{4.20}$$

where δ_p is the maximum field error allowed at the p^{th} target field point. It is most convenient to set the same value for all points, *e.g.* $\delta_p = \delta = 5\%$.

Using sequential quadratic programming via the `fmincon` function in Matlabs® Opti-

misation Toolbox, any FOM can be maximised whilst satisfying the nonlinear inequality constraints in Eq. (4.20). Gradient and shim coils are designed with maximum η^2/L in this work.

The resulting coils are similar to those generated using the finite-length method described in § 4.4.6, but with slightly higher FOMs. This is because there is more freedom for the magnetic field to deviate from the target field in the middle of the ROU, and because the FOM is directly maximised.

4.4.9 Bi-Planar Coils

After the cylindrical geometries discussed so far, the next most common coil geometry is bi-planar for inserting into cylindrical MRI bores, for "open" MRI scanners and for microscopy. The evolution of planar gradient coils has mirrored that of the cylindrical coils with some important differences. Initially, discrete wires were allowed to be positioned on planar surfaces [150, 151]. A bi-planar equivalent of Turner's minimum inductance method [99] was formulated [152–154] and with finite square [155] and circular extent [156]. The SA [98, 130, 134, 137] and GA [142, 143] iterative methods have also been applied to bi-planar gradient coils. Actively shielded (§ 4.5.2) bi-planar gradient have similarly been designed [151, 152, 157], as well as bi-planar shim coils [158, 159].

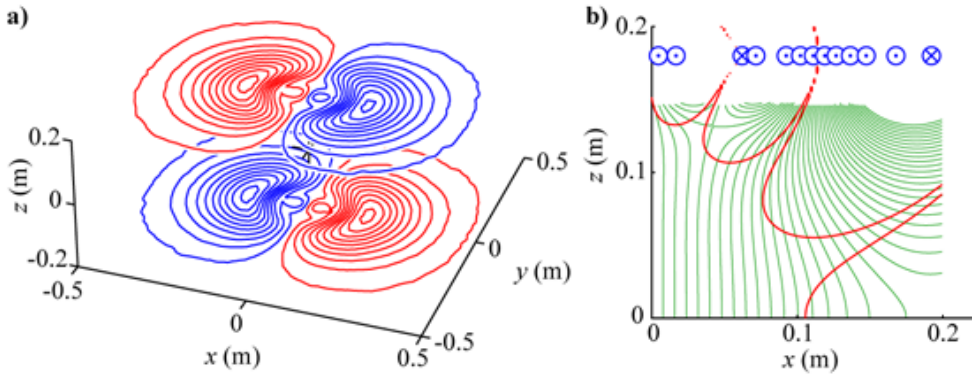

Figure 4.10: **a)** Wires of a bi-planar X-gradient coil (red wires indicate reversed current flow with respect to blue) and **b)** contours of the magnetic field generated by the coil, with 1 μTA^{-1} contour spacing (thin green), overlaid with the $\Delta B_z(\mathbf{r}) = 5\%$ contour (thick red). The wires are also shown that cross into, $\otimes$, and out of, $\odot$, the contour plane.

Pissanetzky [160] developed a method of designing planar gradient coils that is completely free of any symmetry requirements. Figure 4.10 **a)** shows a bi-planar X-gradient coil designed using a variant of this method and **b)** the magnetic field it generates in the $y = 0$

plane. Pissanetzky's method was also used to develop slightly convex versions of planar gradient coil [161]. This method is a type of boundary-element-method that is described in § 4.4.11 and in much greater detail in Chapter 5.

4.4.10 Reduced Symmetry

The gradient and shim coils discussed so far in this chapter have been based upon discrete loops, straight wires, cylindrical, or bi-planar geometry. This is because the mathematics for such elementary geometries is relatively simple, primarily involving Bessel functions and Fourier transforms. In fact, the simplest geometry for coil design in terms of the mathematics is spherical, since it possesses the most symmetry [162]. Figure 4.11 shows a spherical X-gradient coil. The homogeneity of spherical coils is excellent since the current carrying surface completely surrounds the ROU. However, there are some issues with the practicality of building and getting subjects in to and out of spherical gradient coils.

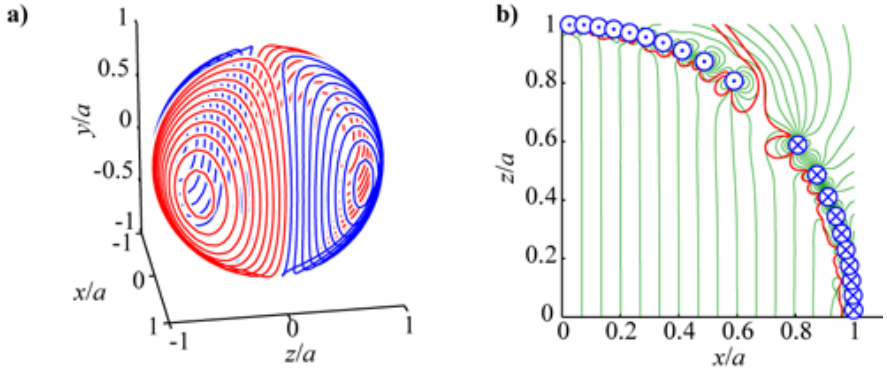

Figure 4.11: **a)** Wires of a spherical X-gradient coil (red wires indicate reversed current flow with respect to blue) and **b)** contours of the magnetic field generated by the coil, with 1 $a^{-1}\mu\mathrm{TA}^{-1}$ contour spacing (thin green), overlaid with the $\Delta B_z(\mathbf{r}) = 5\%$ contour (thick red). The wires are also shown that cross into, $\otimes$, and out of, $\odot$, the contour plane.

For a multitude of reasons, researchers have been motivated to deviate from the most simple geometries. One common symmetry deviation involves locating the ROU closer to one end of a cylindrical coil than the other [91, 129, 132, 163–166] for head only imaging. This allows the radius of the coil to be reduced, and consequentially the efficiency of the coil to be increased (since $\eta \propto a^{-2}$ for gradient coils), providing the coil is short enough below the ROU to comfortably accommodate the subject. Shim coils may also be designed using this offset ROU geometry [167–170]. Symmetric coils are intrinsically torque-balanced. Once the ROU is moved, the symmetry is broken and there may be torques on the coil

when energised within an external magnetic field (Eq. (4.4)), which must be accounted for in the design process or else large torques may be experienced.

Other gradient coil designs that deviate from simple symmetry include cylinders with "flared" conical section ends to improve patient access [171, 172], cylindrical gradient coils with parabolic-shaped return-path wires to help accommodate the shoulders of subjects [173, 174], elliptical cross-section gradients [175], gradients with a shielding surface that incorporates an annular cap [176], hemispherical [177], and combined hemispherical/cylindrical "dome" geometry [178].

4.4.11 Asymmetric Coils

With all of the coils described in the previous section that deviate from the simple spherical, cylindrical, or bi-planar symmetries, additional, often highly complex mathematics are required specific to that geometry for the coil design process. This leads to the inevitable desire to develop a coil design methodology that is general enough to handle all the above geometries and be completely free of any symmetry requirements. Pissanetzky developed such a method as early as 1992 but only applied it to the design of bi-planar gradient coils [160] (§ 4.4.9). Another approach to asymmetric coil design was demonstrated for gradient and shim coils with dual radii [147], but the authors were apparently unaware of the power of the Pissanetzky approach. Little work has been published on this powerful method, with some notable recent exceptions [179–182]. In the course of this thesis, we have adopted this method to design some highly asymmetric gradient, shim as well as other, more exotic coil designs [183–187]. Pissanetzky's approach describes the stream-function on the current carrying surface as a set of piece-wise continuous linear basis functions and therefore is an inverse boundary element method (IBEM). We expand upon this technique and note some modifications and applications in Chapters 5 and 6.

4.5 Shielding

Gradient coils are designed to be switched rapidly to provide spatial localisation for the magnetic resonance signal in MRI (§ 2.5). Shim coils sometimes (§ 3.2.6) also need to be switched rapidly. Gradient and shim coils generate a specific magnetic field in the ROU, and, as a side-effect, a magnetic field outside the coil. From Faraday's Law, Eq. (2.3) it is easy to see that a time-varying magnetic field induces an electric field which causes currents to flow in close conducting surfaces ($\mathbf{J} = \sigma\mathbf{E}$). These currents are circulatory, since they must flow in the surface and $\nabla \cdot \mathbf{J} = 0$, and transient, as can be deduced from

Faraday's Law. The intensity of the eddy-currents is related to the switching time and strength of the gradient coil as well as the conductivity of the eddy-current surface and its proximity to the gradient coil wires. The circulatory eddy-currents generate their own transient magnetic fields which may be of considerable size in the ROU. The most significant surface as a source of eddy-currents in an MRI scanner is often formed by the heat shields of the cryostat which contains the superconducting main magnet wires and cryogens (see Fig. 2.17). This encompasses the gradient coils entirely, and is often very close to them. It is also usually made of stainless steel, which is a good conductor. Eddy-currents induced in the cryostat experience the intense static magnetic field and therefore generate forces on the warm-bore which manifest as acoustic noise [188]

To reduce the effect of eddy-currents without detrimentally affecting the homogeneity of the desired magnetic field in the ROU, magnetic shielding of the gradient coils may be provided. This section describes magnetic shielding for the mitigation of eddy-current-induced transient magnetic fields in the ROU.

4.5.1 Passive Magnetic Shielding

The simplest way to shield the bore of the superconducting magnet cryostat from stray transient magnetic fields is to interpose a thick cylinder of highly conductive material, such as Aluminium between the coil and the cryostat [112]. Such a surface allows the eddy-currents to flow in a material with a thickness much greater than the skin depth of the lowest characteristic frequency in the gradient switching. This means that the eddy-currents will decay relatively rapidly. When such a surface is close to the gradient coils the eddy-current-induced magnetic field in the ROU will more closely resemble the shape of the gradient itself. However, this technique is highly limited as eddy-current-induced magnetic fields are still generated, just in a more controlled manner.

4.5.2 Active Magnetic Shielding

A superior method of magnetically shielding conducting structures in the MRI scanner is to provide active magnetic shielding, as proposed by Mansfield *et al.* [189, 190]. An extra conducting surface with a multitude of current-carrying wires is placed between the primary magnetic field generating wires and the warm bore. These wires are distributed on the surface so as to cancel the radial component of the magnetic field, B_ρ, at this surface when energised. The early work concerned the design of active cylindrical shields for discrete wire gradient coils like those in § 4.3 and was also extended to incorporate multiple shielding surfaces [191].

A similar approach can be used to design actively shielded gradient coils with distributed windings on both the shield and the primary coil surfaces. This has been demonstrated for cylindrical [99, 192] and planar [152] gradient coil geometries. In the case of cylindrical coils, the integrand of Eq. (4.11) (and Eq. (4.13)) is simply multiplied by a shielding factor, $S(a, b, k)$,

$$S(a, b, k) = 1 - \frac{I'_m(ka)K'_m(kb)}{I'_m(kb)K'_m(ka)} \tag{4.21}$$

where a and b are the primary and shield coil radii respectively, to obtain the Fourier transform of the modified primary current density, $j^m_{\phi,P}(k)$. The Fourier transform of the shield current density, $j^m_{\phi,S}(k)$ is found from the relation [112]

$$j^m_{\phi,S}(k) = -j^m_{\phi,P}(k)\frac{aI'_m(ka)}{bI'_m(kb)} \tag{4.22}$$

Figure 4.12 illustrates a cylindrical example of a shielded target field gradient coil. Naturally, active magnetic screening of this sort has further been combined with all the flavours of coil design: stochastic techniques [121, 131, 193] shim coils [124, 169], bi-planar shim coils [158], elliptical cross-section [129, 176], asymmetric ROUs [170], shields with end-caps [194], modular coils [195] and multi-layer gradient coils [196].

These methods essentially identify the current density for the magnetic shield by convolving the primary current density with a well defined function related to the separation between primary and shield surfaces; greater separation results in greater differences between the shielding and primary current densities. Use of this approach is based on the assumption that the shielding surface is of infinite extent, which leads to problems for particularly short coils. A super-shielding (SUSHI) method was developed by which excellent shielding may be achieved without the use of an apodisation function for short cylindrical coils [197–199].

4.6 Miscellaneous Coils

Within NMR there are other magnetic field generating coils that are not simple gradient or shim coils or that have novel designs not covered so far in this chapter. Parker and Hadley used simulated annealing [119] to design a type of gradient coil that had two (or more) disparate linear magnetic field gradient regions to lower the maximum magnetic field intensity, thereby reducing the effect of peripheral nerve stimulation (PNS) [200].

To produce very intense gradient fields, the gradient coils must be highly efficient given a fixed power supply performance. To achieve this, many turns, N_c, of wire may be used

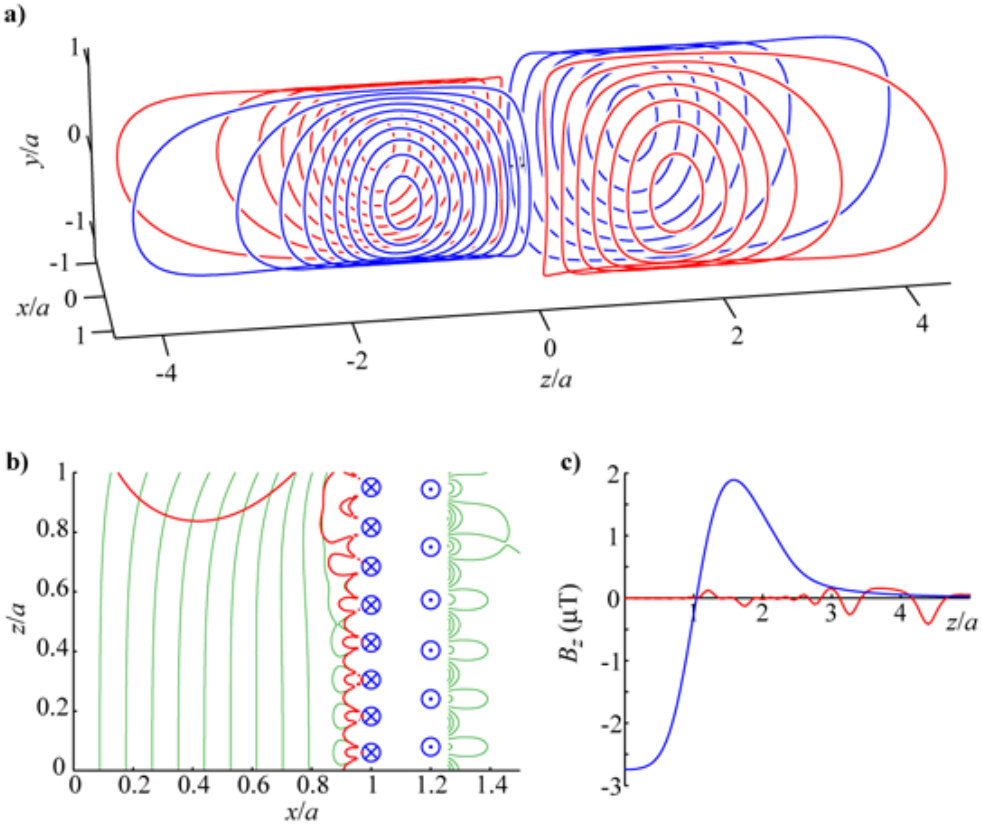

Figure 4.12: **a)** Primary (left, radius a) and shield (right, radius $b = 1.2a$) wires of a shielded, target field X-gradient coil (red wires indicate reversed current flow with respect to blue) and **b)** contours of the magnetic field generated by the coil, with 0.2 $a^{-1}\mu\text{TA}^{-1}$ contour spacing (thin green), overlaid with the $\Delta B_z(\mathbf{r}) = 5\%$ contour (thick red). **c)** shows that axial magnetic field along a line in z at $x = 1.4a$ and $y = 0$ for the shielded coil (red) and unshielded equivalent (blue, see Fig. 4.6). The wires are also shown that cross into, $\otimes$, and out of, $\odot$, the contour plane.

to approximate a calculated current density. This leads to an increase in the inductance of the coil (since $\eta \propto N_c$ and $L \propto N_c^2$) and therefore the rise-time, τ of the gradient ($\tau \approx \frac{LI_a}{V_a}$, where I_a and V_a are the current and voltage provided by the gradient coil amplifier) [100]. L also increases for gradients of the same strength with larger homogeneous ROUs. Clearly there is a trade-off between these characteristics. This led to the idea of modular gradient coils that individually, or in combination, can provide gradient fields with a small ROU with low τ, large ROU with high τ, and high η with high τ for different NMR applications that require these gradient field properties [179, 195].

Taracila *et al.* have recently developed an additional parameter that can be used in the optimisation process of the design of gradient coils [201]. An equation for the vibro-acoustic power of the gradient was formulated in terms of the current density.

Data from multiple disparate regions may be acquired in a single shot using the multiple acquisition with micro B_0 array (MAMBA) technique of Lee and Paley [202, 203]. This method requires current-carrying coils to generate a different intensity of homogeneous magnetic field in different regions of space. Using this approach, data may be acquired simultaneously from disparate regions without the use of switched gradient fields.

Chapter 5

IBEM Coil Design

This section describes the inverse boundary element method (IBEM) of magnetic field design in detail. The first section (§ 5.1) provides a mathematical framework for the IBEM and describes the physical problem. The way in which this mathematical framework can be used to design current-carrying coils that generate a prescribed magnetic field is then described. The final section (§ 5.3) explains how, with the inverse problem solved, solution of the forward problem and other techniques, can be used to find the electromagnetic properties of the coil.

5.1 Mathematical Framework

The mathematical framework for IBEM is derived in terms of the physical magnetostatic problem. Much of this section is taken from the original work by Pissanetzky [160], but uses the notation in Lemdiasov and Ludwig [181]. A recently published paper and thesis by Peeren [180, 204] gives an in depth mathematical treatment of the more general electromagnetic problem.

5.1.1 The Physical Problem

In this system, there exists an electrically conductive object, through which electric current flows, and a region in which a magnetic field is generated by the current in the conducting object. In our model, shown schematically in Fig. 5.1, the following assumptions are made:

(A) The conducting object is a thin conducting surface, S, defined at a point $\mathbf{r}'$ by the unit normal vector to the surface; $\hat{\mathbf{n}}(\mathbf{r}')$.

(B) S may comprise any number of individual sub-surfaces, S_n, where $n = 1 \ldots N_C$.

(C) The current flowing on S is time-invariant and is represented at $\mathbf{r}'$ by the current density vector $\mathbf{J}(\mathbf{r}')$.

(D) $\mathbf{J}(\mathbf{r}')$ must flow on the surface, therefore $\mathbf{J}(\mathbf{r}') \cdot \hat{\mathbf{n}}(\mathbf{r}') = 0$ everywhere on S.

(E) The current density must satisfy the continuity equation and be divergence-free; $\nabla \cdot \mathbf{J}(\mathbf{r}') = 0$.

(F) A time-invariant magnetic field, $\mathbf{B}(\mathbf{r})$, is generated by the current density over a region, V, separated from S.

(G) V may comprise any number of individual sub-regions, V_m, where $m = 1 \ldots N_V$.

(H) There also exists an externally applied, intense magnetic field, $B_0\hat{\mathbf{z}}$. Therefore, we only consider the z-component of the magnetic field generated in V by the conductor, $B_z(\mathbf{r})$ (Eq. (4.2)).

(I) $B_z(\mathbf{r})$ must satisfy Laplace's equation; $\nabla^2 B_z(\mathbf{r}) = 0$.

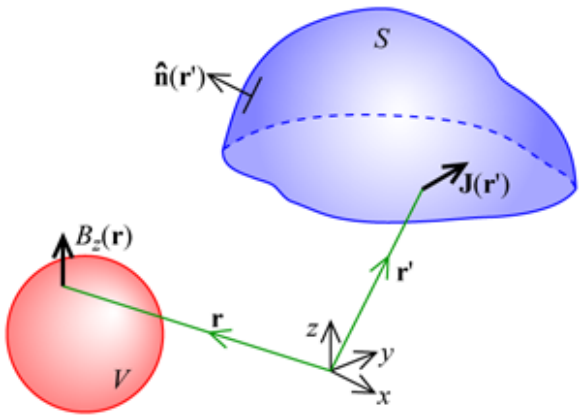

Figure 5.1: The electromagnetic problem.

The principal aim of the forward problem is to calculate $B_z(\mathbf{r})$ from a known $\mathbf{J}(\mathbf{r}')$. This may be achieved by integration of Eq. (5.1) over the surface.

$$d\mathbf{B}(\mathbf{r}) = \frac{\mu_0 I d\mathbf{l} \times (\mathbf{r}' - \mathbf{r})}{4\pi r^3} \tag{5.1}$$

Here, the focus is on the inverse problem where we want to find the $\mathbf{J}(\mathbf{r}')$ that will provide a given $B_z(\mathbf{r})$.

5.1.2 Discretising the problem

To make the inverse problem described in § 5.1.1 solvable numerically it needs to be discretised. First, let us consider the region, V, in which the magnetic field is induced. This can be simply discretised by defining a finite number of points, K, that lie within V. These points, from now on referred to as the target points, can have any position, $\mathbf{r}_k$ (where $k = 1, \ldots, K$) in space except on the surface S, and together define the target region.

Second, we consider the current-carrying surface, S. Since S is a thin surface with arbitrary geometry it may be discretised as a finite set of N_E flat elements, and N nodes at the corners of the elements. The principal sub-component of the discretised surface is the set of nodes. Each element that has a node as a vertex is associated with that node (e.g. each node, n, where $n = 1, \ldots, N_n$, has associated with it a set of elements, $\triangle_{ni}$, where $i = 1, \ldots, N_n$ and N_n is the number of elements associated with the n^{th} node). It is possible to define the surface in terms of quadratic, curved elements [186], and/or polygonal elements [180], but in this work we simply consider flat triangular elements. Figure 5.2 illustrates the discretisation of the problem.

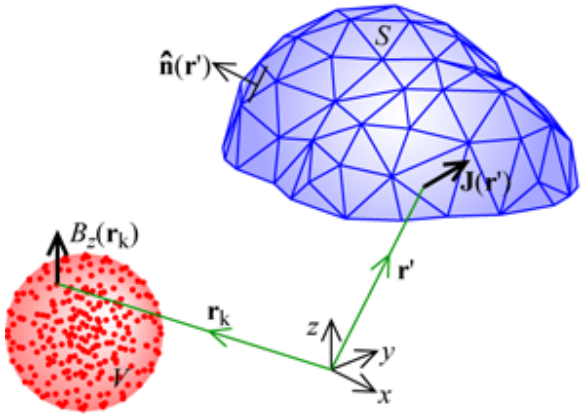

Figure 5.2: The discretised electromagnetic problem.

Discretising the geometry in this way leads us to discretise the target magnetic field, $B_z^t(\mathbf{r})$, to a set of target field values, B_{zk}^t, at the target points, $\mathbf{r}_k$. It also requires that the current density, $\mathbf{J}(\mathbf{r}')$, is discretised into a convenient set of basis functions. At this point we re-introduce the stream-function of the current density, $\psi(\mathbf{r}')$ at $\mathbf{r}'$,

$$\mathbf{J}(\mathbf{r}') = \nabla \times \left[\psi(\mathbf{r}')\hat{\mathbf{n}}(\mathbf{r}')\right] \tag{5.2}$$

and discretise it by defining a stream-function value at each node, I_n

$$\psi(\mathbf{r}') \approx \sum_{n=1}^{N} I_n \psi_n(\mathbf{r}') \tag{5.3}$$

where $\psi_n(\mathbf{r}')$ is the stream-function basis-function for the n^{th} node of the discretised surface. $\psi_n(\mathbf{r}')$ varies linearly across the neighbouring elements and is zero in all elements that do not contain the node n. Combining (5.2) and (5.3) gives an expression for the current density in terms of the stream-function values at the node points, I_n and a set of current basis functions $\mathbf{f}_n(\mathbf{r}')$.

$$\mathbf{J}(\mathbf{r}') \approx \sum_{n=1}^{N} I_n \nabla \times [\psi(\mathbf{r}')\hat{\mathbf{n}}(\mathbf{r}')] = \sum_{n=1}^{N} I_n \mathbf{f}_n(\mathbf{r}') \tag{5.4}$$

The current basis function for a node n and associated triangular element i is defined in terms of the perpendicular distance from the node to the opposite side of the element, $|\mathbf{d}_{ni}|$, and the vector of the opposite side of the triangular element $\mathbf{e}_{ni}$ as shown in Fig. 5.3. If the triangle $\triangle_{ni}$ belongs to the node at n

$$\mathbf{f}_n(\mathbf{r}') = \frac{\mathbf{e}_{ni}}{|\mathbf{e}_{ni}|}\frac{1}{|\mathbf{d}_{ni}|} \qquad i = 1, \ldots, N_n. \tag{5.5}$$

A single basis function $\mathbf{f}_n(\mathbf{r}')$ is made up of N_n vectors $\mathbf{v}_{ni}$, one for every triangle $\triangle_{ni}$ associated with the node n. N_n is usually about 6, but there may be any number of triangles associated with a node. Now the parts of the basis function are

$$\mathbf{v}_{ni} = \frac{\mathbf{e}_{ni}}{|\mathbf{e}_{ni}|}\frac{1}{|\mathbf{d}_{ni}|} \tag{5.6}$$

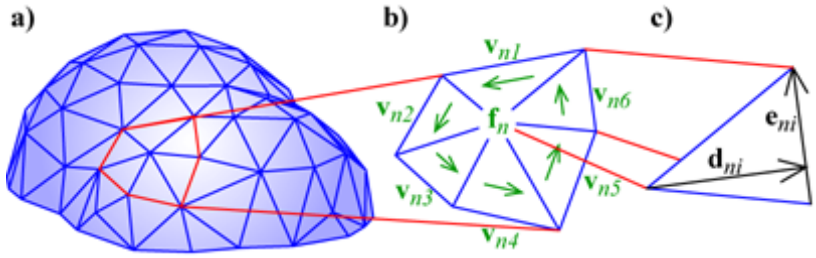

Figure 5.3: **a)** The discretised current carrying surface, **b)** the current density basis function $\mathbf{f}_n$ for the n^{th} node with its constituent parts $\mathbf{v}_{ni}$ $(i = 1, \ldots, 6)$ and **c)** the length, $\mathbf{d}_{ni}$, and width, $\mathbf{e}_{ni}$, vectors that define $\mathbf{v}_{ni}$.

This formalism for the basis function provides a system in which the current density is

divergence-free on the surface.

Figure 5.4 shows a node that lies on an open edge of the surface. It shows that with unconstrained values of I_n there may be current flowing in and out of the edge which is physically impossible in this system. By forcing all I_n values to be equal if they lie on the edge A,

$$I_n = I_A \qquad \text{if} \quad n \in A \qquad n = 1, \ldots, N \tag{5.7}$$

the current on the surface can be conserved. The same must be done for all the edges. This reduces the number of free parameters that defines the discretised current density.

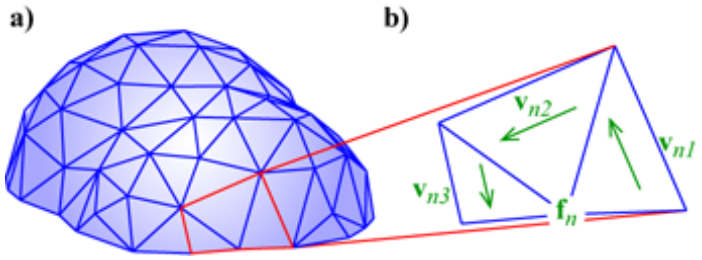

Figure 5.4: **a)** The discretised current carrying surface and **b)** an edge node basis function $\mathbf{f}_n$.

5.1.3 BEM Magnetic Vector Potential

The magnetic vector potential, $\mathbf{A}$ (Eq. (2.15)), can be calculated from the discretised surface current density using

$$\mathbf{A}(\mathbf{r}) \approx \frac{\mu_0}{4\pi} \sum_{n=1}^{N} I_n \int_{S'} \frac{\mathbf{f}_n(\mathbf{r}')}{|\mathbf{r} - \mathbf{r}'|} dS'. \tag{5.8}$$

5.1.4 BEM Magnetic Field

Applying $\mathbf{B} = \nabla \times \mathbf{A}$ gives

$$\mathbf{B}(\mathbf{r}) \approx \frac{\mu_0}{4\pi} \sum_{n=1}^{N} I_n \int_{S'} \nabla \times \frac{\mathbf{f}_n(\mathbf{r}')}{|\mathbf{r} - \mathbf{r}'|} dS'. \tag{5.9}$$

Using a similar approach to that employed in obtaining Eq. (2.16) and considering only the longitudinal component of the magnetic field, B_z, gives

$$B_z(\mathbf{r}) \approx \frac{\mu_0}{4\pi} \sum_{n=1}^{N} I_n \int_{S'} \left[\frac{-f_{ny}(\mathbf{r}')(x-x') + f_{nx}(\mathbf{r}')(y-y')}{|\mathbf{r}-\mathbf{r}'|^3} \right] dS'. \tag{5.10}$$

This is now in the form of a system of N linear equations

$$B_z(\mathbf{r}) \approx \sum_{n=1}^{N} I_n c_n(\mathbf{r}) \tag{5.11}$$

where $c_n(\mathbf{r})$ is

$$c_n(\mathbf{r}) = \frac{\mu_0}{4\pi} \int_{S'} \left[\frac{-f_{ny}(\mathbf{r}')(x-x') + f_{nx}(\mathbf{r}')(y-y')}{|\mathbf{r}-\mathbf{r}'|^3} \right] dS'. \tag{5.12}$$

where the integration over the surface, $\int_{S'} dS'$, is now equivalent to an integration over the surface of elements containing the node n since the n^{th} basis-function is only non-zero over elements containing it.

Because the basis functions are made up of N_n parts, the $c_n(\mathbf{r})$ matrix is calculated by summing over the set of functions linked to each triangular element associated with each node:

$$c_n(\mathbf{r}) = \frac{\mu_0}{4\pi} \sum_{i=1}^{N_n} \int_{S'} \left[\frac{-v_{niy}(\mathbf{r}')(x-x') + v_{nix}(\mathbf{r}')(y-y')}{|\mathbf{r}-\mathbf{r}'|^3} \right] dS' \tag{5.13}$$

where $\mathbf{v}_{ni}$ is the x-component of the i^{th} part of the n^{th} basis function vector in $\triangle_{ni}$.

5.1.5 BEM Self-Inductance

In the absence of hysteresis the formula for the stored magnetic energy, W, of an inductor driven with a current of I_a Amps is given by $W = \frac{1}{2} I_a^2 L$. The self-inductance, L, due to $\mathbf{J}(\mathbf{r}')$ is well known [2],

$$L = \frac{\mu_0}{4\pi I_a^2} \int_S \int_{S'} \frac{\mathbf{J}(\mathbf{r}) \cdot \mathbf{J}(\mathbf{r}')}{|\mathbf{r}-\mathbf{r}'|} dS' dS. \tag{5.14}$$

which can also be discretised by substitution of Eq. (5.4) to give

$$L \approx \frac{\mu_0}{4\pi} \sum_{n=1}^{N} \sum_{m=1}^{N} I_n I_m \int_S \int_{S'} \frac{\mathbf{f}_n(\mathbf{r}) \cdot \mathbf{f}_m(\mathbf{r}')}{|\mathbf{r}-\mathbf{r}'|} dS' dS. \tag{5.15}$$

This is in the form of a quadratic system of equations and can be expressed as

$$L \approx \sum_{n=1}^{N}\sum_{m=1}^{N} I_n I_m L_{mn} \tag{5.16}$$

where

$$L_{mn} = \frac{\mu_0}{4\pi}\int_S\int_{S'} \frac{\mathbf{f}_n(\mathbf{r})\cdot\mathbf{f}_m(\mathbf{r}')}{|\mathbf{r}-\mathbf{r}'|} dS' dS. \tag{5.17}$$

To calculate the self-inductance matrix L_{mn} using the parts of the basis functions $\mathbf{v}_{ni}$ Eq. (5.17) is re-written as

$$L_{mn} = \frac{\mu_0}{4\pi}\sum_i\sum_j (\mathbf{v}_{mi}\cdot\mathbf{v}_{nj})\int_{S_{mi}}\int_{S'_{mi}} \frac{dS' dS}{|\mathbf{r}_{mi}-\mathbf{r}'_{nj}|}. \tag{5.18}$$

5.1.6 BEM Mutual-Inductance

The mutual-inductance between two conductors, A and B, can be expressed in a way similar to Eq. (5.14),

$$L^{AB} = \frac{\mu_0}{4\pi I_a^A I_a^B}\int_{S^B}\int_{S^A} \frac{\mathbf{J}^A(\mathbf{r}')\cdot\mathbf{J}^B(\mathbf{r})}{|\mathbf{r}-\mathbf{r}'|} dS^B dS^A. \tag{5.19}$$

which when discretised becomes

$$L^{AB} \approx \frac{\mu_0}{4\pi}\sum_{n=1}^{N}\sum_{m=1}^{M} I_n I_m \int_{S^A}\int_{S^B} \frac{\mathbf{f}_n^A(\mathbf{r}')\cdot\mathbf{f}_m^B(\mathbf{r})}{|\mathbf{r}-\mathbf{r}'|} dS^B dS^A. \tag{5.20}$$

Here we use this expression to minimise the coupling between the circuit being designed and a known circuit, c. Therefore Eq. (5.20) is reduced to

$$L^c \approx \sum_{n=1}^{N} I_n L_n^c(\mathbf{r}) \tag{5.21}$$

where

$$L_n^c(\mathbf{r}) = \frac{\mu_0}{4\pi}\sum_{m=1}^{M^c} I_m^c \int_S\int_{S^c} \frac{\mathbf{f}_n(\mathbf{r}')\cdot\mathbf{f}_m^c(\mathbf{r})}{|\mathbf{r}^c-\mathbf{r}'|} dS^c dS. \tag{5.22}$$

or

$$L_n^c(\mathbf{r}) = \frac{\mu_0}{4\pi}\sum_{m=1}^{M} I_m^c \sum_i\sum_j (\mathbf{v}_{mi}^c\cdot\mathbf{v}_{nj})\int_{S_{nj}}\int_{S_{mi}^c} \frac{dS^c dS}{|\mathbf{r}_{mi}^c-\mathbf{r}'_{nj}|} \tag{5.23}$$

5.1.7 BEM Resistance

The amount of power dissipated, P, in a coil of resistance, R, carrying I_a Amps current is $P = I^2R$. The resistance can be expressed in terms of $\mathbf{J}(\mathbf{r}')$ [2] using

$$R = \frac{\rho}{tI_a^2}\int_S |\mathbf{J}(\mathbf{r}')|^2 dS \tag{5.24}$$

where t is the thickness of the conductor forming each element. Substituting into Eq. (5.4) gives the discretised version

$$R \approx \frac{\rho}{tI_a^2}\sum_{m=1}^{N}\sum_{n=1}^{N} I_n I_m \int_S |\mathbf{f}_n(\mathbf{r})|^2 dS. \tag{5.25}$$

This is also a quadratic system of equations,

$$R \approx \sum_{n=1}^{N}\sum_{m=1}^{N} I_n I_m R_{mn} \tag{5.26}$$

where

$$R_{mn} = \frac{\rho}{t}\int_S |\mathbf{f}_n(\mathbf{r})|^2 dS. \tag{5.27}$$

When the basis functions are split into their N_n constituent parts, Eq. (5.27) becomes

$$R_{mn} = \frac{\rho}{t}\sum_i \sum_j (\mathbf{v}_{mi}\cdot\mathbf{v}_{nj})A_{mi}^2 \tag{5.28}$$

if the two nodes, m and n, have common triangular elements. If the nodes share no triangles then $R_{mn} = 0$.

5.1.8 BEM Torque

The expression for the torque vector, $\mathbf{M}$, experienced by $\mathbf{J}(\mathbf{r}')$ in an external static magnetic field, $\mathbf{B}_0(\mathbf{r})$, is given by

$$\mathbf{M} = \int_S \mathbf{r}\times[\mathbf{J}(\mathbf{r}')\times\mathbf{B}_0(\mathbf{r})]dS \tag{5.29}$$

Since $\mathbf{B}_0(\mathbf{r})$ here is parallel to the z-axis and approximately uniform and considered to be homogeneous, $\mathbf{B}_0(\mathbf{r}) = B_0\hat{\mathbf{z}}$, so that

$$\mathbf{M} = B_0 \begin{pmatrix} \int_S J_x z dS \\ \int_S J_y z dS \\ -\int_S (J_x x + J_y y) dS \end{pmatrix} \tag{5.30}$$

Applying the discretisation, Eq. (5.4), to this expression results in the approximate equations for the x, y, and z components of the torque in terms of the current basis functions. Furthermore, the equations below are the torques in terms of the vectors, $\mathbf{v}_{mi}$, that constitute the basis functions.

$$M_x = B_0 \int_S J_x z dS \approx B_0 \sum_{n=1}^{N} I_n \sum_{i=1}^{N_n} \int_S v_{nx} z dS \tag{5.31}$$

$$M_y = B_0 \int_S J_y z dS \approx B_0 \sum_{n=1}^{N} I_n \sum_{i=1}^{N_n} \int_S v_{ny} z dS \tag{5.32}$$

$$M_z = -B_0 \int_S (J_x x + J_y y) dS \approx -B_0 \sum_{n=1}^{N} I_n \sum_{i=1}^{N_n} \int_S (v_{nx} x + v_{ny} y) dS. \tag{5.33}$$

5.2 Solving the Inverse Problem

The previous section described the mathematical environment in which the BEM operates. It showed that several coil characteristics can be parameterised in terms of the nodal stream-function values, I_n, via Eqs. (5.11), (5.16), (5.21), (5.26), (5.31), (5.32) and (5.33). Now we can solve the inverse BEM problem. To do this the previously described mathematics were implemented in Matlab® (The Mathworks® Inc., Natick, MA, USA). The following sections of this chapter describe how this was done.

5.2.1 Mesh Generation

Given a set of geometric constraints for the conducting surface or surfaces, and target field region or regions, a discretised model must be created. In this work, we use a powerful 3D modelling program called 3D Studio MAX® (Autodesk® Inc., San Rafael, CA, USA) to generate the meshes and target point data. 3D Studio MAX® is commonly used to model the way products may look when built, and has been used extensively in film, and television. This requires processing of light incident on surfaces, and therefore 3D Studio MAX® deals with thin surfaces very well, while other 3D CAD software deals primarily in parametric solid volumes. It has the ability to model discrete surfaces with complete control over the

mesh and has an ASCII text output that provides a file with all the detail of the geometry. Three types of object are used:

(A) *Surface geometry* - A set of elements and nodes defines the surface, which may have any number of separate sub-surfaces, and must have continuous normals to the surface over each sub-surface.

(B) *Edge nodes* - For each continuous edge of each sub-surface there must be an object that lists the nodes of each edge (see § 5.2.7). It is possible to find the edge nodes from the surface geometry, but it is also simple to define them from the start.

(C) *Target field points* - There must be an object containing the points at which the magnetic field will be prescribed. There may be any number of such objects for each different target field region.

Figure 5.5 show an example of these objects for planar primary and shielding surfaces with a spherical ROU (target region 1), shielding points (target region 2) and the nodes for each edge of the surface geometry.

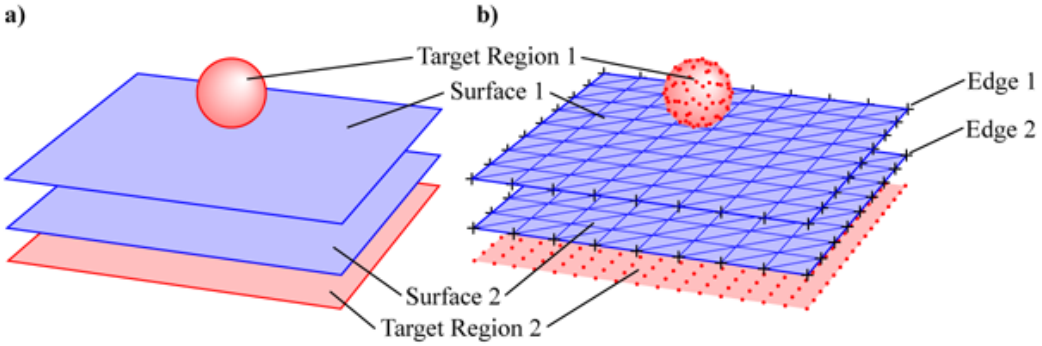

Figure 5.5: **a)** Undiscretised and **b)** discretised surface geometry, target regions, and edge nodes.

5.2.2 Calculating the Basis-Functions

The first step in the calculation process is to generate the basis function parts of the current density flowing in the conducting surface, $\mathbf{v}_{ni}$. This is done by evaluating Eq. (5.6) for each element, $\triangle_{ni}$, belonging to each node, n. Therefore, in triangular elements, there are 3 $\mathbf{v}_{ni}$ vectors for each element relating to a current basis function flowing parallel to each of the edges of the element. The area of each element, A_{ni}, and the position of its centre, $\mathbf{r}_{ni}$, are also calculated at this point for use in later calculations.

5.2.3 Generating the Physical Properties Matrices

The magnetic field, inductance, resistance, and torque components are calculated using Eqs. (5.11), (5.16), (5.21), (5.26), (5.31), (5.32) and (5.33), to yield matrices and vectors with dimensions $(K \times N)$, $(N \times N)$, $(N \times 1)$, $(N \times N)$, $(N \times 1)$, $(N \times 1)$ and $(N \times 1)$ respectively, as shown in Fig. 5.6

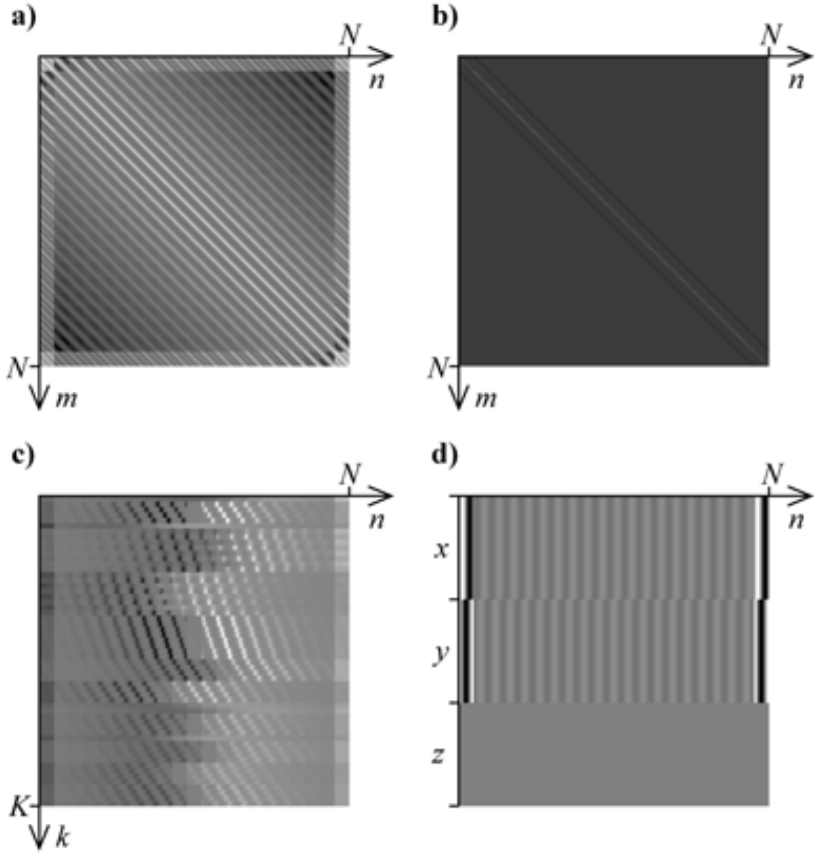

Figure 5.6: The **a)** L_{mn} (log scale), **b)** R_{mn}, and **c)** $c_n(\mathbf{r}_k)$ matrices, and the **d)** T_{xn}, T_{yn}, T_{zn} vectors for a cylindrical surface and spherical ROU.

5.2.4 Gauss-Legendre Integration

To calculate the integrals in the field matrix, the torque vectors, and the self-inductance matrix and mutual-inductance vector, (Eqs. (5.12), (5.31), (5.32), (5.33), (5.17) and (5.21) respectively), a function of position must be integrated over the triangular elements. A standard method for numerically integrating functions over the surface of a triangle is

Gauss-Legendre quadrature [205]. This technique approximates the integral of a function over the element with an appropriately weighted sum of the value of the function at a fixed number of points in the element. Gauss-Legendre integration is performed here on a unit triangle with corners at $(0,0)$, $(1,0)$, and $(0,1)$. The quadrature formula for the integration of an arbitrary function f over the surface of a triangle is

$$\iint_{S_{nj}} f(\mathbf{r})dxdy \approx \sum_{k=1}^{N=n\times n} c_k f(\mathbf{r}_k) \tag{5.34}$$

where $\mathbf{r}_k$ are discrete positions in the triangle and c_k are the weightings given in Table 5.1. The larger the degree of precision, n, is, the more accurate (and time-consuming) the calculation is.

n	u_k	v_k	c_k
n=2	0.211324865	0.166666667	0.197168783
	0.211324865	0.622008467	0.197168783
	0.788675134	0.044658198	0.052831216
	0.788675134	0.166666667	0.052831216
n=3	0.112701665	0.100000000	0.068464377
	0.112701665	0.443649167	0.109543004
	0.112701665	0.787298334	0.068464377
	0.500000000	0.056350832	0.061728395
	0.500000000	0.250000000	0.098765432
	0.500000000	0.443649167	0.061728395
	0.887298334	0.012701665	0.008696116
	0.887298334	0.056350832	0.013913785
	0.887298334	0.100000000	0.008696116

Table 5.1: Gauss-Legendre quadrature coordinates and weightings for numerical integration over the surface of a unit triangle.

To integrate over the triangles in the mesh, a coordinate transform is arranged to transform the triangle so that in the new coordinate system, (u,v), the corners of a triangle in the mesh lie at $(0,0)$, $(1,0)$, and $(0,1)$. The diagram in Fig. 5.7 shows schematically how the coordinates are transformed from (x,y,z) to (u,v). The equations that govern this geometric transformation are

$$
\begin{aligned}
x &= x_1 u + x_2 v + x_3 w \\
y &= y_1 u + y_2 v + y_3 w \\
z &= z_1 u + z_2 v + z_3 w \\
w &= 1 - u - v
\end{aligned} \tag{5.35}
$$

which can be used with the points, (u_k, v_k), in Table 5.1 to give (x_k, y_k, z_k). In this work we use $n = 2$ as the degree of precision.

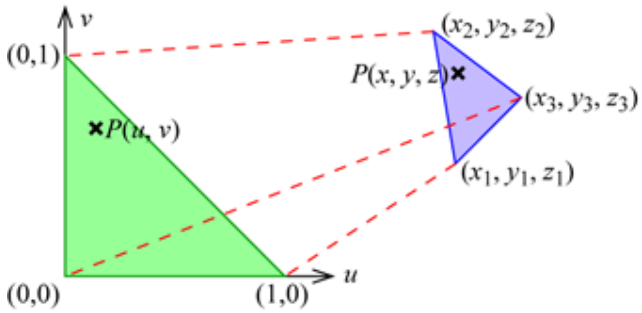

Figure 5.7: Diagram showing how the coordinates are changed from (x, y, z) to (u, v).

Also, when using a coordinate transform, the integral must be scaled to compensate for the scaling due to the transform;

$$
\int_{S_{nj}} f(\mathbf{r}) dS = \left|\left| \frac{\partial \mathbf{r}}{\partial u} \times \frac{\partial \mathbf{r}}{\partial v} \right|\right| \int_U f(u, v) du dv \tag{5.36}
$$

since

$$
dS = \left|\left| \frac{\partial \mathbf{r}}{\partial u} \times \frac{\partial \mathbf{r}}{\partial v} \right|\right| du dv \tag{5.37}
$$

5.2.5 Validity of Approximations

In Ref. [181] an approximation for the mutual inductance of currents passing through two triangles that are separated was used,

$$
L_{mn} = \frac{\mu_0}{4\pi} \sum_i \sum_j (\mathbf{v}_{mi} \cdot \mathbf{v}_{nj}) \frac{A_{mi} A_{nj}}{|\mathbf{r}_{mi} - \mathbf{r}'_{nj}|} \tag{5.38}
$$

which is valid for elements that are separated by large distances, but not for elements

that are close. To check the validity of Eq. (5.38), consider a unit triangle the same as the (u, v) form shown in Fig. 5.7 and another triangle that is the mirror of that triangle in the v-axis. A comparison of the double integral

$$\int_{S_{mi}} \int_{S'_{nj}} \frac{dS' dS}{|\mathbf{r}_{mi} - \mathbf{r}'_{nj}|} \tag{5.39}$$

over the two adjacent triangles using Eqs. (5.34) and (5.38) was made. The Gauss-Legendre quadrature computes the integral (with $n = 2$) to be equal to 0.4129 and Lemdiasov's approximation yields 0.3750, an error of 9.2%.

The same calculation with an additional separation of $\Delta u = 1$ gives 0.1524 for Gauss-Legendre and 0.1500 for the approximation, an error of 1.6%. Furthermore, a separation $\Delta u = 5$ gives values of 0.0442 and 0.0441 for quadrature and approximation respectively. Clearly there is a difference between the outcome of these integration approximations when the triangles are close that becomes negligible at larger separation distances.

5.2.6 Dealing with Singularities

Equations (5.18) and (5.28) require a double integral over the surface, S. This means that there must be double integrals over the same element when $\triangle_{mi} = \triangle_{nj}$. This causes a singularity for the inductance matrix since the $|\mathbf{r}_{mi} - \mathbf{r}'_{nj}|$ term in Eq. (5.16) can be zero. For this case the integral can be calculated from the closed form [206],

$$\begin{aligned} \frac{1}{4A^2} \int_{S_{mi}} \int_{S'_{mi}} \frac{dS' dS}{|\mathbf{r}_{mi} - \mathbf{r}'_{mi}|} &= \frac{1}{6\sqrt{a}} \ln \left(\frac{(a-b+\sqrt{a}\sqrt{a-2b+c})(b+\sqrt{ac})}{(-b+\sqrt{ac})(-a+b+\sqrt{a}\sqrt{a-2b+c})} \right) \\ &+ \frac{1}{6\sqrt{c}} \ln \left(\frac{(b+\sqrt{ac})(-b+c+\sqrt{c}\sqrt{a-2b+c})}{(b-c+\sqrt{c}\sqrt{a-2b+c})(-b+\sqrt{ac})} \right) \\ &+ \frac{1}{6\sqrt{a-2b+c}} \ln \left(\frac{(a-b+\sqrt{a}\sqrt{a-2b+c})(-b+c+\sqrt{c}\sqrt{a-2b+c})}{(b-c+\sqrt{c}\sqrt{a-2b+c})(-a+b+\sqrt{a}\sqrt{a-2b+c})} \right) \end{aligned} \tag{5.40}$$

where $a = (\mathbf{r}_3 - \mathbf{r}_1) \cdot (\mathbf{r}_3 - \mathbf{r}_1)$, $b = (\mathbf{r}_3 - \mathbf{r}_1) \cdot (\mathbf{r}_3 - \mathbf{r}_2)$, $c = (\mathbf{r}_3 - \mathbf{r}_2) \cdot (\mathbf{r}_3 - \mathbf{r}_2)$, and $\mathbf{r}_1$, $\mathbf{r}_2$, $\mathbf{r}_3$, are position the vectors of three nodes of the triangle.

5.2.7 Edge Constraints

The full $c_n(\mathbf{r}_k)$, L_{mn}, R_{mn} matrices and T_{xn}, T_{yn}, T_{zn} vectors are shown in Fig. 5.6. These matrices and vectors (as well as L_n^c) contain rows and columns for each of the edge nodes, which need to be removed and replaced with a single row and column for each edge (*i.e.* if there are N nodes on the surface, N_E of which lie on one of the E edges the N variables in the system are reduced to $N' = N - N_E + E$ variables). The matrices must be properly

reduced before constructing the matrix equation; where the L_{mn} and R_{mn} matrices have dimensions of $N \times N$, they are reduced to $N' \times N'$ as illustrated in Fig. 5.8.

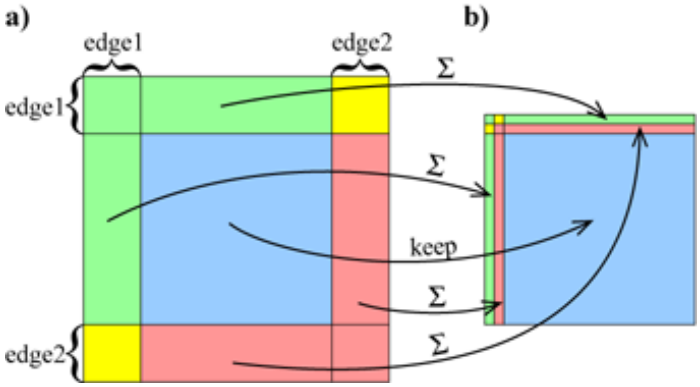

Figure 5.8: Example of reducing the number of variables in the system in **a)** an $N \times N$ matrix for a two-edged surface to **b)** $N' \times N'$. The central blue box correspond to non-edge nodes and remains the same, edge node columns and rows are condensed into 2 columns and 2 rows.

5.2.8 The Optimisation Functional

A functional equation, U, can be created that will be used to optimise the physical parameters to obtain the best possible set of stream-function values and therefore most appropriate coil design (*c.f.* Eqs. (4.14) and (4.19)). Equation (5.41) shows the functional that was used in this work. It is constructed to provide an axial magnetic field, $B_z(\mathbf{r}_k)$, that closely matches that of the desired target field, $B_z^t(\mathbf{r}_k)$. Some deviation from this ideal target field is tolerated, and indeed required, so that the self-inductance, L, and resistance, R, may be minimised. This trade-off is possible to varying degrees via user-definable parameters α and β, and a coil of lower L and R will represent the target field less accurately. Simultaneously, the other terms in the functional act to reduce by as much as is possible the mutual-inductance with other coils and any torques, $\mathbf{M}$, that might otherwise be caused by energising the coil in an intense magnetic field, B_0.

$$
\begin{aligned}
U &= \frac{1}{2}\sum_{k=1}^{K} W(\mathbf{r}_k)\left(B_z(\mathbf{r}_k) - B_z^t(\mathbf{r}_k) + B_{\text{off},z}\right)^2 \\
&\quad + \frac{\alpha}{2}\sum_{n=1}^{N}\sum_{m=1}^{N} I_n I_m L_{mn} + \frac{\beta}{2}\sum_{n=1}^{N}\sum_{m=1}^{N} I_n I_m R_{mn} + \sum_{c=1}^{C}\lambda_c \sum_{n=1}^{N} I_n L_n^c(\mathbf{r}) \\
&\quad - B_0 \sum_{p=1}^{P}\lambda_{px}\sum_{n=1}^{N}\delta_{n\in p} I_n \int_S f_{nx} z\, dS \\
&\quad - B_0 \sum_{p=1}^{P}\lambda_{py}\sum_{n=1}^{N}\delta_{n\in p} I_n \int_S f_{ny} z\, dS \\
&\quad + B_0 \sum_{p=1}^{P}\lambda_{pz}\sum_{n=1}^{N}\delta_{n\in p} I_n \int_S (f_{nx} x + f_{ny} y)\, dS
\end{aligned} \tag{5.41}
$$

where $W(\mathbf{r}_k)$ is a weighting function that can be set by the user to artificially adjust the spatial dependence of the accuracy with which the magnetic field is generated by the coil. It can be set to $W(\mathbf{r}_k) = 1$ if a spatially varying weighting is not required. $B_{\text{off},z}$ is a field offset parameter that is obtained as a solution in the minimisation and may or may not be included in U. It allows a uniform field offset to be present in the resulting magnetic field and can become useful when dealing with highly asymmetric coil designs. The second and third terms of Eq.(5.41) are the self-inductance and power minimisation terms with their associated weightings, α and β. The fourth term is used to minimise the mutual-inductive coupling between C other coils using the Lagrange multipliers, λ_c, for each coil, c. λ_{px}, λ_{py}, λ_{pz} are Lagrange multipliers for the p^{th} surface and $\delta_{n\in p}$ term is equal to 1 if the node n belongs to the p^{th} surface, and 0 if it does not. This allows torque minimisation on any number of surfaces, but in this work we simply minimise the torque of the whole surface, *i.e.* $P = 1$. Any combination of trade-off parameters may be included or excluded, but there needs to be at least one parameter other than the field error term since a system of equations which contains this term is overdetermined and has an infinite number of solutions.

5.2.9 The Matrix Equation

The minimum of the functional, U, is identified by differentiating it with respect to each variable that is to be found (i.e. the I_n values, $B_{\text{off},z}$, and the Lagrange multipliers, λ) to form a linear system of equations. The first N' equations in the system result from setting the partial differential of the functional with respect to each of the stream-function values,

I_m, equal to zero, i.e. $\frac{\partial U}{\partial I_m} = 0$

$$\sum_{m=1}^{N'} \underbrace{\left(\sum_{k=1}^{K} W(\mathbf{r}_k) c_m(\mathbf{r}_k) c_n(\mathbf{r}_k) + \alpha L_{mn} + \beta R_{mn} \right)}_{A} I_n$$
$$+ B_{\text{off},z} \underbrace{\sum_{k=1}^{K} W(\mathbf{r}_k) c_m(\mathbf{r}_k)}_{B} + \sum_{c=1}^{C} \lambda_c \underbrace{L_m^c(\mathbf{r})}_{L_c} + \sum_{p=1}^{P} \tilde{\lambda}_{px} \underbrace{\delta_{n\in p} \int_S -f_{mx} z dS}_{-T_{pA}}$$
$$+ \sum_{p=1}^{P} \tilde{\lambda}_{py} \underbrace{\delta_{n\in p} \int_S -f_{my} z dS}_{-T_{pB}} + \sum_{p=1}^{P} \tilde{\lambda}_{pz} \underbrace{\delta_{n\in p} \int_S (f_{mx} x + f_{my} y) dS}_{T_{pC}}$$
$$= \underbrace{\sum_{k=1}^{K} W(\mathbf{r}_k) c_m(\mathbf{r}_k) B_z^t(\mathbf{r}_k)}_{E}, \qquad m = 1, \ldots, N \tag{5.42}$$

Where $\tilde{\lambda}$ is a Lagrange multiplier combined with the static magnetic field strength, B_0. The rest of the system of equations is created by setting the partial differentiation of the functional with respect to the other variables equal to zero (i.e. $\frac{\partial U}{\partial B_{\text{off},z}} = 0$, $\frac{\partial U}{\partial \lambda_c} = 0$, $\frac{\partial U}{\partial \tilde{\lambda}_{px}} = 0$, $\frac{\partial U}{\partial \tilde{\lambda}_{py}} = 0$, $\frac{\partial U}{\partial \tilde{\lambda}_{pz}} = 0$).

$$\sum_{n=1}^{N'} \underbrace{\left(\sum_{k=1}^{N'} W(\mathbf{r}_k) c_n(\mathbf{r}_k) \right)}_{C} I_n + B_{\text{off},z} \underbrace{\sum_{k=1}^{K} W(\mathbf{r}_k)}_{D} = \underbrace{\sum_{k=1}^{K} W(\mathbf{r}_k) B_{t,z}(\mathbf{r}_k)}_{F} \tag{5.43}$$

$$\sum_{n=1}^{N'} \underbrace{L_n^c(\mathbf{r})}_{L_c} I_n = 0, \qquad c = 1, \ldots, C \tag{5.44}$$

$$\sum_{n=1}^{N'} \underbrace{\left(\delta_{n\in p'} \int_S f_{nx} z dS \right)}_{T_A} I_n = 0, \qquad p' = 1, \ldots, P \tag{5.45}$$

$$\sum_{n=1}^{N'} \underbrace{\left(\delta_{n\in p'} \int_S f_{nx} z dS \right)}_{T_B} I_n = 0, \qquad p' = 1, \ldots, P \tag{5.46}$$

$$\sum_{n=1}^{N'} \underbrace{\left(\delta_{n\in p'} \int_S (f_{nx}x + f_{ny}y)dS\right)}_{T_C} I_n = 0, \qquad p' = 1, \ldots, P \tag{5.47}$$

This linear system of equations (5.42) to (5.47) can be consolidated into a matrix equation,

$$\mathbb{Z}\mathbf{I} = \mathbf{b}. \tag{5.48}$$

As an example of how to construct the matrices $\mathbf{Z}$, $\mathbf{I}$, and $\mathbf{b}$ for minimisation using Eq. (5.48), a one surface ($P = 1$) X-gradient coil is considered, and the matrix equation is then constructed

$$\underbrace{\begin{bmatrix} \begin{pmatrix} \ddots & \ldots & \cdot \\ \vdots & A & \vdots \\ \cdot & \ldots & \ddots \end{pmatrix} \begin{pmatrix} \vdots \\ B \\ \vdots \end{pmatrix} \begin{pmatrix} \vdots \\ L_c \\ \vdots \end{pmatrix} \begin{pmatrix} \vdots \\ -T_{pA} \\ \vdots \end{pmatrix} \begin{pmatrix} \vdots \\ -T_{pB} \\ \vdots \end{pmatrix} \begin{pmatrix} \vdots \\ T_{pC} \\ \vdots \end{pmatrix} \\ (\ \ldots\ C\ \ldots\ ) \quad D \quad 0 \quad 0 \quad 0 \quad 0 \\ (\ \ldots\ L_c\ \ldots\ ) \quad 0 \quad 0 \quad 0 \quad 0 \quad 0 \\ (\ \ldots\ T_{pA}\ \ldots\ ) \quad 0 \quad 0 \quad 0 \quad 0 \quad 0 \\ (\ \ldots\ T_{pB}\ \ldots\ ) \quad 0 \quad 0 \quad 0 \quad 0 \quad 0 \\ (\ \ldots\ T_{pC}\ \ldots\ ) \quad 0 \quad 0 \quad 0 \quad 0 \quad 0 \end{bmatrix}}_{\mathbb{Z}} \underbrace{\begin{bmatrix} \begin{pmatrix} \vdots \\ I_n \\ \vdots \end{pmatrix} \\ B_{\text{off},z} \\ \lambda_c \\ \tilde{\lambda}_{px} \\ \tilde{\lambda}_{py} \\ \tilde{\lambda}_{pz} \end{bmatrix}}_{\mathbf{I}} = \underbrace{\begin{bmatrix} \begin{pmatrix} \vdots \\ E \\ \vdots \end{pmatrix} \\ F \\ 0 \\ 0 \\ 0 \\ 0 \end{bmatrix}}_{\mathbf{b}} \tag{5.49}$$

Equation (5.48) is inverted to find $\mathbf{I}$ which contains the stream functions values, I_n, from which the stream-function, $\psi(\mathbf{r}')$, can be found from Eq. (5.3). Figure 5.9 shows the stream-function, $\hat{\psi}(\mathbf{r}')$, (normalised to unity since its scale is unimportant at this stage) for an X-gradient coil plotted over the cylindrical surface geometry. This particular solution was obtained using, $\alpha = 9 \times 10^{-8}$ and $\beta = 0$ (i.e. no power minimisation).

5.2.10 Calculation time

Calculating the L_{mn}, R_{mn}, $c_n(\mathbf{r}_k)$ matrices and the L_n^c and $\mathbf{M}$ vectors can take a considerable amount of time. The calculation time for these matrices is dependant on the detail of the discretisation, and has a power law relation to the number of nodes, N, in the surface (the calculation time for $c_n(\mathbf{r}_k)$ is also related to the number of target field points, K). Figure 5.10 is a logarithmic graph of the relation between N and the time it takes to calculate

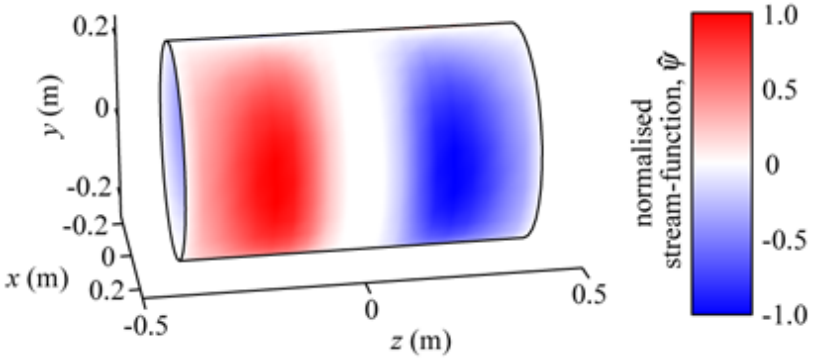

Figure 5.9: The normalised stream-function, $\hat{\psi}(\mathbf{r}')$, plotted over the surface for a cylindrical X gradient coil.

the L_{mn} matrix on an AMD Opteron 2.2GHz processor with 4GB RAM available. The L_{mn} matrix generally takes the longest time to calculate and for large N and K usually takes about half of the whole calculation time depending on the $N : K$ ratio, N, and the proportion of the calculation that is performed by Gauss-Legendre quadrature (§ 5.2.4) or its approximation (Eq. 5.38).

5.2.11 User-Defined Parameters and Engineering Constraints

Apart from the geometrical constraints on the system, there are electromagnetic and engineering constraints that must be considered in order to design a buildable coil that performs satisfactorily. Once the matrices have been calculated they need not be recalculated when changing the user-defined parameters in designing a coil. The first user-defined input to consider is the target magnetic field. In this work we chiefly, but not exclusively, focus our attention on the design of gradient and shim coils which have magnetic fields that conform closely to low-order spherical harmonics (see § 2.2). In this way the target field values can be simply assigned according to the type of gradient or shim that is to be designed and the positions of target points.

After the target field, the most important user-defined parameters are α and β; the self-inductance, and resistance trade-off parameters. Figure 5.11 shows a logarithmic plot of the figure of merit (FOM= $\frac{\eta^2}{L}$) and max(ΔB_z) as α and β are varied illustrating the trade-off. It shows that the FOM is higher for the self-inductance minimised solutions, although it should be noted that the resistance is lower for the resistance mimimised solutions. It is these variables that allow the user to control the properties of the resulting coil design based on any combination of the following common electromagnetic, and engineering constraints:

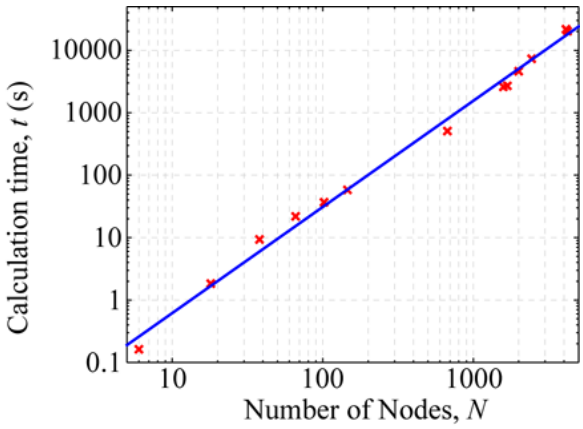

Figure 5.10: The calculation time for the L_{mn} matrix for different numbers of surface nodes with a regression line corresponding to $t = 0.0124n^{1.7}$s.

(A) the magnetic field error, $\Delta B_z(\mathbf{r}_k)$, at any point within the ROU must not exceed a maximum value (e.g. $\Delta B_z(\mathbf{r}_k) \leq 5\%$),

(B) the self-inductance, L, of the coil must be lower than a prescribed value to allow fast switching of the coil (e.g. $L \leq 100\mu$H),

(C) the torque must be reduced to a value close to zero ($|\mathbf{M}| \approx 0$),

(D) the magnetic field leakage onto the nearest conducting surface must not exceed a certain amount (e.g. $B_z^S(\mathbf{r}) \leq 1\mu$T),

(E) the resistance, R, of the coil must not exceed a specified value, so as to ensure that heating of the coil is not excessive (e.g. $R \leq 1\Omega$). This is particularly important for small coils with low L, but high R because of their thin wires.

(F) the spacing between the closest wires of the coil, $\min(\Delta w)$, is greater than the diameter of the wire used to build the coil (e.g. $\min(\Delta w) \geq 3$mm),

The other user-defined variable is the weighting vector, $W(\mathbf{r}_k)$, which controls the importance placed on the accuracy of the magnetic field produced at each point k. This provides many degrees of freedom, and in this work we have primarily used it to adjust the shielding emphasis. This is simply done by setting $W(\mathbf{r}_k) = 1$ if the point $\mathbf{r}_k$ lies in the ROU, and $W(\mathbf{r}_k) = \gamma$ if it lies in the shielding region. γ is therefore a user-defined trade-off parameter that controls the amount of active shielding the coil provides. The values of $W(\mathbf{r}_k)$ can also be set to glean every last bit of performance from a particular coil design.

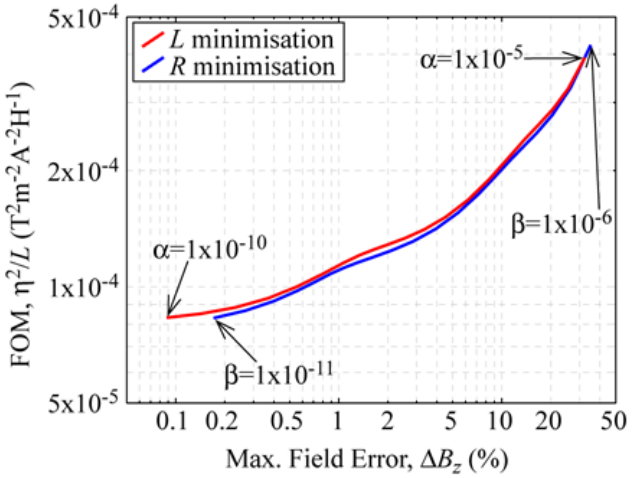

Figure 5.11: The FOM and max(ΔB_z) values as α and β are varied from 1×10^{-10} to 1×10^{-5} and 1×10^{-11} to 1×10^{-6}, respectively. These values are calculated from the continuous current density.

Decreasing $W(\mathbf{r}_k)$ for target points that, by virtue of their position, are easily matched to the target field allows some slight extra self-inductance or resistance reductions without exceeding the homogeneity constraints.

5.3 Solving the Forward Problem

Once the solution to the inverse problem is found, together with the discretised geometry, the I_n values wholly define the electromagnetic system. It is a simple task to find the magnetic field at the positions defined by the $\mathbf{r}_k$ values, the self-inductance, mutual-inductance, resistance, and torque of the coil simply by multiplying the appropriate matrices by the solution vectors using Eqs. (5.11), (5.16), (5.21), (5.26), (5.31), (5.32) and (5.33) respectively.

5.3.1 Wire Paths

Figure 5.12 illustrates how the stream-function is contoured to produce the wire paths for the coil design. This is a 1D example of a theoretical stream-function which has been contoured with 10 contour levels. If $\psi_{\max}$ and $\psi_{\min}$ are the maximum and minimum values of the stream-function, and N_{cont} is the number of desired contour levels (*i.e.* $N_{\text{cont}} = 5$ in Fig. 5.12), the n^{th} contour level, ψ_{Cn}, lies at

$$\psi_{Cn} = \psi_{\min} + \frac{(2n-1)(\psi_{\max} - \psi_{\min})}{4N_{\text{cont}}} \tag{5.50}$$

The position of the wires are mapped onto the z-axis as shown by the red and blue arrows. The wires indicated by blue arrows flow in the opposite direction to the current in the red wires because the gradient of the stream-function in negative.

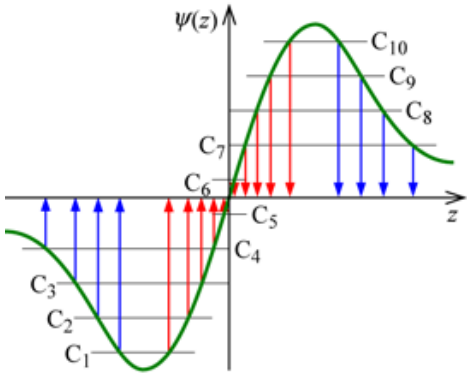

Figure 5.12: A 1D example of how the stream-function is contoured to give the wire paths for the coil design.

5.3.2 3D Contouring

When using arbitrary 3D geometry $\psi(\mathbf{r}')$ needs to be contoured in 3D. This is done here by considering each element in turn by transforming it to (u, v) space as in the Gauss-Legendre quadrature method (§ 5.2.4). The coordinate transform is given in Eq. (5.35). The values of the stream-function at the corners of the triangle, t, $(\psi_{t1}, \psi_{t2}, \psi_{t3})$ are used to define a plane of the stream-function in the triangle in (u, v, ψ) space. The intersection of this plane with planes of constant ψ, representing the contour levels, ψ_{Cn}, gives the equation of the lines of the wires in that triangle,

$$\mathbf{r} = \begin{pmatrix} 0 \\ \left(\frac{\psi_{t3} - \psi_{Cn}}{\psi_{t3} - \psi_{t2}}\right) \\ \psi_{C_n} \end{pmatrix} + s \begin{pmatrix} \psi_{t2} - \psi_{t3} \\ \psi_{t1} - \psi_{t3} \\ 0 \end{pmatrix} \tag{5.51}$$

where the value of s defines where on the line $\mathbf{r}$ is. The portion of these lines that are within the u and v limit of the unit triangle are the wire paths of that triangle as shown in Fig. 5.13. When this process is carried out for all the triangular elements and transformed back into (x, y, z) space with the inverse of the coordinate transform, the result is the wire

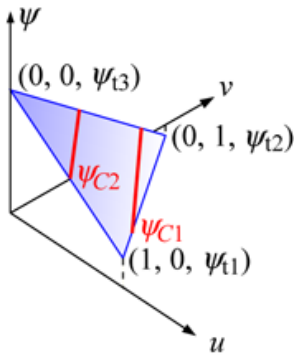

Figure 5.13: One element transformed into parametric (u, v, ψ) space which intersects with 2 contour levels ψ_{C1} and ψ_{C2}.

paths of the coil design. Care must be taken to ensure the correct current flow direction of each wire element. Figure 5.14 **a)** shows the wire paths for a cylindrical X-gradient coil obtained by contouring the stream function shown in Fig. 5.9 in 3D.

5.3.3 Wire Spacing

The minimum wire-spacing is often an engineering constraint which must be compatible with either the width of the wire with which the coil will be wound, or the width of the cut that is made when etching the wire-paths out of copper plate. Therefore, the minimum wire spacing of the coil design is of great importance. The minimum wire spacing is simply found by calculating the distance from one wire to the next in each element, taking care not to consider wire elements on the same contour level.

Increasing β in the functional used for optimisation (Eq. (5.41)) acts to minimise the maximum value of the current density by minimising $|\mathbf{J}(\mathbf{r}')|^2$. Therefore, using power minimisation increases the minimum wire spacing to a greater extent than self-inductance minimisation for the same trade-off in field accuracy.

5.3.4 Properties of the Coil Wire-Paths

The wire-paths of the coil as generated by the contouring algorithm completely define the coil in a realistic manner, since coils are usually constructed based on these wire-paths. We can therefore use the wire-paths to calculate realistic properties of the coil. The efficiency, η is found by invoking the Biot-Savart law, Eq. (4.1), with $I_a = 1$A flowing in the wires, and calculating the field at the target field points, $\mathbf{r}_k$. Performing a fit of these data, $B_z(\mathbf{r}_k)$,

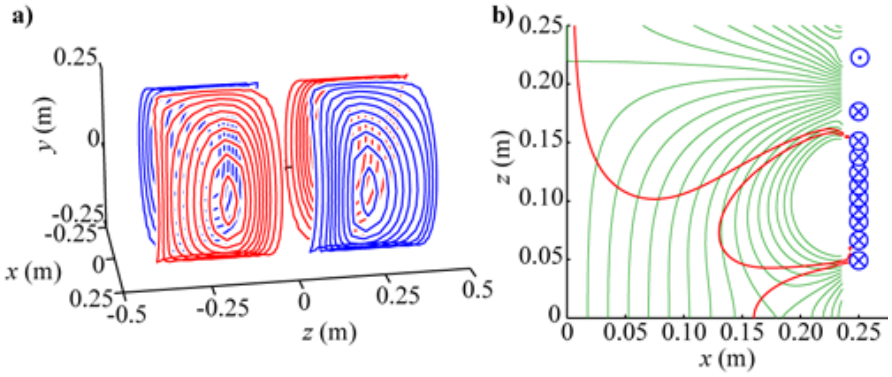

Figure 5.14: **a)** Wires of an IBEM-designed X-gradient coil (red wires indicate reversed current flow with respect to blue) and **b)** contours of the magnetic field generated by the coil with $2\mu\text{TA}^{-1}$ contour spacing (thin green), overlaid with the $\Delta B_z(\mathbf{r}) = 5\%$ contour (thick red). The wires are also shown that cross into, $\otimes$, and out of, $\odot$, the contour plane.

with the target field values, $B_z^t(\mathbf{r}_k)$, yields η from the solution of

$$||\mathbf{B}_z^t - \eta \mathbf{B}_z|| = 0 \tag{5.52}$$

where $\mathbf{B}_z^t$ is a vector of target field values, and $\mathbf{B}_z$ is a vector of magnetic field per unit current values calculated using the same target points with the Biot-Savart law.

The self-inductance, L, and the resistance, R, both vary as the square of the efficiency so a realistic estimate of the self-inductance of the coil can be found by multiplying the output of Eq. (5.16) by η^2. The resistance can also be calculated in a similar manner, but the resulting value is likely to be unrealistic because the resistance is sensitive to the cross-section of the wire used in construction of the coil.

Using the Biot-Savart law also provides a convenient way to check that the discrete wire-paths faithfully represent the continuous current density on the surface. Using Eqs. (4.3) and (5.11) gives the field deviation, $\Delta B_z(\mathbf{r}_k)$, for each of the K target points. This can be compared to the field deviation calculated from the field generated by the 1A energised coil using

$$\Delta B_z^{\text{BS}}(\mathbf{r}_k) = \frac{|B_z^{\text{BS}}(\mathbf{r}_k) - \eta B_z^t(\mathbf{r}_k)|}{\max(\eta |B_z^t(\mathbf{r}_k)|)} \times 100 \tag{5.53}$$

where $B_z^{\text{BS}}(\mathbf{r}_k)$ is the magnetic field at $\mathbf{r}_k$ found by Biot-Savart summation over the wire-paths. Any significant discrepancy between $\Delta B_z^t(\mathbf{r}_k)$ and $\Delta B_z^{\text{BS}}(\mathbf{r}_k)$ the two field deviation measures indicates that the number of contour levels of the stream-function needs

to be increased. More contours clearly make the minimum wire spacing less, which is an engineering constraint.

5.3.5 Torque Calculation

The torque generated by the coil may also be calculated from its wire-paths. This is simply achieved using Eq. (4.4) and summing over all wire-path elements. Checking this value provides a final check to indicate whether any large and potentially dangerous turning forces may be exerted when the coil is energised in a high-field environment. For symmetric coils such as the one shown in Fig. 5.14, the torque is intrinsically balanced. The optimum, torque-balanced solution for an asymmetric coil is different to the optimum, non-torque-balanced solution. Therefore, imposing torque-balancing can detrimentally affect the properties of asymmetric coils but not symmetric ones. This effect can be severe and it may be impossible to design a physically realisable, highly asymmetric coil with torque-balancing.

The X-gradient coils shown in Fig. 5.15 illustrate the effect of torque-balancing on the wire-paths of a coil similar to that in Fig. 5.14 but with the conducting surface shifted by $z = -0.15$m relative to the target field region. The magnitude of the torque vector, $|\mathbf{M}|$, for the non-torque-balanced coil, **a)**, is 2 $\mathrm{NmA^{-1}T^{-1}}$, compared to 0.014 $\mathrm{NmA^{-1}T^{-1}}$ for the torque-balanced coil, **a)**, a factor of 143 decrease. The residual torque in the torque-balanced coil is mostly due to the discretisation of the continuous current density into wires. $\frac{\eta^2}{L}$, decreases from 6.8×10^{-5} to 5.3×10^{-5} $\mathrm{T^2m^{-2}A^{-2}H^{-1}}$ when torque-balancing is imposed, and $\min(\Delta w)$ is decreased from 6.4 to 3.9 mm.

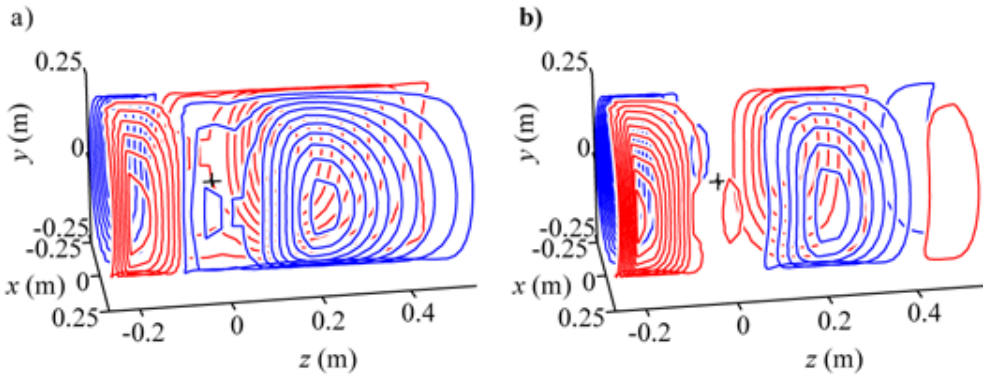

Figure 5.15: Wires of an asymmetric IBEM-designed X-gradient coil (red wires indicate reversed current flow with respect to blue) **a)** without and **b)** with torque-balancing.

5.3.6 Impedance Extraction

FastHenry© [96] is a multipole-accelerated impedance extraction program that takes the wire-paths and their thicknesses and models the electrical impedance of the coil. It is capable of modelling skin depth effects at any driving frequency and can cope with multiple circuits, but here only a DC current in one circuit is used. FastHenry is a reliable tool for predicting the inductance and resistance of a coil design; the value it returns for the inductance of the wire-paths is usually a little higher than the value computed by scaling the value obtained from Eq. (5.16) by η^2.

5.3.7 Mutual-Inductance Minimisation

Figure 5.16 illustrates the effect on a coil design when the mutual inductance term is employed in the optimisation functional Eq. (5.41). Mutual-inductance minimisation is useful when coils have reduced symmetry, since symmetric cylindrical coils are orthogonal to one another and therefore naturally have zero mutual inductance. Coils will also tend to couple if they have a similar form of target field. To demonstrate this, a torque-balanced, asymmetric X-gradient (coil A) with a radius of 0.5 m is shown in Fig. 5.16 **a)** (similar to the coil shown in Fig. 5.15 **b)**). Around this a Z2X shim coil (coil B) $\{n = 3, m = 1\}$ is designed on a symmetric cylinder with radius 0.65m **b)** without and **c)** with the introduction of mutual-inductance minimisation with the asymmetric X-gradient. There are clear differences between the two shim coils. The gradient and shim coil wire-paths for each case were passed to FastHenry© for calculation of the impedance matrix for the 2 circuit system. Equation 5.54 shows the inductance matrix for the coils **a)** and **b)** in Fig. 5.16 and Eq. 5.55 is for **a)** and **c)**, highlighting the reduction in mutual-inductance that is achieved by including this term in the optimisation. Differences between M_{AB} and M_{BA} values (theoretically $M_{AB} = M_{BA}$) and residual mutual-inductances in Eq. (5.55) are thought to be due to numerical calculation errors and approximating the continuous current density by wire paths respectively.

$$\begin{pmatrix} L_A & M_{AB} \\ M_{BA} & L_B \end{pmatrix} = \begin{pmatrix} 166 & 3.7 \\ 3.9 & 232 \end{pmatrix} \mu\text{H} \tag{5.54}$$

$$\begin{pmatrix} L_A & M_{AB} \\ M_{BA} & L_B \end{pmatrix} = \begin{pmatrix} 137 & -0.29 \\ -0.17 & 208 \end{pmatrix} \mu\text{H} \tag{5.55}$$

Mutual-Inductance minimisation reduces the number of solutions available in the same way as the torque-balancing and therefore reduces the FOM for asymmetric coils. For the

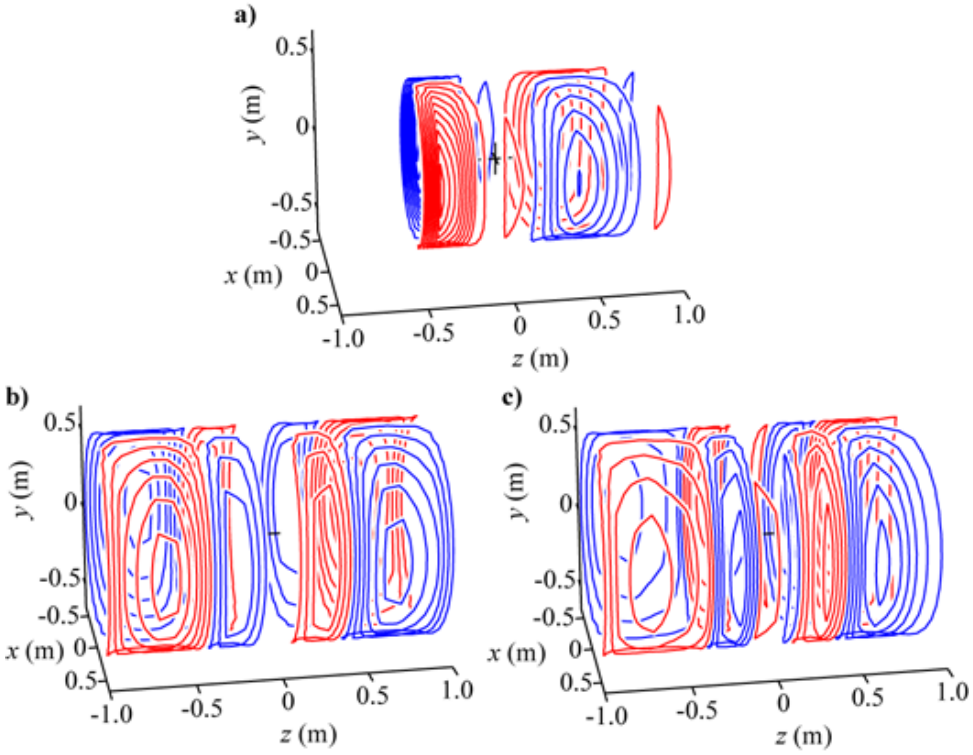

Figure 5.16: **a)** an asymmetric IBEM X-gradient coil and Z2X shim coils **b)** without and **c)** with mutual-inductance minimisation (red wires indicate reversed current flow with respect to blue).

shim coils in Fig. 5.16 **b)** and **c)** the FOM is reduced from 1.24×10^{-6} to 0.95×10^{-6} $\mathrm{T^2m^{-6}A^{-2}H^{-1}}$ for the same $\max(\Delta B_z(\mathbf{r}_k))$, when the mutual inductance is minimised.

Chapter 6

Examples of IBEM Coil Design

In this chapter, several examples of coils designed with the inverse boundary element method (IBEM) described in the previous section (§ 5) are given. There are examples of gradient coils (those with target magnetic fields that conform to the shape of 1^{st} order spherical harmonics), shim coils (those that conform to the shape of any other spherical harmonics) as well as other coils with target magnetic fields that are not spherical harmonic in form. For each example the motivation for the work is given, the electromagnetic problem is described and the pertinent results are presented and discussed, where possible in comparison to previous work by other authors. The properties of all the coils in this chapter, as well as all other chapters, are described in full in Appendix A for ease of comparison. The gradient coil designs described in § 6.1, 6.3, 6.4, and the coil in § 6.12 have recently been published [187].

6.1 Shoulder-Slotted Head Gradient and Shim Set

The first IBEM coil design example is an insertable, three-axis gradient coil set equipped with a shielded Z0 coil and all 2^{nd} order shim coils. The aim was to produce a strong, head gradient and shim coil set with low inductance for fast current switching as required by dynamic shimming [66–68] (see § 3.2.6).

6.1.1 Geometry

This coil set was designed for head imaging on Philips Achieva 3 T and Intera 7 T systems as well as on the 3 T system built at Nottingham University. Therefore, it must fit inside the bores and around the head RF coils of these three systems. The geometrical consequences are that the 800 mm long cylindrical coil surfaces must have diameters between 390 mm

and 450 mm, and therefore the shoulders of the subject must be accommodated by the design. Two rectangular sections of 150 mm width and 220 mm length were removed from either side of the otherwise cylindrical surfaces providing two slots ending 180 mm from the isocentre in which the shoulders of the subject can be accommodated. Figure 6.1 shows the geometry of the current carrying surfaces. The region of uniformity (ROU) used to define the target magnetic field variation $B_z^t(\mathbf{r}_k)$ is a 160mm diameter spherical volume (DSV). The X-, Y-, and Z-gradient coils are designed on 410, 416, and 422 mm diameter surfaces respectively. The 2$^{\text{nd}}$ order shim coils, X2-Y2, XY, Z2, ZX, and ZY, have 428.7, 430.1, 431.5, 432.9, and 434.3 mm diameters respectively. The shielded Z0 shim was not designed using the IBEM, but with the finite-length sinusoidal basis-function method (see § 4.4.8), on 180 mm long cylinders with 397.5 and 435.7 mm primary and shield diameters respectively.

Surfaces were generated in Matlab® (The Mathworks® Inc., Natick, MA, USA) using "DistMesh - a simple mesh generator in Matlab" [207]. This code generates a 2D mesh within specified boundaries using Delaunay triangulation [208] and force minimisation to make the side lengths of each element approximately the same. The circular boundary condition for the cylinder in the ϕ-direction was imposed by making the nodes at $\phi = \pm\pi$ the same and including elements from both positive and negative ϕ.

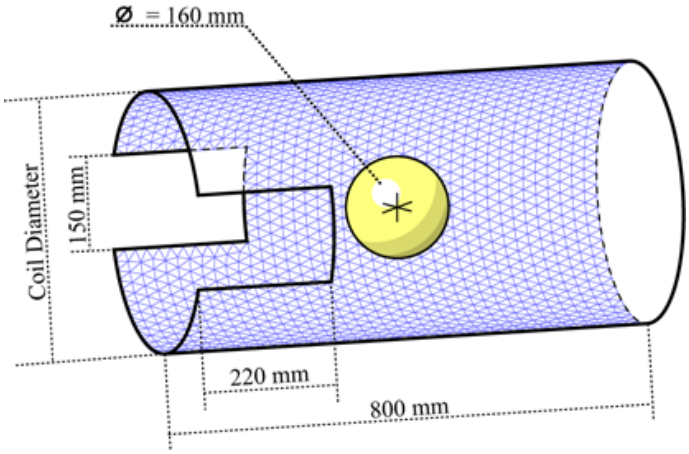

Figure 6.1: Geometry of one surface of the shoulder-slotted, head gradient and shim coil set. The surface boundary is shown in black and the blue triangles represent the elements of the discrete surface. The central sphere is the ROU.

6.1.2 Coil Design Results

All coils were designed to have an inhomogeneity, $\Delta B_z^{\mathrm{ROU}} \leq 5\%$, an inductance, $L \lesssim 100\mu$H and a wire spacing, $\Delta w \geq 3$ mm. The wire-paths of the X-, Y-, and Z-gradient coils are shown in Figs. 6.2 **(a)**, **(c)**, and **(e)**, while **(b)**, **(d)**, and **(f)** are contour plots of the magnetic field, $B_z(\mathbf{r}_k)$, generated by the X-gradient coil in the $y = 0$ plane, by the Y-gradient coil in the $x = 0$ plane and by the Z-gradient coil in the $y = 0$ plane, respectively.

The wire-paths of the 0^{th} and 2^{nd} order shim coils are shown in Fig. 6.3. When designing the X2-Y2 shim coil it was found that while most turns formed complete loops confined to a limited range of azimuthal angles, two loops ran round the coil circumference azimuthally. The resulting coil design would be difficult to build so to make construction easier, the stream-function, ψ, was forced to zero along 4 lines of constant ϕ ($\phi = \pm\pi/4, \pm 3\pi/4$), thereby forcing all wires to form closed loops within their own quadrant. The effect of these extra constraints can be seen in Fig. 6.3 **e)** where no wires cross the $y = x$ or $y = -x$ planes.

Table 6.1 lists the theoretical efficiencies, η, inductances, L, resistances, R, and FOMs, η^2/L, of the shoulder-slotted gradient and shim coils. A more complete collection of coil parameters are given in Appendix A.

Coil	Efficiency, η ($\mu\mathrm{Tm}^{-n}\mathrm{A}^{-1}$)	Self-Inductance, L (μH)	Resistance, R (mΩ)	FOM, η^2/L ($\mathrm{T}^2\mathrm{m}^{-2n}\mathrm{A}^{-2}\mathrm{H}^{-1}$)
Z0	9.4	- (36.9)	115	1.84×10^{-6}
Z	121.2	51.8 (53.1)	51	2.84×10^{-4}
X	99.7	60.3 (63.7)	80	1.65×10^{-4}
Y	119.0	62.3 (54.9)	69	2.27×10^{-4}
Z2	358.0	32.9 (44.7)	53	3.90×10^{-3}
ZX	360.7	66.3 (57.0)	90	1.96×10^{-3}
ZY	411.4	77.2 (69.0)	85	2.19×10^{-3}
X2-Y2	181.0	82.8 (86.8)	98	3.96×10^{-4}
XY	252.0	108.4 (108.6)	109	5.86×10^{-4}

Table 6.1: Efficiencies, η, inductances, L, resistances, R and FOMs of the shoulder-slotted, insert head gradient and shim coil set. L values in brackets and R values were simulated in FastHenry© using 3 mm diameter circular cross-section wire.

For comparison, the gradient and 2^{nd} order shim coils were also designed using the symmetric finite-length, slack method described in § 4.4.8 using the same design criteria; 180 mm length from patient end to isocentre, $\Delta B_z(\mathbf{r}) \leq 5\%$, $L \lesssim 100\mu$H and $\min(\Delta w) \leq 3$ mm. η^2/R was maximised because this increases $\min(\Delta w)$ to a greater extent than maximising

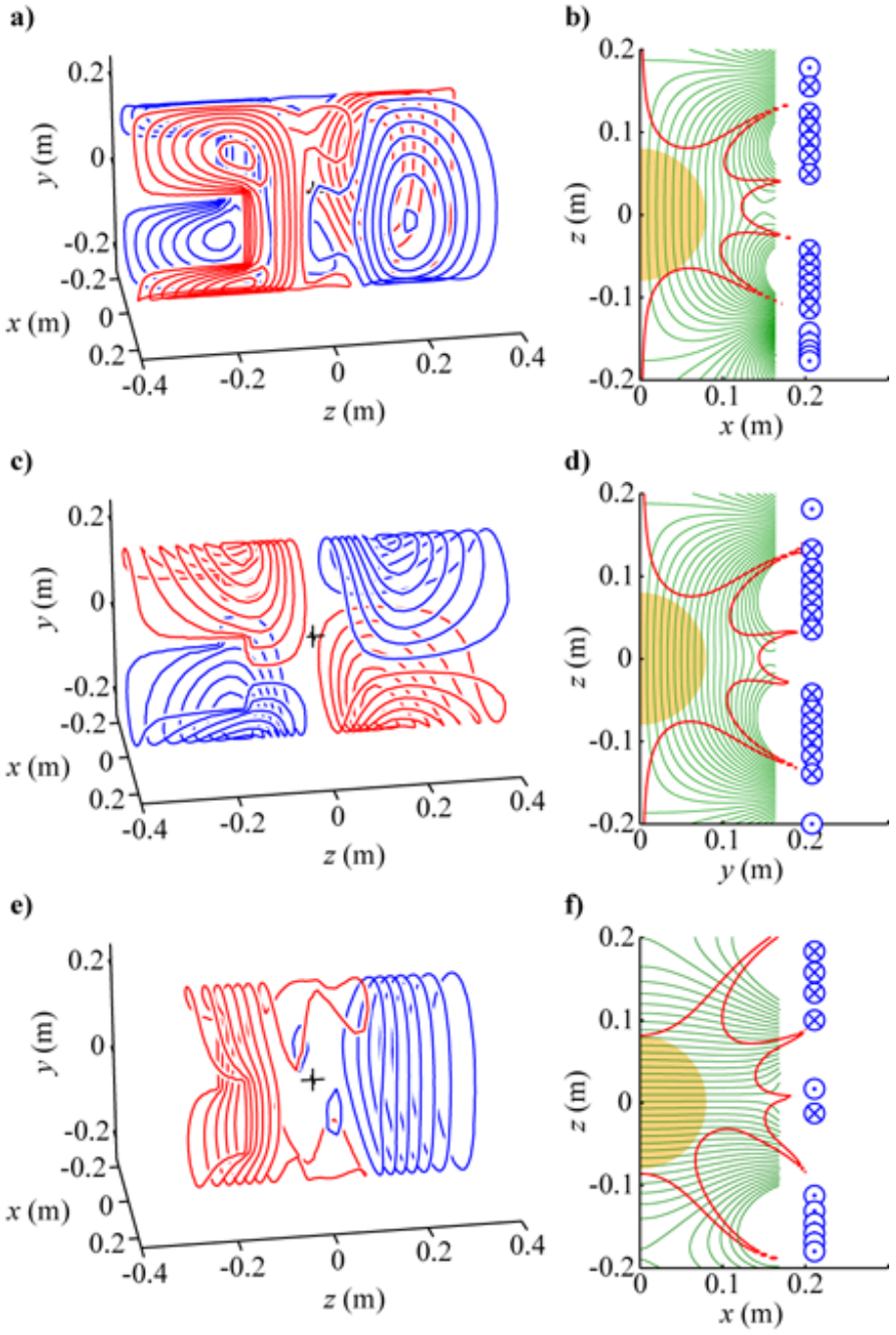

Figure 6.2: Wires of the IBEM-designed, shoulder-slotted **a)** X-, **c)** Y- and **e)** Z-gradient coils (red wires indicate reversed current flow with respect to blue) and **b)**, **d)** and **f)** contours of the magnetic field generated by the coil with $1\mu\text{TA}^{-1}$ contour spacing (thin green lines), overlaid with the $\Delta B_z(\mathbf{r}) = 5\%$ contour (thick red line) and the ROU (orange region). The wires are also shown that cross into, $\otimes$, and out of, $\odot$, the contour plane.

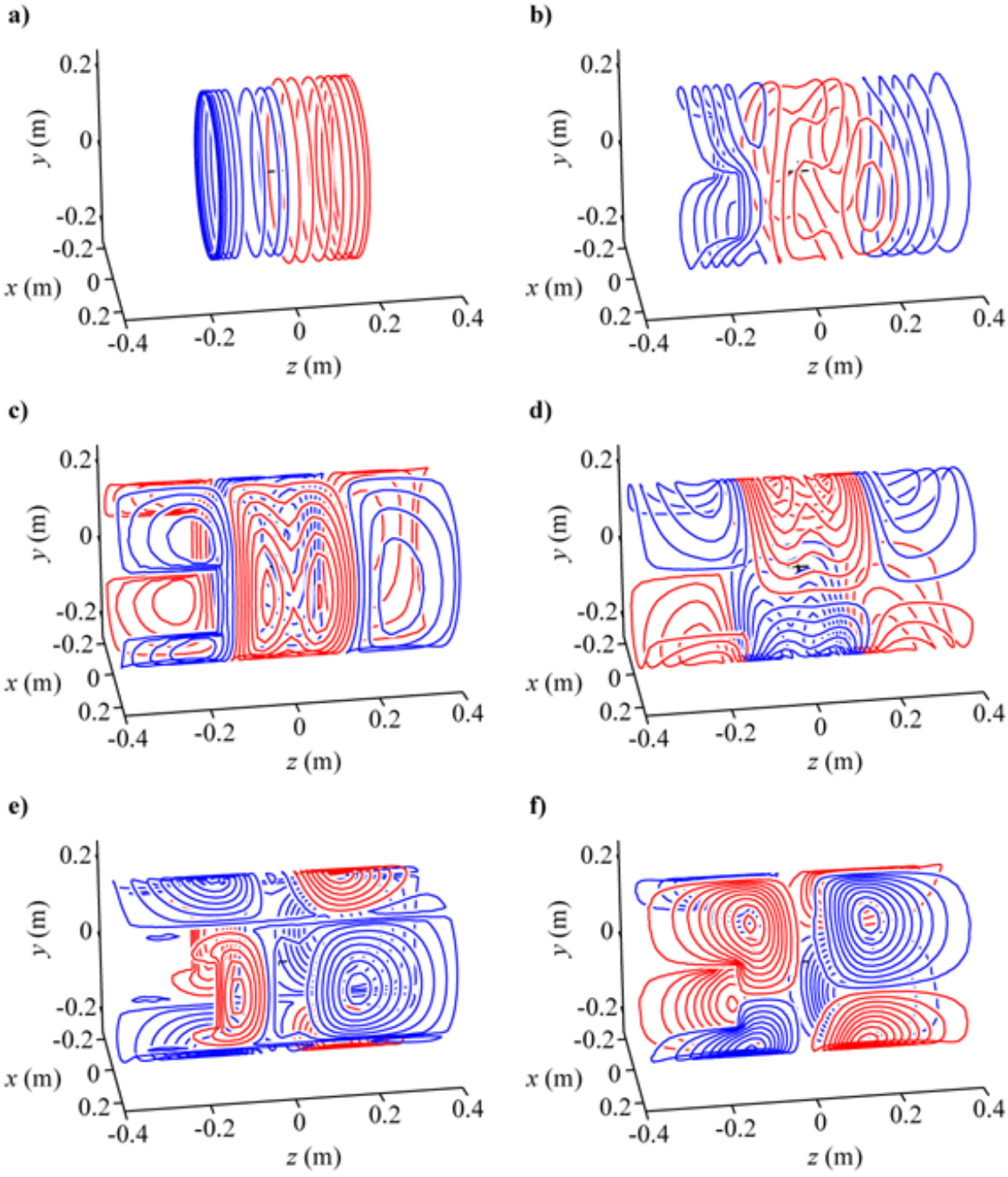

Figure 6.3: Wires of IBEM, shoulder-slotted **a)** Z0, **b)** Z2, **c)** ZX, **d)** ZY, **e)** X2-Y2 and **f)** XY shim coils (red wires indicate reversed current flow with respect to blue). Only the $z < 0$ portion of the Z0 primary and $z > 0$ portion of its shield are shown.

η^2/L, and satisfying the minimum wire spacing constraint for short coils while maintaining a reasonable η is difficult. The X-, Y- and Z-gradient coils were designed on 360 mm long cylinders with 205, 208 and 211 mm radii respectively. It was possible to design the three coils to satisfy all the constraints. The FOMs for the short, cylindrical X-, Y- and Z-gradient coils are 7.1×10^{-5}, 6.4×10^{-5} and 3.0×10^{-4} $\mathrm{T^2m^{-2}A^{-2}H^{-1}}$ respectively. The FOM for the X- and Y-gradient coils are just 46% and 25% of the FOM of the shoulder-slotted equivalents. The η^2/L FOM of the Z-gradient coil is actually 7% higher than its shoulder-slotted equivalent. This is not unexpected as most of the wires in the slotted coil appear superior to the slots in the region of the coil surface spanned by the slack design.

The FOMs of the ZX, ZY, X2-Y2 and XY shim coils were increased by 0%, 14%, 27% and 103% by incorporating the shoulder slots into the design of the 2^{nd} order shim coils. The amount of increase in the FOM is related to the degree to which the shoulder slots impinge on the natural form of the wire-paths for each type of coil. It was found to be impossible to design a Z2 shim coil with such a short length, and few turns that satisfied the design constraints.

The FOM of the X-gradient is significantly, 40%, lower than that of the Y-gradient. This is because the position of the shoulder slots impinges on the location where the return paths of the loops of the X-gradient naturally lie. The $\pi/2$ rotation about the z-axis of the Y-gradient coil with respect to the X-gradient means that the shoulder slots lie in a region of naturally few wires. This effect can be seen in the wire-paths of the X- and Y-gradient coils shown in Fig. 6.2 **a)** and **b)**. It is also true that the FOM of the ZX shim coil is 11% lower than that of the ZY shim, and the FOM of the X2-Y2 shim is 54% lower than that of the XY shim. These lower FOM are a result of the shoulder slots being positioned in the same place as the return paths for the loops of those coils (although some of the FOM reduction in the case of the X2-Y2 can be attributed to the additional constraints on the stream function that were used to reduce the complexity of construction). It can also be observed, from Fig. 6.2 **e)**, that the presence of the shoulder slots does not impinge dramatically on the wire-paths of the Z-gradient coil, implying that is easier to design a short Z-gradient coil than a transverse gradient coil, which is borne out by the similarity between the FOMs of the shoulder-slotted and short, cylindrical Z-gradient coils.

6.1.3 Building the Coil Set

The gradient and shim coil set was constructed at Magnex Scientific Ltd. (Now part of Varian Inc., Yarnton, Oxon., UK). With the exception of the Z0 shim coil, all the coils were built by cutting wire paths out of sheet copper. The wire-paths generated in Matlab®

were turned into 2D CAD drawings for a flat sheet. A garnet abrasive water-jet computer numerical controlled (CNC) cutting machine was then used to make spiral cuts in the copper plates so as to produce the wire-paths. The cut copper sheets were then bonded to a backing of glass-reinforced plastic (GRP) and rolled to the correct radius of curvature. The gradient coils were cut from 2.0 mm thick copper plate while the shim coils were formed from 0.4 mm plate. The Z0 shim was hand-wound with 1.9 mm diameter copper wire. All the coils were assembled onto a GRP former (shown in Fig. 6.4 **a)**) with integral water cooling and a thermocouple temperature sensor and then potted in a Bisphenol-based resin (Grilonit®, Ems-Primid, Domat/Ems, CH) for rigidity. The Z-gradient and the Z2 shim coil had to be made out of two copper plates (since the manufacturing process is not capable of rolling a single copper plate to make a full cylinder) and therefore connections had to be soldered between the plates to ensure correct current flow throughout the coil. If any of the coil designs exhibited small (those with a width approximately the equal to the width of the copper tracks), isolated loops of wire, such as those on the X2-Y2 shim coil, they were omitted from the final design (compare Figs. 6.3 **e)** and 6.4 **c)**) because their effect on the magnetic field is small while their presence increases the complexity of construction. The image in Fig. 6.4 **d)** is of the finished shoulder-slotted gradient and shim set.

6.1.4 Testing the Coil Set

The electromagnetic properties of the gradient and shim coil set were measured and compared to the theoretical values. Table 6.2 details the theoretical, simulated (using FastHenry© [96]) and measured self-inductances, L, and resistances, R, of the coils. The coils were also tested for homogeneity and efficiency using a fluxgate magnetometer (Bartington Instruments, Witney, Oxon., UK) to measure the magnetic field over 7 axial planes with 24 points on each plane over the surface of the 160 mm DSV, which formed the design ROU. The theoretical and measured (by magnetometer and MRI) efficiency, η, of each of the coils and their principal spherical harmonic impurity components are given in Table 6.3. The spherical harmonic impurities are measured relative to a 1 T uniform field. The orthogonality of the X- and Y-gradient coils was measured to be 90.3°.

Figure 6.5 shows axial, sagittal and coronal slices taken from an axial multi-slice image data set obtained using the shoulder-slotted gradient coils acquired with 4 mm isotropic resolution on the Nottingham-built 3T scanner. These gradient-echo, echo-planar images have an echo time of 40 ms.

Using a phantom of known size, the strengths of the 3 gradient coils can be estimated knowing the properties of the scanner. With the switched gradient in the x-direction op-

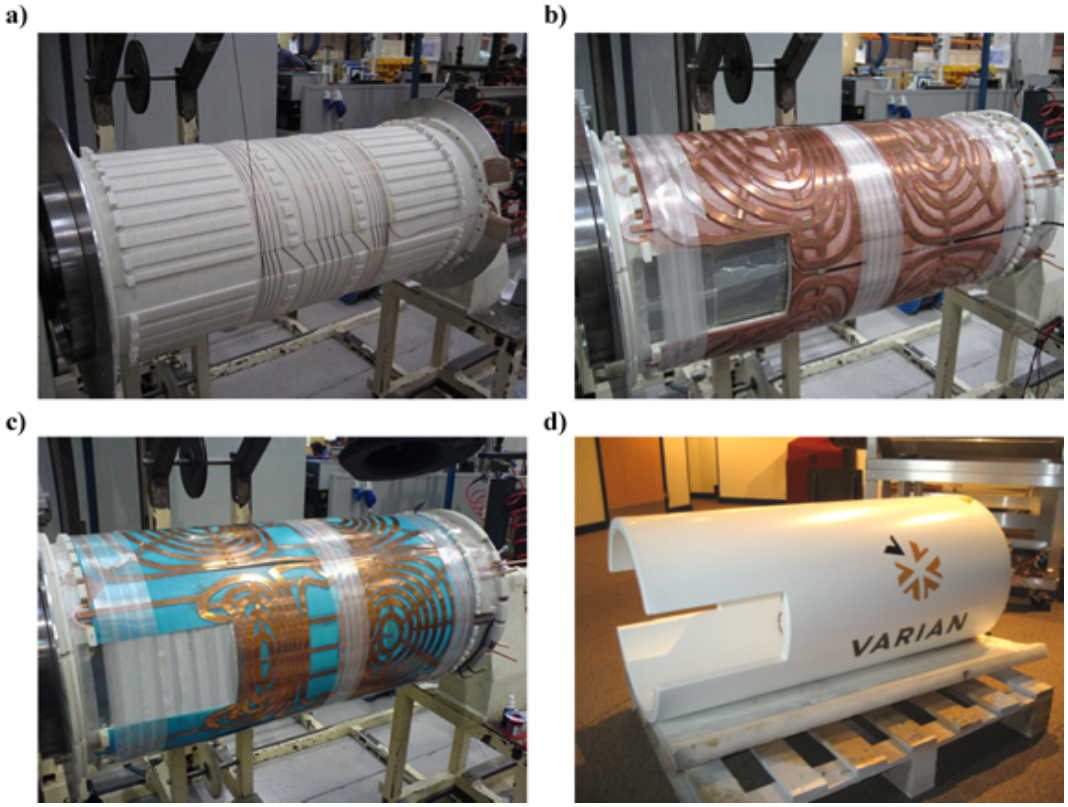

Figure 6.4: The shoulder-slotted, insertable gradient and shim coil set at various stages of manufacture; **a)** the Z0 shim primary coil being wound onto the GRP former, **b)** the Y-gradient coil layer, **c)** the X2-Y2 shim layer and **d)** the finished article.

erating in resonant mode for EPI acquisition means that the x-resolution, Δx, is given by

$$\Delta x = \frac{\pi^2}{\gamma \eta_x I_x \tau} \tag{6.1}$$

where $\gamma = 267.5 \times 10^6$ s^{-1}T^{-1} is the gyromagnetic ratio, η_x is the efficiency of the X-gradient coil, I_x is the current in the X-gradient and τ is the length of one lobe of the sinusoidal gradient waveform, which is $\tau = 472 \pm 5\mu$s since the switched gradient is operating in resonant mode at 1.06 ± 0.01 kHz. A voltage of 2.5 ± 0.1 V was applied across the X-gradient coil implying a maximum current of 150 ± 6 A in the coil. Δx is worked out from the fact that the 195 ± 5 mm diameter agar phantom occupied 46 ± 1 slices of the 3D EPI data set implying $\Delta x = 4.2 \pm 0.2$. Using Eq. (6.1) with these values gives

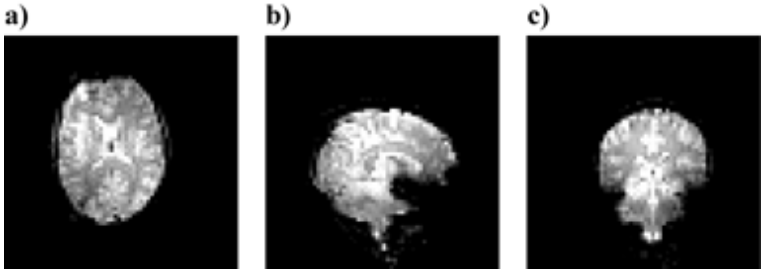

Figure 6.5: **a)** Axial, **b)** sagittal and **c)** coronal slices of an EPI image acquired with the shoulder-slotted gradients at 3T .

$\eta_x = 125 \pm 12\mu\text{Tm}^{-1}\text{A}^{-1}$. Altering the switched gradient to the y-direction allows the measurement of the efficiency of the Y-gradient coil by the same means, giving a value of $\eta_y = 115 \pm 12\mu\text{Tm}^{-1}\text{A}^{-1}$ (since $I_y = 156 \pm 6$ A, $\tau = 516 \pm 5\mu$s and the agar phantom occupies 49 ± 1 slices).

Estimating the efficiency of the Z-gradient involves a similar calculation

$$\Delta z = \frac{\Delta\omega}{\gamma\eta_z I_z} \tag{6.2}$$

where $\Delta\omega$ is half the bandwidth of the RF pulse which is known to be $\Delta\omega = 10700 \pm 100$ Hz and $I_z = 84 \pm 6$ A. Since there appears to be signal in 48 ± 1 slices and $\Delta z = 4.0 \pm 0.2$ mm the Z-gradient efficiency is estimated to be $\eta_z = 120 \pm 13\mu\text{Tm}^{-1}\text{A}^{-1}$.

The magnetic fields generated by the shim coils were mapped at 3T with the same 200 mm diameter, spherical agar phantom and the EPI-based field mapping method shown in Fig. 2.16. For each shim coil a field map is shown in Fig. 6.6 in the relevant central plane (*e.g.* in the $y = 0$ plane for the ZX shim) and below each map is shown the spherical harmonic fit used to estimate the efficiency, η, of the coil. The position of the isocentre of the shim coil set is required for fitting the measured field maps to their perfect spherical harmonic. This is done by iteratively translating the spherical harmonic fitting field until the RMS difference between the fit and the measured field is minimised. The shim coil efficiencies as measured by this field mapping technique are given in Table 6.3.

6.1.5 Discussion

Here we have demonstrated that the IBEM method allows the design of gradient and shim coils on asymmetric surfaces. Bringing the surface in closer to the head increases the strength of these coils since $\eta \propto a^{-2}$ for gradient and $\eta \propto a^{-3}$ for 2^{nd} order shim coils. The

Coil	Self-Inductance, L (μH)		
	Theoretical	Simulated	Measured
Z0	-	36.9	54.6
Z	51.8	53.1	43.8
X	60.3	63.7	57.9
Y	62.3	54.9	52.7
Z2	32.9	44.7	29.8
ZX	66.3	57.0	64.5
ZY	77.2	69.0	64.4
X2-Y2	82.8	86.8	70.7
XY	108.4	108.6	98.6

Table 6.2: Theoretical, simulated and measured inductances of the shoulder-slotted, insert head gradient and shim coil set. Simulated values were obtained using FastHenry© using 3 mm diameter circular cross-section wire.

Coil	Theoretical, Measured (magnetometer) and Measured (MRI) Efficiency, η (μTm^{-1}A^{-1})	Impurities			
		#1 (ppm)	#2 (ppm)	#3 (ppm)	#4 (ppm)
Z0	9.41, 9.66, 9.79	Z2 = -3.3	Z6 = 2.3	Y = 2.2	Z4 = 2.0
Z	121.2, 121.8, 116	Z6 = -25.9	Z3=-12.0	Z5=-7.9	Z2=-5.2
X	99.7, 100.9, 121	Y=5.2	Z2X=3.1	ZX = 2.4	Z4=2.1
Y	119.0, 121.4, 101	Z2Y=5.0	ZY = 4.2	X=-3.6	Z5=-3.0
Z2	358.0, 357.6, 374.7	Z5=-3.8	Z=3.1	Y=1.5	X=1.4
ZX	360.7, 373.0, 391.4	X=-5.3	Z6=3.9	Y=2.4	Z4Y=-1.8
ZY	411.4, 414.8, 439.5	Y=9.5	Z5=-1.6	Z6=1.5	Z2 =-1.4
X2-Y2	181.0, 182.7, 211.6	Z5=-2.5	Z2=-2.1	X=1.9	Z=-1.4
XY	252.0, 253.3, 283.6	Y=2.1	Z6=1.8	ZX=-1.6	Z3X=1.1

Table 6.3: Theoretical, magnetometer- and MRI-measured efficiencies of the shoulder-slotted, insert head gradient and shim coil set and the first four spherical harmonic impurities measured with the magnetometer, in ppm of 1 T.

self-inductance is also reduced as $L \propto a$. Reducing the radius means that the shoulders of subjects must be accommodated for, in this case by removing rectangular slots in the otherwise cylindrical surface. η and $\Delta B_z^{\max}(\mathbf{r}_k)$ of each coil matches well with the theoretical values calculated using Biot-Savart, Eq. (4.1). However, there is some discrepancy between the theoretical and measured self-inductances, particularly for the Z2 shim coil. This discrepancy is thought to originate in the method of manufacture. The current carrying conductors forming the coil are of widely varying width ($\sim$ 3 to 25 mm) whereas the theoretical inductance values were obtained using FastHenry© assuming 3mm diameter cross-section wires. Also, the model did not include interconnects that pass current from one loop to another and into and out of the coils, or soldered joints. These modelling differences are likely to be the cause of the inductances being considerably different to their simulated values.

This coil set is intended to be used to implement dynamic shimming, and has been shown to have self-inductances low enough to allow the shim coil current to be varied on a timescale that will make this feasible ($\lesssim 100\mu$s). Due to the highly restricted space available for coils however, all but the Z0 shim coil are unshielded. This means that imaging may suffer due to eddy currents from switching the gradient coils. The small radii of these coils may however aid the reduction of eddy currents in the cryostat of the superconducting magnet since $B(\mathbf{r}) \propto |\mathbf{r} - \mathbf{r}'|^{-2}$. Also, eddy currents generated when switching the shim coils have been shown to be a limiting factor for dynamic shimming [209]. The problems associated with unshielded and poorly shielded coils may be mitigated by pre-emphasising [92, 93] the gradient and shim waveforms (see § 3.3.1). Otherwise it may be possible to retro-fit shield coils (see § 6.9) to the set providing they can be accommodated within the bore of the magnet.

The EPI image data in Fig. 6.5 obtained at 3T with a 4 mm isotropic resolution compare well with similar EPI images obtained with a different set of gradient coils. It appears that the eddy currents resulting from the lack of shielding have little detrimental effect in the images. It can be seen from the field maps of the shim coils in Fig. 6.6 that there is good agreement between the measured field maps and their spherical harmonic fits. Some discrepancies are caused by the Nyquist ghost, present in the echo-planar images used for field mapping as can be seen in Fig. 6.6 **h)**, some arise from noise in the NMR signal, some from imperfect shimming leading to image distortion and some from the difference between the forms of the scanned and spherical harmonic fields. The MRI-measured efficiencies of the 0^{th} and 2^{nd} order shims in Table 6.3 agree reasonably well with the values measured with the magnetometer. The differences between these values are thought to arise from the error in the estimated image resolution. The efficiency values calculated for the gradient coils

are less trustworthy, because there are more sources of error in their measurement. Despite this they are in reasonable agreement with the values measured using the magnetometer.

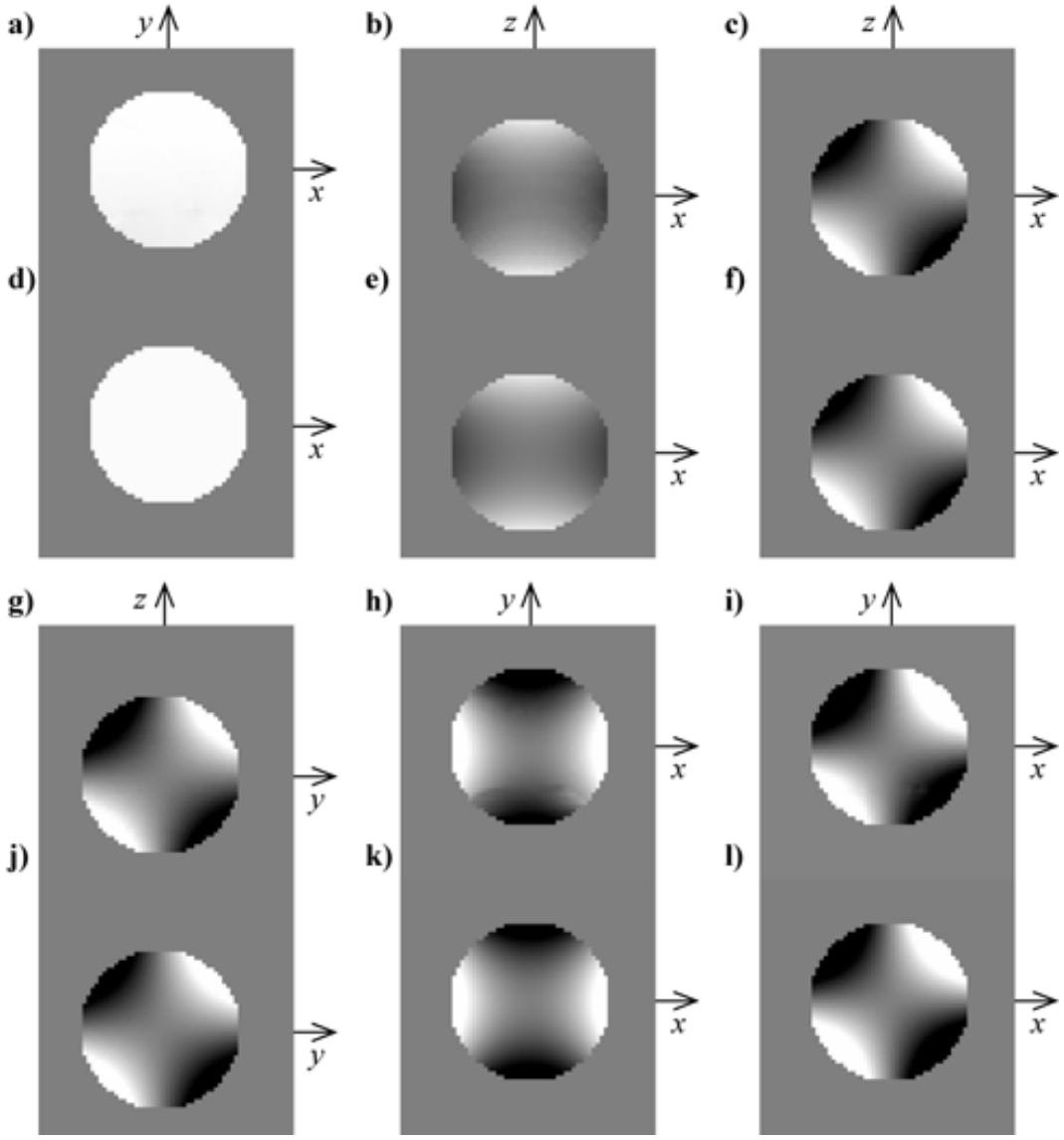

Figure 6.6: Greyscale images showing the magnetic field generated in the central plane of the 160 mm DSV ROU by passing 1 A through the **a)** Z0, **b)** Z2, **c)** ZX, **g)** ZY, **h)** X2-Y2 and **i)** XY shim coils. Directly below them, **d)**, **e)**, **f)**, **j)**, **k)** and **l)**, are the spherical harmonic fits to the measured field maps. For the Z0 field map and its fit, black to white corresponds to -10 to 10 ppm, and for all the other shim coils black to white represents -5 to 5 ppm of 1T.

6.2 Dome Gradient Coils

Following the design of hemispherical gradient coils [177], Leggett *et al.* used an approach similar to the finite-length coil design methods in § 4.4.6 to design highly efficient head gradient coils wound on a hemispherical surface with a short, cylindrical extension [178]. However, the finite-length basis-function formulation used means that the stream-function must be forced to a particular value at the interface between the hemisphere and cylinder. Here we demonstrate the improvement in performance that can be achieved by removing this constraint via use of the IBEM in designing coils.

6.2.1 Geometry

Figure 6.7 shows the geometry of the surfaces used by Leggett *et al.* [178]. The X-, Y- and Z-gradient coil surfaces are hemispheres with 115 mm long cylindrical extensions with 172, 184 and 195 mm radii respectively. The ROU is an oblate spheroid with 155 mm x- and y-diameters and 117 mm z-diameter centered 190 mm from the open end of the coil surfaces.

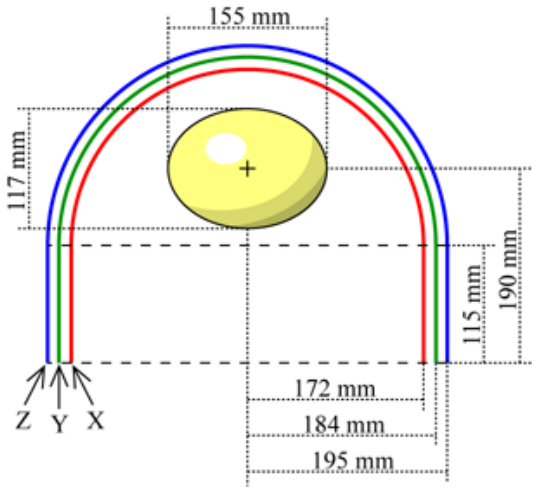

Figure 6.7: The geometry of the dome X-, Y- and Z-gradient coils, where the yellow ovoid is the ROU.

6.2.2 Results

A torque-balanced X-gradient coil was designed to have $\Delta w \geq 3$ mm, $\Delta B_z^{\mathrm{ROU}} \leq 5\%$ and the highest possible FOM. The coils wire-paths are shown in Fig. 6.8 **a)** alongside a contour

plot in the $y = 0$ plane of $B_z(x, 0, z)$. Table 6.4 details the properties of these coils, and Appendix A presents a more comprehensive list of properties. The FOMs for the IBEM X- and Y-gradient coils are 120% and 36% larger and the Z-gradient is 7% lower than the previous coils [178]. There is little difference in the FOM of the Z-gradient coil since the stream-function is symmetric in ϕ and therefore forced to be constant over the boundary between the hemispherical and cylindrical surfaces.

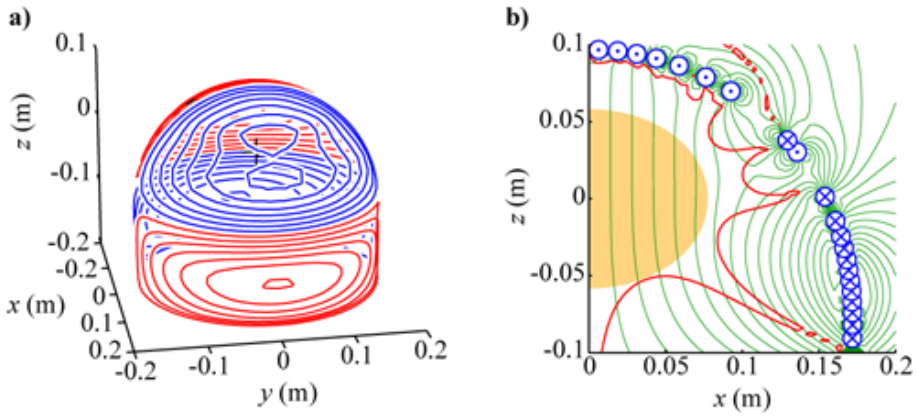

Figure 6.8: **a)** Wires of the IBEM-designed dome X-gradient coil (red wires indicate reversed current flow with respect to blue) and **b)** contours of the magnetic field generated by the coil with $10\mu\text{TA}^{-1}$ contour spacing (thin green lines), overlaid with the $\Delta B_z(\mathbf{r}) = 5\%$ contour (thick red line) and the ROU (orange region). The wires are also shown that cross into, $\otimes$, and out of, $\odot$, the contour plane.

Coil	Efficiency, η ($\mu\text{Tm}^{-1}\text{A}^{-1}$)	Self-Inductance, L (μH)	Resistance, R (mΩ)	FOM, η^2/L ($\text{T}^2\text{m}^{-2n}\text{A}^{-2}\text{H}^{-1}$)
X	356	48.5 (50.1)	48	2.62×10^{-3}
Y	304	54.0 (56.1)	52	1.65×10^{-3}
Z	333	99.3 (96.2)	60	1.15×10^{-3}

Table 6.4: Theoretical efficiencies, inductances, resistances and FOMs of the IBEM-designed dome gradient and shim coil set. L values in brackets and R values were simulated in FastHenry© using 3 mm diameter cirular cross-section wire.

If the inductance is low enough, then using resistance minimisation only permits an increase in the wire spacing, which is a limiting factor in this design. Increasing the number of turns decreases the wire spacing but increases the coils efficiency. Using these two properties an X-gradient coil may be designed with $\eta = 0.62$ $\text{mTm}^{-1}\text{A}^{-1}$ while maintaining

both the $\Delta B_z^{\mathrm{ROU}} \leq 5\%$ and $\Delta w \leq 3$ mm criteria by only employing resistance minimsation via β.

Torque-balancing these coils is essential because the geometry is asymmetric in the z-direction. To illustrate the difference between coils with and without torque-balancing a non-torque-balanced X-gradient coil was also designed. The magnitude of the torque vector for the unbalanced coil is 0.66 $\mathrm{NmA^{-1}T^{-1}}$ compared with 0.00089 $\mathrm{NmA^{-1}T^{-1}}$ for the torque-balanced coil, a reduction of 99.9%. Any residual torques on the torque-balanced coils are a consequence of the discretised nature of the surface mesh and wire-paths. If the same design criteria are applied to the design of an unbalanced X-gradient (*i.e* $\min(\Delta w) \leq 3$ mm and $\Delta B_z(\mathbf{r}_k) \leq 5\%$) then an efficiency of 730 $\mu\mathrm{Tm}^{-n}\mathrm{A}^{-1}$ may be achieved. Operating such a coil with 300A in a 3T magnetic field would generate torques of approximately 600Nm.

6.3 Ultra-Efficient Shielded Dome Head Gradient Coils

The motivation for producing this coil design was to generate the highest possible gradient strengths for human head imaging by placing the current carrying surfaces as close to the region of interest (ROI) as possible. There are several head imaging applications that would benefit from such increased efficiency, including magnetic resonance angiography [210] and diffusion weighted imaging [211, 212]. This example illustrates the ability of the IBEM to produce coils with highly asymmetric geometry.

6.3.1 Geometry

Figure 6.9 shows the geometry of the coil design. The primary surface (red triangles in Fig. 6.9 is created from a 310 mm diameter hemisphere and cylinder of length 165mm squashed in the x-direction to be 265 mm wide. The elliptical cross-section was intended to reflect a head shape while providing a 50 mm gap between the head and the coil surface to accommodate a dome RF coil. The primary surface also has a flat, annular surface attached to it, that fills the radial space between the inner and outer cylinders at the base of the coil. A 520 mm diameter hemisphere, concentric with the inner hemisphere, with a 165 mm cylindrical extension forms the secondary surface. To ensure that no wires in the final coil designs cross from the primary to secondary surface, which would make coil construction unfeasible, the inner and outer coil surfaces are not connected.

The whole surface is discretised into 4224 triangular elements and 2162 nodes. The ROU is an oblate spheroid with a 165 mm width in the x-direction and 210 mm in the y- and z-directions, positioned concentrically with the hemispheres of the surface, and contains 587 evenly distributed target points. The region of shielding (ROS) is formed from an ensemble of points evenly distributed over a 550 mm long cylindrical surface with a 640 mm diameter centred 25 mm above the centre of the ROU in the z-direction.

6.3.2 Results

Figures 6.10 **a)**, **c)** and **e)** show the wire-paths for the X-, Y- and Z-gradient coils. The contours of $B_z(\mathbf{r})$ generated in the $y = 0$ plane by the X- and Z-gradient coils and in the $x = 0$ plane by the Y-gradient are shown in Fig. 6.10 **b)**, **d)** and **f)** overlaid with a contour enclosing the $\Delta B_z \leq 5\%$ region. Table 6.5 gives the η, L and R values of the X-, Y- and Z-gradient coils and a full list of properties can be found in Appendix A. The FOM of these coils are broadly comparable to those of the dome coils in § 6.2, but the coils described here are actively shielded. The FOMs are much greater than previously described cylindrical

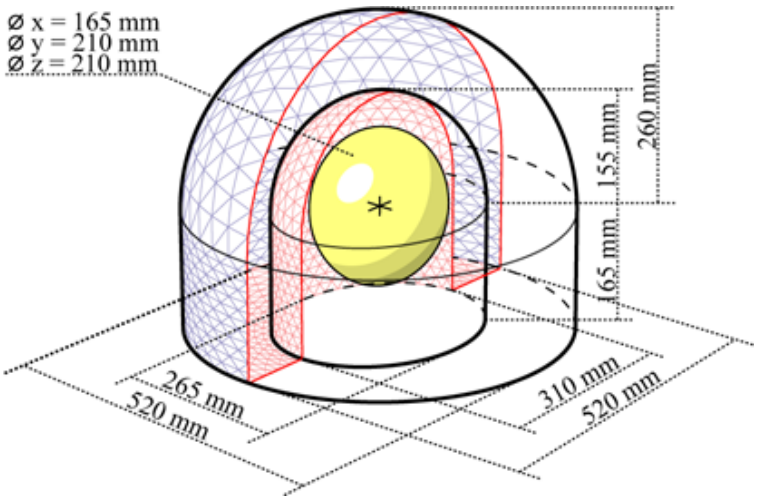

Figure 6.9: Geometry of the ultra-efficient, shielded dome IBEM head gradient coil surface. The two discretised surfaces are represented by blue and red triangles. The central ovoid is the ROU.

insert head gradient coils [91].

Coil	Efficiency, η (μTm^{-1}A^{-1})	Self-Inductance, L (μH)	Resistance, R (mΩ)	FOM, η^2/L (T^{2}m^{-2n}A^{-2}H^{-1})
X	327	58.0 (63.0)	76	1.84×10^{-3}
Y	287	50.3 (56.1)	74	1.64×10^{-3}
Z	456	105 (112)	83	1.98×10^{-3}

Table 6.5: η, L, R and FOM values for the ultra-efficient, shielded dome head gradient coils. L values in brackets and R values are simulated in FastHenry© using 3 mm diameter cirular cross-section wire.

6.3.3 Prototype Construction

A half-scale prototype of the X-gradient coil, shown in Fig. 6.10 **a)**, has been built and tested (see Fig. 6.11). A rapid-prototyping technique known as layered- or laminated-object manufacturing (LOM™) (Helisys Inc., Torrance, CA, USA) [213] was used to build the prototype. This method accepts 3D CAD data describing a solid object and cuts with a laser a multitude of adhesive paper layers that joined together form the solid object. The solid object here was the volume between the inner and outer surfaces (see Fig. 6.9), with the wire-paths of the X-gradient removed from the surface. The prototype coil was

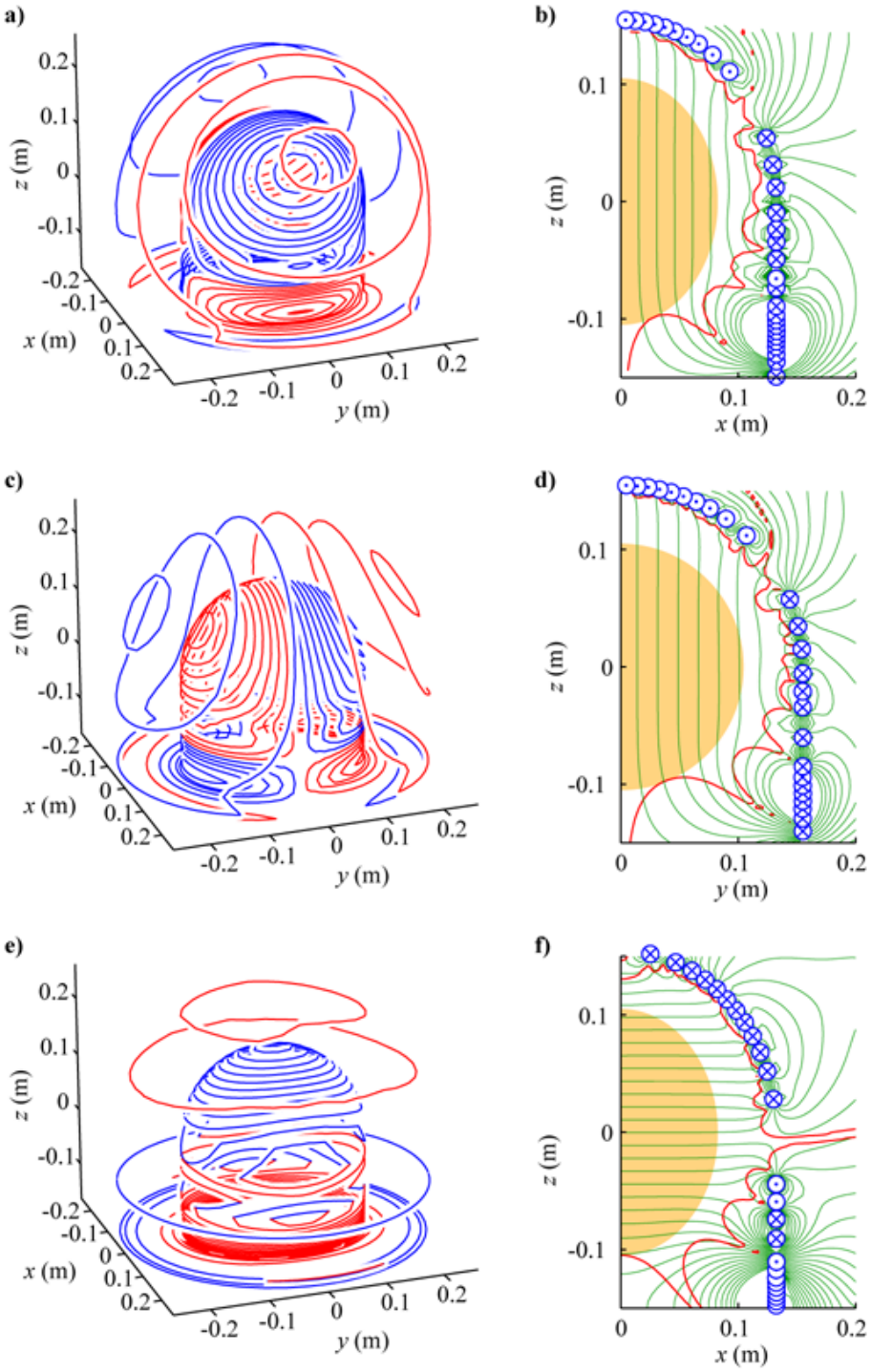

Figure 6.10: Wires of the IBEM-designed, ultra-efficient, shielded dome **a)** X-, **c)** Y- and **e)** Z-gradient coils (red wires indicate reversed current flow with respect to blue) and **b)**, **d)** and **f)** contours of the magnetic field generated by the coil with $5\mu\text{TA}^{-1}$ contour spacing (thin green lines), overlaid with the $\Delta B_z(\mathbf{r}) = 5\%$ contour (thick red line) and the ROU (orange region). The wires are also shown that cross into, $\otimes$, and out of, $\odot$, the contour plane.

then simply made by gluing 0.9 mm diameter wire into the grooves on the surface of the rapid-prototyped object.

The efficiency of the prototype coil was calculated by using the 2-echo, gradient-echo 3D magnetic field mapping sequence in § 2.5.10 to measure the magnetic field distribution within a water phantom (a water-filled condom was used for its high elasticity and tensile strength [214]) for known small drive currents. These maps are scaled to provide a map of the magnetic field per unit current (see Fig. 6.11 **c)**). This magnetic field map was used to calculate the efficiency of the prototype as $\eta = 1.379$ mTm^{-1}A^{-1} which implies an efficiency value of $\eta = 0.345$ mTm^{-1}A^{-1} when scaled to full size. L and R values of the prototype were measured to be 34 μH, and 0.52 Ω respectively with values of 33 μH, and 0.42 Ω found when the prototype coil was modelled in FastHenry© with 0.9mm diameter wire and at the same scale as the prototype. These values are very similar and give confidence in the accuracy of modelling coils in this way.

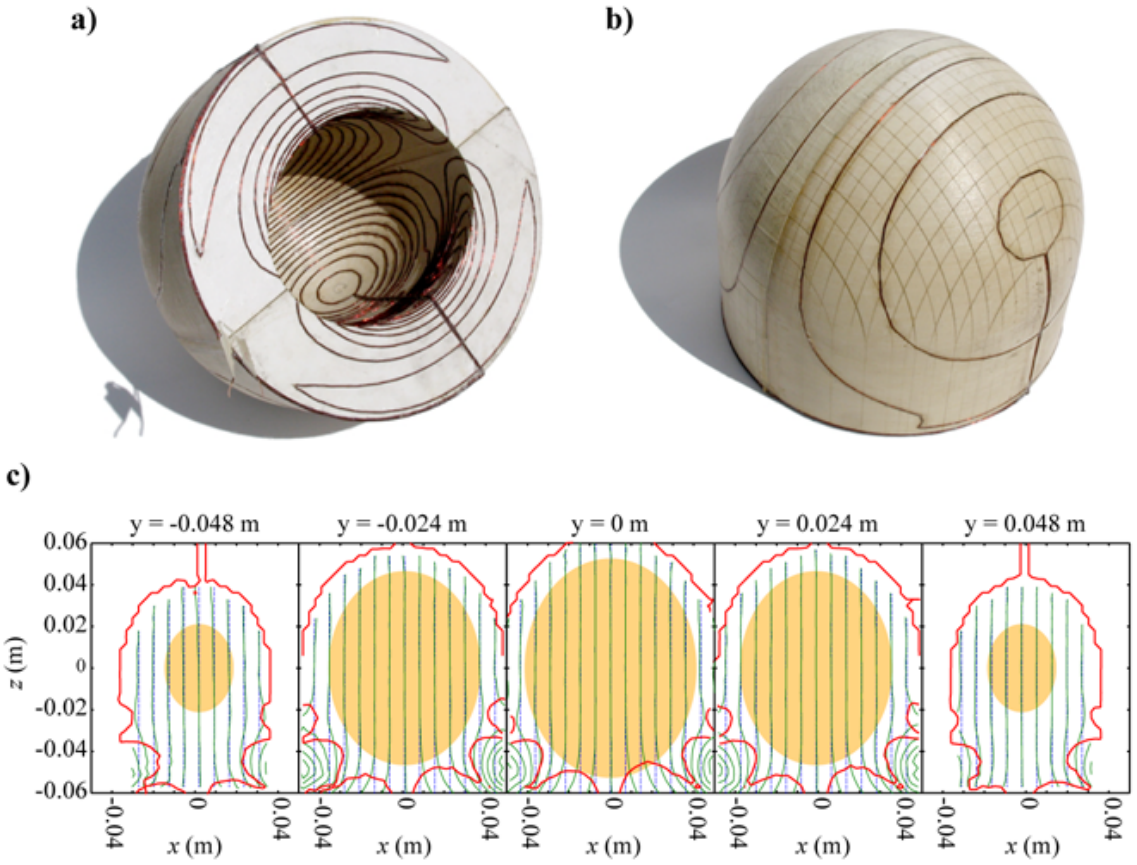

Figure 6.11: **a)** Inside and **b)** outside views of the half-scale prototype ultra-efficient, shielded dome X-gradient coil. **c)** contours of the magnetic field distribution generated by 1 A in the coil (thin green lines) measured with the field mapping sequence and a water phantom with $B_z \propto x$ fit (dotted thin blue lines) and $\Delta B_z \leq 5\%$ inhomogeneity contour (thick red line).

6.4 Ultra-Short Gradient Coils

Here we replicate with the IBEM the work of Shvartsman *et. al.* [172] by generating a set of shielded, cylindrical gradient coils with low length-to-diameter ratio. To produce their coil designs, Shvartsman *et al.* employed straight wires on surfaces formed from conical sections at either end of the coil that connected the primary and shield surfaces. In Ref. [172] the conical surfaces are used to remove the constant stream-function constraints at the ends of the primary and shield coils whilst allowing good access to the subject. The wires on these surfaces must be included in the design process as they contribute to $B_z(\mathbf{r}_k)$. The dimensions of the coils and the design of coils of this geometry is provided in [172]. Using the IBEM, wires may follow any path on the conical surface. The geometry employed by Shvartsman *et al.* [172] is duplicated here so as to illustrate the increase in coil performance which results from the removal of the constraints on the current density that are imposed by the more analytical approach.

6.4.1 Geometry

The coil geometry is illustrated in Fig. 6.12. The inner surface is a short cylinder that generates the magnetic field gradient, the second surface is a longer cylinder that carries wires arranged so as to annul stray fields from the the primary coil and, the third and fourth surfaces are conical sections that connect the first and second surfaces at either end. Therefore there are no edges to the mesh on which boundary conditions must be applied. In applying the IBEM approach, the surface was discretised into 6080 triangular elements and 3040 nodes.

6.4.2 Results

Figure. 6.13 **a)** shows the wire-paths for the ultra-short X-gradient coil, while Fig. 6.13 **b)** is a contour map of the magnetic field produced by the ultra-short X-gradient coil with the 5% magnetic field inhomogeneity contour also shown. Some properties of the three gradient coils is given in Table 6.6 in comparison to the properties of the coils design by Shvartsman *et al.* (there are no data for the Y-gradient in Ref. [172] to compare). A more comprehensive collection of properties are detailed in Appendix A.

The FOM for the X- and Z-gradient coils are 26% and 22% greater for the IBEM coil than those presented by Shvartsman *et al.* This gain in performance is principally a consequence of the removal of the current density constraints on the conical section surfaces. The performance difference is less for the Z-gradient since there is less benefit in placing

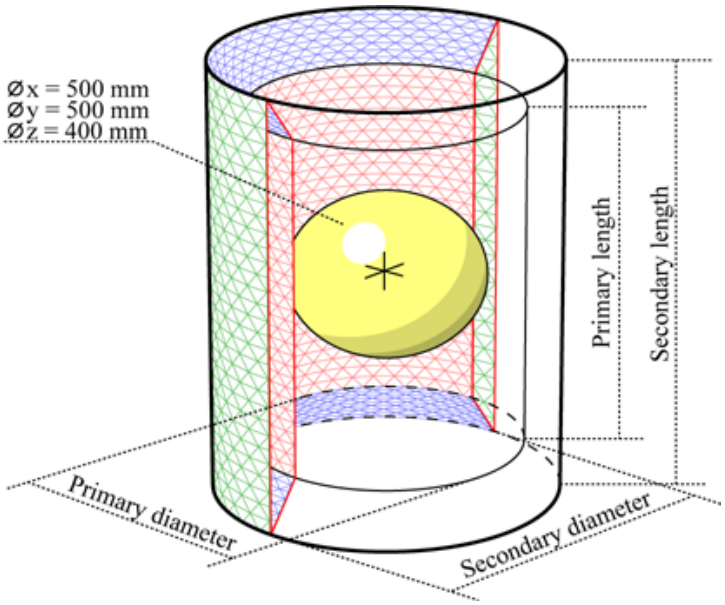

Figure 6.12: Geometry of the ultra-short gradient coil. The surfaces represented by red, green and blue triangles are the primary, shield and conical section surfces respectively. The central ovoid is the ROU.

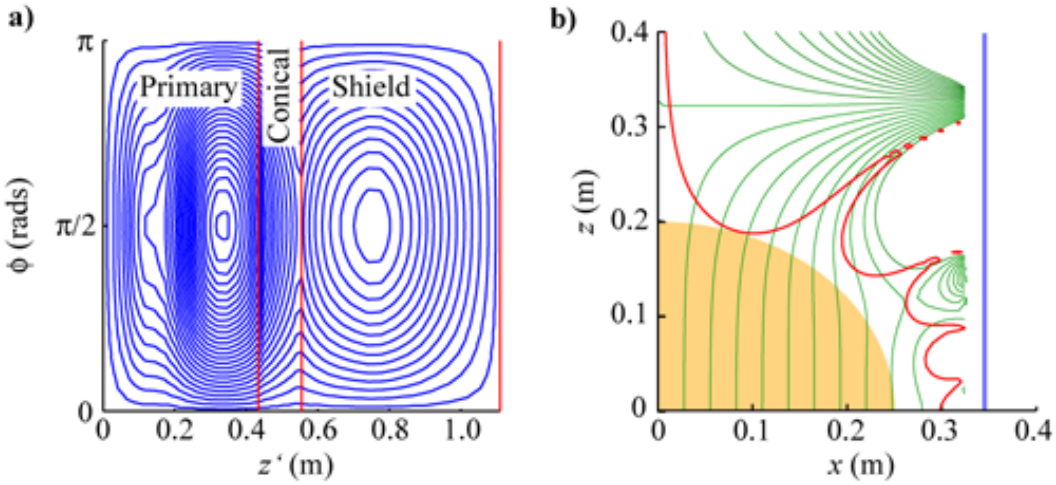

Figure 6.13: **a)** Wires of the ultra-short, shielded, IBEM X-gradient coil with the z'-axis starting at $z = 0$ on the primary surface and increasing, then onto the conical surface and back along the shield surface to $z = 0$ and **b)** contours of the magnetic field generated by the coil with $2\mu\text{TA}^{-1}$ contour spacing (thin green lines), overlaid with the $\Delta B_z(\mathbf{r}) = 5\%$ contour (thick red line) and the ROU (orange region). The primary coil surface is also shown (thick blue line).

Coil	Efficiency, η (μTm^{-1}A^{-1})	Self-Inductance, L (μH)	FOM, η^2/L (T^{2}m^{-2n}A^{-2}H^{-1})
IBEM-designed			
X	72.6	699 (742)	7.55×10^{-6}
Y	76.5	690 (732)	8.48×10^{-6}
Z	115.0	1270 (1339)	10.5×10^{-6}
Shvartsman's			
X	63.2	666	6.00×10^{-6}
Z	76.1	674	8.58×10^{-6}

Table 6.6: η, L and R and FOM values for the ultra-short, shielded gradient coils. L values in brackets are simulated in FastHenry© using 3 mm diameter cirular cross-section wire.

wires on the conical surface as it is far from the ROU and the stream function is constant in ϕ over the interface between these symmetric surfaces.

6.5 Split Gradient Coils for Combined PET/MRI

There is currently considerable interest in combining positron-emission tomography (PET) with MR. The spatial resolution of MR is excellent, and is complemented by the ability of PET to detect small changes in metabolite concentrations. However, conventional photo-multiplier tubes (PMT) used in PET are sensitive to magnetic fields. One proposal to combine these imaging modalities is to use a split MR magnet with space in the centre for light-guides to transmit the light from its source, Lutetium Oxy-Orthosilicate (LSO) crystal PET detectors, to a region where the magnetic field is low enough ($\sim$ 30mT) for shielded PMTs to operate [215]. This means that split gradient coils must be used as well as a split main magnet. For regular cylindrical gradient coils the central region is usually occupied by wires (see Fig. 4.12 for example). Here, this region is unavailable due to the presence of the PET detectors, so designing gradient coils for such a system poses a problem. The set of split coils designed in this work comprises a shielded Z0 shim coil and shielded X-, and Y- and Z-gradient coils.

6.5.1 Geometry

These gradients must be shielded as well as incorporate a central gap of least 118 mm. The current carrying surfaces are shown in the $y = 0$ plane in Fig. 6.14 and the inner and outer radii, and the widths of the gaps of each coil are given in Table 6.7. The total length of the coils is 800 mm, the ROU is an 100 mm DSV, the ROS is an 800 mm long cylinder with a radius of 200 mm. Initially, the surfaces of all the coils comprised 4 cylinders, 2 primary and 2 shield, separated by a central gap. It was impossible to get the required performance from the X- and Y-gradients coils because of the imposition of the ψ = constant boundary conditions at the edges closest to the ROU. Therefore, the design geometry was modified to incorporate an annular surface that connects the primary and shield surfaces for the X- and Y-gradient coils, as shown in Fig. 6.14.

Coil	Inner Radius (mm)	Outer Radius (mm)	Gap Width (mm)
Z0	99.55	154.65	141, 129
X	89.45	148.50	118
Y	92.95	145.90	122
Z	85.60	142.60	132

Table 6.7: Dimensions of the coil surfaces of the split gradient set. The gap width of the inner coil surface is slightly larger than the gap width of its outer surface.

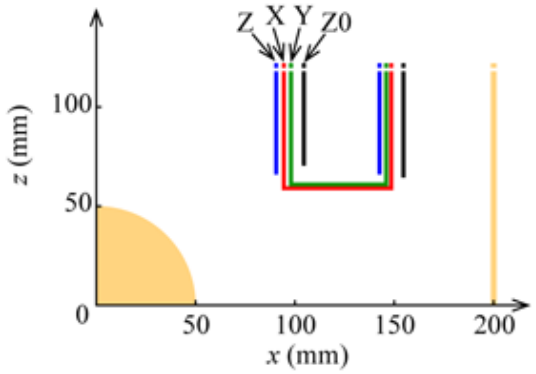

Figure 6.14: Geometry of the 3-axis shielded, split gradient coils and Z0 shim coil in the $y = 0$ plane. All surfaces extend over a distance of 0.4 m in the z-direction.

Different techniques are to be used to construct each coil. The X- and Y-gradient coils will be cut using an abrasive water-jet and the Z-gradient coil and Z0 shim coil will be hand wound with different thicknesses of wire. Therefore, the minimum wire spacing constraints for the X-, Y-, Z- and Z0 coils are 3.6, 3.6, 3.2 and 2mm respectively.

6.5.2 Results

Figure 6.15 shows the wire-paths of the shielded, split X- and Z-gradient coils with their contour plots of the magnetic field per unit current. The Y-gradient is not shown because of its similarity with the X-gradient. Table 6.8 displays the efficiencies, inductances, minimum wire spacings, $\min(\Delta w)$, and FOMs of the four coils. Appendix A details a full list of the properties of these coils.

The shielding of these coils is of vital importance, since the gap is positioned about $z = 0$, the region in which eddy currents generated on conducting surfaces are at their strongest. The maximum magnetic field values generated over the shield surface for the Z0 shim, X-, Y- and Z-gradient coils were 0.71, 0.95, 0.86 and 0.63 μTA^{-1} respectively.

6.5.3 Discussion

In the designs described here, no wires may occupy the central region about $z = 0$, which is where most of the wires reside in conventional coils. These wires are most important since they are the closest to the ROU and contribute most of the magnetic field within it. Using the IBEM it has been possible to design gradient coils that conform to the desired magnetic field specifications and engineering constraints despite the presence of the gap.

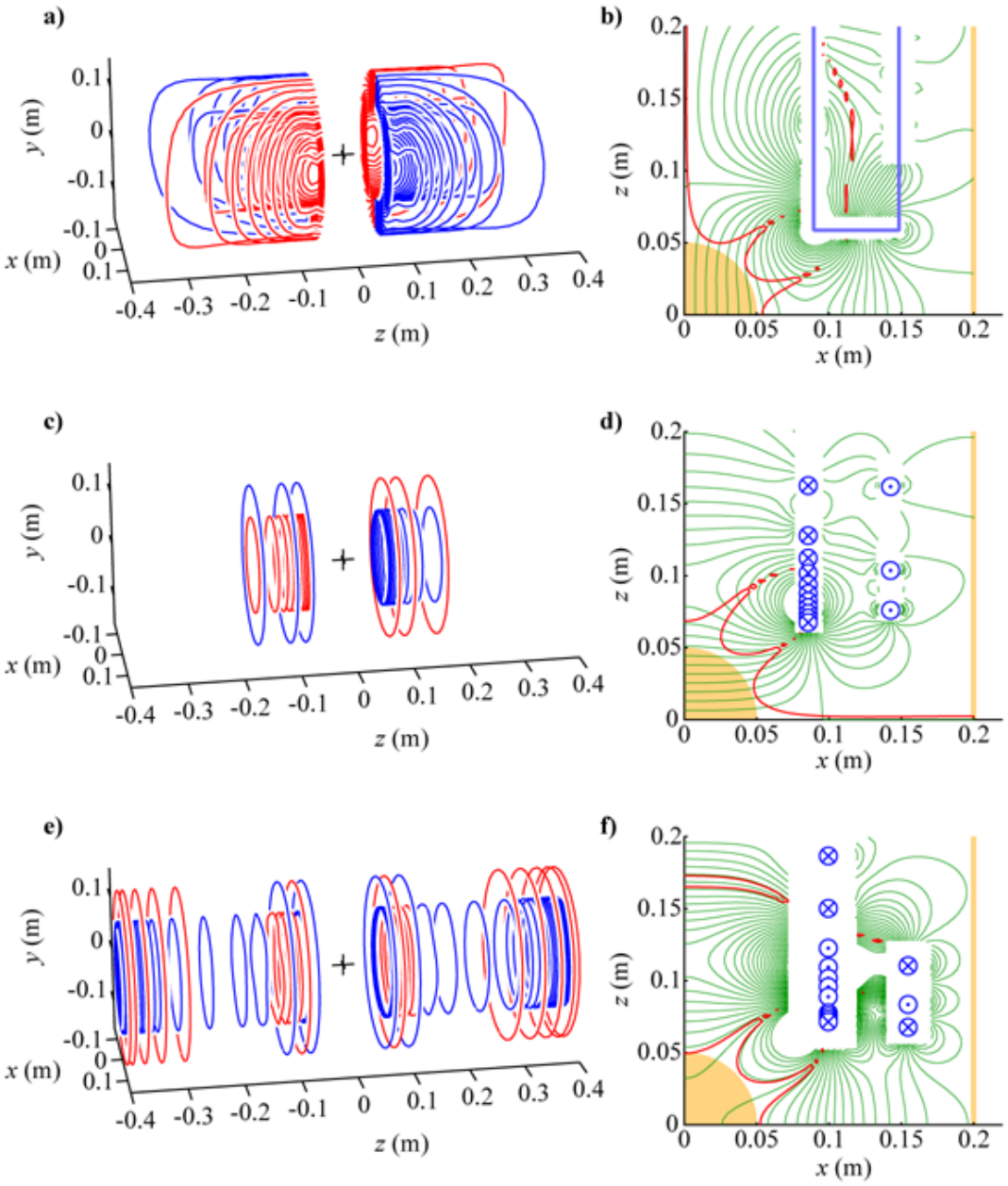

Figure 6.15: Wires of the split IBEM **a)** X- and **c)** Z-gradient and **e)** Z0 shim coil. With **b)** contours of the magnetic field generated by the coils with $5\mu\text{TA}^{-1}$ contour spacing (thin green), overlaid with the $\Delta B_z(\mathbf{r}) = 5\%$ contour (thick red) and the ROU (orange region). The primary coil surface is also shown (thick blue line) as well as the wires that cross into, $\otimes$, and out of, $\odot$, the contour plane.

Coil	Efficiency, η (μTm^{-n}A^{-1})	Self-Inductance, L (μH)	min(Δw) (mm)	FOM, η^2/L (T^{2}m^{-2n}A^{-2}H^{-1})
Z0	15.1	134 (136)	126	1.70 $\times 10^{-6}$
X	679	111 (108)	117	4.16 $\times 10^{-3}$
Y	659	127 (120)	128	3.42 $\times 10^{-3}$
Z	793	46.6 (39.8)	42	1.35 $\times 10^{-2}$

Table 6.8: η, L, FOM and min(Δw) values for the IBEM-designed shielded, split PET/MRI Z0 shim and gradient coil set. L values in brackets are simulated in FastHenry© using 3 mm (2 mm for Z0) diameter circular cross-section wire.

The annular surfaces for the X- and Y-gradient coils may be difficult to construct and the Z-gradient coil has quite a low FOM because it was not provided with an annular surface on which wires may be placed due to difficulties in building such a coil.

Coils become more difficult to design with increasing gap width. In fact, the ratio between the gap length and the coil diameter, the aspect ratio, is an important factor in dictating coil performance. The inclusion of wires on the annular surfaces permits the design of transverse gradient coils with reasonable performance. These coils are currently being constructed by Varian Inc. (Yarnton, Oxon., UK.) and will be used in the combined PET/MRI system being developed at Cambridge University [215].

In this work, the inner coil radii were intended to be approximately 80 to 90 mm. It was found that while the X- and Y-gradients had a good performance due to the primary and shield surfaces being separated by $\sim$ 60 to 70 mm, the Z-gradient coil was very poor and it was impossible to design a Z0 shim coil. Including annular surfaces in the Z and Z0 coils considerably increases the engineering complexity. The inner diameters of the coil were therefore increased (see Fig. 6.14) to reduce the aspect ratio of the gap and make it possible to design good Z-gradient and a Z0 shim coils. It is instructive to compare this aspect ratio with the loop separations of Helmholtz and Maxwell coils, § 4.3.1; it is difficult to design Z0 and Z coils with gaps larger than the loop separation of these discrete coils. This is illustrated by the complexity of the wire-paths of the Z0 shim coil, 6.15 **e)**. Such complexity arises from the fact than enough current carrying surface is not provided, but there is just enough surface here to satisfy the design constraints. A lack of surface results in an ill-conditioned system and the matrices are therefore ill-conditioned also. Such systems are highly sensitive to the input parameters, and can result in highly oscillatory solutions as seen here in the oscillatory stream-function values.

In the IBEM framework, as used in this work the shielding is achieved by forcing the

magnetic field to be as close to zero as possible over a defined region of shielding (ROS). Therefore the efficacy of shielding can only be assessed in terms of the magnetic field. In this case we quote the maximum value of the magnetic field generated over the ROS. This is not a direct measure of the effect of the eddy currents that will occur when the coils are switched, but gives some idea as to the amount of shielding achieved. The form of the magnetic field generated over the ROS is important as well as its magnitude. It is possible to model the eddy currents generated by the coils using a finite element method (FEM), but such analysis was not performed here.

6.6 Single-Layer, 3-Axis Gradient Set

Competition for space in the magnet bore is intense with the space closest to the subject being the most prized. Hughes *et al.* demonstrated that the wire-paths of X- and Y-gradient coils may be modified to occupy the same single layer [216]. The radial space needed for a 3-axis gradient coil set can be dramatically reduced by constructing the X-, Y- and Z-gradient coils on the same layer. Here we show that by segmenting a single cylindrical surface into 3 separate surfaces as shown in Fig. 6.16, one for each gradient coil, a 3-axis gradient coil set may be built on a single layer. The inevitable reduction in coil performance is assessed.

The full cylindrical surface provided for all 3 gradient coils is 1 m long and 0.5 m in diameter. The areas of this surface, S, that are assigned to the X-, Y- and Z-gradient coils are given in Eqs. (6.3) to (6.5), and shown in Fig. 6.16. The ROU is a 250 mm DSV.

$$S_X : \begin{cases} 0.05\text{m} \leq |z| \leq 0.30\text{m} \\ \pi/4 \geq |\phi| \geq 3\pi/4 \end{cases} \tag{6.3}$$

$$S_Y : \begin{cases} 0.05\text{m} \leq |z| \leq 0.30\text{m} \\ \pi/4 \leq |\phi| \leq 3\pi/4 \end{cases} \tag{6.4}$$

$$S_Z : \begin{cases} 0.30\text{m} \leq |z| \leq 0.50\text{m} \\ |z| \leq 0.05\text{m} \end{cases} \tag{6.5}$$

Figures 6.17 **a)** and **c)** shows the wire-paths for the X- and Z-gradients coils respectively (the Y-gradient is the same as the X-gradient with a $\pi/2$ rotation about the z-axis). The field that is generated by passing 1A current through the wire paths is shown in Figs. 6.17 **b)** and **d)**.

This work shows that it is possible to design a 3-axis set of gradient coils on a single layer. In the initial design, the Z-gradient coil surface spanned the region where $0.30\text{m} \leq |z| \leq 0.50\text{m}$. It proved very difficult to design a useful coil on this surface as the central gap is much greater than the Maxwell coil loop separation. Since there is often low current density close to $z = 0$ for transverse coils (see Fig. 4.9), the $|z| \leq 0.05\text{m}$ area of the surface was additionally given over to the Z-gradient coil. This extra surface makes it possible to easily design Z-gradient coils with good performance. It is also possible to design transverse gradient coils with the small surface provided for them. However, there is a significant, but not unexpected, reduction in the performance of these coils due to their severely restricted wire-path positions. When comparing these coils with an equivalent size, 3-layer gradient coil set (assuming the surface is a 1 m long, 0.5 m diameter cylinder) the efficiency, η, of the

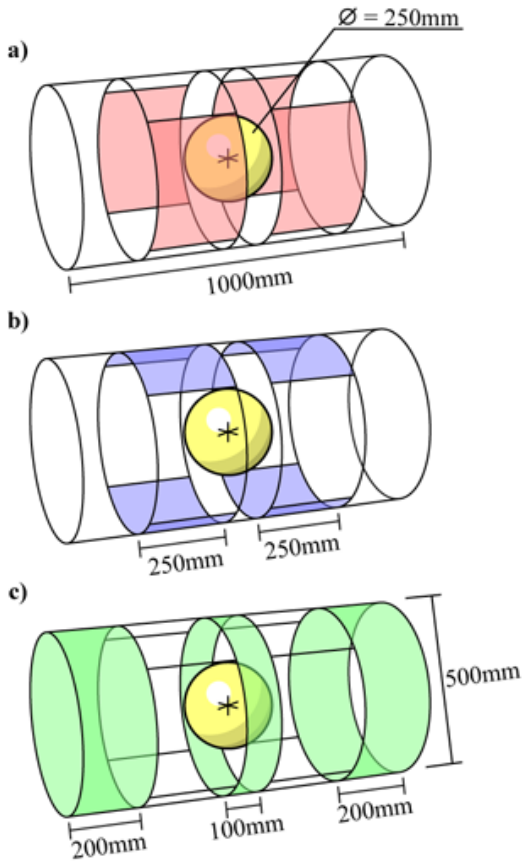

Figure 6.16: Geometry of the single-layer, 3-axis gradient coil set with the **a)** X-, **b)** Y- and **c)** Z-gradient coil surfaces highlighted.

single layer X- and Z-gradient coils is just 51.1% and 52.7% of 3-layer coils with equivalent inductances (considering a layer thickness of 4 mm, the single-layer Y- and Z-gradient have $\eta = 51.9\%$ and 54.4% of the 3-layer coil equivalents). The FOMs for the single-layer X- and Z-gradient coils are 2.3×10^{-5} and 3.4×10^{-5} $\mathrm{T^2m^{-2}A^{-2}H^{-1}}$. Z-gradient coils tend to have higher FOMs than X-gradients, given the same surface. Here, this difference in performance may be reduced by providing more of the surface for the transverse gradient coils, as long as it remains possible to design the Z-gradient coil with adequate homogeneity and minimum wire spacing.

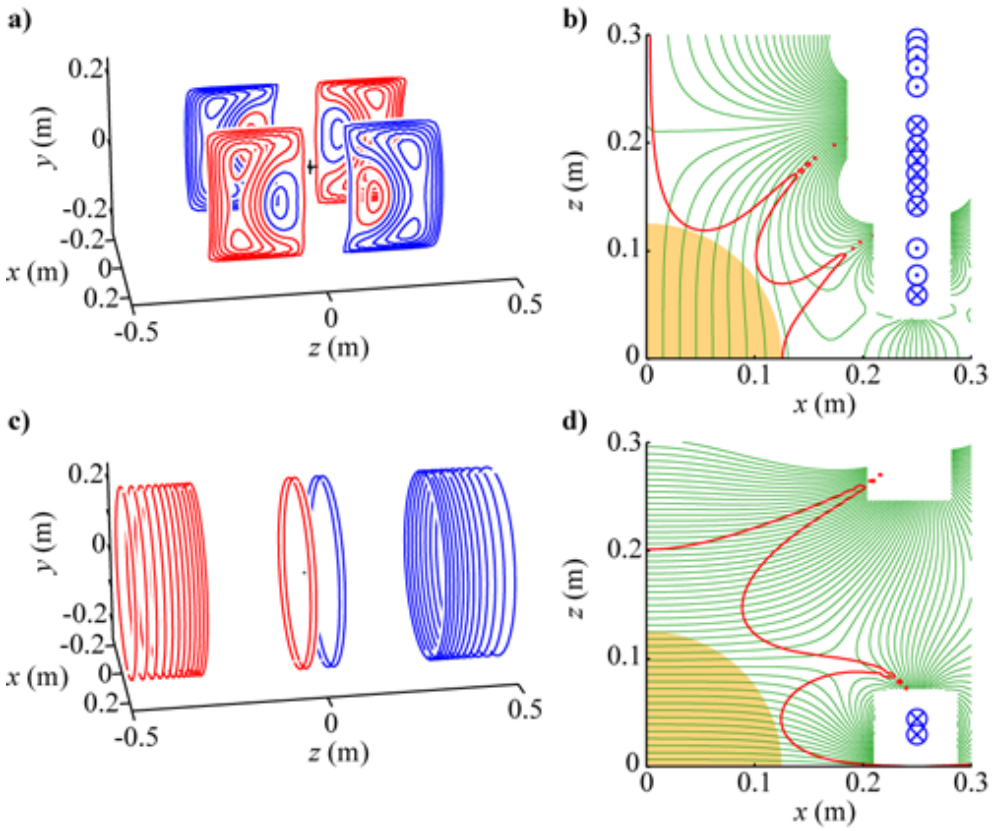

Figure 6.17: Wires of the IBEM-designed, single-layer **a)** X- and **b)** Z-gradient coils (red wires indicate reversed current flow with respect to blue) and **b)** and **d)** contours of the magnetic field generated by those coils with $1\mu\text{TA}^{-1}$ contour spacing (thin green), overlaid with the $\Delta B_z(\mathbf{r}) = 5\%$ contour (thick red) and the ROU (orange region). The wires are also shown that cross into, $\otimes$, and out of, $\odot$, the contour plane.

6.7 An Openable Z-Gradient Coil

Crozier *at al.* proposed, designed and constructed a 3-axis gradient coil set for imaging the limbs of injured patients that was "openable" [217]. The normal cylindrical shape was split in half and hinged so that it could be opened to accommodate the limbs of patients with minimum articulation and subsequently closed for imaging. Designing transverse-gradient coils for such a geometry is simple, since the anti-symmetry of the stream-function in the x-direction (y-direction for the Y-gradient coil) causes lines of $\psi = 0$ in the $x = 0$ plane. Therefore, no current passes from one half to the other. This is not the case for the Z-gradient coil. In the previous work, simulated annealing (an iterative approach § 4.4.7) was used to arrange bundles of wires on the openable coil surface.

Here, the coil described by Crozier *et al.* was initially modelled using the wire positions given in Table 1 of Ref. [217]. Using our performance metrics, § 4.2, $\eta = 588\mu\text{Tm}^{-1}\text{A}^{-1}$ with $\Delta B_z \leq 5.7\%$ over a 200 mm DSV, and $L = 234\mu\text{H}$ and $R = 192\ \text{m}\Omega$. The same surface was created for the IBEM (see Fig. 6.18), a 415 mm long, 250 mm diameter cylinder with a gap of 36 mm about the $x = 0$ plane. In a similar fashion to the approach used by Crozier *et al.* we do not include the return paths in the design process. This is achieved within the IBEM framework by removing the constant ψ boundary conditions for the edges at the gap, whilst keeping those constraints for the edges at the ends of the cylinder. The return paths are wires placed in the gap, and oriented in the z-direction which therefore do not generate B_z. Figure 6.18 shows the IBEM coil geometry where constant ψ is only imposed at the thick green edges.

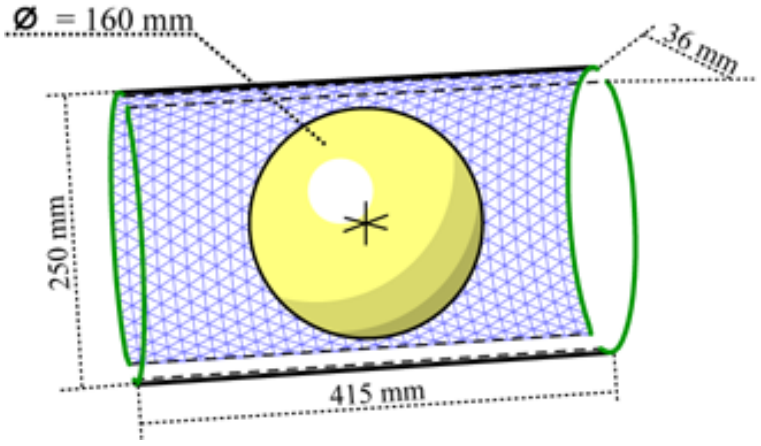

Figure 6.18: Geometry of the openable IBEM Z-gradient coil surface. The blue triangles represent one half of the discretised surface. The central sphere is the ROU.

The efficiency and inductance of the openable Z-gradient coil designed with the IBEM to the values of $560\mu\text{Tm}^{-1}\text{A}^{-1}$ and $127\mu\text{H}$, which corresponds to a 37.6% increase in η compared to the coil described in Ref. [217] for equivalent inductance and ROU size. Figure 6.19 **a)** shows the wire-paths of the openable Z-gradient coil without return paths, whilst **b)** is a contour map of the magnetic field generated in the $y = 0$ plane by passing 1 A current through the coil.

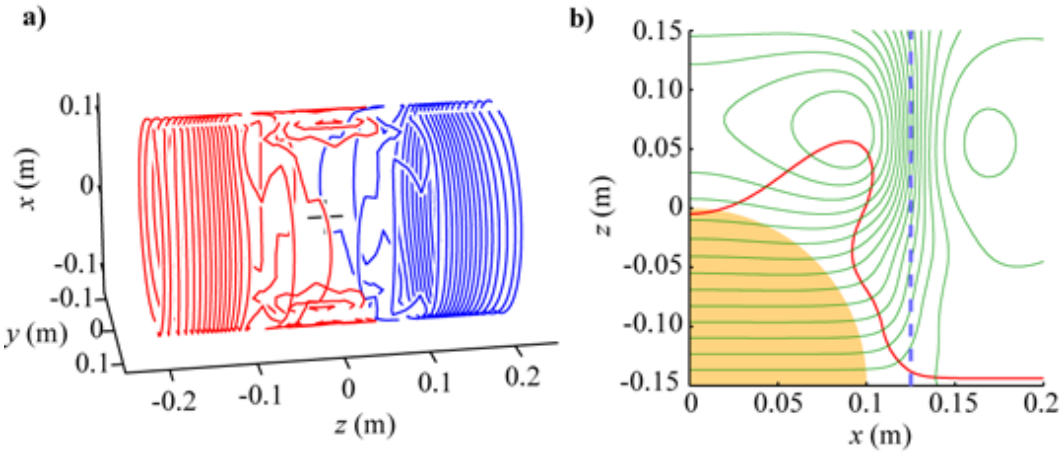

Figure 6.19: **a)** Wires of the openable IBEM-designed Z-gradient coil (red wires indicate reversed current flow with respect to blue) and **b)** contours of the magnetic field generated by the coil with $1\mu\text{TA}^{-1}$ contour spacing (thin green lines), overlaid with the $\Delta B_z(\mathbf{r}) = 5\%$ contour (thick red line) and the ROU (orange region).

This coil design example further demonstrates the versatility of the IBEM. Improved performance is obtained in the design process by omitting the constraint of constance ψ along the edges of the gap. This allows current to flow in to and out of the edges at the gap since $J_\phi = \frac{\partial \psi}{\partial z}$, and ψ may vary in z along these edges. Return paths can then be added to the design manually. It is only justifiable to omit the boundary conditions for edges that are constant in x and y, since this is the only way to ensure that the return paths are oriented axially and thus generate no B_z.

6.8 Bi-Radial Head Shim Coils

Ungersma *et al.* previously used a linear programming (LP) algorithm in conjunction with a mesh of possible wire-paths to design cylindrical shim coils with two different radii that are connected by an annular surface (Fig. 2 in Ref. [147]). By bringing the wire-paths in close to the head, such coils offer improvements in performance compared with conventional cylindrical coils. Here we simulate the field generated by a previously described coil and compare the results with those of a coil designed using the IBEM. Upon simulation, the ZY shim coil from Fig. 9 in Ref. [147] was found to have an efficiency, $\eta = 205\mu\text{Tm}^{-2}\text{A}^{-1}$, and a homogeneity $\Delta B_z \leq 47.2\%$ over a 200 mm DSV. The resistance of the coil is quoted as 0.40 Ω, and the x-component of its torque was calculated to be $T_x = -1.04$ NmA^{-1}. Using the IBEM a homogeneity of 13% is easily achieved with corresponding $\eta = 219\mu\text{Tm}^{-2}\text{A}^{-1}$, $R = 0.69\Omega$ and approximately zero torque for the coil shown in Fig. 6.20 **a)**.

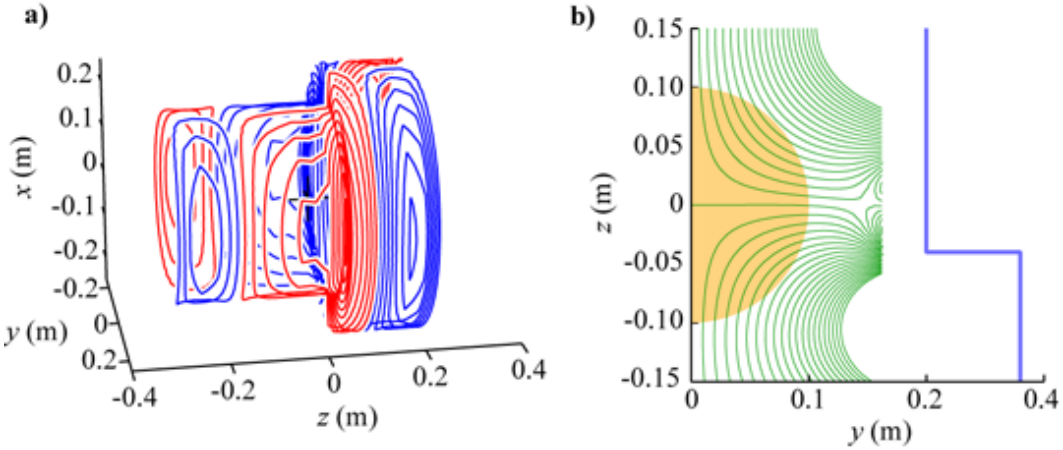

Figure 6.20: **a)** Wires of the bi-radial IBEM, XY shim coil (red wires indicate reversed current flow with respect to blue) and **b)** contours of the magnetic field generated by the coil with $1\mu\text{TA}^{-1}$ contour spacing (thin green), overlaid with the ROU (orange region). The primary coil surface is also shown (thick blue line)

This example demonstrates well the ability of the IBEM to produce a shim coil design on an asymmetric surface for a head-only MR scanner.

6.9 Retro-Fitted Gradient and Shim Shield Coils

Since the IBEM works with target magnetic field values at arbitrary, discrete points in space, it is shown here that is it possible to design active magnetic shielding coils for previously designed primary coils. A somewhat different design strategy is employed; first, we require that the shield coil generates a magnetic field in a region of shielding (ROS) that is equal and opposite to that which is generated by the primary coil, and to thereby annul that magnetic field. Here, the ROS is the surface of the cold-shield of the superconducting magnet cryostat on which eddy-currents are commonly generated. Since the shielding coil generates a magnetic field that is opposite to that of the primary in the ROS, the magnetic field generated in the ROU is likely to be similar in form but opposite in sign to the magnetic field the primary coil generates there. Therefore, we aso require that the magnetic field generated in the ROU is minimal and must have the same spatial variation to that of the field which the primary coil generates to within a specified accuracy; the shield is permitted to alter the magnetic field in the ROU as long as it does so in such a way as to retain a specified degree of homogeneity. Here, our primary coil generates a magnetic field in the ROU that has a maximum inhomogeneity of 5%.

6.9.1 Optimistion Functional

The functional used to design retro-fitted shield coils is different to that used to design the other coils in this chapter. It allows the magnetic field in one region to be finite as long as it is minimal and of a specified shape. The new functional, U, is

$$\begin{aligned} U &= \frac{1}{2}\sum_{k=1}^{K} W(\mathbf{r}_k)\left(B_{zS}(\mathbf{r}_k)+B_z^P(\mathbf{r}_k)\right)^2+\frac{1}{2}\sum_{j=1}^{J} W(\mathbf{r}_j)\left(B_{zS}(\mathbf{r}_j)+CB_z^P(\mathbf{r}_j)\right)^2 \\ &\quad +\frac{\alpha}{2}\sum_{n=1}^{N}\sum_{m=1}^{N} I_n I_m L_{mn}+\frac{\beta}{2}\sum_{n=1}^{N}\sum_{m=1}^{N} I_n I_m R_{mn} \\ &\quad -B_0\sum_{p=1}^{P}\lambda_{px}\sum_{n=1}^{N}\delta_{n\in p}I_n\int_S f_{nx}z\,dS-B_0\sum_{p=1}^{P}\lambda_{py}\sum_{n=1}^{N}\delta_{n\in p}I_n\int_S f_{ny}z\,dS \\ &\quad +B_0\sum_{p=1}^{P}\lambda_{pz}\sum_{n=1}^{N}\delta_{n\in p}I_n\int_S (f_{nx}x+f_{ny}y)\,dS \end{aligned} \tag{6.6}$$

where k ($k=1,\ldots,K$) are indices of target magnetic field points that lie in the ROS, and j ($j=1,\ldots,J$) are the indices of points in the ROU of the primary coil. Therefore,

$B_z^P(\mathbf{r}_k)$ is the magnetic field at a point $\mathbf{r}_k$ in the ROS generated by the primary coil and used here as the target magnetic field for the shield coil design. $B_z^P(\mathbf{r}_k)$ is the magnetic field that the shield coils generates in the ROS. C is a free parameter of the system identified during functional minimisation that scales the target field in the ROU to its optimum. All other symbols in Eq. (6.6) have the same meaning as those described in § 5.2.8. The minimum of U is found by differentiation with respect to the basis-function weights, I_n, the torque Lagrange multipliers, $\tilde{\lambda}_p$ and C, i.e. $\frac{\partial U}{\partial I_n}$, $\frac{\partial U}{\partial \tilde{\lambda}_{px}}$, $\frac{\partial U}{\partial \tilde{\lambda}_{py}}$, $\frac{\partial U}{\partial \tilde{\lambda}_{pz}}$, and $\frac{\partial U}{\partial C}$. The resulting simultaneous equations can be recast in the form of a matrix equation as before (Eq. (5.49)) which is composed of smaller matrices and vectors

$$\underbrace{\begin{bmatrix} \begin{pmatrix} \ddots & \dots & \cdot \\ \vdots & A & \vdots \\ \cdot & \dots & \ddots \end{pmatrix} \begin{pmatrix} \vdots \\ B \\ \vdots \end{pmatrix} \begin{pmatrix} \vdots \\ -T_{pA} \\ \vdots \end{pmatrix} \begin{pmatrix} \vdots \\ -T_{pB} \\ \vdots \end{pmatrix} \begin{pmatrix} \vdots \\ T_{pC} \\ \vdots \end{pmatrix} \\ (\dots \; B \; \dots) \quad D \quad 0 \quad 0 \quad 0 \\ (\dots \; T_{pA} \; \dots) \quad 0 \quad 0 \quad 0 \quad 0 \\ (\dots \; T_{pB} \; \dots) \quad 0 \quad 0 \quad 0 \quad 0 \\ (\dots \; T_{pC} \; \dots) \quad 0 \quad 0 \quad 0 \quad 0 \end{bmatrix}}_{\mathbb{Z}} \underbrace{\begin{bmatrix} \begin{pmatrix} \vdots \\ I_n \\ \vdots \end{pmatrix} \\ C \\ \tilde{\lambda}_{px} \\ \tilde{\lambda}_{py} \\ \tilde{\lambda}_{pz} \end{bmatrix}}_{\mathbf{I}} = \underbrace{\begin{bmatrix} \begin{pmatrix} \vdots \\ E \\ \vdots \end{pmatrix} \\ 0 \\ 0 \\ 0 \\ 0 \end{bmatrix}}_{\mathbf{b}} \tag{6.7}$$

where

$$A = \sum_{k=1}^{K} W(\mathbf{r}_k) c_m(\mathbf{r}_k) c_n(\mathbf{r}_k) + \sum_{j=1}^{J} W(\mathbf{r}_j) c_m(\mathbf{r}_j) c_n(\mathbf{r}_j) + \alpha L_{mn} + \beta R_{mn}, \tag{6.8}$$

$$B = \sum_{j=1}^{J} W(\mathbf{r}_j) c_m(\mathbf{r}_j) B_z^P(\mathbf{r}_j), \tag{6.9}$$

$$D = \sum_{j=1}^{J} W(\mathbf{r}_j) (B_z^P(\mathbf{r}_j))^2 \tag{6.10}$$

and

$$E = \sum_{k=1}^{K} W(\mathbf{r}_k) c_m(\mathbf{r}_k) B_z^P(\mathbf{r}_k). \tag{6.11}$$

6.9.2 Geometry

The geometry of this system is based on the shoulder-slotted coils described in § 6.1. The central ROU is a 160 mm DSV, and the ROS is formed from the inner surface of the cold shield of the cryostat of an MRI scanner, for which we use is a 1.2 m long, 0.9 m diameter cylinder. The shielding surface is also formed from a 1.2 m long cylinder with a 0.55 m diameter.

6.9.3 Results

The magnetic field that the shoulder-slotted X-gradient coil, (shown in Fig. 6.2 **b)**), generates with 1 A current is calculated over the ROU and the ROS, at a total of $K + J = 544 + 265 = 809$ points. This was used as the target magnetic field for the design of a coil on the shielding surface that maximally annuls the magnetic field in the ROS whilst minimally increasing $\Delta B_z^{\mathrm{ROU}}$ and minimally reducing the efficiency, η of the combined coil. The original X-gradient coil is shown in Figs. 6.21 **a)** for comparison with its separately designed shield coil **c)**. The magnetic field that the combined coil generates is shown in the contour plot depicted in Fig. 6.21 **b)** and **d)** is the magnetic field along the line $x = 0.45$ m, $y = 0$ m, -1 m$\leq z \leq 1$ m on the cold shield generated by the primary, shield, and combined coil with 1 A current.

The maximum magnetic field in the ROS is just 0.094 $\mu\mathrm{TA}^{-1}$ compared with 1.8 $\mu\mathrm{TA}^{-1}$ for the unshielded coil; a reduction of 95%. The residual magnetic field on the shield is a result of the low number of windings on the shielding surface.

As a result of adding the shield the efficiency of the X-gradient coil is reduced to 70.2 $\mu\mathrm{Tm}^{-1}\mathrm{A}^{-1}$ from 100.0$\mu\mathrm{Tm}^{-1}\mathrm{A}^{-1}$, the homogeneity in the ROU is marginally improved from 5.0% to 4.6 %, the inductance increased from 63.7 μH to 75.2 μH and the resistance is also increased from 80 mΩ to 159 mΩ.

6.9.4 Discussion

We have shown here that it is possible to design shield coils for gradient coils (equally valid for shim coil) that maximally reduce the stray magnetic fields in a given region whilst minimally affecting the magnetic field gradient in the ROU. The radial placement of the shield coil is of vital importance. The closer it is to the primary, the more it will detrimentally affect the gradient field as well as the combined coils inductance and resistance. However, placing the shield coil close to the shielding region will cause difficulties with the discretisation of the system; many target points will be required for the ROS to prevent the shield coil annulling the magnetic field at each target point individually. Also, placing the shield

further from the primary coil will mean that less wires will be needed in the shield coil. Less wires may represent the continuous current density on the surface poorly and lead to inefficient shielding. This is shown somewhat in Fig. 6.21 **d)** where the magnetic field at the shielding surface (green line) is not entirely cancelled due to the lack of wires in the $z \approx -0.15$ m region of the shield coil.

Considerably better shielding may be achieved with more windings and proportionally lower current in the shield coil, but this is not desirable since either the two coils must be driven with different amplifiers or connected in parallel so as to split the currents appropriately. Accurately calibrating the amplifiers to generate synchronous and correctly scaled currents in two different coils is not straightforward and adds to the cost of the gradient systems. The two coils are inductively coupled so that driving them in parallel means when switching the gradient energy may be transferred from one to the other and circulating currents may be introduced in the parallel circuit.

In the shield coil shown in Fig. 6.21 **c)** several loops of current with alternating sense are present at both ends of the coil. This is likely to be a consequence of the difference in lengths of the primary coil and the shielding surface and ROS. The fall-off of the magnetic field in the ROS from the primary coil is difficult to mimic at the increased radius of the shield coil. These extra loops ensure that the magnetic field is maximally annulled at $|z| > 0.4$ m.

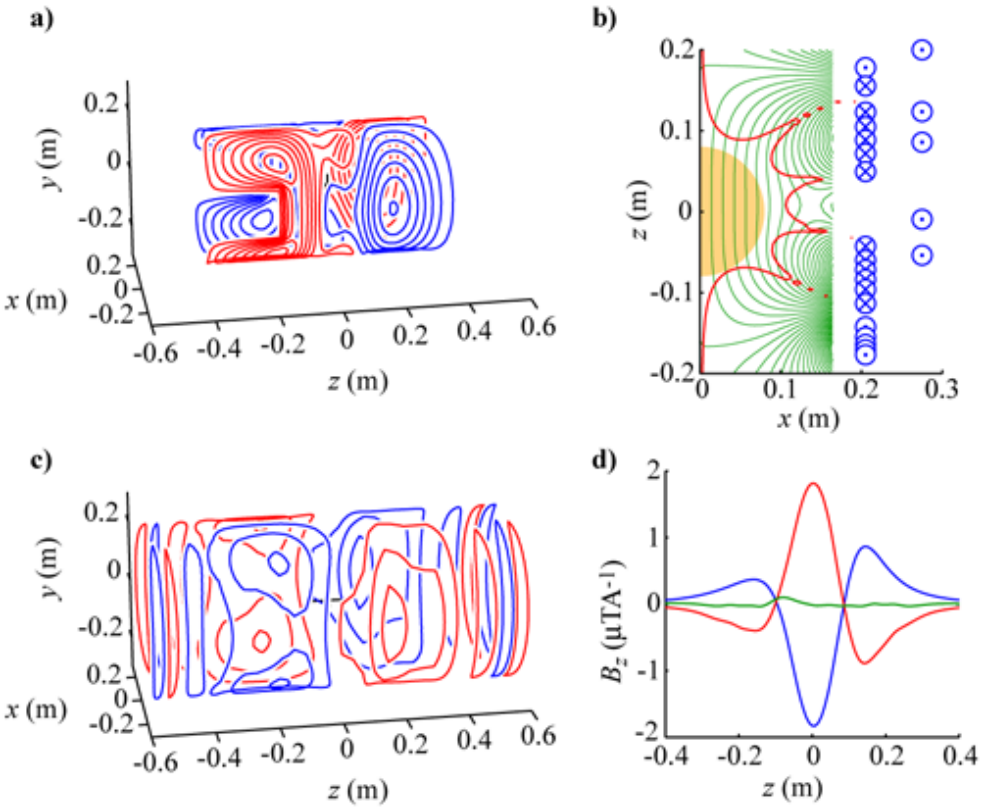

Figure 6.21: Wires of IBEM, shoulder-slotted **a)** X-gradient and **c)** its separately-designed shield coil (red wires indicate reversed current flow with respect to blue) and **b)** contours of the magnetic field generated by the combined coil with $1\mu\text{TA}^{-1}$ contour spacing (thin green lines), overlaid with the $\Delta B_z(\mathbf{r}) = 5\%$ contour (thick red line) and the ROU (orange region). The wires are also shown that cross into, $\otimes$, and out of, $\odot$, the contour plane. **d)** The magnetic field generated by the primary (dashed blue line), shield (dotted red line) and combined (solid green line) along a line $x = 0.45$ m, $y = 0$ m in the ROS.

6.10 Multiple Region Gradient Coils

Some MR techniques require rapidly switched, very strong magnetic field gradients which can cause magnetostimulation of nerves [218, 219]. One proposed solution is to reduce the maximum intensity of the magnetic field produced by the gradient coil in order to lower $\frac{\partial \mathbf{B}}{\partial t}$ which dictates the magnitude of $\mathbf{E}$, the source of magnetostimulation [220]. One way that this can be achieved is by employing coils that generate a magnetic field gradient in multiple regions [220, 221]. Figure 6.22 shows that the IBEM method is capable of designing such coils by reproducing the multiple region Z-gradient coil for which the results are given in Fig. 10 of Ref. [220]. The magnetic field generated by passing 1 A current through a conventional Z-gradient coil is represented by the blue line in Fig. 6.22 **b)**, and the red line is the magnetic field generated by passing 0.504 A through the wire-paths in **a)**. Lower current in the multiple region coil is used to generate the same modulus of the gradient of the magnetic field in the two ROUs as is produced by the conventional Z-gradient coil. The maximum magnetic field generated along the z-axis by the two-region Z-gradient coil is 52% of the maximum generated by the conventional Z-gradient coil.

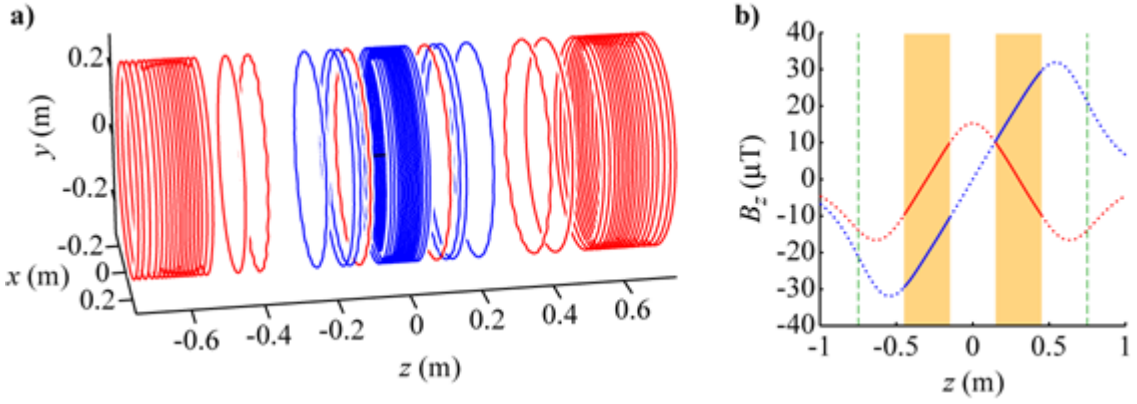

Figure 6.22: Wires of the IBEM, multiple-region **a)** Z-gradient coil (red wires indicate reversed current flow with respect to blue) and **b)** the magnetic field generated along the z-axis by 1 A in a conventional Z-gradient coil (blue line) and by 0.504 A in the multiple-region Z-gradient coil (red line). The orange regions are the ROUs and the extent of the coils is shown by the green dashed line at $|z| = 0.8$ m.

6.11 Shim Coils with PCA-Derived Basis Set

MR scanners are generally equipped with a set of shim coils (see § 4.3.2) each of which individually generates a spherical harmonic-shaped (§ 2.2) magnetic field in the ROU. This is a convenient orthogonal basis set for spherically, and cylindrically symmetric systems. In combination, shim coils can be made to generate magnetic fields of any shape, that can be described by low spatial frequencies. To correct for high spatial frequency components of the magnetic field inhomogeneity, more shim coils generating higher order harmonics need to be provided, which becomes difficult due to space restrictions within the bore of the magnet and because the efficiency of shim coils decreases with increasing order. Typically, the magnetic field generated by susceptibility differences of tissues contain significant amounts of spherical harmonics up to and above 10^{th} order. It is impractical to have a 10^{th} order shim set since this would require a total of 121 separate shim coils with the 10^{th} order coils being uselessly weak. The strength of high order shim coils can be dramatically increased by reducing their radius since the coil efficiency scales with radius, a, as $\eta \propto a^{-(n+1)}$. Dynamic shimming [66–68] (§ 3.2.6) has been shown to be more effective at mitigating these susceptibility-induced magnetic field inhomogeneities. The most significant problems occur in the inferior part of the frontal cortex superior to the ethmoid and sphenoid sinuses, and in the temporal lobe superior to the auditory air spaces. Parcellated dynamic shimming is a concept that is shown by simulation in the next chapter to be even more effective [222, 223]. Other methods have been proposed to locally shim the common problem areas with pieces of material with large positive or negative susceptibilities placed near to those areas [71–73, 224] (see § 3.2.7).

6.11.1 Principal Component Analysis

Here we turn to a different orthogonal set of basis-functions for decomposing the susceptibility-induced magnetic field inhomogeneity inside the head which is is based on the common features of head-induced field variation in a small subject group. Since this field is not very symmetric (the main symmetry is in the x-direction, running from left to right) an arbitrary-shaped decomposition is obtained here by principal component analysis (PCA). PCA projects a data set into a new coordinate system where the first coordinate has the largest variance of the data set and the second coordinate has the largest variance uncorrelated to the first component *etc.* In this way the principal component of the data contains the "most important aspect" of all the data.

Consider a matrix $\mathbb{B}$ comprising the vectors $\mathbf{B}_i$ where $i = 1, \ldots, N$

$$\mathbb{B} = [\mathbf{B}_1, \ldots, \mathbf{B}_i, \ldots, \mathbf{B}_N], \tag{6.12}$$

where $\mathbf{B}_i$ is the 3D, masked magnetic field data of the i^{th} subject re-ordered into a vector. Therefore, $\mathbb{B}$ is an $M \times N$ matrix where M is the number of magnetic field data points per subject, and N is the number of subjects. The singular value decomposition (SVD) of $\mathbb{B}$ is

$$\mathbb{B} = \mathbb{U}\mathbb{S}\mathbb{V}^T \tag{6.13}$$

where $\mathbb{S}$ is a matrix containing a vector of the positive, non-increasing singular values, $\mathbf{s}$, of $\mathbb{B}$ along the diagonal with all other elements equal to zero. If $\mathbb{B}$ is real then $\mathbb{U}$ and $\mathbb{V}$ are both orthogonal matrices ($\mathbb{U}\mathbb{U}^T = \mathbb{I}$ and $\mathbb{V}\mathbb{V}^T = \mathbb{I}$ where $\mathbb{I}$ is the identity matrix). $\mathbb{V}$ contains the orthonormal basis vector directions of $\mathbb{B}$ which are the normal vectors of the principal components. $\mathbb{U}$ contains orthonormal vectors that give the normalised position of each column of $\mathbb{B}$ in the new coordinate system. For square matrices, the SVD reduces to the Eigenvalue decomposition where $\mathbb{V}^T = \mathbb{U}^T$ such that $\mathbb{B} = \mathbb{U}\mathbf{s}\mathbb{U}^T$, and $\mathbf{s}$ is a vector of the eigenvalues.

Here, the SVD is used to obtain the first J principal components, $\mathbf{Y}_j$ ($j = 1, \ldots, J$) of N field maps $\mathbf{B}_i$ ($i = 1, \ldots, N$) by multiplying the first J singular values the by first J basis vector directions

$$\mathbb{Y}_J = \mathbb{S}_J \mathbb{V}_J^T \tag{6.14}$$

where $\mathbb{Y}_J = [\mathbf{Y}_1, \ldots, \mathbf{Y}_j, \ldots, \mathbf{Y}_J]$.

The principal component vectors $\mathbf{Y}_j$ can be reshaped back into 3D to the same space as inhabited by the original magnetic field data. The first J principal components can then be used as the target magnetic field variation in the design of J PC shim coils.

6.11.2 PCA Results

11 subjects were scanned with the 2-echo, gradient echo field mapping sequence described in § 2.5.10. The phase data from the 2 echoes were unwrapped using a region-growing phase unwrapping algorithm [225], and subtracted from one another to obtain ppm-scaled magnetic field maps. The skulls were stripped from the modulus data using the brain extraction tool (BET) [226], and the resulting skull-stripped head data were used to generate masks to be applied to the magnetic field maps. The masks were also used to approximately align the field map data across subjects. An iterative approach (a least-squares, nonlinear

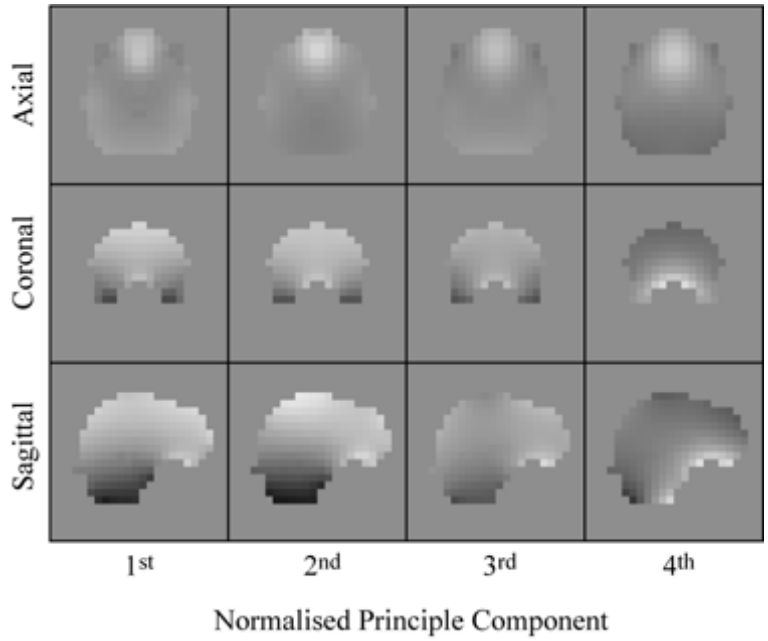

Figure 6.23: Axial, coronal and sagittal slice images of the magnetic field variation of the 1^{st} 2^{nd} 3^{rd} and 4^{th} normalised principal components shown in slices that intersect the large magnetic field deviation above the nasal sinus.

optimisation using the `lsqnonlin` function in Matlabs® Optimisation Toolbox) was taken to translate the masks in the x-, y- and z-directions such that the sum of the product of each mask with the first mask was maximised. It is reasonable to expect that any asymmetry in the x-direction (left to right) would diminish with increasing number of subjects used as sample magnetic field data. To eliminate any asymmetry in the x-direction the magnetic field maps were forced to be symmetric by averaging with field maps reflected in the x-direction.

Principal component analysis was then used to obtain the first 4 principal components. Figure 6.23 shows the normalised magnetic field maps corresponding to the first 4 principal components and Fig. 6.24 shows the scalings of the components that best approximate the magnetic field field for each subject.

6.11.3 PC Shim Coil Design Results

Figure 6.25 shows the wire-paths of the shim coil that is designed to generate the 1^{st} principal component. The root-mean-squared (RMS) difference between the target magnetic field (shown in Fig. 6.23) and the field generated by this coil is 0.12 μTA^{-1}, which is 2.2% of the

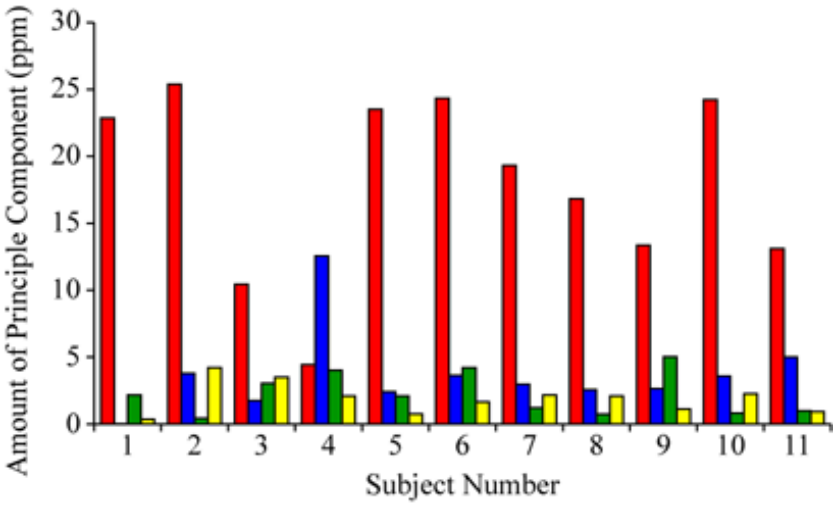

Figure 6.24: Graph of the amount of the first 4 normalised principal components present in each of the subjects. Red, blue, green and yellow bars represent the 1^{st} 2^{nd} 3^{rd} and 4^{th} principal components respectively.

range from maximum to minimum magnetic field values in the ROU. The wire-paths for the other three principal component shim coils are omitted for brevity, however the RMS field errors for the 2^{nd} 3^{rd} and 4^{th} PC coils are 0.11, 0.17 and 0.14 μTA^{-1}, which are 2.5%, 1.7% and 3.2% of the range of magnetic field from maximum to minimum in the ROU.

6.11.4 PC-Based Shimming Results

The first four PC shim coils were designed (the first is shown in Fig. 6.25) and the magnetic field over the ROU calculated using Biot-Savart summation over the wire-paths. Shimming was simulated for the field maps of the 11 subjects with 4 PC shim coils, 4 spherical harmonic (SH) shim coils, and with 4 PC and 4 SH shim coils. This was performed in Matlab® by pseudoinverting a matrix containing vectors of the field of each shim coil $\mathbb{A}$ (where $\mathbb{A} = [\mathbf{A}_1, \ldots, \mathbf{A}_k, \ldots, \mathbf{A}_K]$, and $\mathbf{A}_k$ is the magnetic field of the k^{th} shim coil $k = 1, \ldots, K$) and multiplying by the vector of the magnetic field in the head of each subject $\mathbf{B}_i$, $\mathbf{I} = \mathbb{A}^{\dagger}\mathbf{B}_i$, where $\mathbf{I}$ is a vector of the amount of current needed in each shim coil to minimise $||\mathbb{A}\mathbf{I} - \mathbf{B}_i||_2$. The RMS residual magnetic field for each shimming regime is given in Fig. 6.26.

The effect of changing the axial position of the head relative to the PC shim coils was investigated by simulating the shimming as described above for a range of offset z-positions from -50 mm to +50 mm. Figure 6.27 shows the variation of the RMS residual field with

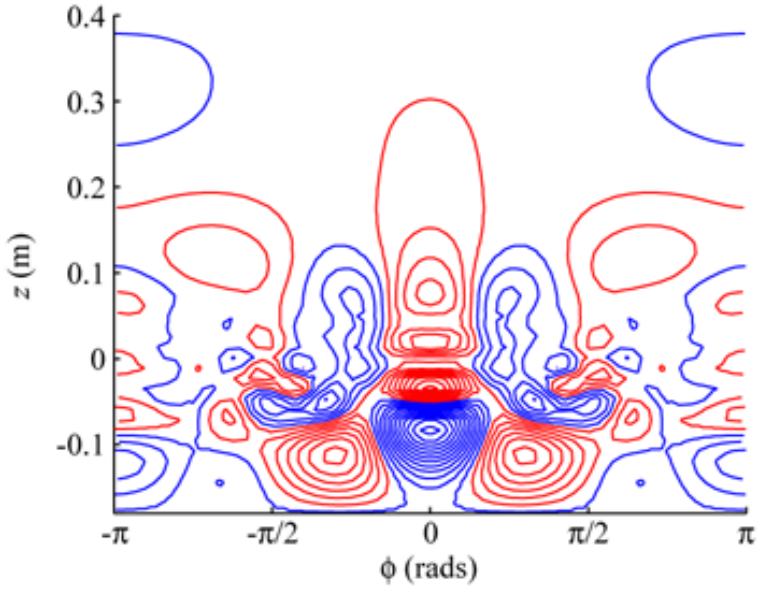

Figure 6.25: Wires of the 1st principal component shim coil (red wires indicate reversed current flow with respect to blue).

offset position for shimming with the 4 PC coils, the 4 SH coils, and all 8 shim coils in combination.

6.11.5 Discussion

Here we have shown that is is possible to derive a new basis set for shimming the magnetic field inside the head. This basis set is obtained directly from field maps taken from a sample of subjects, and reflects the common shape of the magnetic field inhomogeneities. Singular value decomposition is used to obtain the principal components of the field of the subjects in the sample. The sample consisted of 11 volunteers, which is a small number but sufficient to demonstrate the feasibility of this concept. A considerably larger, and more varied sample of subjects would provide a more inclusive set of principal components. For a larger sample size it may be necessary to use a greater number of basis functions in order to be able to accurately reproduce the magnetic field distributions in most of the population.

It can be seen from Fig. 6.24 that the 1st principal component is dominant in all but one of the magnetic field maps of the subjects. In subject 4 there is a larger contribution from the 2nd principal component. This indicates that the magnetic field distribution in subject 4 was substantially different from the rest of the sample, and illustrates the need for a larger sample size. Here we tried to mimic the effect of a larger sample size by making

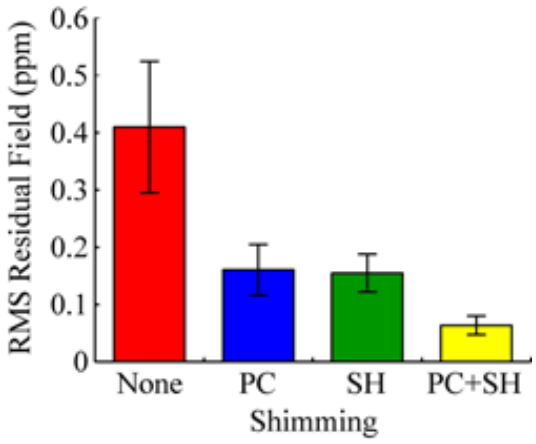

Figure 6.26: Graph of the RMS residual magnetic field of all subjects with no simulated shimming, shimmed with 4 principal component shim coils, 4 spherical harmonic shim coils (Z0, X, Y and Z) and all 8 shim coils. The error bars indicate the standard deviation over the 11 subjects.

the field maps symmetric in x. Over many subjects, any left-right asymmetry may tend to disappear. It also has the effect of making the resulting coils potentially more simple to build.

The geometry, and in particular the scale, of the surface provided on which to design these coils is of primary importance. The coil shown in Fig. 6.25 was designed on a 240 mm diameter cylinder. This may not be large enough to fit 100% of people inside, however it is essential to get the surface of this coil as close to the head as possible. One way of improving these coils would be to generate a far more closely fitting mask capable of accommodating a large variety of head shapes whilst remaining as close to the head as possible. In most MR scanners the RF coil tends to occupy the closest radial region to the head, so its presence must also be considered.

The wire-paths of the 1$^{\text{st}}$ PC shim coil (Fig. 6.25) form a highly complicated pattern. This is because the target magnetic field contains significant amounts of high spatial frequency components. To generate these high spatial frequencies, even more high spatial frequencies must be present in the stream-function of the surface current density. This is because the field from a wire falls off with an inverse relation to distance. This need for higher spatial frequencies in the coil than in the ROU is mathematically illuminated by the central equation in the target field coil design method, Eq. (4.11). The Fourier transform of the current density, $j_\phi^m(k)$, is multiplied by modified bessel functions, $K'_m(|k|a)I_m(|k|\rho)$, to obtain the Fourier transform of the magnetic field variation in the ROU. The two Bessel

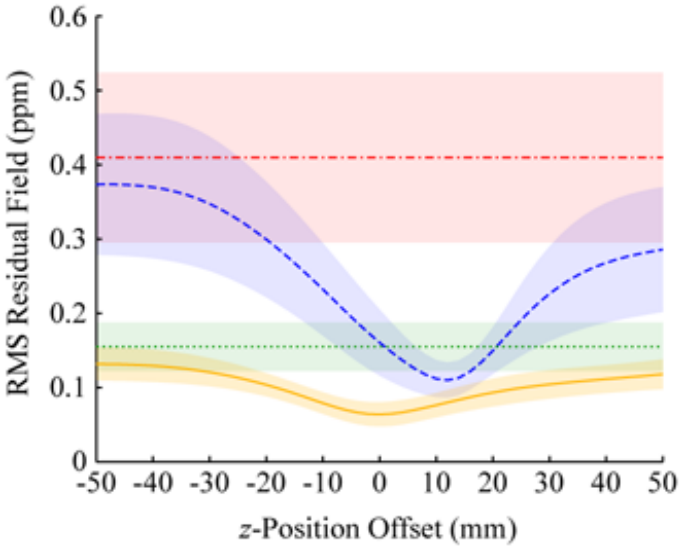

Figure 6.27: Graph of the RMS residual magnetic field of 11 subjects with no simulated shimming (red dash-dotted line), shimmed with 4 principal component shim coils (blue dashed line), 4 spherical harmonic shim (green dotted line) coils (Z0, X, Y and Z) and all 8 shim coils (orange solid line). The shaded regions indicate the standard deviation over the 11 subjects.

functions tend to zero for large arguments, and therefore reduces the intensity of high spatial frequency components. This means that there will always be less high spatial frequency components in the magnetic field than in the current density. It is therefore also the case that to represent a desired target magnetic field, there must be higher spatial frequencies in the current density that generates it. The further the current carrying surface is away from the ROU, the larger this effect becomes.

There is a clear improvement in the magnetic field homogeneity when shimming the 11 subjects with 4 spherical harmonics. This indicates that the field maps were obtained under poor shim conditions. The PCA was performed on these maps despite the presence of linear gradients in the magnetic field inhomogeneity. The results presented in Fig. 6.26 show that when PC shim coils are used in conjunction with the SH shim coils significant improvement in magnetic field homogeneity is achieved. MR scanners are capable of shimming by adjustment of the linear gradient waveforms, so it may be beneficial to remove any linear gradients from the magnetic field maps before the PCA. That way the shimming basis set will be a hybrid, spherical harmonic, and principal component basis set. This may also be extended to 2^{nd} order spherical harmonics.

Figure 6.27 shows the relationship between the efficacy of shimming with respect to an offset z-positioning of the shim coils relative to the head. Over a range of about 20 mm about the optimum position ($\sim +12$ mm offset) shimming with the PC shim coils significantly outperform the SH shim coils. For z-direction misalignments outside of this range, shimming with the SH shim coils is more effective than shimming with the PC shim coils. More importantly however, the shimming efficacy can only ever be improved by using the PC shim coils in combination with the SH shim coils, providing that the calculation of the shim currents is performed in a numerically robust fashion (*i.e.* using a pseudoinversion fitting technique).

6.12 2D MAMBA Coils

This example describes the design of a coil for use with the multiple acquisition with the Micro B_0 Array (MAMBA) technique [202, 203]. Implementation of MAMBA requires a coil which generates multiple regions of uniform magnetic field within the imaging volume. The magnetic field strengths are different within each of these regions, usually following a stepped profile across the imaging volume. Image data can thus be acquired simultaneously from the different regions. Lee *et. al.* [227] developed a target field method for designing the coils needed for this novel imaging technique, and here we show that the IBEM is capable of designing MAMBA coils with the same biplanar geometry as Lee *et.al.* which have highly asymmetric magnetic field requirements (see Fig. 6.28 (c)). The 16 distinct target regions are each composed of a 6×6 grid of target points, and the magnetic field in these regions is required to vary in 1 mT steps from -7 mT to +8 mT. There are 5200 triangular elements and 2746 nodes in the discretised surface.

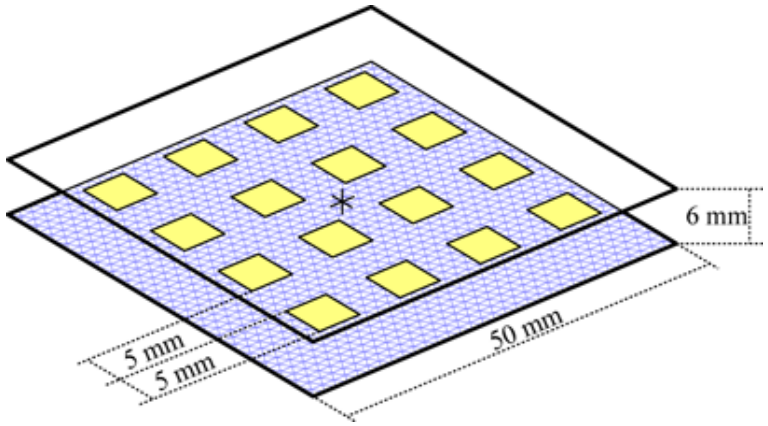

Figure 6.28: Geometry of a 4×4 region 2D MAMBA array coil surface. The blue triangle are the elements of the lower half of the surface, and the yellow squares represent the positions of the ROUs.

To compare with the coil in the original paper, a 2D MAMBA coil was designed to have an average field error (using Eq. (6.15), from Eq. 16 in Ref. [227]) of $b \leq 1.9\%$.

$$b = \frac{|\Delta B|_{\text{mean}}}{1\text{mT}} \times 100\% \tag{6.15}$$

Only power minimisation was employed with 66 contours of the stream function chosen so as to give at least 1 mm spacing between the closest wires. With this coil, only 21 A are needed to generate the same 1 mT step field, 48 A less. The wire paths for one of the

two identical plates of the 2D MAMBA coil is shown in Fig. 6.29 **(a)**, and **(b)** shows the magnetic field generated when 21 A flows in the coils on both plates in the $z = 0$ plane.

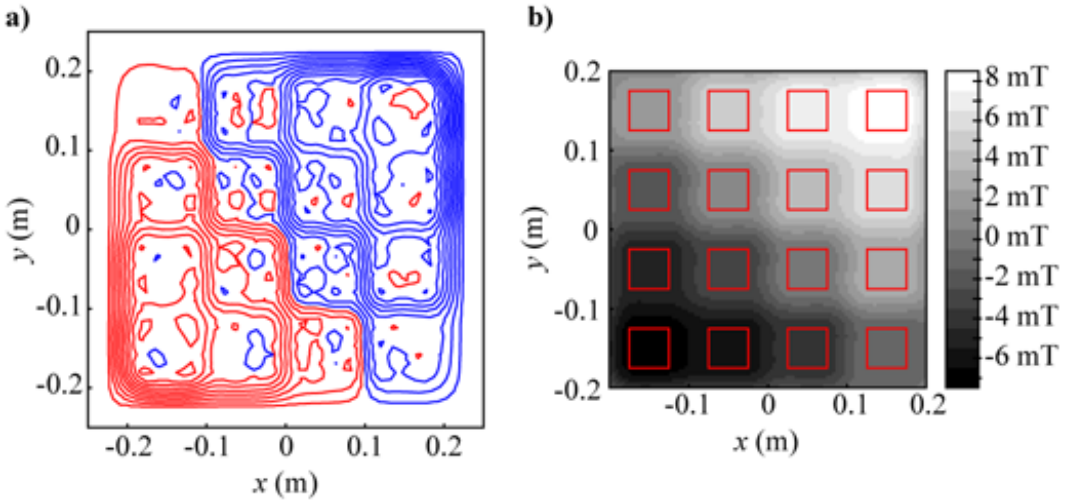

Figure 6.29: **a)** Wires of the IBEM 2D MAMBA coil (red wires indicate reversed current flow with respect to blue and only every other wire is shown) and **b)** the magnetic field generated by 21 Amps in the coil with 1mT contour spacing, overlaid with the the ROUs (red squares).

It is unlikely that the final coil built in Ref. [227] will be capable of producing an average magnetic field error of less than 1.9%. If β, the resistance minimisation parameter, is increased in this design, the ΔB_z will increase but less current would be required for the same field strength, and the wire-paths would become less complex.

6.13 Discussion

The shoulder-slotted insert gradient and shim coil set presented in § 6.1 is the first practical example of the IBEM, and it is one that is fully worked from concept to production. 2D meshing software was employed to generate the meshes which were converted to 3D by employing cylindrical coordinates. Because of this meshing method the circular boundary condition in ϕ needs to be enforced by making the nodes on the $\phi = \pm\pi$ boundaries the same and by assigning adjacent elements from either side of the $\phi = \pm\pi$ divide to these nodes. This meshing method may be responsible for some small reduction in the performance of these coils over the newer meshing techniques. 3D Studio MAX® (Autodesk®, Inc., San Rafael, CA, USA) was used to generate the meshes for all the other examples in this section, as it provides an intuitive 3D interface, and complete control over the elements and nodes of the surface, without which it would be extremely difficult to build the meshes for the non-cylindrical and complicated coil geometries addressed in other sections of this chapter.

The results obtained from measuring the magnetic field that the coils generate with a magnetometer agree very well (values are all within 5% and most are ∼1% different) with Biot-Savart integration over the wire-paths generated by the IBEM. The efficiency is increased by reducing the radii of the coils, but this is partially mitigated by the removal of sections to accommodate the shoulders of subjects. It is worth noting that it may be possible to equalise the performance of the X- and Y-gradient coils by rotating them by 45° about the z-axis, but this would increase the complexity of imaging with such coils. The self-inductances simulated in FastHenry© agree less well with the values measured directly with an inductance meter, but are all within 20% apart from the Z2 shim coil which is 33% lower than expected. The simulated resistances are considerably different to the simulated values. The discrepancies between the simulated and measured impedances is thought to arise from the addition of the soldered connecting wires between loops, return paths in and out of the coil and the widely varying wire cross-section necessary of the abrasive water-jet cut copper plates.

We have also demonstrated that it is possible to force the stream-function to specific values *within* the surface using the IBEM. This is done for the X2-Y2 shim coil to prevent wires from crossing boundaries at $\phi = \pm 3\pi/4$ and $\pm\pi/4$. The challenges of engineering the shoulder slotted coils, particularly potting the coil in resin, were overcome by the experienced engineers at Magnex Scientific Ltd. (now part of Varian Inc., Yarnton, Oxon., UK).

The coil design examples in § 6.2 and 6.4 are theoretical evaluations of the improvement in performance that can be obtained with the IBEM over the more restrictive finite-length,

truncated sinusoidal basis-function methods [172, 178]. Restrictions on the form of the stream-function at the interface between surfaces are removed with the IBEM and the FOM's of the coils are consequentially increased. This increase in performance is greater for transverse dome gradient coils than for Z-gradient coils since the $\psi = 0$ constraint at the surface interfaces are more limiting. For these coils a significant performance increase is also observed with the ultra-short X-gradient coil as the prescription that ψ must be the same at the end of the shield surface as the end of the primary is no longer required.

Nerve stimulation in the body is reduced with head-only gradient coils, so it is possible to employ stronger and more rapidly switched magnetic field gradients. The ultra-efficient, shielded dome gradient coils described in § 6.3 represent an attempt to design insert, head gradient coils with the highest possible performance by placing the current carrying surface as close as possible to the head. To meet this goal, the coil surface was made highly asymmetric, and this example shows that the IBEM is capable of designing coils on surfaces with low symmetry. This asymmetry is used to help design gradient coils of high efficiency, but it causes some difficulty with building such a coil for imaging. Here, a half-scale prototype was constructed using a rapid prototyping technique [213], but a different fabrication technique would need to be identified to produce a practical full scale coil for imaging. The magnetic field distribution, efficiency, and inductance values of the prototype X-gradient coil were all found to be in very good agreement with the simulated values.

Section 6.5 gives details of the design of 3-axis gradient coils (with a Z0 shim coil) with a central gap. These were designed for combined PET-MRI, but may also be applicable to other multi-modal MR applications. It was necessary to incorporate an annular surface in the design of transverse gradient coils for this application to produce coils with adequate performance, but the engineering challenges of also incorporating annular surfaces for the Z-gradient and Z0 shim coils were too great. The lack of an annular surface makes them difficult to design, especially the Z0 shim coil whose shielding is poor when compared to a coil with no gap.

A 3-axis gradient coil set was designed with the IBEM on a single layer in § 6.6 similar in concept to some previous work [181, 216]. It was impossible to design a good Z-gradient with two cylindrical surfaces at the ends of the coil so an additional small cylindrical region was provided at the centre. This example shows how different coils benefit from being built on particular parts of a surface. If these areas are not provided it becomes very difficult to design a coil. The FOMs of the X-, Y- and Z-gradient coils were approximately halved compared to a conventional 3-layer equivalent gradient coil set. This method is applicable to all gradient and shim coils, for example, the ZX and ZY shim coils may be built on the same layer. This may be beneficial for systems in which little radial space is provided for

the gradient and shim coils. The performance of such coils is however inevitably lowered.

In § 6.7 the constant stream-function edge constraints imposed in all other examples were removed for some of the edges of this surface. This was done to design an openable Z-gradient coil without including any of the return paths in the design. The performance of this coil is 37.6% greater than a coil which was previously designed using simulated annealing [217] on the same surface with no return-paths included.

A different arbitrary geometry method was previously used to design a bi-radial ZY shim coil, which had a predefined set of possible wire positions [147]. We mimicked this work with the IBEM and demonstrated the improvement that can be gained by allowing the current to flow in any direction on the surface. This demonstrates the ability of this method to design shim coils with magnetic fields that conform to spherical harmonics with orders higher than 1 on an asymmetric surface.

In § 6.9 a novel approach to gradient coil shielding is given within the IBEM framework. We alter the optimisation functional (§ 5.2.8) to allow the field in the ROU to be finite as long it is of the same form as a target magnetic field, Eq. (6.9.1). The functional is constructed in such a way that the scale of the inevitable canceling field produced by the shield coil in the ROU is minimised as part of the optimisation process. This concept is similar to the residual eddy current effect (RECE) work of Shvartsman *et al.* [172], although it is not the eddy currents that are considered here. Choosing the right radius on which to place the shield is important, and obtaining the maximum field cancellation in the ROS is difficult. It involves altering the number of contours of the stream-function on the shielding surface to get as close as possible to full shielding. Then, by altering the self-inductance/resistance minimisation parameters, α and β, the magnitude of the shield field can be finely adjusted to maximally annul stray fields from any primary coil.

The examples in § 6.9, 6.10, 6.11, 6.12 all involve the design of coils with target magnetic fields that do not conform to the shape of low order spherical harmonics. Together they demonstrate the ability of the IBEM to design coils that generate asymmetric magnetic fields. Also, the PC shim coils and the 2D MAMBA coil demonstrate an inherent limitation of designing coils that generate target magnetic fields, in that high spatial frequencies in the magnetic field are difficult and sometimes impossible to generate. The high spatial frequencies present in the target magnetic fields of the PC shim coils may limit the practicality and ability of this concept although the simulations in § 6.11.1 show a considerable reduction in the magnetic field inhomogeneity in the heads of the 11 subjects. Certainly, these coil greatly benefit from being positioned as close to the ROU as possible. Figure 6.27 demonstrates the sensitivity of this shimming technique to misalignment of the head relative to the coils in the z-direction. If the principal component coils are used in conjunction with

the 1st order spherical harmonic shim coils, a lower RMS residual field is always achieved. Since orthogonality between the PC shim coils and the gradient coils of the system is not prescribed, it may be useful to employ mutual-inductance minimisation with the gradients when designing such PC shim coils to ensure that the gradient do not induce currents in them during imaging by inductive coupling.

6.13.1 General Observations

The majority of the calculation time for the IBEM is needed for evaluation of the matrices that govern the self-inductance, resistance, magnetic field, and torque of the system in terms of the basis-functions. The time required to calculate the matrix data of a variety of coils with varying numbers of nodes, N, on the same computer, an AMD Opteron$^{\text{TM}}$ 2.2GHz processor with 4GB RAM available, was collated and power law regressions of the form $t = aN^p$ ($t = aN^pK^q$ in the case of the $c_n(\mathbf{r})$ matrix) were performed. Figure 6.30 is a plot of the L_{mn} and R_{mn} calculation times as a function of the number of nodes in the surface, N. Equations (6.16), (6.17), (6.18) and (6.19) give the power law dependencies of the L_{mn}, $c_n(\mathbf{r})$, R_{mn} and M_x, M_y, M_z matrices in terms of N and the number of target magnetic field points, K. Equations (6.16) and (6.18) are shown in Fig. 6.30, and illustrate that, in general, the inductance matrix requires the largest proportion of the total calculation time to generate.

$$t_{L_{mn}} = (5.4 \times 10^{-8})N^{2.23} \text{ hrs} \tag{6.16}$$

$$t_{c_n(\mathbf{r})} = (3.8 \times 10^{-10})N^{1.82}K^{1.02} \text{ hrs} \tag{6.17}$$

$$t_{R_{mn}} = (1.5 \times 10^{-9})N^{2.54} \text{ hrs} \tag{6.18}$$

$$t_{M_x+M_y+M_z} = (1.2 \times 10^{-9})N^{2.05} \text{ hrs} \tag{6.19}$$

The coils in this chapter constitute a wide array of coil geometries and target magnetic field variations. The results demonstrate that using the IBEM a coil may still be designed when both are highly asymmetric. Figure 6.31 further illustrates this ability by showing the wire-paths for **a)** an X-gradient coil designed on the surface of a teapot, and **b)** a shielded Z-gradient coil on the surface of a mug. The current carrying surface and the target magnetic field cannot be completely arbitrary however. There must be enough surface, and in the right place with respect to the ROU, to reproduce the target magnetic field adequately. Also

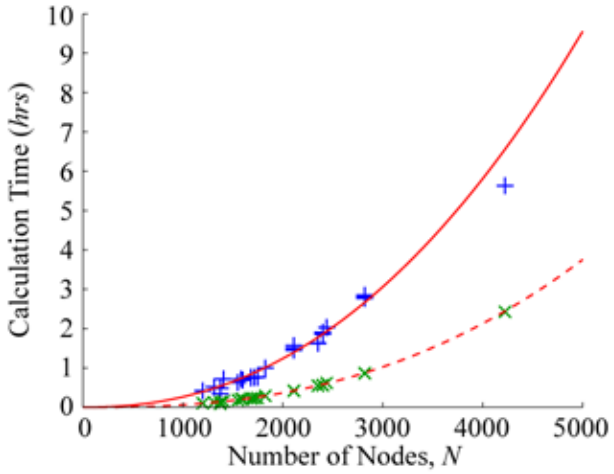

Figure 6.30: Calculation times for the L_{mn} (blue +) and R_{mn} (green $\times$) matrices as a function of N with the power law regression curves (red lines).

the target magnetic field must possess spatial frequencies below that which the geometry allows or they will not be reproduced by the discrete wires of the coil.

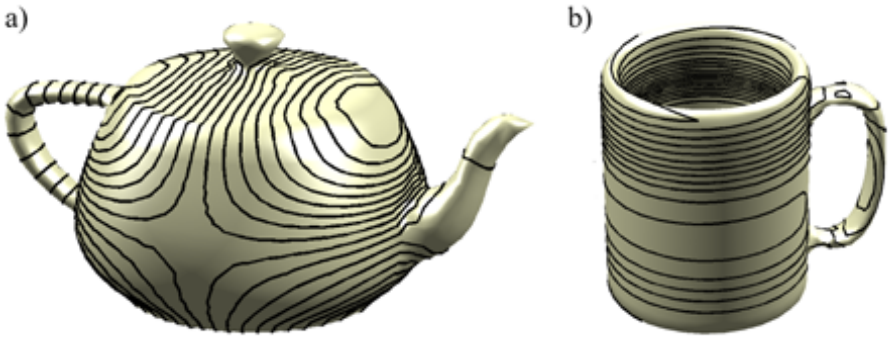

Figure 6.31: It's time for tea! Examples of **a)** an X-gradient coil on a teapot-shaped surface, and **b)** a shielded Z-gradient coil designed on the surface of a mug.

6.13.2 Future Work

Some coil designs that may be useful that have not been tried so far with the IBEM are:

(A) Gradient coils that are constructed from a multitude of planar annular surfaces. This idea is similar to the work of Bowtell and Peters [228]. It may be able to generate

very high magnetic field gradient strengths and good shielding by utilising all the 3D space available for it in the bore of a scanner.

(B) The PCA analysis may be improved upon by obtaining data from a much larger and more varied sample of subjects to derive the principal components. Also, defining a surface that is as close to the head as possible while still allowing access for most subjects will result in an improved representation of the target magnetic field by the coil.

(C) Some interest has been shown in creating multiple region gradient coils where a gradient is generated in different regions, like the Z-gradient coil in § 6.10. It may be possible to expand upon this concept and design gradient coils with more ROUs than 2 [229]. Also, coils similar to the MAMBA coils § 6.12, may be improved further with this method. This could be potentially useful for multiple simultaneous NMR experiments and multiple simultaneous animal imaging.

(D) Multiple region gradient coils have been proposed for fast imaging in conjunction with parallel RF coils [230]. It is possible to separate out two regions that are encoded at the same frequency using the sensitivity profile of the parallel RF coil array and reconstruction techniques.

There are also several improvements that could be made to the coil design software. Peeren [180, 204] demonstrated the possibility of using elements that are not triangular in geometry. The most interesting prospect is to employ circularly symmetric elements to construct meshes. This reduces the dimensionality of the parameterised surface from 2 to 1, and consequently greatly reduces the number of basis-functions, thus the calculation time should be reduced dramatically. This will also result in considerably smoother wire-paths, with little or no artefacts from the mesh. Clearly, elements of this shape are not applicable to geometries that are not circularly symmetric.

In addition to all the physical properties of the coil that are parameterised in this work (§ 5.1.4 to 5.1.8) , the residual eddy current effect (RECE) [172], may be parameterised by generating an intermediate matrix that would transform the $c_n(\mathbf{r})$ into a new matrix reflecting the effect of the eddy currents in nearby conducting surfaces immediately after switching the coil. A term may then be added to the functional minimised in the coil design in a similar way to that which is used in § 6.9 and in Eq. 12 in Ref. [172] to allow the magnetic field in the ROU to be altered by the eddy-currents, but only with a magnetic field that is of the same shape as the target magnetic field. These eddy currents can then be compensated for with gradient pre-emphasis § 3.3.1 [92, 93]. Implementing the RECE

in the IBEM would additionally require modelling and meshing the eddy-current surfaces. It should be feasible to incorporate the induced electric field inside the body into the coil design optimisation process to minimise peripheral nerve stimulation.

A further improvement that could be made to the software is to integrate it better with the 3D meshing software, and to give it a front-end. 3D Studio MAX® is a sophisticated program that is controllable by its own language. It may be beneficial to write MACROs for it to automatically generate the geometry of the system, especially for designing many coils of a similar geometry.

It is clear that it is possible to design coils of almost any geometry using the IBEM, but it is also clear that it would be impossible to generate a specified magnetic field by providing a very small current carrying surface for the coil. There is a tradeoff between the accuracy with which the magnetic field is represented by the coil, and the size of the current bearing surface. The minimum wire spacing, desired efficiency, inductance, resistance *etc.* are all involved in this tradeoff. It would be interesting to analyse this tradeoff in some way so as to obtain a method to predict whether a particular coil is possible to design, and what performance one could expect, before meshing it, calculating the matrices, and adjusting the coil design parameters to try and obtain a satisfactory coil. The condition number, κ, of the $\mathbb{Z}$ matrix (Eq. (5.48)) which contains all the information about the geometry of the system and α, β and γ, may characterise the ease with which a particular coil may be designed. κ is high for an ill-conditioned matrix, which in turn is a consequence of a poorly posed-problem. It is known that κ has a linear relation to both α and β for the range of values for which a useful coil is produced. The size of this linear region may determine the range of values of α and β that may be used for a particular geometry.

Chapter 7

Parcellated Dynamic Shimming

7.1 Introduction

The principles of shimming for removal of magnetic field inhomogeneity and the need for improved shimming methods, such as dynamic shimming [66–68], for high-field MRI were discussed in Chapter 3.

In the work described in this chapter we expand upon the dynamic shimming concept and propose parcellated dynamic shimming, in which the shimming sub-volumes are no longer slices, but cuboids [222]. This further reduces the spatial extent of the sub-volumes so that the magnetic field inhomogeneity, ΔB_0 is better approximated with a limited number of spherical harmonics (§ 2.2). We test this hypothesis by simulation of the parcellated shimming procedure using magnetic field maps of the heads of 11 subjects.

7.2 Methods

7.2.1 Magnetic Field Inhomogeneity Data

Head field data were acquired using a two-echo, 3D gradient-echo sequence, with echo times $T_{E1} = 2.2$ms and $T_{E1} = 20.0$ms on a Phillips 3T Achieva MRI scanner. Each data set took less than 2 minutes to acquire. The phases, ϕ, of the two echoes were phase unwrapped [231], then subtracted and scaled to yield maps of the magnetic field offset, ΔB_0, in Tesla (T) using Eq. (7.1).

$$\Delta B_0 = \frac{\phi_{TE2} - \phi_{TE1}}{\gamma(T_{E2} - T_{E1})} \tag{7.1}$$

where $\gamma = 267.5 \times 10^6$ s^{-1}T^{-1} is the gyromagnetic ratio. This is then expressed in

parts-per-million (ppm) of the static magnetic field, B_0, which, in this case is 3T. Eleven such ΔB_0 data sets were acquired from consenting, healthy volunteers with 2 mm isotropic resolution with a matrix size of $96 \times 96 \times 66$, which was zero padded to $96 \times 96 \times 96$ for convenience.

Magnetic field maps of each shim coil were generated by calculation of the appropriate spherical harmonic on the same matrix of points as the field data, $B(\mathbf{r})$. Such maps may also, and more accurately, be obtained by directly mapping the field generated by actual shim coils. Previous work [183] provided scalings for the shim coil efficiencies based on an insertable gradient and 2nd order shim coil set, § 6.1. The coils were designed using a distributed wire pattern, arbitrary geometry technique § 5 [160, 181] to have high efficiency and low inductance because the currents in the shim coils will need to be switched rapidly. The coil efficiencies, η are given in $\mathrm{mTm}^{-n}\mathrm{A}^{-1}$ in Table 7.1, where n is the order of the coil.

Shim Type	{Order, Degree} $\{n, m\}$	Field Equation	Efficiency, η ($\mu\mathrm{Tm}^{-n}\mathrm{A}^{-1}$)
Z0	{0, 0}	1	9.1
Z	{1, 0}	z	121
X	{1, 1}	x	100
Y	{1, -1}	y	119
Z2	{2, 0}	$z^2 - \frac{1}{2}\left(x^2 + y^2\right)$	340
ZX	{2, 1}	$3zx$	360
ZY	{2, -1}	$3zy$	411
X2-Y2	{2, 2}	$3(x^2 + y^2)$	181
XY	{2, -2}	$6xy$	252
Z3	{3, 0}	$z^3 - \frac{3}{2}z\left(x^2 + y^2\right)$	-
Z2X	{3, 1}	$\frac{3}{2}x\left(4z^2 - \left(x^2 + y^2\right)\right)$	-
Z2Y	{3, -1}	$\frac{3}{2}y\left(4z^2 - \left(x^2 + y^2\right)\right)$	-
Z(X2-Y2)	{3, 2}	$15z\left(x^2 + y^2\right)$	-
XYZ	{3, -2}	$30xyz$	-
X3	{3, 3}	$15x\left(x^2 - 3y^2\right)$	-
Y3	{3, -3}	$-15y\left(y^2 - 3x^2\right)$	-

Table 7.1: Shim field equations and efficiencies for shim coils up to 3rd order. Here n and m are the order and degree of the spherical harmonic. The 3rd order shim coil efficiencies are not required for any calculations in this work.

7.2.2 Global Shimming

The shim currents, I^{shim}, required for shimming can be obtained by pseudoinversion, †, of a matrix describing the shim fields, $\mathbf{B}_0^{\text{shim}}$, multiplied by the field required to maximally null ΔB_0

$$I^{\text{shim}} = -\Delta B_0 \left(\mathbf{B}_0^{\text{shim}}\right)^{\dagger} \tag{7.2}$$

where $I^{\text{shim}} = \left[I^{\{0,0\}}, I^{\{1,0\}}, I^{\{1,1\}}, \ldots, I^{\{n,m\}}\right]$ and $\mathbf{B}_0^{\text{shim}} = \left[\mathbf{B}_0^{\{0,0\}}, \mathbf{B}_0^{\{1,0\}}, \mathbf{B}_0^{\{1,1\}}, \ldots, \mathbf{B}_0^{\{n,m\}}\right]$. $I^{\{n,m\}}$ is the current to be passed through the shim that produces the spherical harmonic with order n and degree m, and $\mathbf{B}_0^{\{n,m\}}$ is the magnetic field generated by passing 1 Amp current through the $\{n, m\}$ shim coil at the set of measurement points.

7.2.3 Dynamic Shimming

Equation (7.2) is solved separately for each imaging slice in dynamic shimming [66]. The calculated currents are applied to the shim coils for the time period in which the appropriate slice is being imaged. Therefore ΔB_0 and $\mathbf{B}_0^{\text{shim}}$ only contain magnetic field values of the slice that is to be calculated.

ΔB_0 becomes essentially two dimensional in dynamic shimming. This means some shim fields become degenerate. For example, in dynamic shimming where axial slices are acquired and shimmed individually, z is treated as constant throughout the sub-volume and therefore the Z0 shim and Z-gradient, the X-gradient and ZX shim and the Y-gradient and ZY shim become degenerate. Through-slice gradients can still detrimentally affect the quality of the image. A magnetic field variation through the slice will cause dephasing and signal loss. The issue of shim degeneracy and through-slice linear gradients for oblique slices has been discussed by Koch *et al.* [232].

7.2.4 Parcellated Dynamic Shimming

Equation (7.2) is solved for each sub-volume in parcellated dynamic shimming, but now ΔB_0 and $\mathbf{B}_0^{\text{shim}}$ contain values from a small cuboidal region. Both global shimming and dynamic shimming are special cases of parcellated shimming; global shimming simply has one shimming sub-volume with the same extent as the imaging volume, and dynamic shimming has a shimming sub-volume with 2 dimensions the same as the imaging volume, and the other is 1 voxel thick.

In this work we investigate how the geometry of the shimming sub-volume affects the efficacy of the shim. To characterise the geometry of the sub-volumes we introduce a dimensionless parameter we call the "compactness" of the sub-volume and represent it with the symbol C

$$C = \frac{\sqrt[3]{V}}{\sqrt{SA}} \tag{7.3}$$

where V is the volume which the shimming sub-volume occupies, an important parameter in its own right, and SA is the surface area of the sub-volume. C has the property that it is large for sub-volume geometries that are compact, such as a cube, and small for flat geometries with large extent, such as a thin slab.

We introduce the efficacy of shimming, ε, as a percentage that describes how much of ΔB_0 has been annulled due to shimming, and is given by

$$\varepsilon = \frac{\sigma_{\text{pre}} - \sigma_{\text{post}}}{\sigma_{\text{pre}}} \times 100 \tag{7.4}$$

where σ_{pre} is the root-mean-squared (RMS) magnetic field value before any shimming has taken place, and σ_{post} is the RMS residual magnetic field after the shim has been performed

$$\sigma_{\text{pre}} = ||\Delta B_0|| \tag{7.5}$$

$$\sigma_{\text{post}} = ||\Delta B_0 - I^{\text{shim}}\mathbf{B}_0^{\text{shim}}|| \tag{7.6}$$

where $||.||$ denotes the l^2-norm.

7.2.5 Parcellation Schemes

The way in which the whole volume is sub-divided is referred to as the "parcellation scheme" and is defined by the dimensions of the sub-volume. For instance, for the data analysed here, dynamic shimming with axial slices may be termed the $96 \times 96 \times 1$ scheme, and a more compact parcellation scheme may be $24 \times 24 \times 16$. These two schemes have the same volume, $V = 9216$ voxels (or 73728 mm^3), but a compactness $C = 0.153$ and 0.404 respectively. In this work we chose that any dimension could be sub-divided into 1, 2, 3, 4, 6, 8, 12, 18, 24, 32, 48, or 96 parts. If the scan size is not conveniently factorised, it may simply be cropped or zero-padded to a convenient size. We also prescribed that the minimum volume for a parcellation scheme is 9216 voxels. There are consequently 313

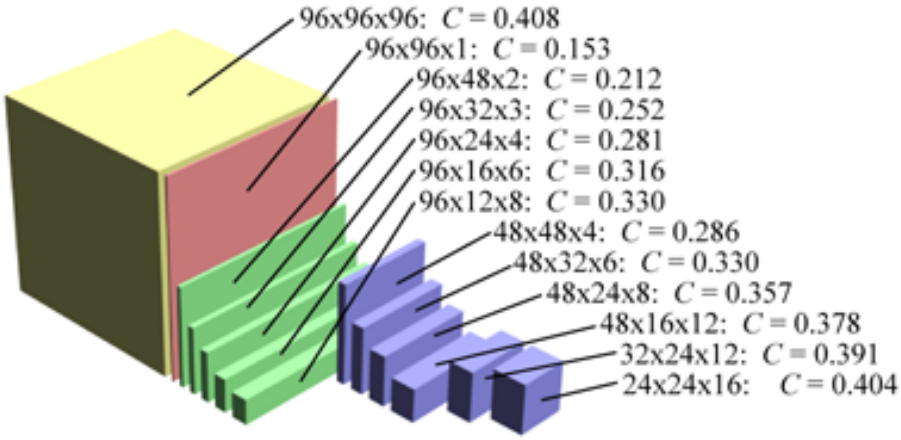

Figure 7.1: Sub-volumes of possible parcellation schemes of a $96 \times 96 \times 96$ voxel region that contain 9216 voxels. These may be rotated to obtain other schemes. The full volume is also shown.

different possible parcellation schemes that conform to these criteria with volumes ranging from 9216 to 884736 voxels and compactness values from $C = 0.153$ to 0.408. For all these parcellation schemes we simulate 1$^{\text{st}}$, 2$^{\text{nd}}$ and 3$^{\text{rd}}$ order shimming, and record the resulting efficacy, ε, for all 11 subjects. Figure 7.1 shows the shapes of all the parcellation schemes containing 9216 voxels, and the full imaging volume.

A convenient way to categorise the 313 different parcellation schemes is to consider the number of dimensions of the full imaging volume that the sub-volume fully spans. Clearly, the global shimming ($96 \times 96 \times 96$) scheme spans the imaging volume in all 3 dimensions (shown as yellow in Fig. 7.1), and all the dynamic shimming schemes span 2 dimensions (red in Fig. 7.1). 195 of the 313 schemes have just one full dimension (green in Fig. 7.1), and the remaining 114 have no dimensions that span the whole imaging volume (blue in Fig. 7.1). Parcellation schemes in which the sub-volume spans at least one dimension of the whole volume are likely to be more straightforward to implement practically.

7.2.6 Current Constraints

The simulations discussed so far have not considered the current restrictions that are inevitably present in a real system. Shim coils possess a resistance, and the amount of current that can be passed through them is limited by the heating effect and the capabilities of the power supply used to drive them. This in turn limits the magnitude of the spherical harmonic that a particular shim coil is capable of generating. Simply truncating the current to

the maximum allowed if the calculation prescribes a greater than possible current leads to a non-optimal shim; it is better to take into account the current limitations when solving Eq. (7.2) [58]. Here we have simulated the effect of placing a restriction on the amount current available, $I^{\max}$, on ε for a few different parcellation schemes when considering up to and including 2^{nd} order shims (Table 7.1). This is done using the `lsqlin` function in Matlabs Optimisation Toolbox®, which uses a subspace trust region method based on the interior-reflective Newton method as described in Ref. [233].

7.3 Results

The comparison between the efficacy of global shimming, axial, coronal, and sagittal dynamic shimming, and the best performing parcellation scheme averaged over all 11 subjects is shown in Fig. 7.2. This figure shows the results for shimming with all shim terms up to 1^{st} order, 2^{nd} order, and 3^{rd} order, and the error bars on the graph indicate the standard deviation over all subjects.

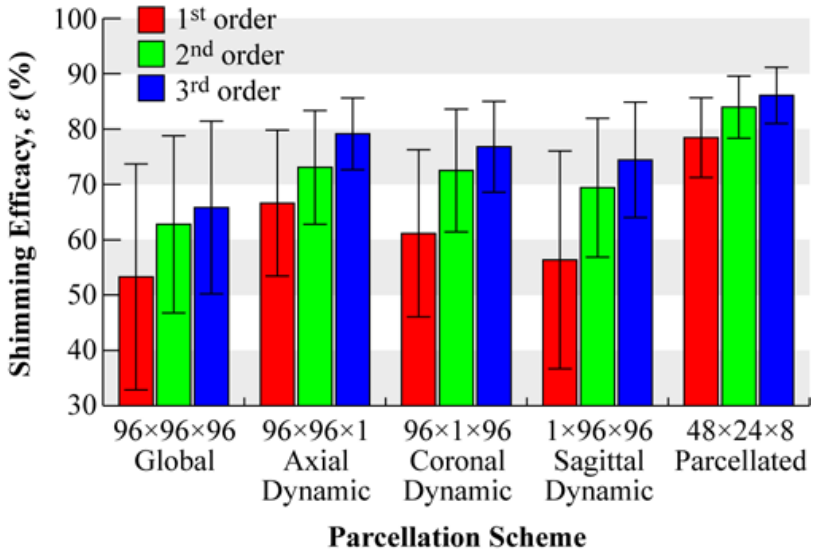

Figure 7.2: Efficacy of shimming, ε, (Eq. (7.4)) for global, dynamic, and best parcellated shimming schemes averaged over all 11 subjects. Results for 0^{th}, 1^{st}, 2^{nd}, and 3^{rd} order shims terms sets are shown as well as error bars indicating the standard deviation of ε over all subjects.

Figure 7.3 shows ε against C for all parcellation schemes that contain 9216 voxels per sub-volume and Fig. 7.4 shows the efficacy of shimming against the cube-rooted volume of

the sub-volume parcellation scheme, $\sqrt[3]{V}$. Fig. 7.4 illustrates that the average ε of schemes with a particular volume increases with decreasing volume. The way in which constraining the current in the shims, based on the shim coil efficiencies in Table 7.1, affects the efficacy of shimming for 2nd order shimming with the parcellation schemes; $96 \times 96 \times 96$, $96 \times 96 \times 1$, $96 \times 12 \times 8$ and $48 \times 24 \times 8$ is demonstrated in Fig. 7.5. These are the best performing schemes with 3, 2, 1 and 0 dimensions that span the full imaging volume. A range of logarithmically spaced current limits were used from 0.001A to 10A.

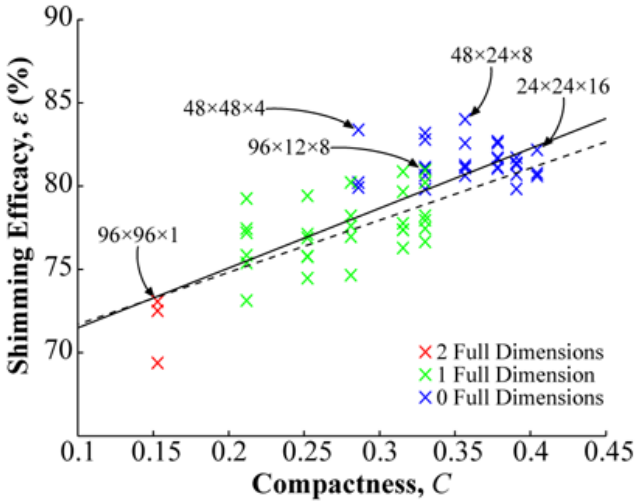

Figure 7.3: ε versus C for 2nd order parcellated dynamic shimming for schemes containing 9216 voxels per sub-volume. Those with 2, 1 and 0 dimensions that span the whole imaging volume are show in red, green and blue respectively, and some potentially useful schemes are labelled. Linear regression lines are plotted for all the data (solid line) and just for those schemes with 1 or 2 full dimensions (dashed).

As an example, axial, coronal and sagittal anatomical, and field map images as well as histograms of ΔB_0 in one subject are shown in Fig. 7.6. It demonstrates the homogeneity improvement that can be gained by using dynamic rather than global shimming, and furthermore the improvement of parcellated versus dynamic shimming.

7.4 Discussion

Shimming on small cuboidal regions provides the means to obtain more artefact free imaging data than global or dynamic shimming by reducing the magnetic field inhomogeneity further. However, the implementation of an imaging protocol that is compatible with parcellated dynamic shimming has yet to be demonstrated. With echo volumar imaging (EVI)

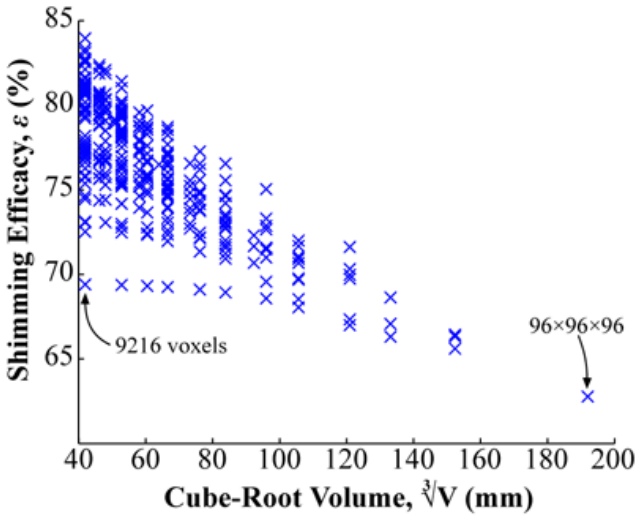

Figure 7.4: The shimming efficacy versus the cube-root of the volume of the parcellation sub-volume.

[234] it is possible to acquire data from small cuboidal regions, but the excitation of such a region is problematic. Preferably, the shimming, excitation, and acquisition protocols should be compatible and introduce no extra time penalty, reduction of signal-to-noise (SNR) or loss of sensitivity to functional activity over established methods for high speed brain imaging.

Applying saturation pulses [235] to areas outside the sub-volume to be imaged would require the magnetisation in suppressed regions to recover to equilibrium before being imaged. With careful ordering of sub-volume acquisition, any time penalty caused by this may be reduced, but this solution is far from practical. It has been shown that arbitrary 3-dimensional shaped regions can be excited using 3D spatially-selective tailored radio-frequency pulses (3D SSTRF) [76, 77, 79]. Such pulses tend to be long in duration and cause off-resonance issues which have been addressed in the cited works. Also, using EVI, with no image dimensions that span the full imaging volume means that there will need to be an increased number of acquisitions, which will increase the scan time. Therefore, if 2D SSTRF [236] pulses are used to excite a rectangular column, the 3$^{\text{rd}}$ non-spatially selective excited dimension, could be used as the frequency encoding direction, thus preserving the short time of the scan. This is the reason for distinguishing between parcellation schemes with 1 and 0 full dimensions, as only those with a full dimension are compatible with time-efficient scanning of the volume without use of 3D RF excitation. The time needed for a 2D SSTRF is less than for a 3D pulse, but is still significantly long. The time required for

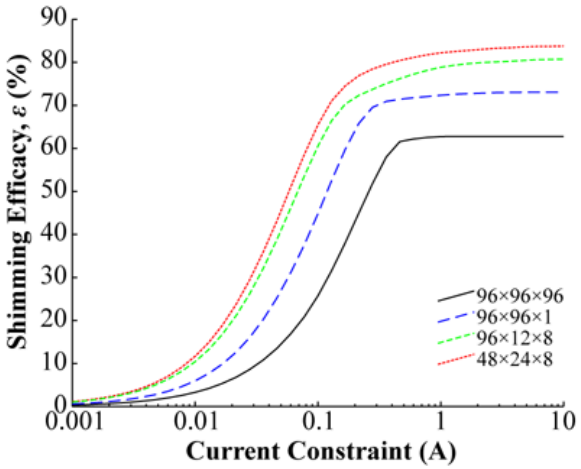

Figure 7.5: The shimming efficacy as the maximum absolute current limit is altered for the schemes; $96 \times 96 \times 96$, $96 \times 96 \times 1$, $96 \times 12 \times 8$ and $48 \times 24 \times 8$.

these 2D and 3D SSTRF pulses may be dramatically reduced by using parallel transmission techniques (such as transmit SENSE) [237].

The gradients and shims with variations in the slice-select direction become degenerate in single slice dynamic shimming schemes. This reduces the number of shim terms available for shimming. However through-slice linear gradients may still cause signal loss in images. This can be ameliorated by taking into account the adjacent slices to the imaging slice and applying a gradient that is the inverse of the average through-slice gradient. This will only correct the average through-slice gradient, any variation of the gradient across the slice cannot be corrected.

The data represented by Fig. 7.2 indicates the improved efficacy of shimming that is achieved with parcellated dynamic shimming over other methods. It also shows the improvement that can be gained from employing higher order shim terms. Interestingly, the performance of the $48 \times 24 \times 8$ parcellated dynamic shimming with linear shim terms is approximately equal to that of dynamic shimming with up to 3^{rd} order shim terms. This result makes parcellated dynamic shimming a very promising technique since it may achieve very good shimming with little or no additional hardware. However, it would require increased complexity of data acquisition.

Figure 7.3 shows a clear trend between the compactness, C, of the sub-volume and the efficacy of shimming, ε. However, over the 11 subjects used in this study, the parcellation scheme that performed best was that with sub-volume dimensions $48 \times 24 \times 8$ where $C_{48\times24\times8} = 0.357$. It was not the best scheme for all the subjects, but overall performed

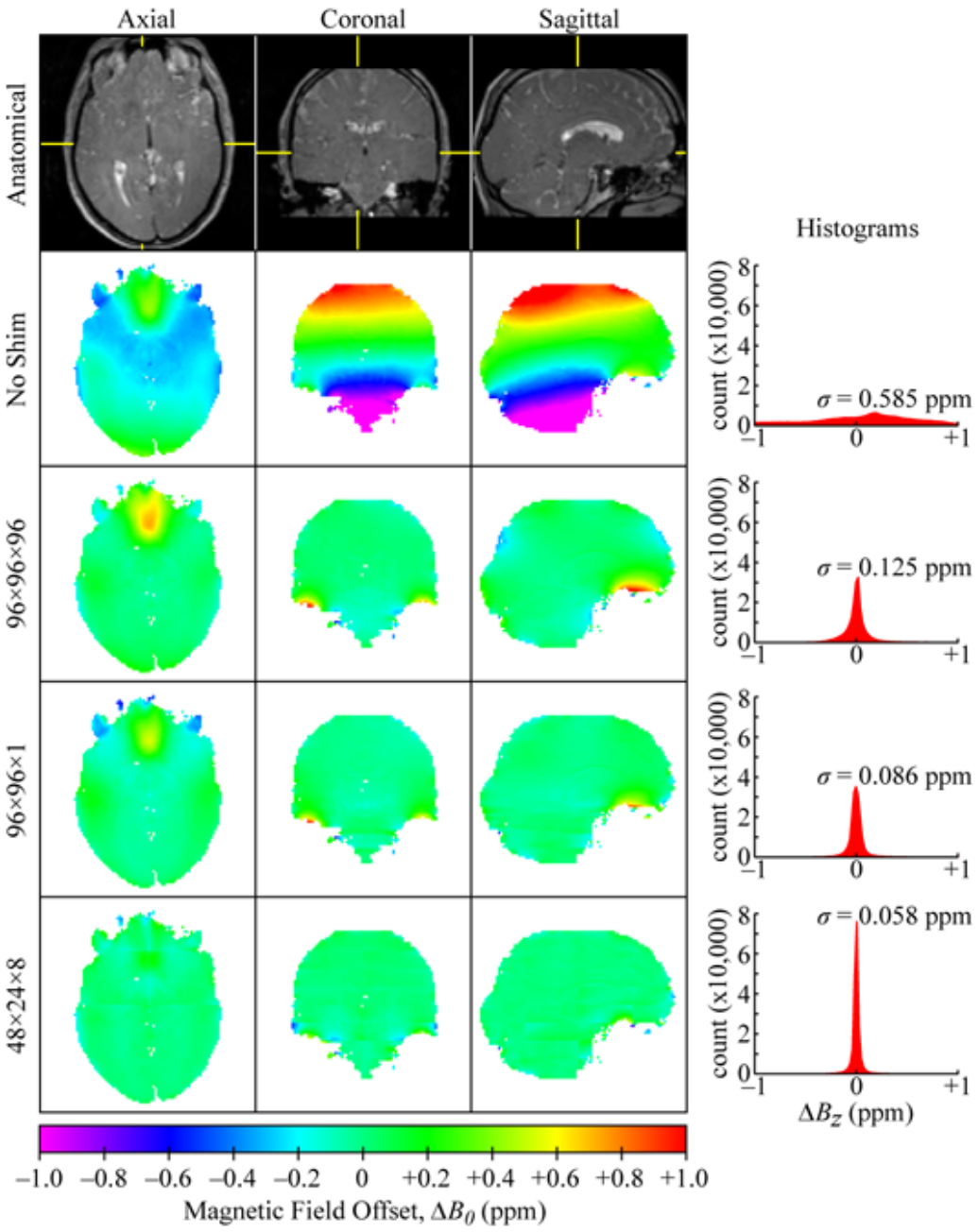

Figure 7.6: Anatomical images showing the slice positions and maps of the magnetic field offset in sagittal, coronal, and axial slices of one subject before and after 2nd order shimming with $96 \times 96 \times 96$, $96 \times 96 \times 1$ and $48 \times 24 \times 8$ parcellation schemes. Histograms and RMS values of the magnetic field offset for each scheme are also shown.

most efficiently. This fact that the best scheme is not the most compact indicates that the choice of resolution, field of view (FOV) and the specific morphology of ΔB_0 for each subject are important factors in determining which parcellation scheme performs best. The excellent performance of the $48 \times 24 \times 8$ scheme suggests that segmenting into many partitions in the z-direction (inferior-superior) is more important than for other directions. This is also supported by the fact that axial dynamic shimming out-performs the coronal and sagittal versions, and also since the static magnetic field, B_0, is oriented along the z-axis and field distortions are generated in the inferior frontal cortex, superior to the sphenoid and ethmoid sinuses, and the inferior temporal cortex superior to the external auditory canal and mastoid air cells. ΔB_0 generally exhibits reflectional symmetry about the central sagittal slice, which is one possible reason that schemes which only divide the x-direction into two halves perform well. Also, parcellation schemes that have one dimension spanning the imaging volume in the x-direction generally outperform those with one dimension spanning the y- or z-directions.

If the parcellated dynamic shimming method is considered to be a generalisation of global and dynamic shimming, a further generalisation could be conceived: a subdivision of the imaging volume into cuboidal sub-volumes of varying size. With this approach, it may offer some benefit to use large sub-volumes in areas of the brain where small variations in ΔB_0 occur and to use smaller sub-volumes in other regions with higher ΔB_0 intensity and spatial frequency. It can be observed from the parcellated scheme field map images in Fig. 7.6 that excellent shimming may be achieved by placing the boundary between adjacent sub-volumes across an area of high field inhomogeneity, such as the inferior frontal cortex. An adaptive mesh refinement (AMR) algorithm [238] based on the shape of the measured ΔB_0 may be able to decide the best arbitrary subdivision of the whole volume. Furthermore, employing non-cuboidal, tessellating sub-volumes provides an even more generalised concept, and may yield more efficient shimming, but combining these more generalised concepts with imaging protocols would be very difficult indeed.

The shimming efficacy measure, ε, is a good parameter for estimating the resulting reduction in ΔB_0 and therefore any imaging artefacts due to ΔB_0. It is not possible, however, to achieve $\varepsilon = 100\%$ since some noise and errors are present in the field maps. Noise in the field maps may simply arise from random noise in the phase data received from the scanner. More significant errors in the field map occur from chemical shift differences of tissues in the body, flow, incorrect masking of the brain region, and most significantly here from the phase-unwrapping algorithm. The phase-unwrapping algorithm used in this work [231] first unwraps each slice of the data sequentially and then unwraps in the 3$^{\text{rd}}$ dimension. Any unconnected brain regions within a slice may not have consistent unwrapped phase and

therefore result in erroneous ΔB_0 values in that region.

Figure 7.5 shows the way in which limiting the current in the shims alters ε. It is evident that ε begins to reduce earlier as the current limit is lowered for dynamic shimming compared with conventional whole volume shimming and even more so for parcellated dynamic shimming. This indicates that for these schemes more intense shim fields are required if they are to achieve their full potential. If the currents were simply truncated to their maximum values the advantage of using parcellated and dynamic shimming may be lost, and it is therefore essential to take these limits into account when calculating the shim currents. The level of the current limit is dependant on the properties of the gradient and shim coils and the power supply with which they are driven and may not be the same for all the shims.

7.5 Conclusions

The primary aim of this work is to show that parcelled dynamic shimming provides a more effective method than conventional multi-slice dynamic shimming in reducing the magnetic field inhomogeneities in the head. This has been achieved by simulated shimming of 3D magnetic field inhomogeneity maps obtained from 11 subjects with a double, gradient echo field mapping sequence. The efficacy of shimming was calculated as a percentage of the root-mean-square field offset before and after shimming where, using up to 2^{nd} order shim terms, global (whole volume), dynamic, and parcellated dynamic shimming achieved efficacies of $63 \pm 16\%$, $73 \pm 10\%$ and $84 \pm 6\%$ respectively.

The results obtained in this work indicate that far greater improvements in magnetic field homogeneity, and therefore susceptibility-induced artefacts reduction, can be gained from implementing parcellated dynamic shimming than the improvement that can be gained from adding more orders of shim coils to systems while employing global or dynamic shimming. It additionally shows that parcellated dynamic shimming with just linear shim terms can perform as well as conventional dynamic shimming using up to 3^{rd} order shim terms. This reduces the need for additional hardware which is not currently supplied with MRI scanners, at the expense of increased complexity of data acquisition.

While this work has entirely focussed on homogenising the magnetic field generated by susceptibility differences of tissues inside the human head, it is a general technique that could be applied to other parts of the body, or to other animals or situations entirely. The motivation for this focus was to minimise the sensitivity losses in functional studies of brain activity, and to provide distortion and artefact free anatomical reference images, particularly at high static field strengths ($\gtrsim$ 3T) where these effects become increasingly severe.

Chapter 8

Conclusions

8.1 Summary

In this thesis I have discussed the problem of making an intense magnetic field highly homogeneous within objects of inhomogeneous magnetic susceptibility, such as a human head. This problem is motivated by the requirements of magnetic resonance imaging (MRI) for very high field homogeneity. In particular, with the current trend in MRI for ever higher magnetic fields, the magnetic field inhomogeneities generated as a result of different magnetic susceptibilities within the human body become more intense and problematic. The signal-to-noise ratio (SNR) of MRI increases with static magnetic field strength and functional MRI (fMRI), which is used to detect the haemodynamic response associated with increased local neuronal activity, benefits from this SNR increase. It also benefits from the increased T_2^* contrast afforded in high-field systems. fMRI relies on echo-planar imaging (EPI) which is highly sensitive to magnetic field inhomogeneities because of its long data acquisition time, which counteracts some of the benefit of performing fMRI at high-field. Other applications of MRI that benefit from the increased SNR at high field are also detrimentally affected by susceptibility induced magnetic field inhomogeneity.

I have discussed the many approaches that have been proposed to make the magnetic field more homogeneous, and to reduce its effect on MR images. The work of this thesis has focussed on trying to implement dynamic shimming as this approach appears to be a powerful solution and tackles the cause of the problem rather than treating the symptoms. The standard (available on all MRI scanners) shimming method is to adjust the current in a set of shim coils that each generate a different spherical harmonic shaped magnetic field to cancel maximally the magnetic field inhomogeneity present in the object being scanned. Dynamic shimming is more effective since it permits a different set of shim currents to be

applied for each slice of a multi-slice data acquisition. The 2nd order shim coils that most scanners are currently equipped with tend to have high inductances, and therefore it takes too long for the current in them to be altered between the acquisition of successive slices. This means that the implementation of dynamic shimming requires the availability of new, low-inductance shim coils and their integration with other scanner hardware. In addition, low-latency control hardware must be provided to apply the shim currents to these coils dynamically.

In this thesis a set of insertable, head gradient and shim coils for dynamic shimming have been described. The coil set was made to be insertable because of the desire to use the gradient and shim set in 3 different MRI scanners (Philips Achieva 3T, Intera 7T and Nottingham-built 3T) with different bore diameters and RF coil sizes. The radial size restriction meant that the shoulders of the subject had to be accommodated by the coil set. Here we incorporated rectangular slots in the geometry for the shoulders. The asymmetry of this design required the use of an inverse boundary element method (IBEM) for gradient and shim coil design. This IBEM was used to design the shoulder-slotted, insert head gradient and shim coil set which was subsequently built and tested at 3T.

The versatility of the IBEM was extended by incorporating 3D Studio MAX® (Autodesk®, Inc., San Rafael, CA, USA), a powerful 3D graphics package with complete control over the construction of meshes, and a 3D contouring algorithm. Current-carrying, magnetic field generating coils of widely varying geometry were designed using this approach demostrating the power of the IBEM. These include a set of shielded, dome-shaped head gradient coils with very high efficiency, a very short shielded gradient coil set with flared ends, a set of gradient coils with a central gap for combined PET/MRI, a 3-axis gradient coil set on a single surface, an openable Z-gradient coil, a bi-radial shim coil, retro-fitted active magnetic screening for existing coils, a multiple region gradient coil, a set of shim coils based on a principal component target field basis-set and a coil that generates multiple regions of uniform field offset with different intensities for simultaneous acquisition from multiple regions. Using the IBEM rather than conventional coil design methods generally resulted in an increase in coil performance due to the removal of constraints on the form of the current density. The IBEM has also opened up the possibilities for coil design and has led to a potentially useful, novel shimming technique that no longer uses spherical harmonics as its basis set.

In this thesis I have also presented a novel technique called parcellated dynamic shimming, which is a generalised version of dynamic shimming, in that it involves performing the shimming process over cuboidal sub-volumes rather than slices. In this manner, the extent of the region that is shimmed with the same currents is reduced. It has been shown by

simulation that this method is significantly more effective at annulling the magnetic field inhomogeneities in the heads of 11 subjects than conventional shimming or slice-by-slice dynamic shimming. The performance of parcellated dynamic shimming with 0^{th} and 1^{st} order shim fields was shown to be similar to that of conventional dynamic shimming with up to 3^{rd} order shim coils. This remarkable performance, if borne out by experiment, may mean that no additional hardware will be required, since adjustment of the 1^{st} shims can be effected rapidly because the gradient coils of an MRI system are optimised for fast switching. However, this increase in performance, and potential reduction in the additional cost from new hardware comes at the expense of increased complexity of acquisition. To acquire the data within the parcellated shimming regime, it is proposed that echo-volumar imaging (EVI) is used. This would have to be employed in conjunction with a 3D spatially-selective excitation to avoid signals from outside the EVI acquisition region folding over into the acquisition region. 3D spatially-selective RF pulses may be employed, possibly with the aid of parallel transmission for rapid excitation.

8.2 Future Work

The insertable head gradient and shim set that has been designed and built during this thesis may be useful in homogenising the magnetic field in high-field MRI scanners. The first task is to integrate the coil set with the scanners. To make this coil set capable of dynamic shimming is a considerable task. First, a reliable method of quickly acquiring field map data from the object being scanned needs to be implemented. It has been seen that the common FASTMAP [54, 55] and related method are subject to errors, and that a full 3D field map (§ 2.5.10) would be more robust. The next major difficulty is to turn the phase data acquired into the optimum shim currents. This task needs to be accomplished rapidly so as not to significantly increase the time of the scan. The method used here require phase unwrapping, which can take some time. Alternative field mapping sequences that do not require phase unwrapping [239] could be employed to speed up the generation of the 3D maps of the magnetic fields. Computing the shim currents once the magnetic field data is obtained is relatively rapid since the pseudoinversion can be performed in advance. Finally, these shim currents need to be applied to the coils with a set of amplifiers that are able to alter the current rapidly and accurately.

The parcellated dynamic shimming technique described in this thesis is a promising method for high-field MRI. It has been shown by simulation to be highly effective at reducing the magnetic field inhomogeneities caused by differences in magnetic susceptibility in the head, but there are some significant problems that need to be overcome before it can be

fully implemented. To begin it would be sensible to demonstrate its efficacy for 1st order shimming since this means that extra hardware needed for 2nd order dynamic shimming would not be required. Getting the right shim currents into the gradient coils is a problem of modifying the scanner software to this effect. As a first step to demonstrating the efficacy of parcellated dynamic shimming, echo-volumar imaging (EVI) needs to be successfully implemented at 3 and 7 Tesla. The acquisition of small cuboidal volumes could be performed adequately if outer volume suppression techniques can be used to saturate the magnetisation from outside the cuboidal volume [235]. This would have disadvantages for performing the parcellated shimming dynamically, but would allow the shimming and data acquisition aspects of this method to be experimentally verified. To dynamically shim each sub-volume between the EVI acquisitions, 3D spatially-selective radio-frequency (3DSSRF) pulses [76, 77, 79] may be of great use. These pulses are capable of exciting arbitrary shaped volumes in 3D within the sample. However, 3DSSRF pulses tend to be complex and require too long to execute. With the advent of parallel RF transmission [237], these pulses may be dramatically shortened to a duration that would be compatible with common imaging techniques, such as fMRI.

It would also be interesting to pursue the novel principal-component-shimming method described in this thesis. The work carried out here showed by simulation that improvements in the homogeneity of the magnetic field may be achieved with principal component (PC) shim coils in conjunction with 1st order spherical harmonic shim coils. The effectiveness of this method relies on the sample magnetic field map data, so it would be useful to use a great many more magnetic field maps to perform the PC analysis. This method could be demonstrated experimentally by designing and building a prototype set of PC shim coils and writing software to calculate the PC shim currents. The benefit of this method over other non-spherical-harmonic-based local shimming techniques is that it can be simply performed during the set up of the scan and, providing the currents are calculated correctly, will only improve the magnetic field inhomogeneity. A new coil surface geometry may need to be found since these coils need to be placed very close to the head, and may cause discomfort.

The IBEM has been shown to be a very powerful technique, but it can be made more powerful by several additions. First, since many coils are circularly symmetric in the azimuthal direction, a dramatic increase in calculation speed is achievable by incorporating this symmetry into the shape of the boundary elements. This would also result in more smooth wire paths. Second, additional terms may be included in the optimisation functional. A term that minimises the effect of the eddy currents induced in a nearby conducting surface on the field in the region of interest (ROI) can be incorporated into the design. It has been shown previous to this work that gradient coils may be designed that allow eddy

currents to be generated, but only in a way that generates transient magnetic fields in the ROI that are of the same form as the gradient field and can be easily compensated for by gradient pre-emphasis. Another term that could be included in the functional is one that minimises the induced electric field inside the body, to reduce the effect of peripheral nerve stimulation, which is currently limiting the slew rate of gradient coils. The method of designing active magnetic screening for coils is an interesting one that it would be good to test experimentally, by constructing such a coil. There are also a great many more possibilities for coil design with the IBEM, which could be explored for a variety of applications, not just in MRI.

8.3 Final Conclusions

Dynamic shimming is a method that has the potential to improve the quality of almost all of the applications of MRI that benefit from the signal-to-noise ratio increase at high (≥ 3 T) magnetic field strength. With the aim of implementing dynamic shimming, a set of insertable gradient and shim coils with low inductance have been designed, constructed and tested. An inverse boundary element method (IBEM) was employed to design these coils, and was found to be a very powerful tool for designing current carrying coils that are to generate a specified magnetic field. The way in which the IBEM was implemented in this work allowed a variety of coils to be produced, illustrating the benefits of this coil design method.

In addition, two novel shimming techniques have been developed. The first is parcellated dynamic shimming, a generalisation of dynamic shimming in which the shimming process is performed over small cuboidal sub-volumes of the whole volume. It has been demonstrated by simulation that this method is considerably more effective at reducing the susceptibility induced magnetic field inhomogeneity in the heads of 11 subjects than conventional dynamic shimming. The second shimming technique is of the use of a set of shim coils that generate a magnetic field variation derived from principal component analysis of the magnetic field maps of many subjects. This method is capable of shimming out higher spatial frequencies than is currently possible, and has been shown by simulation to only improve the homogeneity of the magnetic field when used together with standard spherical harmonic shimming techniques.

Bibliography

[1] P. Mansfield and A. A. Maudsley. Medical Imaging by NMR. *British Journal of Radiology*, **50**(591), 188–194, (1977).

[2] J. D. Jackson. *Classical Electrodynamics, 3rd Edition*. John Wiley and Sons, Ltd., (1998).

[3] M. H. Levitt. *Spin Dynamics: Basics of Nuclear Magnetic Resonance*. John Wiley and Sons, Ltd., (2001).

[4] R. H. Hashemi and W. G. Bradley. *MRI: The Basics*. Lippincott Williams and Wilkins, (1997).

[5] C. M. Collins, B. Yang, Q. X. Yang, and M. B. Smith. Numerical Calculations of the Static Magnetic Field in Three-Dimensional Multi-Tissue Models of the Human Head. *Magnetic Resonance Imaging*, **20**(5), 413–424, (2002).

[6] M. J. Caola. Solid Harmonics And Their Addition Theorems. *Journal of Physics A: Mathematical And General*, **11**(2), L23–L25, (1978).

[7] I. I. Rabi, J. R. Zacharias, S. Millman, and P. Kusch. A New Method of Measuring Nuclear Magnetic Moment. *Physical Review*, **53**(4), 318, (1938).

[8] F. Bloch, W. W. Hansen, and M. Packard. Nuclear Induction. *Physical Review*, **69**, 127, (1946).

[9] E. M. Purcell, H. C. Torrey, and R. V. Pound. Resonance Absorption by Nuclear Magnetic Moments in a Solid. *Physical Review*, **69**, 37–38, (1946).

[10] E. L. Hahn. Spin Echoes. *Physical Review*, **80**(4), 580–594, (1950).

[11] P. C. Lauterbur. Image Formation By Induced Local Interactions: Examples Employing Nuclear Magnetic-Resonance. *Nature*, **242**(5394), 190–191, (1973).

[12] A. Kumar, D. Welti, and R. R. Ernst. NMR Fourier Zeugmatography. *Journal of Magnetic Resonance*, **18**(1), 69–83, (1975).

[13] A. Haase, J. Frahm, D. Matthaei, W. Hanicke, and K. D. Merboldt. FLASH Imaging - Rapid NMR Imaging Using Low Flip-Angle Pulses. *Journal of Magnetic Resonance*, **67**(2), 258–266, (1986).

[14] J. Frahm, A. Haase, and D. Matthaei. Rapid NMR Imaging Of Dynamic Processes Using The FLASH Technique. *Magnetic Resonance In Medicine*, **3**(2), 321–327, (1986).

[15] P. Mansfield. Multi-Planar Image Formation Using NMR Spin Echoes. *Journal of Physics C: Solid State Physics*, **10**(3), L55–L58, (1977).

[16] S. Ogawa, D. W. Tank, R. Menon, J. M. Ellermann, S. G. Kim, H. Merkle, and K. Ugurbil. Intrinsic Signal Changes Accompanying Sensory Stimulation: Functional Brain Mapping With Magnetic Resonance Imaging. *Proceedings of the National Acadamy of Sciences of the USA*, **89**(13), 5951–5955, (1992).

[17] A. N. Garroway, P. K. Grannell, and P. Mansfield. Image Formation in NMR by a Selective Irradiative Process. *Journal of Physics C: Solid State Physics*, **7**(24), L457–L462, (1974).

[18] J. Pauly, D. Nishimura, and A. Macovski. A k-Space Analysis of Small-Tip-Angle Excitation. *Journal of Magnetic Resonance*, **81**, 43–56, (1989).

[19] D. B. Twieg. The k-Trajectory Formulation of the NMR Imaging Process with Applications in Analysis and Synthesis of Imaging Methods. *Medical Physics*, **10**(5), 610–621, (1983).

[20] S. Ljunggren. A Simple Graphical Representation of Fourier-Base Imaging Methods. *Journal of Magnetic Resonance*, **54**(2), 338–343, (1983).

[21] W. A. Edelstein, J. M. S. Hutchison, G. Johnson, and T. Redpath. Spin Warp NMR Imaging and Applications to Human Whole-Body Imaging. *Physics in Medicine and Biology*, **25**(4), 751–756, (1980).

[22] C. B. Ahn, J. H. Kim, and Z. H. Cho. High-Speed Spiral-Scan Echo Planar NMR Imaging .1. *IEEE Transactions on Medical Imaging*, **5**(21), 2–7, (1986).

[23] R. A. de Graaf. In Vivo *NMR Spectroscopy: Principles and Techniques*. John Wiley and Sons, Ltd., (1998).

[24] F. Roméo and D. I. Hoult. Magnet Field Profiling: Analysis and Correcting Coil Design. *Magnetic Resonance in Medicine*, **1**(1), 44–65, (1984).

[25] D. F. Hillenbrand, K. M. Lo, W. F. B. Punchard, T. G. Reese, and P. M. Starewicz. High-Order MR Shimming: A Simulation Study of the Effectiveness of Competing Methods, Using an Established Susceptibility Model of the Human Head. *Applied Magnetic Resonance*, **29**, 39–64, (2005).

[26] S. Crozier, C. Snape-Jenkinson, and L. Forbes. The Stochastic Design of Force-Minimized Compact Magnets for High-Field Magnetic Resonance Imaging Applications. *IEEE Transactions on Applied Superconductivity*, **11**(2), 4014–4022, (2001).

[27] R. Bhagwandien, R. van Ee, R. Beersma, C. J. Bakker, M. A. Moerland, and J. J. Lagendijk. Numerical Analysis of the Magnetic Field for Arbitrary Magnetic Susceptibility Distributions In 2D. *Magnetic Resonance Imaging*, **10**(2), 299–313, (1992).

[28] R. Bhagwandien, M. A. Moerland, C. J. Bakker, R. Beersma, and J. J. Lagendijk. Numerical Analysis of the Magnetic Field for Arbitrary Magnetic Susceptibility Distributions In 3D. *Magnetic Resonance Imaging*, **12**(1), 101–107, (1994).

[29] S. Li, G. D. Williams, T. A. Frisk, B. W. Arnold, and M. B. Smith. A Computer Simulation of the Static Magnetic Field Distribution in the Human Head. *Magnetic Resonance in Medicine*, **34**(2), 268–275, (1995).

[30] S. Li, B. J. Dardzinski, C. M. Collins, Q. X. Yang, and M. B. Smith. Three-Dimensional Mapping of the Static Magnetic Field Inside the Human Head. *Magnetic Resonance in Medicine*, **36**(5), 705–714, (1996).

[31] B. Yang, C. M. Collins, and M. B. Smith. Calculation of Static Magnetic Field Distortions in a Multi-tissue Human Head Model for MRI. *Proceedings of the International Society for Magnetic Resonance in Medicine*, **9**, 616, (2001).

[32] M. Jenkinson, J. M. Wilson, and P. Jezzard. Perturbation Calculation of B_0 Field For Non-Conducting Materials. *Proceedings of the International Society for Magnetic Resonance in Medicine*, **10**, 2325, (2002).

[33] T.-K. Truong, B. D. Clymer, D. W. Chakeres, and P. Schmalbrock. Three-Dimensional Numerical Simulations Of Susceptibility-Induced Magnetic Field Inhomogeneities In The Human Head. *Magnetic Resonance Imaging*, **20**(10), 759–770, (2002).

[34] K. Shmueli, P. Kinchesh, H. G. Parkes, D. L. Thomas, and R. J. Ordidge. AIRHEAD: an AnthropomorphIc Realistic HEAD Phantom to Test Susceptibility Artifact Reduction Techniques. *Proceedings of the International Society for Magnetic Resonance in Medicine*, **13**, 157, (2005).

[35] I. R. Young, I. J. Cox, D. J. Bryant, and G. M. Bydder. The Benefits Of Increasing Spatial Resolution As A Means Of Reducing Artifacts Due To Field Inhomogeneities. *Magnetic Resonance Imaging*, **6**(5), 585–590, (1988).

[36] K. D. Merboldt, J. Finsterbusch, and J. Frahm. Reducing Inhomogeneity Artifacts in Functional MRI of Human Brain Activation - Thin Sections vs Gradient Compensation. *Journal of Magnetic Resonance*, **145**(2), 184–191, (2000).

[37] K. Herberlein and X. Hu. Improved Shim By Subject Head Positioning. *Proceedings of the Society for Magnetic Resonance in Medicine*, **9**, 1157, (2001).

[38] Y. Zhao, A. W. Anderson, and J. C. Gore. Computer Simulation Studies of the Effects of Dynamic Dhimming on Susceptibility Artifacts in EPI at High Field. *Journal of Magnetic Resonance*, **173**(1), 10–22, (2005).

[39] K. Farahani, U. Sinha, S. Sinha, L. C.-L. Chiu, and R. B. Lufkin. Effect Of Field Strength On Susceptibility Artifacts In Magnetic Resonance Imaging. *Computerized Medical Imaging and Graphics*, **14**(6), 409–413, (1990).

[40] K. M. Lüdeke, P. Röschmann, and R. Tischler. Susceptibility Artefacts in NMR Imaging. *Magnetic Resonance Imaging*, **3**(4), 329–343, (1985).

[41] S. Posse and W. P. Aue. Susceptibility Artifacts In Spin-Echo And Gradient-Echo Imaging. *Journal of Magnetic Resonance*, **88**(3), 473–492, (1990).

[42] J. R. Reichenbach, R. Venkatesan, D. A. Yablonskiy, M. R. Thompson, S. Lai, and E. M. Haacke. Theory And Application Of Static Field Inhomogeneity Effects In Gradient-Echo Imaging. *Journal of Magnetic Resonance Imaging*, **7**(2), 266–279, (1997).

[43] A. M. Abduljalil, A. Kangarlu, Y. Yu, and P. M. Robitaille. Macroscopic Susceptibility in Ultra High Field MRI. II: Acquisition of Spin Echo Images From the Human Head. *Journal of Computer Assisted Tomography*, **23**(6), 842–844, (1999).

[44] A. M. Abduljalil and P. M. Robitaille. Macroscopic Susceptibility in Ultra High Field MRI. *Journal of Computer Assisted Tomography*, **23**(6), 832–841, (1999).

[45] P. Jezzard and R. S. Balaban. Correction for Geometric Distortion in Echo Planar Images from B_0 Field Variations. *Magnetic Resonance in Medicine*, **34**(1), 65–73, (1995).

[46] T. G. Reese, T. L. Davis, and R. M. Weisskoff. Automated Shimming At 1.5 T Using Echo-Planar Image Frequency Maps. *Journal of Magnetic Resonance Imaging*, **5**(6), 739–745, (1995).

[47] W. Conover. *Practical Guide to Shimming Superconducting NMR Magnets*, chapter 2, pages 37–51. John Wiley & Sons, Ltd., (1984).

[48] G. N. Chmurny and D. I. Hoult. The Ancient and Honourable Art of Shimming. *Concepts in Magnetic Resonance*, **2**(3), 131–149, (1990).

[49] R. R. Ernst. Measurement and Control of Magnetic Field Homogeneity. *Review of Scientific Instruments*, **39**(7), 998–1012, (1968).

[50] M. Tochtrop, W. Vollmann, D. Holz, and C. Leussler. Automatic Shimming of Selected Volumes in Patients. *Proceedings of the Society for Magnetic Resonance in Medicine*, **6**, 816, (1987).

[51] D. Holz, D. Jensen, R. Proksa, M. Tochtrop, and W. Vollmann. Automatic Shimming For Localized Spectroscopy. *Medical Physics*, **15**(6), 898–903, (1988).

[52] W. H. Press, B. P. Flannery, S. A. Teukolsky, and W. T. Vetterling. *Numerical Recipes in C: The Art of Scientific Computing*. Campbridge University Press, (1992).

[53] M. G. Prammer, J. C. Haselgrove, M. Shinnar, and J. S. Leigh. A New Approach to Automatic Shimming. *Journal of Magnetic Resonance*, **77**, 40–52, (1988).

[54] R. Gruetter and C. Boesch. Fast, Noniterative Shimming of Spatially Localized Signals. *In Vivo* Analysis of the Magnetic Field along Axes. *Journal of Magnetic Resonance*, **96**, 323–334, (1992).

[55] R. Gruetter. Automatic, localized *in vivo* Adjustment of All First- and Second-Order Shim Coils. *Magnetic Resonance in Medicine*, **29**(6), 804–811, (1993).

[56] J. Shen, R. E. Rycyna, and D. L. Rothman. Improvements on an *in Vivo* Automatic Shimming Method (FASTERMAP). *Magnetic Resonance in Medicine*, **38**(5), 834–839, (1997).

[57] L. M. Klassen and R. S. Menon. Robust Automated Shimming Technique Using Arbitrary Mapping Acquisition Parameters (RASTAMAP). *Magnetic Resonance in Medicine*, **51**(5), 881–887, (2004).

[58] H. Wen and F. A. Jaffer. An *in vivo* Automated Shimming Method Taking into Account Shim Current Constraints. *Magnetic Resonance in Medicine*, **34**(6), 898–904, (1995).

[59] J. Frahm, K. D. Merboldt, and W. Hänicke. Direct FLASH MR Imaging of Magnetic Field Inhomogeneities by Gradient Compensation. *Magnetic Resonance in Medicine*, **6**(4), 474–480, (1988).

[60] Q. X. Yang, B. J. Dardzinski, S. Li, P. J. Eslinger, and M. B. Smith. Multi-Gradient Echo with Susceptibility Inhomogeneity Compensation (MGESIC): Demonstration of fMRI in the Olfactory Cortex at 3.0 T. *Magnetic Resonance in Medicine*, **37**(3), 331–335, (1997).

[61] R. T. Constable. Functional MR Imaging Using Gradient-Echo Echo-Planar Imaging In The Presence Of Large Static Field Inhomogeneities. *Journal of Magnetic Resonance Imaging*, **5**(6), 746–752, (1995).

[62] Q. X. Yang, G. D. Williams, R. J. Demeure, T. J. Mosher, and M. B. Smith. Removal of Local Field Gradient Artifacts in T_2^*-Weighted Images at High Fields by Gradient-Echo Slice Excitation Profile Imaging. *Magnetic Resonance in Medicine*, **39**(3), 402–409, (1998).

[63] R. Constable and D. Spencer. Composite Image Formation In z-Shimmed Functional MR Imaging. *Magnetic Resonance in Medicine*, **42**(1), 110–117, (1999).

[64] G. H. Glover. 3D z-Shim Method for Reduction of Susceptibility Effects in BOLD fMRI. *Magnetic Resonance in Medicine*, **42**(2), 290–299, (1999).

[65] R. Deichmann, O. Josephs, C. Hutton, D. R. Corfield, and R. Turner. Compensation of Susceptibility-Induced BOLD Sensitivity Losses in Echo-Planar fMRI Imaging. *NeuroImage*, **15**(1), 120–135, (2002).

[66] A. M. Blamire, D. L. Rothman, and T. Nixon. Dynamic Shim Updating: A New Approach Towards Optimized Whole Brain Shimming. *Magnetic Resonance in Medicine*, **36**(1), 159–165, (1996).

[67] G. Morrell and D. Spielman. Dynamic Shimming For Multi-Slice Magnetic Resonance Imaging. *Magnetic Resonance in Medicine*, **38**(3), 477–483, (1997).

[68] R. A. de Graaf, P. B. Brown, S. McIntyre, D. L. Rothman, and T. W. Nixon. Dynamic Shim Updating (DSU) For Multislice Signal Acquisition. *Magnetic Resonance in Medicine*, **49**(3), 409–416, (2003).

[69] A. Jesmanowicz, J. S. Hyde, W. F. B. Punchard, and P. M. Starewicz. Method for Shimming a Static Magnetic Field in a Local MRI Coil, *US Patent, 6,294,972*, (2001).

[70] A. Jesmanowicz, P. Starewicz, and J. S. Hyde. Determination of Shims Needed for Correction of Tissue Susceptibility Effects in fMRI. *Proceedings of the International Society for Magnetic Resonance in Medicine*, **8**, 1378, (2000).

[71] A. Jesmanowicz, V. Roopchansingh, R. W. Cox, P. Starewicz, W. F. B. Punchard, and J. S. Hyde. Local Ferroshims Using Office Copier Toner. *Proceedings of the International Society for Magnetic Resonance in Medicine*, **9**, 617, (2001).

[72] J. L. Wilson, M. Jenkinson, and P. Jezzard. Optimization of Static Field Homogeneity in Human Brain Using Diamagnetic Passive Shims. *Magnetic Resonance in Medicine*, **48**(5), 906–914, (2002).

[73] J.-J. Hsu and G. H. Glover. Mitigation Of Susceptibility-Induced Signal Loss In Neuroimaging Using Localized Shim Coils. *Magnetic Resonance in Medicine*, **53**(2), 243–248, (2005).

[74] Z. H. Cho and Y. M. Ro. Reduction Of Susceptibility Artifact In Gradient-Echo Imaging. *Magnetic Resonance in Medicine*, **23**(1), 193–200, (1992).

[75] N.-k. Chen and A. M. Wyrwicz. Removal Of Intravoxel Dephasing Artifact In Gradient-Echo Images Using A Field-Map Based RF Refocusing Technique. *Magnetic Resonance in Medicine*, **42**(4), 807–812, (1999).

[76] V. A. Stenger, F. E. Boada, and D. C. Noll. Three-Dimensional Tailored RF Pulses for the Reduction of Susceptibility Artifacts in T_2^*-Weighted Functional MRI. *Magnetic Resonance in Medicine*, **44**(4), 525–531, (2000).

[77] J. M. Pauly, B. S. Hu, S. J. Wang, D. G. Nishimura, and A. Macovski. A Three-Dimensional Spin-Echo Or Inversion Pulse. *Magnetic Resonance in Medicine*, **29**(1), 2–6, (1993).

[78] V. A. Stenger, F. E. Boada, and D. C. Noll. Multishot 3D Slice-Select Tailored RF Pulses for MRI. *Magnetic Resonance in Medicine*, **48**(1), 157–165, (2002).

[79] V. A. Stenger, F. E. Boada, and D. C. Noll. Variable-Density Spiral 3D Tailored RF Pulses. *Magnetic Resonance in Medicine*, **50**(5), 1100–1106, (2003).

[80] P. B. Roemer, W. A. Edelstein, C. E. Hayes, S. P. Souza, and O. M. Mueller. The NMR Phased Array. *Magnetic Resonance in Medicine*, **16**(2), 192–225, (1990).

[81] D. K. Sodickson and W. J. Manning. Simultaneous Acquisition of Spatial Harmonics (SMASH): Fast Imaging with Radiofrequency Coil Arrays. *Magnetic Resonance in Medicine*, **38**(4), 591–603, (1997).

[82] K. P. Pruessmann, M. Weiger, M. B. Scheidegger, and P. Boesiger. SENSE: Sensitivity Encoding for Fast MRI. *Magnetic Resonance in Medicine*, **42**(5), 952–962, (1999).

[83] M. A. Griswold, P. M. Jakob, Q. Chen, J. W. Goldfarb, W. J. Manning, R. R. Edelman, and D. K. Sodickson. Resolution Enhancement In Single-Shot Imaging Using Simultaneous Acquisition Of Spatial Harmonics (SMASH). *Magnetic Resonance in Medicine*, **41**(6), 1236–1245, (1999).

[84] R. Bammer, S. L. Keeling, M. Augustin, K. P. Pruessmann, R. Wolf, R. Stollberger, H. P. Hartung, and F. Fazekas. Improved Diffusion-Weighted Single-Shot Echo-Planar Imaging (EPI) in Stroke Using Sensitivity Encoding (SENSE). *Magnetic Resonance in Medicine*, **46**(3), 548–554, (2001).

[85] M. Weiger, K. P. Pruessmann, R. Osterbauer, P. Börnert, P. Boesiger, and P. Jezzard. Sensitivity-Encoded Single-Shot Spiral Imaging for Reduced Susceptibility Artifacts in BOLD fMRI. *Magnetic Resonance in Medicine*, **48**(5), 860–866, (2002).

[86] G. H. Glover and C. S. Law. Spiral-In/Out BOLD fMRI For Increased SNR and Reduced Susceptibility Artifacts. *Magnetic Resonance in Medicine*, **46**(3), 515–522, (2001).

[87] J. L. Wilson, M. Jenkinson, I. de Araujo, M. L. Kringelbach, E. T. Rolls, and P. Jezzard. Fast, Fully Automated Global and Local Magnetic Field Optimization for fMRI of the Human Brain. *Neuroimage*, **17**(2), 967–976, (2002).

[88] R. M. Weisskoff and T. L. Davis. Correcting Gross Distortion on Echo Planar Images. *Proceedings of the Society for Magnetic Resonance in Medicine*, **11**, 4515, (1991).

[89] T. S. Sumanaweera, G. H. Glover, T. O. Binford, and J. R. Adler. MR Susceptibility Misregistration Correction. *IEEE Transactions on Medical Imaging*, **12**(2), 251–259, (1993).

[90] Y. M. Kadah and X. Hu. Simulated Phase Evolution Rewinding (SPHERE): A Technique for Reducing B_0 Inhomogeneity Effects in MR Images. *Magnetic Resonance in Medicine*, **38**(4), 615–627, (1997).

[91] D. C. Alsop and T. J. Connick. Optimization of Torque-Balanced Asymmetric Head Gradient Coils. *Magnetic Resonance in Medicine*, **35**(6), 875–886, (1996).

[92] M. Morich, D. A. Lampman, W. Dannels, and F. T. D. Goldie. Exact Temporal Eddy Current Compensation In Magnetic Resonance Imaging Systems. *IEEE Transactions on Medical Imaging*, **7**(3), 247–254, (1988).

[93] P. Jehenson, M. Westphal, and N. Schuff. Analytical Method For The Compensation Of Eddy-Current Effects Induced By Pulsed Magnetic-Field Gradients In Nmr Systems. *Journal of Magnetic Resonance*, **90**(2), 264–278, (1990).

[94] R. Turner. Gradient Coil Design: A Review Of Methods. *Magnetic Resonance Imaging*, **11**(7), 903–920, (1993).

[95] J.-M. Jin. *Electromagnetic Analysis and Design in Magnetic Resonance Imaging*. CRC Press LLC, (1998).

[96] M. Kamon, M. J. Tsuk, and J. K. White. FASTHENRY: A Multipole-Accelerated 3-D Inductance Extraction Program. *IEEE Transactions on Microwave Theory and Techniques*, **42**, 1750–1758, (1994).

[97] J. W. Carlson, K. A. Derby, K. C. Hawryszko, and M. Weideman. Design And Evaluation Of Shielded Gradient Coils. *Magnetic Resonance in Medicine*, **26**(2), 191–206, (1992).

[98] V. Vegh, H. W. Zhao, D. M. Doddrell, I. M. Brereton, and G. J. Galloway. The Design of Planar Gradient Coils. Part II: A Weighted Superposition Method. *Concepts in Magnetic Resonance Part B: Magnetic Resonance Engineering*, **27B**(1), 25–33, (2005).

[99] R. Turner. Minimum Inductance Coils. *Journal of Physics E: Scientific Instruments*, **21**(10), 948–952, (1988).

[100] Bowtell and Robyr. Multilayer Gradient Coil Design. *Journal of Magnetic Resonance*, **131**(2), 286–294, (1998).

[101] H. S. Lopez, F. Liu, A. Trakic, and S. Crozier. Torque-Figure of Merit Trade-off in Multi-Layer Asymmetric Gradient Coils. *Proceedings of the International Society for Magnetic Resonance in Medicine*, **14**, 778, (2006).

[102] C.-N. Chen and D. I. Hoult. *Biomedical Magnetic Resonance Technology*. IOP Publishing Ltd., (1989).

[103] M. J. E. Golay and N. J. Rumson. Nuclear Magnetic Resonance Apparatus, *US Patent, 3,569,823*, (1971).

[104] W. A. Anderson. Electrical Current Shims for Correcting Magnetic Fields. *Review of Scientific Instruments*, **32**(3), 241–250, (1961).

[105] I. Zupančič. Current Shims For High-Resolution Nuclear Magnetic Resonance On Problem Of Correcting Magnetic Field Inhomogeneities. *Journal of Scientific Instruments*, **39**(12), 621–624, (1962).

[106] R. S. Parker, I. Zupančič, and J. Pirš. Coil System To Produce Orthogonal, Linear Magnetic-Field Gradients. *Journal of Physics E: Scientific Instruments*, **6**(9), 899–900, (1973).

[107] I. Zupančič and J. Pirš. Coils Producing A Magnetic-Field Gradient For Diffusion Measurements With NMR. *Journal of Physics E: Scientific Instruments*, **9**(1), 79–80, (1976).

[108] V. Bangert and P. Mansfield. Magnetic-Field Gradient Coils For NMR Imaging. *Journal of Physics E: Scientific Instruments*, **15**(2), 235–239, (1982).

[109] M. A. Brideson, L. K. Forbes, and S. Crozier. Determining Complicated Winding Patterns for Shim Coils Using Stream Functions and the Target-Field Method. *Concepts in Magnetic Resonance*, **14**(1), 9–18, (2002).

[110] D. I. Hoult and R. Deslauriers. Accurate Shim-Coil Design And Magnet-Field Profiling By A Power-Minimization-Matrix Method. *Journal of Magnetic Resonance Series A*, **108**(1), 9–20, (1994).

[111] R. Turner. A Target Field Approach To Optimal Coil Design. *Journal of Physics D: Applied Physics*, **19**(8), L147–L151, (1986).

[112] R. Turner and R. M. Bowley. Passive Screening Of Switched Magnetic Field Gradients. *Journal of Physics E: Scientific Instruments*, **19**(10), 876–879, (1986).

[113] M. Engelsberg, R. E. D. Souza, and C. M. D. Pazos. The Limitations Of A Target Field Approach To Coil Design. *Journal of Physics D: Applied Physics*, **21**(7), 1062–1066, (1988).

[114] E. C. Wong, A. Jesmanowicz, and J. S. Hyde. Coil Optimization for MRI by Conjugate Gradient Descent. *Magnetic Resonance in Medicine*, **21**(1), 39–48, (1991).

[115] E. R. Andrew and E. Szczesniak. Low Inductance Transverse Gradient System Of Restricted Length. *Magnetic Resonance Imaging*, **13**(4), 607–613, (1995).

[116] W. W. Brey, T. H. Mareci, and J. Dougherty. A Field-Gradient Coil Using Concentric Return Paths. *Journal of Magnetic Resonance Series B*, **112**(2), 124–130, (1996).

[117] F. Shi and R. Ludwig. Magnetic Resonance Imaging Gradient Coil Design By Combining Optimization Techniques With The Finite Element Method. *IEEE Transactions on Magnetics*, **34**(3), 671–683, (1998).

[118] H. Lu, A. Jesmanowicz, S.-J. Li, and J. S. Hyde. Momentum-Weighted Conjugate Gradient Descent Algorithm For Gradient Coil Optimization. *Magnetic Resonance in Medicine*, **51**(1), 158–164, (2004).

[119] S. Crozier and M. Doddrell. Gradient Coil Design by Simulated Annealing. *Journal of Magnetic Resonance Series A*, **103**, 354–357, (1993).

[120] K. Adamiak, A. J. Czaja, and B. K. Rutt. Optimizing Strategy For MR-Imaging Gradient Coils. *IEEE Transactions on Magnetics*, **30**(6), 4311–4313, (1994).

[121] S. Crozier, L. K. Forbes, and D. M. Doddrell. The Design of Transverse Gradient Coils of Restricted Length by Simulated Annealing. *Journal of Magnetic Resonance Series A*, **107**(1), 126–128, (1994).

[122] S. Crozier and D. M. Doddrell. A Design Methodology For Short, Whole-Body, Shielded Gradient Coils For MRI. *Magnetic Resonance Imaging*, **13**(4), 615–620, (1995).

[123] M. L. Buszko, M. F. Kempka, E. Szczesniak, D. C. Wang, and E. R. Andrew. Optimization of Transverse Gradient Coils with Coaxial Return Paths by Simulated Annealing. *Journal of Magnetic Resonance Series B*, **112**(3), 207–213, (1996).

[124] S. Crozier, S. Dodd, and D. M. Doddrell. A Novel Design Methodology For Nth Order, Shielded Longitudinal Coils For NMR. *Measurement Science and Technology*, **7**(1), 36–41, (1996).

[125] Y. P. Du and D. L. Parker. Evaluation Of Gradient Inhomogeneity In The Optimal Design Of Gradient Coils. *Magnetic Resonance Imaging*, **14**(2), 201–207, (1996).

[126] Y. P. Du and D. L. Parker. Studies On The Performance Of Circular And Elliptical Z-Gradient Coils Using A Simulated Annealing Algorithm. *Magnetic Resonance Imaging*, **15**(2), 255–262, (1997).

[127] Y. P. Du and D. L. Parker. Optimal Design Of Gradient Coils In MR Imaging: Optimizing Coil Performance Versus Minimizing Cost Functions. *Magnetic Resonance in Medicine*, **40**(3), 500–503, (1998).

[128] S. Crozier and D. M. Doddrell. A Simple Design Methodology For Elliptical Cross-Section, Transverse, Asymmetric, Head Gradient Coils For MRI. *IEEE Transactions On Biomedical Engineering*, **45**(7), 945–948, (1998).

[129] S. Crozier, K. Luescher, G. Hinds, W. U. Roffmann, and D. M. Doddrell. Designs For An Asymmetric Gradient Set And A Compact Superconducting Magnet For Neural Magnetic Resonance Imaging. *Review of Scientific Instruments*, **70**(10), 4062–4066, (1999).

[130] D. Tomasi and H. Panepucci. Magnetic Fields Mapping With The Phase Reference Method. *Magnetic Resonance Imaging*, **17**(1), 157–160, (1999).

[131] D. Tomasi. Stream Function Optimization For Gradient Coil Design. *Magnetic Resonance in Medicine*, **45**(3), 505–512, (2001).

[132] D. Tomasi, R. Xavier, B. Foerster, H. Panepucci, A. Tannús, and E. Vidoto. Asymmetrical Gradient Coil For Head Imaging. *Magnetic Resonance in Medicine*, **48**(4), 707–714, (2002).

[133] S. J. Dodd, D. S. Williams, C. Olson, A. C. Silva, A. P. Koretsky, and C. Ho. An Open Transverse Z-Gradient Coil Design For Magnetic Resonance Imaging. *Review of Scientific Instruments*, **73**(5), 2208–2210, (2002).

[134] V. Vegh, H. W. Zhao, G. J. Galloway, D. M. Doddrell, and I. M. Brereton. The Design of Planar Gradient Coils. Part I: A Winding Path Correction Method. *Concepts*

in Magnetic Resonance Part B: Magnetic Resonance Engineering, **27B**(1), 17–24, (2005).

[135] D. L. Parker and J. R. Hadley. Gradient Arrays for High Performance Multiple Region MRI. *Proceedings of the International Society for Magnetic Resonance in Medicine*, **14**, 521, (2006).

[136] F. Qi, X. Tang, W. M. Wang, Y. F. Shen, S. P. Liu, and Z. D. Jiang. A New Simulated Annealing Method of Designing NMR Biplanar Shim Coils. *Progress in Natural Science*, **16**(7), 747–752, (2006).

[137] V. Vegh, H. W. Zhao, I. M. Brereton, G. J. Galloway, and D. M. Doddrell. A Wave Equation Technique for Designing Compact Gradient Coils. *Concepts in Magnetic Resonance Part B: Magnetic Resonance Engineering*, **29B**(2), 62–74, (2006).

[138] V. Vegh, H. Sanchez, I. M. Brereton, and S. Crozier. Toward Designing Asymmetric Head Gradient Coils for High-Resolution Imaging. *Concepts in Magnetic Resonance Part B: Magnetic Resonance Engineering*, **31B**(1), 1–11, (2007).

[139] B. J. Fisher, N. Dillon, T. A. Carpenter, and L. D. Hall. Design By Genetic Algorithm Of A Z-Gradient Set For Magnetic-Resonance-Imaging Of The Human Brain. *Measurement Science and Technology*, **6**(7), 904–909, (1995).

[140] B. J. Fisher, N. Dillon, A. A. Wilkinson, T. A. Carpenter, and L. D. Hall. Design And Evaluation Of A Transverse Gradient Set For Magnetic Resonance Imaging Of The Human Brain. *Measurement Science and Technology*, **7**(5), 838–843, (1996).

[141] J. Chládek, P. Konzbul, P. Ošmera, and A. Gottvald. Evolutionary And Genetic Optimization Of NMR Gradient And Shim. *IEEE Transactions on Magnetics*, **36**(4), 1102–1105, (2000).

[142] B. J. Fisher, N. Dillon, T. A. Carpenter, and L. D. Hall. Design Of A Biplanar Gradient Coil Using A Genetic Algorithm. *Magnetic Resonance Imaging*, **15**(3), 369–376, (1997).

[143] G. B. Williams, B. J. Fisher, C. L.-H. Huang, T. A. Carpenter, and L. D. Hall. Design of Biplanar Gradient Coils for Magnetic Resonance Imaging of the Human Torso and Limbs. *Magnetic Resonance Imaging*, **17**(5), 739–754, (1999).

[144] K. Adamiak, B. K. Rutt, and W. J. Dabrowski. Design Of Gradient Coils For Magnetic-Resonance-Imaging. *IEEE Transactions on Magnetics*, **28**(5), 2403–2405, (1992).

[145] P. Konzbul and K. Švéda. Shim Coils for NMR and MRI Solenoid Magnets. *Measurement Science and Technology*, **6**(8), 1116–1123, (1995).

[146] P. Konzbul, K. Sveda, and A. Srnka. Design Of Matrix Shim Coils System For Nuclear Magnetic Resonance. *IEEE Transactions on Magnetics*, **36**(4), 1732–1735, (2000).

[147] S. E. Ungersma, H. Xu, B. A. Chronik, G. C. Scott, A. Macovski, and S. M. Conolly. Shim Design Using a Linear Programming Algorithm. *Magnetic Resonance in Medicine*, **52**(3), 619–627, (2004).

[148] K. C. Chu and B. K. Rutt. Mr Gradient Coil Heat Dissipation. *Magnetic Resonance In Medicine*, **34**(1), 125–132, (1995).

[149] M. Poole and R. Bowtell. Short, Low Inductance Insert Shim Coils Designed Using the Slack Method. *Proceedings of the International Society for Magnetic Resonance in Medicine*, **13**, 775, (2005).

[150] I. Frollo. Parallel Plane Gradient System For NMR Experiments. *Review of Scientific Instruments*, **60**(11), 3442–3446, (1989).

[151] K. Yoda. Analytical Design Method of Self-Shielded Planar Coils. *Journal of Applied Physics*, **67**(9), 4349–4353, (1990).

[152] R. Bowtell and P. Mansfield. Gradient Coil Design Using Active Magnetic Screening. *Magnetic Resonance in Medicine*, **17**(1), 15–9; discussion 19–21, (1991).

[153] M. A. Martens, L. S. Petropoulos, R. W. Brown, J. H. Andrews, M. A. Morich, and J. L. Patrick. Insertable Biplanar Gradient Coils For Magnetic Resonance Imaging. *Review of Scientific Instruments*, **62**(11), 2639–2645, (1991).

[154] H. Liu. Finite Size Bi-Planar Gradient Coil for MRI. *IEEE Transactions on Magnetics*, **34**(4), 2162–2164, (1998).

[155] H. Liu and C. Truwit. True Energy-Minimal and Finite-Size Biplanar Gradient Coil Design for MRI. *IEEE Transactions on Medical Imaging*, **17**(5), 826–830, (1998).

[156] L. S. Petropoulos. Finite Size Disc Gradient Coil Set For Open Vertical Field Magnets. *Magnetic Resonance Imaging*, **18**(5), 615–624, (2000).

[157] E. C. de Caparelli, D. Tomasi, and H. Panepucci. Shielded Biplanar Gradient Coil Design. *Journal of Magnetic Resonance Imaging*, **9**(5), 725–731, (1999).

[158] L. Forbes and S. Crozier. Novel Target-Field Method For Designing Shielded Biplanar Shim And Gradient Coils. *IEEE Transactions on Magnetics*, **40**(4), 1929–1938, (2004).

[159] L. Forbes, M. Brideson, and S. Crozier. A Target-Field Method To Design Circular Biplanar Coils For Asymmetric Shim And Gradient Fields. *IEEE Transactions on Magnetics*, **41**(6), 2134–2144, (2005).

[160] S. Pissanetzky. Minimum Energy MRI Gradient Coils of General Geometry. *Measurement Science and Technology*, **3**(7), 667–673, (1992).

[161] C. H. Moon, H. W. Park, M. H. Cho, and S. Y. Lee. Design of Convex-Surface Gradient Coils for a Vertical-Field Open MRI System. *Measurement Science and Technology*, **11**(8), N89–N94, (2000).

[162] H. Liu and L. S. Petropoulos. Spherical Gradient Coil For Ultrafast Imaging. *The 41st Annual Conference On Magnetism And Magnetic Materials*, **81**(8), 3853–3855, (1997).

[163] C. C. Myers and P. B. Roemer. Highly Linear Asymmetric Transverse Gradient Coil Design for Head Imaging. *Proceedings of the Society for Magnetic Resonance in Medicine*, **12**, 711, (1991).

[164] D. C. Alsop. A Torque-Balanced, Asymmetric Gradient Coil for Imaging of the Brain. *Proceedings of the Society for Magnetic Resonance in Medicine*, **12**, (1993).

[165] A. M. Abduljalil, A. H. Aletras, and P. M. L. Robitaille. Torque Free Asymmetric Gradient Coils For Echo-Planar Imaging. *Magnetic Resonance In Medicine*, **31**(4), 450–453, (1994).

[166] T. Xin, Z. Donglin, and B. Shanglian. A New Design Method for Asymmetrical Head Gradient Coils Used for Superconducting MRI Scanner. *Progress in Natural Science*, **14**(9), 753–757, (2004).

[167] L. K. Forbes and S. Crozier. A Novel Target-Field Method For Finite-Length Magnetic Resonance Shim Coils: I. Zonal Shims. *Journal of Physics D: Applied Physics*, **34**(24), 3447–3455, (2001).

[168] L. K. Forbes and S. Crozier. A Novel Target-Field Method For Finite-Length Magnetic Resonance Shim Coils: II. Tesseral Shims. *Journal of Physics D: Applied Physics*, **35**(9), 839–849, (2002).

[169] L. K. Forbes and S. Crozier. A Novel Target-Field Method For Magnetic Resonance Shim Coils: III. Shielded Zonal And Tesseral Coils. *Journal of Physics D: Applied Physics*, **36**(2), 68–80, (2003).

[170] M. A. Brideson, L. K. Forbes, and S. Crozier. Winding Patterns For Actively Shielded Shim Coils With Asymmetric Target-Fields. *Measurement Science and Technology*, **14**(4), 484–493, (2003).

[171] D. A. Lampman, M. A. Morich, and L. Petropoulos. Wide Aperature Gradient Set, *US Patent*, *5,497,089*, (1996).

[172] S. Shvartsman, M. Morich, G. Demeester, and Z. Zhai. Ultrashort Shielded Gradient Coil Design with 3D Geometry. *Concepts in Magnetic Resonance Part B: Magnetic Resonance Engineering*, **26B**(1), 1–15, (2005).

[173] M. Morich, L. Petropoulos, and D. Lampman. Magnetic Resonance Insert Gradient Coils with Parabolic Returns for Improved Access, *US Patent*, *5,485,087*, (1996).

[174] S. Shvartsman, G. DeMeester, and M. Morich. Discrete Design of an Insert Gradient Coil for Head Imaging in High Field MRI. *Proceedings of the International Society for Magnetic Resonance in Medicine*, **14**, 1371, (2006).

[175] Q. Liu, D. G. Hughes, and P. S. Allen. General Expressions for the Magnetic Field and Stored Energy of Elliptic Cylinder Coils. *Journal of Magnetic Resonance Series B*, **113**(3), 222–227, (1996).

[176] T. N. Baig, T. P. Eagan, L. S. Petropoulos, W. A. Edelstein, M. Finnerty, X. Chen, and R. W. Brown. Shielding And Energy Advantages Of Capped Elliptical Coil Structures. *Proceedings of the International Society for Magnetic Resonance in Medicine*, **14**, 520, (2006).

[177] D. Green, J. Leggett, and R. Bowtell. Hemispherical Gradient Coils For Magnetic Resonance Imaging. *Magnetic Resonance in Medicine*, **54**(3), 656–668, (2005).

[178] J. Leggett, D. Green, and R. Bowtell. Insert Dome Gradient Coils for Brain Imaging. *Proceedings of the International Society for Magnetic Resonance in Medicine*, **14**, 779, (2006).

[179] R. Kimmlingen, M. Gebhardt, J. Schuster, M. Brand, F. Schmitt, and A. Haase. Gradient System Providing Continuously Variable Field Characteristics. *Magnetic Resonance in Medicine*, **47**(4), 800–808, (2002).

[180] G. N. Peeren. Stream Function Approach For Determining Optimal Surface Currents. *Journal of Computational Physics*, **191**(1), 305–321, (2003).

[181] R. A. Lemdiasov and R. Ludwig. A Stream Function Method For Gradient Coil Design. *Concepts in Magnetic Resonance Part B: Magnetic Resonance Engineering*, **26B**(1), 67–80, (2005).

[182] A. vom Endt, R. Kimmlingen, J. Riegler, E. Eberlein, and F. Schmitt. A High-Performance Head Gradient Coil For 7T Systems. *Proceedings of the International Society for Magnetic Resonance in Medicine*, **14**, 1370, (2006).

[183] M. Poole and R. Bowtell. An Insertable, Shoulder-Slotted Gradient and Shim Set for Dynamic Shimming. *Proceedings of the British Chapter of the International Society for Magnetic Resonance in Medicine*, **12**, 02, (2006).

[184] M. Poole and R. Bowtell. Ultra-Efficient Shielded Dome Gradient Coils. *Proceedings of the British Chapter of the International Society for Magnetic Resonance in Medicine*, **12**, P22, (2006).

[185] M. Poole and R. Bowtell. Ultra-Short Shielded Gradient Coils. *Proceedings of the European Society for Magnetic Resonance in Medicine and Biology*, **23**, 740, (2006).

[186] C. Cobos Sanchez, L. Marin, R. W. Bowtell, H. Power, P. Glover, A. A. Becker, and I. A. Jones. Application of Higher-Order Boundary Element Method to Gradient Coil Design. *Proceedings of the British Chapter of the International Society for Magnetic Resonance in Medicine*, **12**, P23, (2006).

[187] M. Poole and R. Bowtell. Novel Gradient Coils Designed Using a Boundary Element Method. *Concepts in Magnetic Resonance Part B: Magnetic Resonance Engineering*, **in press**, (2007).

[188] W. A. Edelstein, R. A. Hedeen, R. P. Mallozzi, S.-A. El-Hamamsy, R. A. Ackermann, and T. J. Havens. Making MRI Quieter. *Magnetic Resonance Imaging*, **20**(2), 155–163, (2002).

[189] P. Mansfield and B. Chapman. Active Magnetic Screening Of Gradient Coils In NMR Imaging. *Journal of Magnetic Resonance*, **66**(3), 573–576, (1986).

[190] P. Mansfield and B. Chapman. Active Magnetic Screening of Coils for Static and Time-Dependent Magnetic Field Generation in NMR Imaging. *Journal of Physics E: Scientific Instruments*, **19**(7), 540–545, (1986).

[191] P. Mansfield and B. Chapman. Multishield Active Magnetic Screening Of Coil Structures In NMR. *Journal of Magnetic Resonance*, **72**(2), 211–223, (1987).

[192] R. Bowtell and P. Mansfield. Screened Coil Designs For NMR Imaging In Magnets With Transverse Field Geometry. *Measurement Science and Technology*, **1**(5), 431–439, (1990).

[193] D. Tomasi, E. C. Caparelli, H. Panepucci, and B. Foerster. Fast Optimization of a Biplanar Gradient Coil Set. *Journal of Magnetic Resonance*, **140**(2), 325–339, (1999).

[194] T. N. Baig, T. P. Eagan, L. S. Petropoulos, T. Kidane, W. A. Edelstein, and R. W. Brown. Gradient Coil With Active Endcap Shielding. *Concepts in Magnetic Resonance Part B: Magnetic Resonance Engineering*, **31B**(1), 12–23, (2007).

[195] P. R. Harvey and E. Katznelson. Modular Gradient Coil: A New Concept In High-Performance Whole-Body Gradient Coil Design. *Magnetic Resonance in Medicine*, **42**(3), 561–570, (1999).

[196] J. Leggett, S. Crozier, and R. W. Bowtell. Actively Shielded Multi-Layer Gradient Coil Designs With Improved Cooling Properties. *Journal of Magnetic Resonance*, **165**(2), 196–207, (2003).

[197] R. W. Brown and S. M. Shvartsman. Supershielding: Confinement Of Magnetic Fields. *Physical Review Letters*, **83**(10), 1946–1949, (1999).

[198] S. M. Shvartsman, R. W. Brown, Y. C. Cheng, T. P. Eagan, H. Fujita, M. A. Morich, L. S. Petropoulos, and J. D. Willig. Application of the SUSHI Method to the Design of Gradient Coils. *Magnetic Resonance in Medicine*, **45**(1), 147–155, (2001).

[199] S. Shvartsman, R. Brown, Y.-C. Cheng, T. Eagan, and J. Willig. Supershielding: Trapping of Magnetic Fields. *IEEE Transactions on Magnetics*, **37**(5), 3116–3119, (2001).

[200] P. Mansfield, A. M. Blamire, R. Coxon, P. Gibbs, D. N. Guilfoyle, P. Harvey, and M. Symms. Snapshot Echo-Planar Imaging Methods Current Trends And Future Perspectives. *Philosophical Transactions Of The Royal Society Of London Series A - Mathematical Physical And Engineering Sciences*, **333**(1632), 495–506, (1990).

[201] V. Taracila, L. S. Petropoulos, and R. W. Brown. Novel Design Method For Gradient Coil Structures With Reduced Acoustic Noise Characteristics. *Proceedings of the International Society for Magnetic Resonance in Medicine*, **14**, 1366, (2006).

[202] K. J. Lee, M. N. Paley, I. D. Wilkinson, and P. D. Griffiths. Fast two-dimensional MR imaging by Multiple Acquisition with Micro B_0 Array (MAMBA). *Magnetic Resonance Imaging*, **20**(1), 119–125, (2002).

[203] M. N. Paley, K. J. Lee, J. M. Wild, E. H. Whitby, and P. D. Griffiths. Interleaved Pulsed MAMBA: A New Parallel Slice Imaging Method. *Magnetic Resonance in Medicine*, **48**(6), 1043–1050, (2002).

[204] G. N. Peeren. *Stream Function Approach For Determining Optimal Surface Currents*. PhD thesis, Technische Universiteit Eindhoven, (2003).

[205] H. T. Rathod, K. V. Nagaraja, B. Venkatesudu, and N. L. Ramesh. Gauss Legendre Quadrature Over A Triangle. *Journal of the Indian Institute of Science*, **84**, 183–188, (2004).

[206] T. F. Eibert and V. Hansen. On The Calculation Of Potential Integrals For Linear Source Distributions On Triangular Domains. *IEEE Transactions On Antennas And Propagation*, **43**(12), 1499–1502, (1995).

[207] P.-O. Persson and G. Strang. A Simple Mesh Generator in MATLAB. *SIAM Review*, **46**(2), 329–345, (2004).

[208] B. Delaunay. Sur La Sphère Vide. *Bulletin of the Russian Academy of Sciences*, **7**, 793–800, (1934).

[209] S. Clare, M. Jenkinson, and J. Evans. High Order Dynamic Shimming: Issues of Implementation without Eddy Current Compensation. *ISMRM Workshop on Advances in High Field MR*, **5**, (2007).

[210] E. K. Yucel, C. M. Anderson, R. R. Edelman, T. M. Grist, R. A. Baum, W. J. Manning, A. Culebras, and W. Pearce. Magnetic Resonance Angiography: Update on Applications for Extracranial Arteries. *Circulation*, **100**(22), 2284–2301, (1999).

[211] E. O. Stejskal and J. E. Tanner. Spin Diffusion Measurements: Spin Echoes in the Presence of a Time-Dependent Field Gradient. *The Journal of Chemical Physics*, **42**(1), 288–292, (1965).

[212] P. Brugières, P. Thomas, A. Maraval, H. Hosseini, C. Combes, A. Chafiq, L. Ruel, S. Breil, M. Peschanski, and A. Gaston. Water Diffusion Compartmentation at High b Values in Ischemic Human Brain. *American Journal of Neuroradiology*, **25**(5), 692–698, (2004).

[213] M. Feygin. Apparatus and Method for Forming an Integral Object From Laminations, *US Patent*, *4,752,352*, (1988).

[214] P. Kestelman. Condom Testing: Part 2. *Planned Parenthood in Europe Regional Information Bulletin*, **3**(1), 4–6, (1974).

[215] A. J. Lucas, R. C. Hawkes, R. E. Ansorge, G. B. Williams, R. E. Nutt, J. C. Clark, T. D. Fryer, and T. A. Carpenter. Development of a Combined microPET-MR System. *Technology in Cancer Research and Treatment*, **5**(4), 826–830, (2006).

[216] D. G. Hughes, R. Teshima, Q. Liu, and P. S. Allen. Compact, Cylindrical, Distributed-Current, Transverse-Gradient Coils for Use in MRI. *Journal of Magnetic Resonance Series B*, **110**(2), 158–163, (1996).

[217] S. Crozier, W. U. Roffmann, K. Luescher, C. Snape-Jenkinson, L. K. Forbes, and D. M. Doddrell. An "Openable," High-Strength Gradient Set for Orthopedic MRI. *Journal of Magnetic Resonance*, **139**(1), 81–89, (1999).

[218] T. F. Budinger, H. Fischer, D. Hentschel, H. E. Reinfelder, and F. Schmitt. Physiological-Effects Of Fast Oscillating Magnetic-Field Gradients. *Journal of Computer Assisted Tomography*, **15**(6), 909–914, (1991).

[219] W. Irnich and F. Schmitt. Magnetostimulation in MRI. *Magnetic Resonance in Medicine*, **33**(5), 619–623, (1995).

[220] D. L. Parker and J. R. Hadley. Multiple-Region Gradient Arrays For Extended Field Of View, Increased Performance, And Reduced Nerve Stimulation In Magnetic Resonance Imaging. *Magnetic Resonance in Medicine*, **56**(6), 1251–1260, (2006).

[221] A. Oppelt. Nuclear Magnetic Resonance Tomography Device And Method For Its Operation, *US Patent 6,255,821*, *6,255,821*, (2001).

[222] M. Poole and R. Bowtell. Volume Parcellation for Improved Efficiency of Dynamic Shimming. *Proceedings of the British Chapter of the International Society for Magnetic Resonance in Medicine*, **13**, P2271, (2005).

[223] M. Poole and R. Bowtell. Evaluation of Parcellated Dynamic Shimming. *ISMRM Workshop on Advances in High Field MR*, **5**, (2007).

[224] K. M. Koch, P. B. Brown, D. L. Rothman, and R. A. de Graaf. Sample-Specific Diamagnetic And Paramagnetic Passive Shimming. *Journal of Magnetic Resonance*, **182**(1), 66–74, (2006).

[225] W. Xu and I. Cumming. A Region-Growing Algorithm for InSAR Phase Unwrapping. *IEEE Transactions on Geoscience and Remote Sensing*, **37**(1), 124–134, (1999).

[226] S. M. Smith. Fast Robust Automated Brain Extraction. *Human Brain Mapping*, **17**(3), 143–155, (2002).

[227] K. Lee, M. Paley, D. Barber, I. Wilkinson, and P. Griffiths. Target Field Design For MAMBA Step Fields. *Concepts in Magnetic Resonance Part B: Magnetic Resonance Engineering*, **20B**(1), 1–8, (2004).

[228] R. Bowtell and A. Peters. Analytic Approach To The Design Of Transverse Gradient Coils With Co-Axial Return Paths. *Magnetic Resonance in Medicine*, **41**(3), 600–608, (1999).

[229] F. Okada, S. Handa, and K. Kose. Gradient Coil Array for the Super-Parallel MRI: Theory and Design. *Proceedings of the International Society for Magnetic Resonance in Medicine*, **15**, 3287, (2007).

[230] J. Hennig, M. Zaitsev, , and O. Speck. PatLoc: Imaging in Non-Bijective, Curvilinear Magnetic Field Gradients. *Proceedings of the International Society for Magnetic Resonance in Medicine*, **15**, 453, (2007).

[231] N. Saad and S. Peled. Easy 3D Phase Unwrapping. *Proceedings of the International Society for Magnetic Resonance in Medicine*, **13**, 2251, (2005).

[232] K. M. Koch, S. McIntyre, T. W. Nixon, D. L. Rothman, and R. A. de Graaf. Dynamic Shim Updating On The Human Brain. *Journal of Magnetic Resonance*, **180**(2), 286–296, (2006).

[233] T. F. Coleman and Y. Y. Li. An Interior Trust Region Approach For Nonlinear Minimization Subject To Bounds. *SIAM Journal On Optimization*, **6**(2), 418–445, (1996).

[234] P. Mansfield, A. M. Howseman, and R. J. Ordidge. Volumar Imaging Using NMR Spin Echoes: Echo-Volumar Imaging (EVI) at 0.1 T. *Journal of Physics E: Scientific Instruments*, **22**(5), 324–330, (1989).

[235] S. Singh, B. K. Rutt, and R. M. Henkelman. Projection Presaturation: A Fast And Accurate Technique For Multidimensional Spatial Localization. *Journal of Magnetic Resonance*, **87**(3), 567–583, (1990).

[236] P. A. Bottomley and C. J. Hardy. Two-Dimensional Spatially Selective Spin Inversion And Spin-Echo Refocusing With A Single Nuclear Magnetic Resonance Pulse. *Journal of Applied Physics*, **62**(10), 4284–4290, (1987).

[237] U. Katscher, P. Bornert, C. Leussler, and J. S. van den Brink. Transmit SENSE. *Magnetic Resonance in Medicine*, **49**(1), 144–150, (2003).

[238] M. J. Berger and P. Colella. Local Adaptive Mesh Refinement For Shock Hydrodynamics. *Journal o f Computational Physics*, **82**(1), 64–84, (1989).

[239] K. Bartusek, Z. Dokoupil, and E. Gescheidtova. Magnetic Field Mapping Around Metal Implants Using an Asymmetric Spin-Echo MRI Sequence. *Measurement Science and Technology*, **17**(12), 3293–3300, (2006).

Appendix A

Tables of Coil Properties

This appendix details many properties of the coils described in this thesis. It is intended to serve as a way of presenting the data without putting it all in the main body of the text, and to allow comparisons between all the coils to be simply made. Each table of this appendix is split into four sections as outlined below.

Information about the coil design is given in the first section of the table such as a name for the coil, the method used to design it, the geometry of the coil and a reference to where it appears in the main body of the thesis. It also gives the type of coil, *i.e.* a Z-gradient, and the order, n, and degree, m, of the spherical harmonic it is designed to produce. Not all the coils in this thesis are designed to generate magnetic fields that conform to the shape of spherical harmonics. The scale of the coil is given, which for cylindrical geometries is the radius of the current carrying cylinder, but in cases where the surface is asymmetric it is used as a measure that describes the approximate scale of the coil. The volume of the region of uniformity (ROU), V, of the coil is given in m^3. For coils that were not designed with a method that prescribes a target ROU, such as the minimum inductance method § 4.4.3, an ellipsoid is fitted to the region over which the error in the magnetic field is less than 5%. V is then equal to the volume of this ellipsoid. For methods that parameterise the current density, the number of basis functions used in the parameterisation is given in the first section of the table, as well as the number of target points used to prescribe the form of the desired magnetic field.

The second section of the table lists the input parameters used to obtain the coil design. These parameters commonly include the inductance and resistance minimisation trade-off parameters, α and β. If the coil incorporates active magnetic screening, the shielding weighting factor, γ, (*e.g.* § 5.2.8) is given. The number of turns or wire, N_{cont}, that are used to approximate the continuous current density, is given. For coils designed with discrete

methods, N_{cont}, is the number of turns of wire used in the design. Another row is provided to note if mutual inductance minimisation has been employed in the design process and with which coil.

The third section of the table details the main properties of the coil design. The efficiency, η, (sometimes referred to as the coil sensitivity) of the coil is the first result presented in this section of the table. It characterises the scale of the magnetic field the coil generates with 1A flowing in it relative to the target field, and is in units of $\mu\text{Tm}^{-n}\text{A}^{-1}$ for coils that are designed to generate a magnetic field in the form of spherical harmonics. For coils that do not generate spherical harmonic shaped magnetic fields the units of η are μTA^{-1}. The next two rows present $\max(\Delta B_z)$ and $\max(B_z^S)$, the maximum error in the magnetic field over the ROU, and the region of shielding (ROS) respectively. These numbers are expressed as a percentage of the maximum value of magnetic field generated over the ROU and calculated using Eq. (4.3). The first of each of these two figures is calculated using the continuous current density, and the second figure is worked out via Biot-Savart integration over the wire-paths of the coil. Any discrepancy between these values is a consequence of the discretisation of the current density into wires. Another measure that has been used in other gradient coil design work is the non-linearity and non-uniformity of the magnetic field generated by the coil as given by Eqs. (24, 25) in Ref. [198].

Since self-inductance, L, and resistance, R, of a coil design are important properties, often minimised in the design process, they are given in these tables. The first L value is a theoretical value that is calculated in the coil design process and scaled using η. The second L and R values are simulated in FastHenry©, a multipole impedance extraction tool [96]. Unless otherwise stated, the coil was simulated using 2.659×2.659 mm square cross-section wire, which has the same cross-sectional area as 3 mm diameter circular cross-section wire. The spacing between the two closest wires of the coil, $\min(\Delta w)$, is given since this is often an important engineering constraint. Finally in this section of the table, the x- and y-components of the torque vector, M_x and M_y, are calculated by integration of the cross product of the static magnetic field, $\mathbf{B}_0(\mathbf{r})$, and the direction of flow of current over the wire-path of the whole coil design (5.29). Any torque values less than 1×10^{-6} $\text{NmA}^{-1}\text{T}^{-1}$ are rounded to 0. Since $\mathbf{B}_0(\mathbf{r})$ is always defined as uniform and oriented in the z-direction (*i.e.* $\mathbf{B}_0(\mathbf{r}) = B_z$) the z-component of the torque vector, $M_z = 0$.

The bottom portion of the table presents the η^2/L figure of merit (FOM) and the scale-normalised FOM, $a^{(2n+3)}\eta^2/L$, which have units of $\text{T}^2\text{m}^{-2n}\text{A}^{-2}\text{H}^{-1}$ and $\text{T}^2\text{m}^3\text{A}^{-2}\text{H}^{-1}$ respectively. Again, n is treated as equal to zero for coils that were designed to generate magnetic fields that do not conform to the shape of a spherical harmonic.

The last three properties are the slew-rate, SR, the rise-time, τ, and the maximum

gradient strength, $G_{\max}$ which are given by Eqs. (A.1), (A.2) and (A.3) and have the units of $\mathrm{Tm}^{-n}\mathrm{s}^{-1}$, μs and mTm^{-n} respectively. These are important properties when comparing the operational performance of coils when they are connected to a power supply.

$$SR = \frac{V_a \eta}{L} \tag{A.1}$$

$$\tau = \frac{L I_a}{V_a} \tag{A.2}$$

$$G_{max} = I_a \eta \tag{A.3}$$

where an $I_a = 600$A, $V_a = 600$V power supply is assumed for all the gradient coils, and $I_a = 5$A, $V_a = 20$V for all shim coils in this thesis unless otherwise stated.

The following are the proportionalities of some of the properties to the scale of the coil, a. These are essential when comparing coils of different sizes.

$$\eta \propto a^{-(n+1)} \tag{A.4}$$

$$L \propto a \tag{A.5}$$

$$R \propto a \tag{A.6}$$

$$|\mathbf{M}| \propto a^2 \tag{A.7}$$

$$SR \propto a^{-(n+2)} \tag{A.8}$$

$$G_{\max} \propto a^{-(n+1)} \tag{A.9}$$

$$\tau \propto a \tag{A.10}$$

Property	Coil			
Name	Helmholtz	Maxwell	Z2 Shim	Golay
Design Method	Discrete	Discrete	Discrete	Discrete
Geometry	Cylinder	Cylinder	Cylinder	Cylinder
Reference	Fig. 4.1 **a)**	Fig. 4.2 **a)**	Fig. 4.3 **a)**	Fig. 4.4 **a)**
Coil Type	Z0 Shim	Z-Gradient	Z2 Shim	X-Gradient
SH Order, n	0	1	2	1
SH Degree, m	0	0	0	1
Coil Scale, a (m)	1.0	1.0	1.0	1.0
Ellipsoidal ROU, V (m^3)	0.613	1.186	2.1886	0.642
No. Basis Functions, N	-	-	-	-
No. Target Points, K	-	-	-	-
Self-Inductance Min., α	-	-	-	-
Resistance Min., β	-	-	-	-
Shielding Weight, γ	-	-	-	-
Turns/ψ-Contours, N_{cont}	1	1	7	1
Mutual-Inductance Min. (μH)	-	-	-	-
η, ($\mu \text{Tm}^{-n}\text{A}^{-1}$)	0.899	0.810	2.19	0.913
$\max(\Delta B_z)$ (%)	-, 5.0	-, 5.0	-, 5.0	-, 5.0
$\max(B_z^S)$ (%)	-, -	-, -	-, -	-, -
Nonuni., Nonlin. (%)	-, -	-, -	-, -	-, -
L (μH)	-, 17.8	-, 16.7	-, 504.6	-, 47.1
R (mΩ)	76	31	215	83
$\min(\Delta w)$ (mm)	-	-	3	-
M_x ($\text{NmA}^{-1}\text{T}^{-1}$)	0	0	0	0
M_y ($\text{NmA}^{-1}\text{T}^{-1}$)	0	0	0	0
η^2/L ($\text{T}^2\text{m}^{-2n}\text{A}^{-2}\text{H}^{-1}$)	4.55×10^{-8}	3.93×10^{-8}	2.23×10^{-8}	1.00×10^{-8}
$a^{(2n+3)}\eta^2/L$ ($\text{T}^2\text{m}^3\text{A}^{-2}\text{H}^{-1}$)	4.55×10^{-8}	3.93×10^{-8}	2.23×10^{-8}	1.00×10^{-8}
SR ($\text{Tm}^{-n}\text{s}^{-1}$)	1.01	29.1	0.087	6.57
τ (μs)	4.45	16.7	126.2	83.4
$G_{\max}$, (mTm^{-n})	0.0045	0.486	0.011	0.5478

Table A.1: Coil Properties.

Property	Coil			
Name	Turner	Turner	Apodised	Carlson
Design Method	Target Field	Min Ind[a]	Min Ind[a]	Finite Length
Geometry	∞ Cylinder	∞ Cylinder	∞ Cylinder	Cylinder
Reference	Fig. 4.6 **a)**	Fig. 4.7 **a)**	Fig. 4.8 **b)**	Fig. 4.9 **a)**
Coil Type	X-Gradient	X-Gradient	X-Gradient	X-Gradient
SH Order, n	1	1	1	1
SH Degree, m	1	1	1	1
Coil Scale, a (m)	1.0	1.0	1.0	1.0
Ellipsoidal ROU, V (m^3)	3.179	2.372	2.527	2.291
No. Basis Functions, N	-	29	29	19
No. Target Points, K	∞	29	29	21
Self-Inductance Min., α	-	-	-	1×10^{-8}
Resistance Min., β	-	-	-	0
Shielding Weight, γ	-	-	-	-
Turns/ψ-Contours, N_{cont}	10	10	10	10
Mutual-Inductance Min. (μH)	-	-	-	-
η, ($\mu \text{Tm}^{-n}\text{A}^{-1}$)	5.00	5.10	5.24	4.28
max(ΔB_z) (%)	-, 5.0	-, 5.0	-, 5.0	-, 5.0
max(B_z^S) (%)	-, 48.3[b]	-, -	-, -	-, -
Nonuni., Nonlin. (%)	-, -	-, -	-, -	-, -
L (μH)	-, 735.2	-, 583.9	-, 578.1	-, 542.4
R (mΩ)	546	549	494	452
min(Δw) (mm)	92.8	30.8	41.9	17.4
M_x ($\text{NmA}^{-1}\text{T}^{-1}$)	0	0	0	0
M_y ($\text{NmA}^{-1}\text{T}^{-1}$)	0	0	0	0
η^2/L ($\text{T}^2\text{m}^{-2n}\text{A}^{-2}\text{H}^{-1}$)	3.40×10^{-8}	4.45×10^{-8}	4.75×10^{-8}	3.38×10^{-8}
$a^{(2n+3)}\eta^2/L$ ($\text{T}^2\text{m}^3\text{A}^{-2}\text{H}^{-1}$)	3.40×10^{-8}	4.45×10^{-8}	4.75×10^{-8}	3.38×10^{-8}
SR ($\text{Tm}^{-n}\text{s}^{-1}$)	5.49	5.24	5.44	4.73
τ (μs)	735.2	583.9	578.1	542.4
G_{max}, (mTm^{-n})	3.00	3.06	3.14	2.57

Table A.2: Coil Properties.

[a] Minimum Inductance

[b] Evaluated over an infinitely long, 1.4m diameter cylinder, for comparison with the shielded example in Table A.3.

Property	Coil			
Name	Bi-planar	Spherical	Shielded	X
Design Method	IBEM	IBEM	Target Field	IBEM
Geometry	Bi-Planar	Sphere	∞ Cylinders	Cylinder
Reference	Fig. 4.10 **a)**	Fig. 4.11 **a)**	Fig. 4.12 **a)**	Fig. 5.14 **a)**
Coil Type	X-Gradient	X-Gradient	X-Gradient	X-Gradient
SH Order, n	1	1	1	1
SH Degree, m	1	1	1	1
Coil Scale, a (m)	0.2	1.0	1.0	0.25
Ellipsoidal ROU, V (m^3)	0.0042	1.44	3.13	0.0048
No. Basis Functions, N	3082	1298	-	672
No. Target Points, K	66	1298	∞	57
Self-Inductance Min., α	2.3×10^{-7}	5.2×10^{-6}	-	9.5×10^{-8}
Resistance Min., β	0	0	-	0
Shielding Weight, γ	-	-	-	-
Turns/ψ-Contours, N_{cont}	10	10	10	10
Mutual-Inductance Min. (μH)	-	-	-	-
η, ($\mu \text{Tm}^{-n}\text{A}^{-1}$)	125	15.8	2.27	114
max(ΔB_z) (%)	5.0, 5.0	4.9, 5.0	5.0, 5.0	5.1, 5.0
max(B_z^S) (%)	-, -	-, -	-, 20.4[a]	-, -
Nonuni., Nonlin. (%)	16.0, 4.6	1.8, 1.1	-, -	0.6, 17.3
L (μH)	101, 108	495, 564	-, 589	133, 145
R (mΩ)	100	361	1109	118
min(Δw) (mm)	7.62	49.1	121.6	10.3
M_x ($\text{NmA}^{-1}\text{T}^{-1}$)	$< 1 \times 10^{-6}$	-1.9×10^{-4}	0	9.9×10^{-4}
M_y ($\text{NmA}^{-1}\text{T}^{-1}$)	$< 1 \times 10^{-6}$	$< 1 \times 10^{-6}$	0	$< 1 \times 10^{-6}$
η^2/L ($\text{T}^2\text{m}^{-2n}\text{A}^{-2}\text{H}^{-1}$)	1.56×10^{-4}	5.07×10^{-7}	8.75×10^{-9}	9.84×10^{-5}
$a^{(2n+3)}\eta^2/L$ ($\text{T}^2\text{m}^3\text{A}^{-2}\text{H}^{-1}$)	4.99×10^{-8}	5.07×10^{-7}	8.75×10^{-9}	9.61×10^{-8}
SR ($\text{Tm}^{-n}\text{s}^{-1}$)	693	16.8	2.31	472
τ (μs)	108	564	589	145
G_{max}, (mTm^{-n})	75.0	9.5	1.36	68.4

Table A.3: Coil Properties.

[a]Evaluated over an infinitely long, 1.4m diameter cylinder, for comparison with the shielded example in Table A.2.

Property	Coil			
Name	Torque	No-Torque	Coupled	Uncoupled
Design Method	IBEM	IBEM	IBEM	IBEM
Geometry	Asym Cyl[a]	Asym Cyl[a]	Cylinder	Cylinder
Reference	Fig. 5.15 **a)**	Fig. 5.15 **b)**	Fig. 5.16 **b)**	Fig. 5.16 **c)**
Coil Type	X-Gradient	X-Gradient	Z2X Shim	Z2X Shim
SH Order, n	1	1	3	3
SH Degree, m	1	1	1	1
Coil Scale, a (m)	0.25	0.25	0.65	0.65
Ellipsoidal ROU, V (m^3)	0.0048	0.0048	0.00134	0.00134
No. Basis Functions, N	672	672	630	630
No. Target Points, K	57	57	66	66
Self-Inductance Min., α	2.7×10^{-8}	1.7×10^{-8}	5.0×10^{-11}	2.0×10^{-11}
Resistance Min., β	0	0	0	0
Shielding Weight, γ	-	-	-	-
Turns/ψ-Contours, N_{cont}	10	10	10	10
Mutual-Inductance Min. (μH)	-	-	6.6[b]	0.3[b]
η, ($\mu \text{Tm}^{-n}\text{A}^{-1}$)	79.3	64.8	25.2	20.5
max(ΔB_z) (%)	4.7, 5.0	5.9, 5.0	10.1, 9.3	10.1, 13.5
max(B_z^S) (%)	-, -	-, -	-, -	-, -
Nonuni., Nonlin. (%)	57.2, 38.1	66.3, 40.5	-, -	-, -
L (μH)	92.2, 102.2	78.6, 88.7	511, 579	440, 508
R (mΩ)	99	93	449	468
min(Δw) (mm)	6.33	3.92	15.5	11.8
M_x ($\text{NmA}^{-1}\text{T}^{-1}$)	1.8×10^{-4}	6.9×10^{-5}	-9.1×10^{-4}	-1.1×10^{-4}
M_y ($\text{NmA}^{-1}\text{T}^{-1}$)	2.0×10^{0}	1.4×10^{-2}	1.7×10^{-5}	-2.2×10^{-2}
η^2/L ($\text{T}^2\text{m}^{-2n}\text{A}^{-2}\text{H}^{-1}$)	6.83×10^{-5}	5.34×10^{-5}	1.24×10^{-6}	9.53×10^{-7}
$a^{(2n+3)}\eta^2/L$ ($\text{T}^2\text{m}^3\text{A}^{-2}\text{H}^{-1}$)	6.67×10^{-8}	5.21×10^{-8}	2.54×10^{-8}	1.95×10^{-8}
SR ($\text{Tm}^{-n}\text{s}^{-1}$)	466	438	0.87	0.81
τ (μs)	102	89	145	127
$G_{\max}$, (mTm^{-n})	47.6	38.9	0.126	0.103

Table A.4: Coil Properties.

[a] Asymmetric Cylinder.

[b] The mutual inductive coupling with an asymmetric 0.5 m radius cylindrical X-gradient coil.

Property	Coil			
Name	X	Y	Z	Z0
Design Method	IBEM	IBEM	IBEM	Slack
Geometry	S Slot[a]	S Slot[a]	S Slot[a]	Cylinder
Reference	Fig. 6.2 **a)**	Fig. 6.2 **c)**	Fig. 6.2 **e)**	Fig. 6.3 **a)**
Coil Type	X-Gradient	Y-Gradient	Z-Gradient	Z0 Shim
SH Order, n	1	1	1	0
SH Degree, m	1	-1	0	0
Coil Scale, a (m)	0.205	0.208	0.211	0.19875
Ellipsoidal ROU, V (m^3)	0.00214	0.00214	0.00214	0.00214
No. Basis Functions, N	2869	2908	2982	10
No. Target Points, K	93	93	93	63
Self-Inductance Min., α	1.0×10^{-8}	2.6×10^{-7}	7.5×10^{-8}	-
Resistance Min., β	1.2×10^{-9}	0	3.5×10^{-9}	-
Shielding Weight, γ	-	-	-	-
Turns/ψ-Contours, N_{cont}	7	7	7	10
Mutual-Inductance Min. (μH)	-	-	-	-
η, ($\mu \text{Tm}^{-n}\text{A}^{-1}$)	99.7	119.0	121.2	9.4
max(ΔB_z) (%)	5.0, 5.1	5.0, 6.1	5.0, 5.1	-, 1.11
max(B_z^S) (%)	-, 23.1[b]	-, -	-, -	-, 2.5
Nonuni., Nonlin. (%)	16.6, 0.1	15.7, 4.9	3.2, 15.8	-, -
L (μH)	60.3, 63.7	62.3, 54.9	51.8, 53.1	-, 36.9
R (mΩ)	80	69	51	115
min(Δw) (mm)	3.7	5.9	7.8	5.3
M_x ($\text{NmA}^{-1}\text{T}^{-1}$)	$< 1 \times 10^{-6}$	1.2×10^{-5}	-5.0×10^{-5}	$< 1 \times 10^{-6}$
M_y ($\text{NmA}^{-1}\text{T}^{-1}$)	5.5×10^{-5}	4.1×10^{-3}	-1.5×10^{-1}	$< 1 \times 10^{-6}$
η^2/L ($\text{T}^2\text{m}^{-2n}\text{A}^{-2}\text{H}^{-1}$)	1.65×10^{-4}	2.27×10^{-4}	2.84×10^{-4}	1.84×10^{-6}
$a^{(2n+3)}\eta^2/L$ ($\text{T}^2\text{m}^3\text{A}^{-2}\text{H}^{-1}$)	5.97×10^{-8}	8.85×10^{-8}	1.19×10^{-7}	1.43×10^{-8}
SR ($\text{Tm}^{-n}\text{s}^{-1}$)	939	1301	1369	3.92
τ (μs)	63.7	54.9	53.1	12.0
G_{max}, (mTm^{-n})	59.8	71.4	72.7	0.047

Table A.5: Coil Properties.

[a] Shoulder Slotted.

[b] Evaluated along an axial line at $x = 0.45$ m and $y = 0$ m as shown in Fig. 6.21 **d)** for comparison with the retro-fitted shielded equivalent in Table A.11.

Property	Coil			
Name	Z2	ZX	ZY	X2-Y2
Design Method	IBEM	IBEM	IBEM	IBEM
Geometry	S Slot[a]	S Slot[a]	S Slot[a]	S Slot[a]
Reference	Fig. 6.3 **b)**	Fig. 6.3 **c)**	Fig. 6.3 **d)**	Fig. 6.3 **e)**
Coil Type	Z2 Shim	ZX Shim	ZY Shim	X2-Y2 Shim
SH Order, n	2	2	2	2
SH Degree, m	0	1	-1	2
Coil Scale, a (m)	0.21575	0.21645	0.2172	0.21435
Ellipsoidal ROU, V (m^3)	0.00214	0.00214	0.00214	0.00214
No. Basis Functions, N	3039	3033	3038	3206
No. Target Points, K	93	93	93	93
Self-Inductance Min., α	1.3×10^{-9}	1.0×10^{-8}	1.95×10^{-8}	8.5×10^{-9}
Resistance Min., β	1.7×10^{-10}	0	0	7.0×10^{-11}
Shielding Weight, γ	-	-	-	-
Turns/ψ-Contours, N_{cont}	6	7	7	9
Mutual-Inductance Min. (μH)	-	-	-	-
η, ($\mu \text{Tm}^{-n}\text{A}^{-1}$)	358	361	411	181
max(ΔB_z) (%)	5.0, 6.1	5.0, 5.3	5.0, 6.9	5.0, 8.0
max(B_z^S) (%)	-, -	-, -	-, -	-, -
Nonuni., Nonlin. (%)	-, -	-, -	-, -	-, -
L (μH)	32.9, 44.7	66.3, 57.0	77.2, 69.0	82.8, 86.8
R (mΩ)	53	90	85	98
min(Δw) (mm)	7.0	4.2	7.9	5.8
M_x ($\text{NmA}^{-1}\text{T}^{-1}$)	-5.3×10^{-5}	$< 1 \times 10^{-6}$	6.3×10^{-6}	-2.1×10^{-4}
M_y ($\text{NmA}^{-1}\text{T}^{-1}$)	9.3×10^{-3}	1.1×10^{-4}	-1.9×10^{-3}	2.8×10^{-2}
η^2/L ($\text{T}^2\text{m}^{-2n}\text{A}^{-2}\text{H}^{-1}$)	3.90×10^{-3}	1.96×10^{-3}	2.19×10^{-3}	3.96×10^{-4}
$a^{(2n+3)}\eta^2/L$ ($\text{T}^2\text{m}^3\text{A}^{-2}\text{H}^{-1}$)	8.48×10^{-8}	4.37×10^{-8}	5.00×10^{-8}	8.23×10^{-9}
SR ($\text{Tm}^{-n}\text{s}^{-1}$)	160	127	119	42
τ (μs)	11.2	14.3	17.3	21.7
$G_{\max}$, (mTm^{-n})	1.8	1.8	2.1	0.9

Table A.6: Coil Properties.

[a]Shoulder Slotted.

Property	Coil			
Name	XY	Dome X	Dome Y	Dome Z
Design Method	IBEM	IBEM	IBEM	IBEM
Geometry	S Slot[a]	Domed	Domed	Domed
Reference	Fig. 6.3 **f)**	Fig. 6.8 **a)**	§ 6.2.2	§ 6.2.2
Coil Type	XY Shim	X-Gradient	Y-Gradient	Z-Gradient
SH Order, n	2	1	1	1
SH Degree, m	-2	1	-1	0
Coil Scale, a (m)	0.21505	0.172	0.184	0.195
Ellipsoidal ROU, V (m^3)	0.00214	0.00147	0.00147	0.00147
No. Basis Functions, N	3045	1313	1313	1313
No. Target Points, K	93	325	325	325
Self-Inductance Min., α	2.3×10^{-8}	4.0×10^{-6}	2.4×10^{-6}	9.0×10^{-7}
Resistance Min., β	1.1×10^{-10}	3.0×10^{-9}	4.5×10^{-9}	0
Shielding Weight, γ	-	-	-	-
Turns/ψ-Contours, N_{cont}	9	7	7	7
Mutual-Inductance Min. (μH)	-	-	-	-
η, ($\mu \text{Tm}^{-n}\text{A}^{-1}$)	252	357	304	333
max(ΔB_z) (%)	5.0, 5.3	5.0, 5.1	5.0, 5.0	5.0, 5.2
max(B_z^S) (%)	-, -	-, -	-, -	-, -
Nonuni., Nonlin. (%)	-, -	0.9, 15.7	1.2, 15.4	12.1, 0.5
L (μH)	108.4, 108.6	48.5, 50.0	54.0, 56.1	99.3, 96.2
R (mΩ)	109	48	52	60
min(Δw) (mm)	3.4	3.1	3.0	4.7
M_x ($\text{NmA}^{-1}\text{T}^{-1}$)	$< 1 \times 10^{-6}$	-1.6×10^{-5}	-1.6×10^{-5}	-1.0×10^{-6}
M_y ($\text{NmA}^{-1}\text{T}^{-1}$)	2.0×10^{-4}	8.9×10^{-4}	8.9×10^{-6}	$< 1 \times 10^{-6}$
η^2/L ($\text{T}^2\text{m}^{-2n}\text{A}^{-2}\text{H}^{-1}$)	5.86×10^{-4}	2.62×10^{-3}	1.65×10^{-3}	1.15×10^{-3}
$a^{(2n+3)}\eta^2/L$ ($\text{T}^2\text{m}^3\text{A}^{-2}\text{H}^{-1}$)	1.25×10^{-8}	3.94×10^{-7}	3.47×10^{-7}	3.25×10^{-7}
SR ($\text{Tm}^{-n}\text{s}^{-1}$)	46.4	4263	3241	2077
τ (μs)	27.2	50.1	56.1	96.2
G_{max}, (mTm^{-n})	1.3	214	182	200

Table A.7: Coil Properties.

[a] Shoulder Slotted.

Property	Coil			
Name	Dome X	X	Y	Z
Design Method	IBEM	IBEM	IBEM	IBEM
Geometry	Dome	Shld Dome[a]	Shld Dome[a]	Shld Dome[a]
Reference	§ 6.2.2	Fig. 6.10 **a)**	Fig. 6.10 **c)**	Fig. 6.10 **e)**
Coil Type	X-Gradient	X-Gradient	Y-Gradient	Z-Gradient
SH Order, n	1	1	1	1
SH Degree, m	1	1	-1	0
Coil Scale, a (m)	0.172	0.14375[b]	0.14375[b]	0.14375[b]
Ellipsoidal ROU, V (m^3)	0.00147	0.00381	0.00381	0.00381
No. Basis Functions, N	1313	2162	2162	2162
No. Target Points, K	325	1085	1085	1085
Self-Inductance Min., α	0	3.1×10^{-6}	4.7×10^{-6}	2.95×10^{-6}
Resistance Min., β	9.0×10^{-8}	0	0	2.0×10^{-9}
Shielding Weight, γ	-	1	1	1
Turns/ψ-Contours, N_{cont}	12	10	10	10
Mutual-Inductance Min. (μH)	-	-	-	-
η, ($\mu \text{Tm}^{-n}\text{A}^{-1}$)	618	327	287	456
max(ΔB_z) (%)	5.0, 5.1	4.8, 5.0	4.9, 5.0	5.0, 5.0
max(B_z^S) (%)	-, -	0.5, 2.4	0.6, 2.0	0.8, 1.5
Nonuni., Nonlin. (%)	0.7, 16.1	5.0, 22.5	0.7, 21.0	25.6, 3.3
L (μH)	147, 146	58.0, 63.0	50.3, 56.1	105, 112
R (mΩ)	84	76	74	83
min(Δw) (mm)	3.0	4.4	5.9	3.0
M_x ($\text{NmA}^{-1}\text{T}^{-1}$)	$< 1 \times 10^{-6}$	-8.0×10^{-6}	5.1×10^{-3}	-3.5×10^{-4}
M_y ($\text{NmA}^{-1}\text{T}^{-1}$)	-1.2×10^{-3}	9.3×10^{-4}	4.4×10^{-5}	-6.5×10^{-4}
η^2/L ($\text{T}^2\text{m}^{-2n}\text{A}^{-2}\text{H}^{-1}$)	2.62×10^{-3}	1.84×10^{-3}	1.64×10^{-3}	1.98×10^{-3}
$a^{(2n+3)}\eta^2/L$ ($\text{T}^2\text{m}^3\text{A}^{-2}\text{H}^{-1}$)	3.59×10^{-7}	1.13×10^{-7}	1.01×10^{-7}	1.22×10^{-7}
SR ($\text{Tm}^{-n}\text{s}^{-1}$)	2547	3114	3070	2442
τ (μs)	146	63.0	56.1	112.0
$G_{\max}$, (mTm^{-n})	371	196	172	274

Table A.8: Coil Properties.

[a] Shielded Dome.

[b] Average radius of the inner surface.

Property	Coil			
Name	Short X	Short Y	Short Z	PET X
Design Method	IBEM	IBEM	IBEM	IBEM
Geometry	Ultra-Short	Ultra-Short	Ultra-Short	Central Gap
Reference	Fig. 6.13 **a)**	§ 6.4.2	§ 6.4.2	Fig. 6.15 **a)**
Coil Type	X-Gradient	X-Gradient	Y-Gradient	Z-Gradient
SH Order, n	1	1	1	1
SH Degree, m	1	-1	0	1
Coil Scale, a (m)	0.344	0.336	0.356	0.08945
Ellipsoidal ROU, V (m^3)	0.0524	0.0524	0.0524	0.000524
No. Basis Functions, N	3040	3040	3040	2820
No. Target Points, K	1067	1067	1067	1115
Self-Inductance Min., α	1.7×10^{-7}	1.7×10^{-7}	1.34×10^{-7}	0
Resistance Min., β	0	5.0×10^{-10}	0	1.0×10^{-7}
Shielding Weight, γ	0.1	0.1	0.1	0.5
Turns/ψ-Contours, N_{cont}	27	27	21	18
Mutual-Inductance Min. (μH)	-	-	-	-
η, ($\mu \text{Tm}^{-n}\text{A}^{-1}$)	72.6	76.5	115.0	679
$\max(\Delta B_z)$ (%)	5.0, 5.0	5.0, 5.0	4.9, 5.0	4.3, 4.3
$\max(B_z^S)$ (%)	3.3, 3.6	3.3, 3.5	2.6, 2.7	2.0, 2.8
Nonuni., Nonlin. (%)	2.1, 22.5	2.9, 22.8	18.1, 0.9	15.5, 14.6
L (μH)	699, 742	690, 732	1270, 1339	111, 108
R (mΩ)	636	612	822	117
$\min(\Delta w)$ (mm)	5.6	6.1	5.5	4.2
M_x ($\text{NmA}^{-1}\text{T}^{-1}$)	-3.3×10^{-5}	-2.7×10^{-4}	-1.3×10^{-6}	$< 1 \times 10^{-6}$
M_y ($\text{NmA}^{-1}\text{T}^{-1}$)	-9.0×10^{-3}	2.0×10^{-6}	1.4×10^{-6}	4.6×10^{-6}
η^2/L ($\text{T}^2\text{m}^{-2n}\text{A}^{-2}\text{H}^{-1}$)	7.55×10^{-6}	8.48×10^{-6}	1.05×10^{-5}	4.16×10^{-3}
$a^{(2n+3)}\eta^2/L$ ($\text{T}^2\text{m}^3\text{A}^{-2}\text{H}^{-1}$)	3.64×10^{-8}	3.64×10^{-8}	6.00×10^{-8}	2.38×10^{-8}
SR ($\text{Tm}^{-n}\text{s}^{-1}$)	58.7	62.7	51.5	3783
τ (μs)	636	732	1339	117
$G_{\max}$, (mTm^{-n})	43.6	45.9	69.0	407

Table A.9: Coil Properties.

Property	Coil			
Name	Pet Y	PET Z	PET Z0	X[a]
Design Method	IBEM	IBEM	IBEM	IBEM
Geometry	Central Gap	Central Gap	Central Gap	1 Layer
Reference	§ 6.5.2	Fig. 6.15 **c)**	Fig. 6.15 **e)**	Fig. 6.17 **a)**
Coil Type	Y-Gradient	Z-Gradient	Z0 Shim	X-Gradient
SH Order, n	1	1	0	1
SH Degree, m	-1	0	0	1
Coil Scale, a (m)	0.09295	0.0856	0.09955	0.25
Ellipsoidal ROU, V (m^3)	0.000524	0.000524	0.000524	0.0082
No. Basis Functions, N	2820	2400	2400	1748
No. Target Points, K	1115	1754	1754	578
Self-Inductance Min., α	0	0	0	0
Resistance Min., β	1.2×10^{-7}	2.0×10^{-6}	8.0×10^{-9}	4.0×10^{-9}
Shielding Weight, γ	1	5	0.7	-
Turns/ψ-Contours, N_{cont}	20	7	19	6
Mutual-Inductance Min. (μH)	-	-	-	-
η, ($\mu \text{Tm}^{-n}\text{A}^{-1}$)	659	793	15.1	65.1
$\max(\Delta B_z)$ (%)	5.2, 5.2	5.0, 5.0	4.9, 5.1	5.0, 5.0
$\max(B_z^S)$ (%)	2.0, 2.6	1.5, 1.6	5.0, 4.7	-, -
Nonuni., Nonlin. (%)	16.4, 12.6	4.3, 19.0	-, -	27.4, 19.8
L (μH)	127, 120	46.6, 39.8	134, 136	181, 173
R (mΩ)	128	42	126	121
$\min(\Delta w)$ (mm)	3.6	3.2	2.0	3.05
M_x ($\text{NmA}^{-1}\text{T}^{-1}$)	$< 1 \times 10^{-6}$	$< 1 \times 10^{-6}$	$< 1 \times 10^{-6}$	$< 1 \times 10^{-6}$
M_y ($\text{NmA}^{-1}\text{T}^{-1}$)	2.8×10^{-6}	$< 1 \times 10^{-6}$	$< 1 \times 10^{-6}$	$< 1 \times 10^{-6}$
η^2/L ($\text{T}^2\text{m}^{-2n}\text{A}^{-2}\text{H}^{-1}$)	3.42×10^{-3}	1.35×10^{-2}	1.70×10^{-6}	2.34×10^{-5}
$a^{(2n+3)}\eta^2/L$ ($\text{T}^2\text{m}^3\text{A}^{-2}\text{H}^{-1}$)	2.37×10^{-8}	6.21×10^{-8}	1.68×10^{-9}	2.29×10^{-8}
SR ($\text{Tm}^{-n}\text{s}^{-1}$)	3292	11955	2.22	226.3
τ (μs)	120	39.8	34.0	173
$G_{\max}$, (mTm^{-n})	395	475.8	75.5	39.1

Table A.10: Coil Properties.

[a]The Y-gradient coil has identical properties since it is on the same layer as the X-gradient.

Property	Coil			
Name	Z	Openable Z	Biradial ZX	Retro-Shield
Design Method	IBEM	IBEM	IBEM	IBEM
Geometry	1 Layer	Openable	Biradial	Cylinder
Reference	Fig. 6.17 **c)**	Fig. 6.19 **a)**	Fig. 6.20 **a)**	Fig. 6.21 **c)**
Coil Type	Z-Gradient	Z-Gradient	ZX Shim	X-Shield
SH Order, n	1	1	2	1
SH Degree, m	0	0	1	1
Coil Scale, a (m)	0.25	0.125	0.24	0.205
Ellipsoidal ROU, V (m^3)	0.0082	0.0021	0.0042	0.00214
No. Basis Functions, N	1376	1550	1104	2112
No. Target Points, K	578	1026	258	809
Self-Inductance Min., α	1.0×10^{-7}	2.5×10^{-5}	0	8.0×10^{-9}
Resistance Min., β	2.3×10^{-7}	0	1.0×10^{-9}	0
Shielding Weight, γ	-	-	-	10
Turns/ψ-Contours, N_{cont}	6	10	10	7
Mutual-Inductance Min. (μH)	-	-	-	-
η, ($\mu \text{Tm}^{-n}\text{A}^{-1}$)	160	560	219	70.2^a
max(ΔB_z) (%)	5.1, 5.1	5.2, 5.6	12.7, 13.0	-, 4.6^a
max(B_z^S) (%)	-, -	-, -	-, -	-, $1.7^{a\,b}$
Nonuni., Nonlin. (%)	1.3, 22.5	24.4, 3.7	-, -	15.6^a , 4.1^a
L (μH)	744, 718	125, 127	93, 106	-, 75.2^a
R (mΩ)	222	180	685	159^a
min(Δw) (mm)	4.8	4.7	5.2	3.7^a
M_x ($\text{NmA}^{-1}\text{T}^{-1}$)	$< 1 \times 10^{-6}$	$< 1 \times 10^{-6}$	$< 1 \times 10^{-6}$	$1.7 \times 10^{-4\,a}$
M_y ($\text{NmA}^{-1}\text{T}^{-1}$)	$< 1 \times 10^{-6}$	$< 1 \times 10^{-6}$	-3.0×10^{-3}	$-1.7 \times 10^{-2\,a}$
η^2/L ($\text{T}^2\text{m}^{-2n}\text{A}^{-2}\text{H}^{-1}$)	$3.46{\times}10^{-5}$	$2.54{\times}10^{-3}$	$5.17{\times}10^{-4}$	$6.55{\times}10^{-5\,a}$
$a^{(2n+3)}\eta^2/L$ ($\text{T}^2\text{m}^3\text{A}^{-2}\text{H}^{-1}$)	$3.38{\times}10^{-8}$	$7.66{\times}10^{-8}$	$2.37{\times}10^{-8}$	$2.37{\times}10^{-8\,a}$
SR ($\text{Tm}^{-n}\text{s}^{-1}$)	134	2652	41.2	560.1^a
τ (μs)	718	127	27	75^a
G_{max}, (mTm^{-n})	96	336	1095	42.1^a

Table A.11: Coil Properties.

[a] Value calculated from the primary and retro-fitted shield in combination.

[b] Evaluated along an axial line at $x = 0.45$ m and $y = 0$ m as shown in Fig. 6.21 **d)** for comparison with the unshielded equivalent in Table A.5.

Property	Coil			
Name	Multi Z	PC[a] 1	PC[a] 2	PC[a] 3
Design Method	IBEM	IBEM	IBEM	IBEM
Geometry	Cylinder	Asym Cyl[b]	Asym Cyl[b]	Asym Cyl[b]
Reference	Fig. 6.22 **a)**	Fig. 6.25	§ 6.11.3	§ 6.11.3
Coil Type	Z-Gradient	PC[a]	PC[a]	PC[a]
SH Order, n	1	-	-	-
SH Degree, m	0	-	-	-
Coil Scale, a (m)	0.3	0.12	0.12	0.12
Ellipsoidal ROU, V (m^3)	0.0239[c]	0.0011[d]	0.0011[d]	0.0011[d]
No. Basis Functions, N	2352	2352	2352	2352
No. Target Points, K	1274	2108	2108	2108
Self-Inductance Min., α	8.5×10^{-8}	0	0	0
Resistance Min., β	0	1.0×10^{-9}	1.0×10^{-9}	1.0×10^{-9}
Shielding Weight, γ	-	-	-	-
Turns/ψ-Contours, N_{cont}	20	10	10	10
Mutual-Inductance Min. (μH)	-	-	-	-
η, ($\mu \text{Tm}^{-n}\text{A}^{-1}$)	138	0.90	1.63	7.76
max(ΔB_z) (%)	4.2, 5.0	3.8[e]	5.0[e]	2.9[e]
max(B_z^S) (%)	-, -	-, -	-, -	-, -
Nonuni., Nonlin. (%)	-, -	-, -	-, -	-, -
L (μH)	764, 782	28.9, 30.4[f]	30.9, 42.1[f]	101, 111[f]
R (mΩ)	313	406[f]	507[f]	951[f]
min(Δw) (mm)	5.6	1.6	1.8	1.4
M_x ($\text{NmA}^{-1}\text{T}^{-1}$)	$< 1 \times 10^{-6}$	-3.3×10^{-4}	-2.2×10^{-3}	-4.3×10^{-3}
M_y ($\text{NmA}^{-1}\text{T}^{-1}$)	$< 1 \times 10^{-6}$	$< 1 \times 10^{-6}$	$< 1 \times 10^{-6}$	$< 1 \times 10^{-6}$
η^2/L ($\text{T}^2\text{m}^{-2n}\text{A}^{-2}\text{H}^{-1}$)	2.48×10^{-5}	2.78×10^{-8}	8.60×10^{-8}	5.96×10^{-7}
$a^{(2n+3)}\eta^2/L$ ($\text{T}^2\text{m}^3\text{A}^{-2}\text{H}^{-1}$)	6.03×10^{-8}	4.80×10^{-11}	1.49×10^{-10}	1.03×10^{-9}
SR ($\text{Tm}^{-n}\text{s}^{-1}$)	106	0.59	0.77	1.40
τ (μs)	782	7.6	10.5	27.8
$G_{\max}$, (mTm^{-n})	82.8	0.0045	0.00815	0.039

Table A.12: Coil Properties.

[a] Principal component.
[b] Asymmetric cylinder.
[c] Volume of 2 cylindrical ROUs.
[d] Approximate volume occupied by 2108 voxels.
[e] RMS percentage field deviation.
[f] Simulated with 1 mm diameter circular cross-section wire.

Property	Coil			
Name	PC[a] 4	2D MAMBA	Teapot	Mug
Design Method	IBEM	IBEM	IBEM	IBEM
Geometry	Asym Cyl[b]	2D MAMBA	Teapot	Mug
Reference	§ 6.11.3	Fig. 6.29 **a)**	Fig. 6.31 **a)**	Fig. 6.31 **b)**
Coil Type	PC[a]	Multi Z0	X-Gradient	Z-Gradient
SH Order, n	-	-	1	1
SH Degree, m	-	-	1	0
Coil Scale, a (m)	0.12	0.06[c]	0.743[d]	0.365[d]
Ellipsoidal ROU, V (m^3)	0.0011[e]	0.0004[f]	0.30	0.249
No. Basis Functions, N	2352	2746	1289	1521
No. Target Points, K	2108	576	578	1105
Self-Inductance Min., α	0	0	2.0×10^{-6}	5.0×10^{-7}
Resistance Min., β	1.0×10^{-9}	9.5×10^{-8}	0	0
Shielding Weight, γ	-	-	-	0.1
Turns/ψ-Contours, N_{cont}	10	33	10	10
Mutual-Inductance Min. (μH)	-	-	-	-
η, ($\mu \text{Tm}^{-n}\text{A}^{-1}$)	3.66	47.1	32.3	100
max(ΔB_z) (%)	4.56[g]	1.9, 1.9	5.8, 5.8	4.5, 5.0
max(B_z^S) (%)	-, -	-, -	-, -	3.0, 13.1
Nonuni., Nonlin. (%)	-, -	-, -	4.8, 26.5	21.2, 5.9
L (μH)	59.3, 57.3	1690, -	333, 374	123, 145
R (mΩ)	645	-	269	224
min(Δw) (mm)	1.6	1.0	19.7	9.6
M_x ($\text{NmA}^{-1}\text{T}^{-1}$)	-4.2×10^{-3}	$< 1 \times 10^{-6}$	3.5×10^{-4}	-4.2×10^{-4}
M_y ($\text{NmA}^{-1}\text{T}^{-1}$)	$< 1 \times 10^{-6}$	$< 1 \times 10^{-6}$	-1.0×10^{-2}	-1.6×10^{-2}
η^2/L ($\text{T}^2\text{m}^{-2n}\text{A}^{-2}\text{H}^{-1}$)	2.26×10^{-7}	1.31×10^{-6}	3.14×10^{-6}	8.13×10^{-5}
$a^{(2n+3)}\eta^2/L$ ($\text{T}^2\text{m}^3\text{A}^{-2}\text{H}^{-1}$)	3.91×10^{-10}	2.81×10^{-10}	7.11×10^{-7}	5.7×10^{-7}
SR ($\text{Tm}^{-n}\text{s}^{-1}$)	1.28	0.56	51.8	413.8
τ (μs)	14.3	443	374	145
$G_{\max}$, (mTm^{-n})	0.0183	236	19.4	500

Table A.13: Coil Properties.

[a] Principal component.
[b] Asymmetric cylinder.
[c] Separation of the two plates of wire.
[d] Average distance of the elements from the origin for the highly asymmetric shape.
[e] Approximate volume occupied by 2108 voxels.
[f] Approximate volume occupied by the 576 points in a plane.
[g] RMS percentage field deviation.